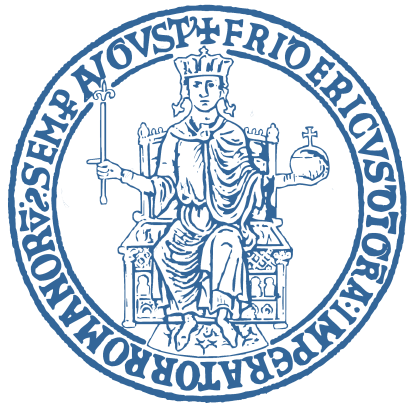

Università degli Studi di Napoli "Federico II"

Department of Industrial Engineering
Aerospace ~ Division

Doctoral Course in

Industrial Engineering

Ph.D. Dissertation

Structural Health Monitoring of complex structures based on propagation and scattering of Guided Ultrasonic Waves in composite media

Doctoral Coordinator
Prof. Michele Grassi

Supervisor
Prof. Fabrizio Ricci

Candidate
Vittorio Memmolo

Academic Year 2016/2017

Ai miei genitori, sulle cui spalle
la faccio da Gigante . . .
Ad Elena, con cui nella Storia
la mia Vita Immortale . . .

Contents

Abstract

The major concern of aerospace and transportation engineering during the last years has been related to increase performances and safety with energy savings. Composite materials have been indeed widely adopted with the aim to design high performance and lighter components. However, random events such as certain low velocity impacts may induce barely visible or not visible failure due to their complex mechanics behavior. Impact induced damages in stiffened composite structures are usually accommodated with constrained design and strictly maintenance tasks which increase operational costs above all else and decrease the advantages for which composites have been massively introduced. To overcome such drawbacks, an integrated structure providing monitoring of critical components appears a reasonable solution. A condition-based approach could be able to relax the maintenance strategy minimizing aircraft downtime as well. Moreover the design constraints would be avoided further increasing the structural performance with a more ecological friendly aircraft. Although this is a very long time perspective, for the first demand Structural Health Monitoring (SHM) systems, providing information about the structural efficiency, appear to be the best solution.

Within this context, the work deals with detection, localization and size assessment of sudden failures like delamination and disbondings with on-line monitoring technique by permanently attached piezoelectric transducers (PZT) capable to excite and sense guided ultrasonic waves. Composite stiffened structures typically designed for aircraft wing-box are mainly investigated. Delamination between several layers and disbondings are carried out inducing low velocity impacts with the attempt to analyze different and complex damage scenarios. Two different approaches are mainly proposed. Anti-symmetric propagation based technique (global approach) using the A_0 Lamb wave mode for interrogation demand is first presented to obtain a fast end effective localization of damage, no matter the failure type is. A reliable solution is also provided using a multi-parameter approach to increase the probability of detection. The obtained algorithm is implemented in a graphic user interface developed and coded by the author. Different features, including customized selection of ultrasonic time histories, statistical threshold definition and interactive tools for self-diagnosis of sensors and complex geometry representation are developed to obtain an effective tool for global damage diagnosis.

Although the promising results obtained with a fewer computational time required respect to classic tomographic approaches, size and severity of damage can be assessed only statistically relating the metric adopted to the flaw dimension. However, their deterministic assessment is crucial where the stringers adopted to reinforce thin walled structures are affected by not visible disbondings. This fact leads to the separation between the stiffener and the hosting structure preventing the collaboration between parts with a dangerous drawback for loading absorbing. For the last demand, usually disbonding stoppers are designed to prevent critical decrease of load carrying capacity below the limit design loads. Towards a condition based approach, a novel detection technique capable to predict arrival time of guided waves redirected by stringers to detect any possible change in a specific scattering area is presented. Hence, the reflections of wave interacting with stiffeners can be analyzed to improve

the diagnostic leading to a point by point interrogation (local approach). Theoretical aspects are investigated to correctly exploit the technique leading to a geometrical reduction to describe the propagation of the A_0 mode including boundary (stringer) reflections. The model is capable to return the optimal design of the system achieving a high performance diagnostic. Several measurements are carried out to validate the adopted propagation model and a promising result in agreement with classic ultrasonic nondestructive testing is thus obtained and discussed. Furthermore it is shown that accounting Lamb wave reflections improves the localization accuracy respect a general purpose reconstruction algorithm while making use of fewer number of sensors possible or increase the probability of detection combining both methodologies.

The mentioned results are achieved with large experimental campaigns as well as comprehensive numerical simulations with the aim to better understand the physics of wave propagation in composite media typically adopted in the aerospace field. Several strategies have been investigated using finite element methods with the attempt to reduce the experimental costs as well as system validation efforts. Using an effective equivalent single layer approach, the flexural behavior of the A_0 mode has been modeled correctly. The proposed simulated environment allows to correctly relate the propagation and damage interaction behavior to effective features to detect damage with fewer efforts possible. Moreover, a preliminary and strategic analysis for the global approach is indeed carried out with the attempt to verify the feasibility of a numerical framework for system performance assessment using a (model assisted) probability of detection approach.

The concluding part of the work focuses on a preliminary investigation of a transducer self-diagnostic procedure, aimed to in-situ monitoring of the sensors and actuators used in the SHM methodologies presented. Due to the large number of distributed PZTs needed to correctly interrogate the structure, confirming if sensors/actuators are functioning properly during operation is a crucial process to minimize false alarms in the diagnosis. The procedure verified is based on the capacitive analysis of piezoelectric sensors, which is manifested in the imaginary part of the measured electrical admittance. Even though a further investigation is needed to study more complex sensor fault scenarios, the final algorithm is able to simultaneously sort sensors and detect damages with information gathered from healthy transducers.

Chapter 1

Composite Maintenance Fundamentals

Contents

Structural Health Monitoring (SHM) approaches are usually demanded to autonomously provide diagnosis and prognosis of complex (composite) structures using sophisticated techniques. Which begs the question; what is the reason aiming an autonomous (further) complex system integrated in a (formerly) complex structure? Nowadays, aircrafts and, generally, transportation systems are demanded to meet challenging constraints, to last long and to withstand deterioration. Thus, they need a dedicated and detailed design and they have to be checked according to a scheduled inspection and maintenance program ensuring those constraints to be satisfied during lifetime. Apparently, there is no motivation to move from a standard design-maintenance philosophy to a more complex and not well known monitoring approach. Namely, it is worth discarding many years of experience in aircraft (optimum) maintenance and starting again to optimize the aircrafts lifetime including

SHM? In this context, the present chapter is aimed to first provide motivations and objectives leading to structural health monitoring philosophy. The critical issue is focused around the massive introduction of composites, which is first explained and then oriented towards the aerospace design and maintenance fields. The necessity of inspections and the typically addressed non destructive techniques (NDT) are briefly introduced showing then the efficient solution provided by a SHM system as a NDT integration in the structure. Finally, an overview and different topics of SHM system are described to definitely introduce such field and define the related techniques.

1.1 Benefits of composite within aerospace field

Composite materials have been widely and increasingly employed to design high performance structures, mostly increasing stress to weight ratio to obtain lighter and stiffer components while compared with metallic structures. In the aerospace field, composites have been extensively adopted instead of classic aluminum alloys to reduce fuel consumation and/or increase payload. Keeping fixed the payload, a small weight reduction indeed ensures less consumation and even less fuel is necessary to be stored according to the typical *snowball effect* while designing aircrafts and estimating the weight [1]. An important aspect consists of the flexible design of the structure according to anisotropic properties of composite materials [2], making them even more efficient for load cases and conditions typically withstanded by aerostructures [3]. Composite materials indeed offer the possibility to design stiffness and strength characteristics of the final structure by suitably selecting the type of reinforcing fibers and the distribution of the reinforcing directions; namely they allow to adapt these features as a function of the applied loads and structural requirements. Finally, the possibility to create structural component with fewer connections possible (e.g. Boeing 787 *one piece barrel*) definitely made composites so successful.

Summarizing all benefits may be introduced by adopting such materials, it is possible to emphasize that composites:

- provide superior performances when compared to steel or aluminum;
- reduce the weight of the final component;
- reduce the maintenance costs;
- reduce or eliminates corrosion issues;
- have better fatigue resistance;
- show less thermal expansion;

- allow enhanced properties via tailorable properties:
  - mechanical;
  - electrical;
  - anisotropic.

Without discuss every point, it is possible to declare that with an all-composite aircraft, the principal aims can be broadly divided in:

- to save on weight and therefore fuel;
- to achieve easier and cheaper manufacturing;
- to ensure less maintenance and hence lower operating costs;
- to improve flying qualities.

Such expected advantages induced the world leading aircraft manufacturers (i.e. *Boeing Company* and *Airbus S.A.S*) to move from all-aluminum aircrafts towards vehicles increasingly made of carbon fibre reinforced plastics (CFRP). Composite materials have been adopted for a long time in secondary structures, interiors and other parties for the proved benefits. Introduced in the '80s with a large amount of technology innovations, the primary structures of the Airbus A320 are of composite construction with aramid fibre (AFRP), glass fibre (GFRP) and carbon fibre (CFRP) reinforced plastics. The A320 is indeed the first subsonic aircraft to incorporate composite primary structures. Then, the launch of the Airbus A380 was a commercial and a technical challenge to Boeing in the market sector. With that project, Airbus announced to move from the traditional all-aluminum aircraft, with approximately 22% of it made using composites. On the other hand, Boeing responded to the Airbus commercial and technical challenge with the mid-size 787 *Dreamliner*. It is indeed the first airliner with the use of composite materials as the primary material in the construction of its airframe, namely the first almost all-composite aircraft, with approximately 50% composites by weight, or 80% by volume. The 787 is the first major commercial airplane to have a composite fuselage, composite wings, and use composites in most other airframe components [4]. Furthermore, the 787 was designed to be the first production airliner with the fuselage comprising one-piece composite barrel sections instead of the multiple aluminum sheets and some 50,000 fasteners used on existing aircrafts [5]. Each 787 aircrft contains approximately 35 tons of carbon fiber reinforced polymer (CFRP), made with 23 tons of carbon fiber distributed on fuselage, wings, tail, doors, and interior. The CFRP adopted here is approximately the same of that used for A380 manufacturing, although the completely different dimensions. From that time a

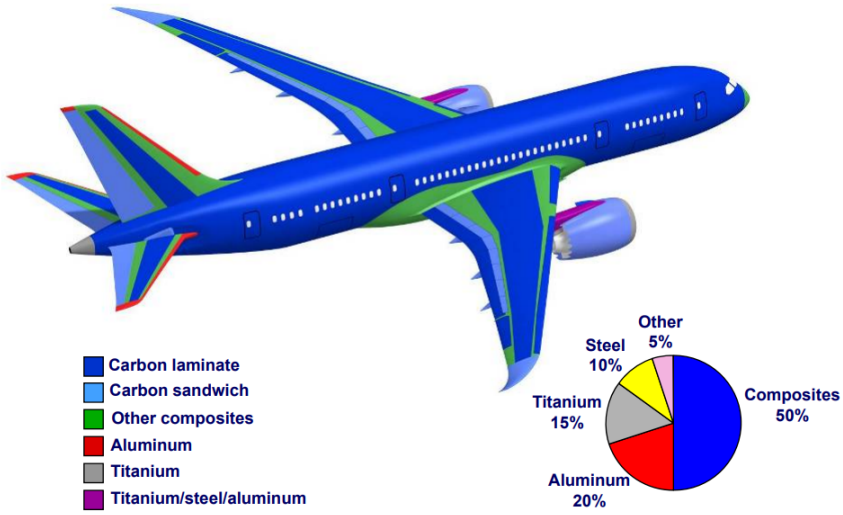

Figure 1.1: Composite solutions applied throughout the Boeing B787 Dreamliner [6].

primary structure made of composite moved from a novelty to the state of the art to increase structural performances. After suggesting Boeing's use of composite materials for the 787 fuselage was premature and designing the new aircraft with a relatively limited amount of composites, Airbus announced indeed its massive use for the new redesigned A350 XWB, confirming in early September 2007 the adoption of composite fuselage frames for the aircraft structure. As a matter of facts, the A350 XWB airframe is actually made out of 53% composites: carbon fibre reinforced plastic for the outer and centre wing box (covers, stringers, spars), fuselage (skin, frame, keel beam, and rear fuselage) and the empennage (horizontal and vertical tailplanes); 19% aluminum and $Al - Li$ for ribs, floor beams and gear bays; 14% titanium for landing gears, pylons and attachments; 6% steel and 8% miscellaneous. Instead, the Boeing 787 is 50% composites, 20% aluminum, 15% titanium, 10% steel, and 5% other (see Figure 1.1). The trend is unavoidably in favor of increasing composites parts, as depicted in Figure 1.2 and confirmed also by other manufacturers of narrow body jet aircrafts, like Bombardier CSeries and Learjet, which are the first in commercial aircrafts to use dry fiber composites. Both feature integrally stiffened upper and lower wingskins, front spar and rear spar, all made from carbon composites, which are mechanically fastened together along with aluminum ribs.

The design of 787 Dreamliner is the focal point of composite implementation within aircrafts, remolding the airline industry. The advantages introduced are evident and in line with those aforementioned. The Boeing's *Plastic Dream Machine* demonstrated that:

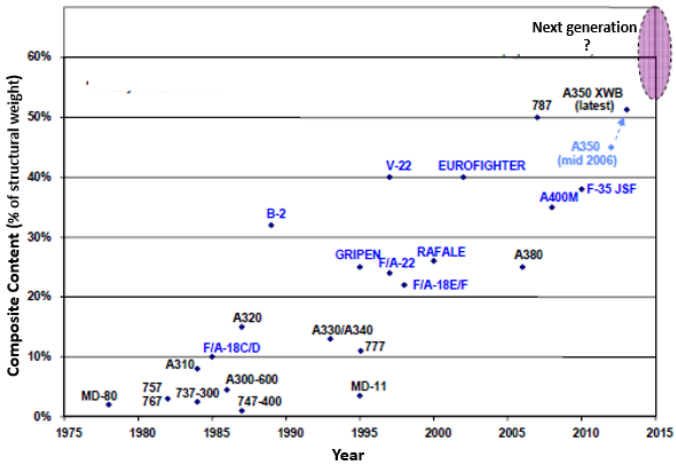

Figure 1.2: The use of composite in modern structural design. Civil (black) and military (blue) aircrafts [7].

- jets made of composites require far fewer parts, so there is less to bolt together;
- these plastics weigh less than aluminum, with weight reduction and improved fuel efficiency (the planes burn less fuel. Together with improved engines, 20% drop in fuel costs is obtained with that aircraft);
- the use of composites improves passenger comfort. The superior strength of the composite fuselage allows the passenger cabin to withstand higher pressurization – equal to the air pressure at an altitude of 6,000 feet instead of the usual 8,000 feet. Moreover larger windows can be designed in favour of passengers pleasure;
- composites are corrosion resistant and it is easier to control cabin temperature, humidity, and ventilation;
- composites are even tougher than aluminum alloys. Together with other aspects, the higher durability allows maintenance costs to be much lower than for aluminum planes (30% drop in maintenance costs is expected for 787 in service aircrafts).

The operational costs, involving inspections and maintenance operation, have been estimated to be 25% of the life cycle cost of an aircraft. That is where the role of composite materials is really crucial. Just to detail and prove their advantages in this context, a comparison of intervals between principal maintenance tasks is reported in Table 1.1 for Boeing commercial aircrafts including a relevant percentage of composite materials. According to the manufacturer, the maintenance frequency is indeed reduced mainly by the introduction of the new materials.

Boeing	767	777	787
Carbon Percentage	3	12	50
Line Maintenance Inteval (hrs)	500	600	1000
Base Maintenance Inteval (months)	500	600	1000
Heavy structural Inspection (years)	6	8	12

Table 1.1: Comparison of maintenance intervals of Boeing commercial aircrafts including a relevant percentage of composite materials. Source: the Boeing company.

However, the A350 project, where a hybrid metal-composite fuselage was designed and regarded as less risky, prompted concerns about the safety risks of widespread use of this type of material. Basically carbon fiber, unlike metal, does not visibly show cracks and fatigue, namely the critical aspect *exciting* the present work. As a matter of facts, also the "dream machine" designed by Boeing become more complex than expected when managing composites. The Boeing 767 was developed from 1978 and the first delivery was about four years later in 1982. The development of Boeing 787 began on 2003, the first flight set for August 2007 and fist delivery set for May 2008. Actually, the first test flight has been conducted on December 2009 (with more than 2 years delay) and the first delivery on October 2011 (with more than three years delay). Which begs the question appeared on Aerospace Testing International on September 2008; it is worth discarding 75 years of experience of aluminum aircraft and starting again? Most of the delay in development of 787 aircraft is due to the massive composites introduction, where the mechanics knowledge is far from the experience gained with aluminum alloys. A critical point, which is also limiting the benefits introduced by composites, is the failure mechanism. Basically, metals are ductile, and elastic deformation warns that a failure is about to happen, which normally leaves sufficient time for measures to prevent sudden failure. This behavior is well exploited in aviation, where design is based on damage tolerance. Composites, on the other hand, are brittle and this means that fracturing occurs more suddenly, leaving a limited window of opportunity for timely warning. Composites are highly susceptible to hidden flaws that may arise from manufacturing defects, foreign object impact, mechanical and thermal fatigue. Many of these defects can occur at any time during service of the structure. Proper maintenance at regular intervals is thus critical to ensure the safety of these structures, adding large amounts to their costs of operation.

Structural Health Monitoring fits in this context to reduce such limitations simply introducing monitoring, inspection and damage detection as an integral part of the structure. However, before moving into details of this topic, a brief overview of structural failure principles and composite materials behaviour is presented in the next

section with the attempt to clarify how the aircraft design and lifetime are affected and which are the real benefits while introducing effective SHM.

1.2 Design of composite materials

While it is true that composites provide many benefits, nonetheless the complex mechanics directly affect the design of aerostructures and maintenance approaches. As a matter of facts, large part of such an improvement of structural performance introducing new materials is canceled while accounting unforeseen events, like manufacturing uncertainties, environmental effects, sudden failures and design safety introducing the so called *knockdown factors*. At the same time, the unexpected and unstable response of composites due to their brittle nature requires continuous inspections and strict maintenance tasks which decrease the expected reduction of costs. Even though they are the key factors demanding structural health monitoring strategies, it is often neglected the relation between such aspects and how the benefits while introducing composites are affected and far from that expected. That is the concept of this section in which the effect of failure principles and unforeseen events are introduced and connected to design and maintenance approaches which are actually in use within aerospace field.

1.2.1 Failure principles

The modes of failure of a structure can be put in two general categories, namely, structural failure and material failure. The former is characterized by the loss of ability to perform the intended structural function (e.g. elastic buckling and flutter) and always it may be attributed to excessive deflections of the structure and may not necessarily involve breakage of the structure itself. On the other hand, material failure usually involves excessive permanent deformation or fracture of the material. The presence of crack (delaminations in composite structures can be considered as cracks) may be bearable but may also be devastating for the structure, requiring multiple inspections to ensure the structure efficiency. To investigate the onset of the crack growth, the stress intensity factor K at the crack tip is a key parameter and it can be expressed as:

$$K(\sigma, a) = C\sigma\sqrt{\pi a} \tag{1.1}$$

where σ is the applied stress, a is the crack length, and C is a constant depending on the specimen geometry and loading distribution. It is remarkable that the stress intensity factor increases not only with the applied stress but also with the crack length. As the crack grows, it also grows and a critical state may be achieved when the

crack growth becomes rapid and uncontrollable. The value of K associated with rapid crack extension is called the critical stress intensity factor K_c. For a given material, the onset of rapid crack extension always occurs at the same stress intensity value, K_c. For different specimens, having different initial crack lengths and geometries, the stress level at which rapid crack extension occurs, may be different. However, the K_c value will always be the same. Therefore, K_c is a property of the material. Thus, the condition for fracture to occur is that the local stress intensity factor exceeds the value K_c, i.e.:

$$K(\sigma, a) \geq K_c \tag{1.2}$$

The concepts of linear fracture mechanics can be employed to analyze a given structure and predict the crack size that will propagate spontaneously to failure under the specified loading. This critical crack size can be determined from the critical stress intensity factor as defined in Eq. (1.1). A fatigue crack that has been initiated by cyclic loading, or other damage mechanism, may be expected to grow under sustained cyclic loading until it reaches a critical size beyond which will propagate rapidly to catastrophic failure. Typically, the time taken by a given crack damage to grow to a critical size represents a significant portion of the operational life of the structure. In assessing the useful life of a structure, several things are needed such as:

- understanding of the crack-initiation mechanism;
- definition of the critical crack size, beyond which the crack propagates catastrophically;
- understanding the crack-growth mechanism that makes a subcritical crack propagate and expand to the critical crack size.

It has been found that crack growth phenomenon has several distinct regions as shown in Figure 1.3:

1. an initial region in which the crack growth is very slow;
2. a linear region in which the crack growth is proportional with the number of cycles;
3. a nonlinear region in which the crack growth rate is proportional with the number of cycles on the $log - log$ representation.

According to $Paris/Erdogan$ Law, the fatigue crack-growth rate depends on the alternating stress and crack length:

$$\frac{da}{dN} = f(\Delta\sigma, a, C) \tag{1.3}$$

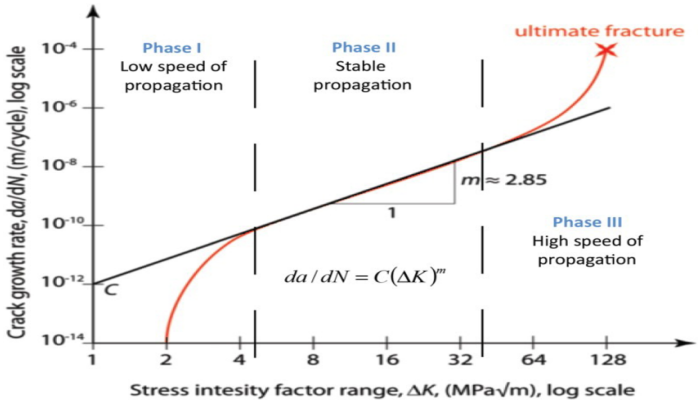

Figure 1.3: Typical fracture mechanics fatigue crack propagation behaviour [8].

where $\Delta\sigma$ is the peak-to-peak range of the cyclic stress, a is the crack length, and C is a parameter that depends on mean load, material properties, and other secondary variables. In view of Eq. (1.3), it seems appropriate to assume that the crack-growth rate will depend on the cyclic stress intensity factor, ΔK, i.e.,

$$\frac{da}{dN} = C_{EP}(\Delta K)^n \tag{1.4}$$

where ΔK is the peak-to-peak range of the cyclic stress intensity factor, n is the slope of the log-log line, and C_{EP} is an empirical parameter that depends upon material properties, test frequency, mean load, and some secondary variables. Paris law represents well the central part of the curve in Figure 1.3. However, the complete crack-growth behavior has three separate phases:

1. crack nucleation;
2. steady-state regime of linear crack growth on the *log-log scale*;
3. transition to the unstable regime of crack extension and fracture.

Such a situation is indeed depicted in Figure 1.3, where Region 1 corresponds to the crack nucleation phase, Region 2 to linear growth, and Region 3 to transition to the unstable regime. Threshold values for ΔK that delineate one region from the other seem to exist; the locations of these regions in terms of stress intensity factor vary significantly from one material to another.

During life cycle of the structure some inspection are required to avoid the unstable regime and various design criteria have been developed during the history of aviation to ensure the resistance of the structure when it is subject to multiple load cycles and they can be broadly divided in three different philosophies [9]:

- Safe Life;
- Fail Safe;
- Damage Tolerance.

The first approach is designed to ensure, for a given design life, the resistance to workloads without the generation of fatigue cracks; namely, the adequate fatigue life is achieved by limiting its allowed operational life. During its application to commercial aircraft in the 1950's, this approach is too expensive while achieving acceptable safety, since a combination of material scatter and inadequate fatigue analyses resulted in the premature retirement of healthy components. The approach is still in-use today in such structures as high-strength steel landing gear. However, due to the damage sensitivities and relatively flat fatigue curves of composite materials, a safe-life approach is not appropriate.

The fail safe approaches contemplate the eventual presence of damage in some points of the structure, limiting catastrophic effects by introducing redundant elements; when the failure of one of them occurs, the load is distributed on the intact ones. From a practical standpoint, the approach forces the structure to contain multiple load paths by requiring specific load-carrying capability with assumed failures of one or more structural elements. This approach achieved acceptable safety levels more economically, and, due to the relative severity of the assumed failures, was generally effective at providing sufficient opportunity for timely detection of structural damage. Its redundant-load-path approach also effectively addressed accidental damage and corrosion. However, the method does not allow for explicit limits on the maximum risk of structural failure, and it does not demonstrate that all partial failures with insufficient residual strength are obvious. Moreover, structural redundancy is not always efficient in addressing fatigue damage, where similar elements under similar loading would be expected to have similar fatigue-induced damage.

The damage tolerance philosophy has been included in regulations since the 1970's evolving out of the "Safe Life" and "Fail Safe" approaches. It was initially developed and used for metallic materials, but have more recently been extended and applied to composite structure. Damage tolerance provides a measure of the structure's ability to sustain design loads with a level of damage or defect and be able to perform its operating functions. Consequently, the concern with damage tolerance is ultimately with the damaged structure having adequate residual strength and stiffness to continue in service safely until the damage can be detected by scheduled maintenance inspection (or malfunction) and be repaired or until the life limit is reached. The extent of damage and detectability determines the required load level to be sustained. As a matter of facts, safety is the primary goal of damage tolerance. Usually, components designed

using this approach are *slow crack growth structures*, namely made up with elements that present a long period for crack propagation or using components preventing cracks to grow above a certain dimension and named crack stoppers.

Regarding the typologies of damage, the structure of an aircraft is subject to the following main sources:

1. environmental deterioration;
2. accidental damage;
3. fatigue damage.

Environmental deterioration (typically corrosion) of a mechanical component is due to its chemical interaction with the weathering and in general with the surrounding environment. In the field of aircraft constructions, for reasons of weight, the structures must have high efficiency, thus the presence of corrosion is a problem of considerable importance. Accidental damage is usually derived by contact, by impact with an object or even by a human error attributable to manufacturer, to flight operations or to a wrong way of proceeding during maintenance. Inspection intervals within which an accidental damage can be detected, are related to the type of damage and likely to the consequences caused by it. As a matter of facts such damage occurs randomly, and in some cases discovered during a routine inspection which is not focused on that. It is indeed unforeseen in its definition. Fatigue damage is instead related to the material deterioration due to fatigue stresses caused by repeated or even randomly varying in time loads; the stresses induced in the aircraft's structure during flight, takeoff and landing operations are all critical load conditions. A fatigue damage typically begins with a small fracture, initially very difficult to detect with common methods: liquid penetrant inspection, X-rays, etc.; as the crack increases in dimensions because of load cycles, the effects of stress concentration becomes higher, and the speed of propagation of the crack also becomes even greater until the collapse level is reached.

Composites are some of the most critical type of materials with respect to fatigue, where the crack initiation may be due to accidental damage as well. For reasons inherent in their internal structure, they suffer much more than any other conventional metallic material of problems related to damage. Typically for composites are matrix cracking, delaminations, fiber fractures, interfacial debondings, and all these kind of damage, especially those accidentally induced and then occurring in fatigue problems, are very critical. The most problematic aspect of damage in composites is that they can be produced by events involving very small values of energies; as an example delaminations might occur, at interfaces between different oriented adjacent plies, as a result of impacts with external objects involving energies of the order of some

Joules. Typically these low velocity impacts produce so small damage within the material that they can't be detected through a simple visual inspection because they are characterized by small external indentation (not visible or barely visible damages).

The damage tolerance approach involves the use of inspection procedures and structural design concepts to protect safety, rather than the traditional factors of safety used for Ultimate Loads [9]. The overall damage tolerance database for a structure should include information on residual strength characteristics, sensitivities to damage growth and environmental degradation, maintenance practices, and in-service usage parameters and damage experiences. However, a sort of "defect" factor based on degree of detectability has been the basis for establishing minimum damage tolerance residual strengths for composite structures in requirements proposed for inclusion in [10]. These strength requirements are identical to those for metal structure having critical defects or damage with a comparable degree of detectability. Requirements for cyclic loading prior to residual strength testing of test components are also identical. The application of this philosophy is thus introducing knockdown factors affecting the design of composite structures. New methods of investigation have been developed to reduce the gap between theoretical and practical benefits, including SHM. As discussed below both composite design and aircraft maintenance strategies are definitely affected and could both benefit by integrating SHM capabilities. The next section shows the typical accommodation of residual strain actually in use among aircraft manufacturers due to the complex impact mechanics briefly introduced as well.

1.2.2 Composite design within aerospace manufacturers

Impact damage to composite structures is unique in that it may not be visible or may be barely visible, making it more difficult for a repair technician or aviation worker to detect that damage [11]. Impact induced damage is indeed a very complicated phenomenon, requiring the basic mechanics and damage mechanism understanding. Some concerns have been raised when damages have to be detected in composite materials especially due to such complex mechanics. The impact behavior of composite materials has been studied experimentally by many authors [12, 13, 14]. and the complexity of the physical phenomena demands detailed investigation to numerical modeling making difficult to extend analytical solutions to complex structures [15, 16, 17, 18, 19, 20]. The low velocity impact damage in laminated composite plate structures can be recognized as a debilitating threat; it has a significant effect on the strength and durability of the laminates; it is an inevitable event and needs appropriate design solutions to be addressed [21]. As a matter of facts, a lot of work is still necessary to improve the modeling of the damage developing during impact on composite laminates to better assess numerically their residual mechanical characteristics in order to optimize their

design [22].

In composite structure, the damage caused by an impact event is typically more severe and even less visible than in metals. As a results, composite materials are sensitive to many aspects of in-service use for which it is difficult to provide design data. While subjected to out-of-plane loading or minor objects drop, like tools during assembly or maintenance operation, composite laminates reveal a brittle behavior which may lead to significant damages. These damages are classically divided in two parts [23]: (i) intralaminar damages, i.e. the damages developing inside the ply like matrix cracking, fiber/matrix debonding or fibers breakages, and (ii) interlaminar damages, i.e. the damages developing at the interface between two consecutive plies, namely delamination. Such damages are particularly dangerous because they drastically reduce the residual mechanical characteristics of the structure. The reduction in compression after impact (CAI) strength due to the low velocity impact is for instance of particular concern. Generally the loss in strength may be up to 60% of the undamaged value and typically industrial designers limit compressive strains to the range of 3000 to 4000 $\mu\epsilon$ [24]. This significant reduction in design allowables is also a result of the fact that testing coupons cannot simulate the behavior of larger realistic structures because their dynamic response to low velocity impact may be quite different and it is not economic to perform impact tests on relatively large panels so as to evaluate impact behavior and damage development. In addition to the compressive strength, the impact damage can decrease also the fatigue strength of a composite.

Composite structure failure is often caused by the development of different damage mechanisms which begin locally. In fiber-reinforced laminates, delamination is the most common damage mode. It is where the fiber-reinforced laminate behavior differentiate from that of metallic structures inducing a primary concerns in composite aircraft design. Delamination is caused by high interlaminar stresses and relatively low interlaminar strengths of such composites, that show also very low through-thickness strength. The delamination usually occurs between layers with different fiber orientations. Two adjacent layers with different fiber orientation introduce a mismatch of flexural and extensional rigidity through the thickness that combined with the low resistance of the matrix, lead the composite material to be very sensitive to separation of these interfaces. For this reasons, a major source of delamination damage is from low-velocity impact where usually matrix cracks develop first in the plies (shear or bending cracks) and delaminations then grow from these cracks at the ply interfaces [21]. The delamination indeed rarely occurs as an independent damage mode; when a shear or bending crack in a layer reaches an interface between two layers oriented in different ways it is unable to easily penetrate the upper layers and it can spread like delamination. Relevant efforts have been spent in the past years to understand how

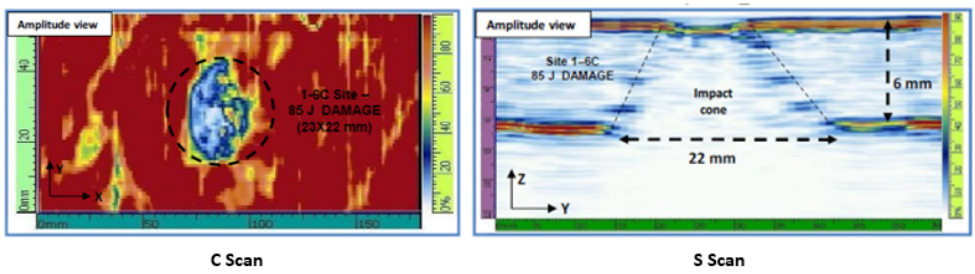

Figure 1.4: Carbon-epoxy plate subject to a low velocity impact. Thickness = 6mm. Energy = 85J.

delaminations arise within the composite laminates. The investigation conducted in [25] demonstrated indeed that the delaminations only occur when there is a change in ply orientations and develop mostly alongside the direction of fibers in the lower ply of the interface. The size, shape and distribution of delaminations utilizing several evaluative techniques is investigated in [26], where the classic "peanut" shape is found at almost every interface through-the-thickness. Several additional studies have revealed this characteristic shape and the complexities of the related mechanics [27, 28, 15].

Nevertheless the improved knowledge achieved in the last years, a major concern regards the detectability of damage. The impact induced damage evolution in composite laminates can be divided into two stages: (i) bending or shear stresses initiate the micro cracks in matrix, (ii) propagation of the micro cracks into the nearby interface yields to the delamination. The two kinds of damage, matrix crack and delamination, are connected and their relationship is responsible for the damage mechanism occurring under low velocity impact. This phenomena results in a very small surface indentation even when the through thickness damage is greater than an emerging flaw due to the mixed crack-delamination evolution. The structure of a damage typically obtained while a composite structure is subject to low velocity impact is showed in Figure 1.4, where a classic ultrasonic non destructive evaluation (NDE) is depicted. Specifically, it regards the case of a 6mm CFRP plate designed for a lower wing panel of a commercial aircraft and loaded with a low velocity impact of 85J using a drop weight machine with one inch tip. The peanut shape and the relevant extent of damage is evident from the c-scan image (in plane view of the damage). Furthermore the s-scan (section view of the damage) shows how the laminate is corrupted through the thickness with several delaminations arising among several layers resulting in the typical impact cone due to the complex failure mechanics (cracks-delamination mixed failure). However, although the conformation of the damage appears evident, the only visible item is the indentation on the upper surface which is of the order of few hundred µm and quite not visible.

As a matter of facts, actually the complexities of composite response to low velocity

impacts and the detectability of emerging damages require the design of structure to be appropriately addressed. Basically, in a damage tolerance approach, the presence of hidden failures due to barely visible damages is accounted during the design, generally accomplished by limiting the design strain level for ultimate and limit combined load design criteria [29]. Another common design approach limiting the benefits of composites is operated to preserve the collaboration of reinforcements. In this context, the typical problem regards the stiffened composite structures where the stringers adopted for reinforcing thin walled structures [3] may be affected by not visible disbondings even when subjected to low energy impacts. As in the case of delamination, the punctual load leads to complex damage mechanics resulting in the separation between the stringer and the hosting structure preventing the collaboration between parts with a dangerous drawback for loading absorbing. Hence, disbonding stoppers are usually included into the design to avoid separations between stiffeners and skin above the maximum size ensuring safe structural collaboration [29]. As a matter of facts, connectors are indeed necessary where the introduction of composites would avoid or limit any type of connection between different parts to reduce weight as well as manufacturing and maintenance costs.

This rough damage tolerance approach therefore breaks down the benefits encouraging composites introduction. There are indeed two primary damage tolerance requirements described in [30]: (i) damage growth characterization, and (ii) residual strength capability. The certification demands the demonstration of required levels of static strength, durability and damage tolerance as well as the ability to predict stiffness properties. Demonstration of compliance for composite structure includes sustaining design ultimate loads with damage at the threshold of visual detectability (barely visible impact damage, BVID) and sustaining design limit loads with clearly visible damage. In addition, it must be demonstrated that levels of damage smaller than those that reduce the residual strength to design limit load capability will not experience detrimental growth under operational loading conditions.

For instance, considering the applied strains, materials and design concepts, a no-growth approach for damage tolerance has been adopted in the case of Boeing B777 empennage [9]. This approach is based on demonstrating that any damage that is visually undetectable will not grow under operational loads. This means that structures with undetectable damage must be capable of carrying ultimate load for the operational life of the airplane. The advisory circular [29] includes acceptable means of compliance in the following areas: (i) effects of environment (including design allowables and impact damage); (ii) static strength (including repeated loads, test environment, process control, material variability and impact damage); (iii) fatigue and damage tolerance evaluation; (iv) other items - such as flutter, flammability,

lightning protection, maintenance and repair. According to such items, the no-growth behavior of B777 CFRP structure has been demonstrated in numerous subcomponent tests. Following the typical *building block* approach in use within aeronautical field, two full-scale cyclic load tests have been performed inserting damage sites during several test sequences. In addition, the full-scale tests demonstrated the following characteristics required for damage tolerance compliance [9]:

- manufacturing anomalies allowed according process specifications will not grow for the equivalent of more than two design service lives;
- visible damage due to foreign-object impact will not grow for the duration of two major inspection intervals (i.e. two "C" checks, 4000 flights per "C" check);
- the structure can sustain specified residual strength loads with damage that can reasonably be expected in service;
- the structure can sustain specified static loads ("continued safe flight loads") after incurring inflight discrete-source damage.

To demonstrate residual strength capability, the test box has been further damaged with visible impacts. Visible damages are those that are easily detected by scheduled maintenance inspections. Fatigue testing representative of two inspection intervals again verified the no-growth approach. Tests are also conducted to provide certification data for failure modes not readily predicted by currently accepted analysis methods. For example: strength after barely detectable impact damage, called threshold of detectability (TOD) impact damage in FAA advisory material; flaw growth from TOD impact damage; strength after detectable damage; flaw growth rates from detectable damage; lightning strike resistance; flame resistance.

Summarizing what is emerging analyzing a real certification stage of an aeronautical composite structure, during the design phase, it is necessary to demonstrate that not visible and barely visible damages occurring at every time do not affect the safety of the aircraft between adjacent inspection checks. To detail how a safety design may be affected by unforeseen events, the typical trend of residual stress/strain versus impact energy level is schematized in Figure 1.5. A first low energy range is connected to not visible damages as it is not inducing any failure (namely below the energy level ensuring the onset of a hidden failure). Then, the residual strain/stress deeply decreases while the impact energy level ensures a slightly increasing damage which is barely visible. That failure is indeed characterized by a through thickness delamination where not any indentation is visible (inner visibility) or together with a slightly visible indentation (external visibility) which is not always appreciable by visual inspection. Then, the damage appears increasingly evident according to the

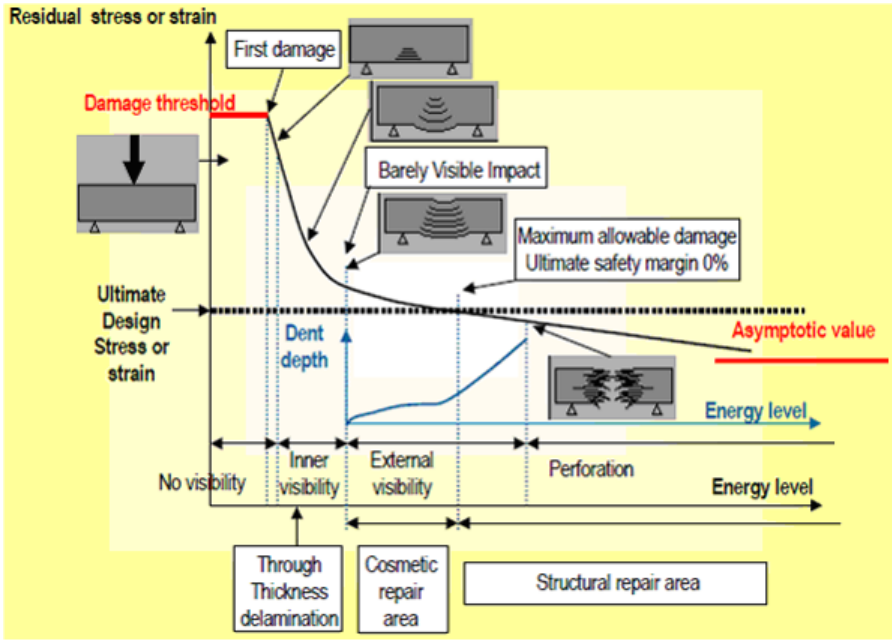

Figure 1.5: Schematic representation of residual strain versus energy level and derived design constraint.

energy level. That is the limit for ultimate design stress or strain where any safety factor is not considered yet.

Furthermore, as above mentioned, the damage is not the only event introducing knockdown factors. Other aspects to be accounted are reported in Figure 1.6, whose scheme shows how they define the allowable design region merely with a reduction of allowabe stress/strain. Composite structures are indeed sized using limit allowables, which results appreciably lower than material ultimate due to the introduced tolerance (see Figure 1.7) According to Boeing design manuals and [9], the design limit allowable $s_{d.l.a.}$ can be calculated for first approximation introducing a scatter to the ultimate material allowable $s_{m.u.a.}$ as follows:

$$s_{d.l.a.} = 0.5 \times s_{m.u.a.} \tag{1.5}$$

This definitely means that a huge amount of weight reduction expected introducing composite materials is wasted. That is where the SHM introduction may provide more relaxed design, limiting the allowables to the residual stress or strain associated to the minimum damage detectable with an integrated system (i.e.: the system target) capable to identify emerging flaws where any other detection is not possible.

As a matter of facts, the standardization and reliability required to move from

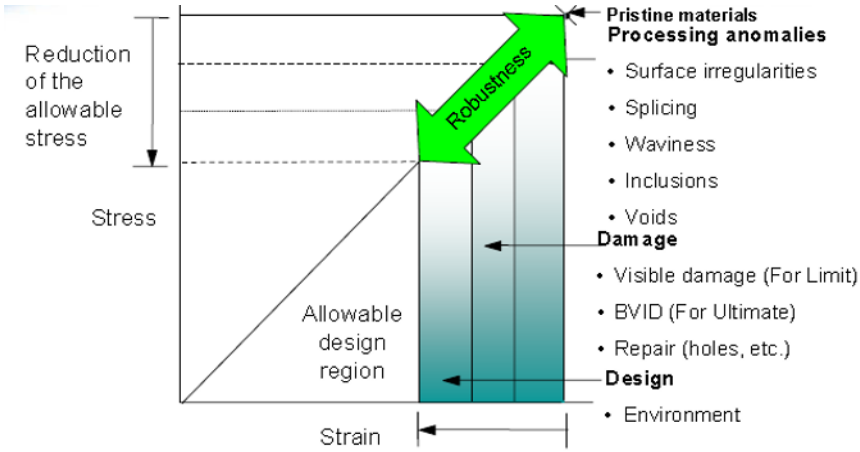

Figure 1.6: Schematic representation of scattering factors constraining the composite design.

the damage tolerance to a *condition-based* design actually makes far from application the integration of SHM technology during the structural design to avoid knockdown factors due to detection of inner visible damages. However, due to the results that this type of system may potentially achieve, SHM appears to be the only way to design high performance and lighter components reaching the advantages expected fully up to now. For these reasons, the condition-based design is referred here as *long-time* perspective of SHM. Instead, the *short-time* perspective introducing SHM is related to the damage assessment procedure adopted during lifetime and connected again with damage tolerance approach which is based on scheduled inspections to ensure safety. Such interesting aspect is remarked in the next section before finally introducing the SHM framework in Sec. 1.4

1.3 Failure assessment during lifetime

The Paris law or similar approaches are useful to define the remaining life of structure, but the particular evolution of the crack in structures subjected to cyclic loads requires a skillful inspection planning. As a matter of facts, extreme conditions in which aerospace structures are expected to work lead to continuously check the ability of the component to support the expected loads and it is primarily a flight safety consideration. Damage tolerance ensures the structure can continue of carrying the agreed-upon regulation loads despite any damage or degradation (e.g. impacts induced failures). As indeed defined in the previous section with the example given by the Boeing B77 empennage, the damage tolerance is defined in connection with the prescribed checks no matter the growth approach is. Consequently, the concern with

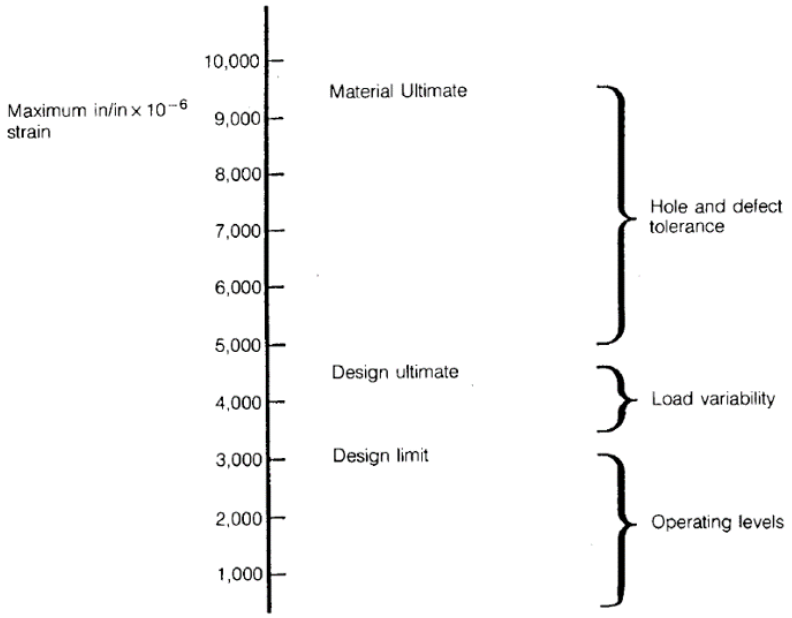

Figure 1.7: Typical design allowables for carbon fibers reinforced plastics (CFRP).

damage tolerance is ultimately with the damaged structure having adequate residual strength and stiffness to continue in service safely at least until the damage can be detected by following scheduled maintenance inspections.

The focus of damage tolerance evaluations should be on ensuring safety in every unforeseen event, not solely on likely scenarios of damage, like that tested within B777 program. As a consequence, an important part of a structural development program is to determine the damages that the structure is capable of carrying at the various required load levels (ultimate, limit, etc.). This information can be used to develop appropriate maintenance, inspection and real-time monitoring techniques to ensure safety. Structure certified with an approach that allows the presence of a damage no matter the damage growth is, must have associated in service inspection techniques, which are capable of adequately detecting damage before it becomes critical. In addition, if the damage growth is allowed, it must be predictable such that inspection intervals can be reliably defined.

In this context in-service inspection procedures play a major role so that structural regions and elements are classified with respect to required nondestructive inspection (NDI) and NDE sensitivity. Inspection intervals are usually established on the basis of

crack growth information assuming a specified initial flaw size and a *detectable* crack size, the latter depending on the level of available NDI/NDE procedure and equipment. Cracks larger than that are presumed to be discovered and repaired with a defined confidence level. That is the target of the NDE equipment usually assessed with *Probability of Detection* approaches [31]. Furthermore, the inspection intervals must be such that an undetected flaw will not grow to critical size before the next inspection. Due to their key role, the use of NDI/NDE techniques and the establishment of appropriate inspection intervals have progressed considerably especially in the case of composites.

For this reason, the next section is dedicated to a brief review of non destructive inspection methods in use for composites to further introduce their actual role in the damage assessment procedure and the introduction of SHM as their natural evolution (*short-term* perspective).

1.3.1 Non destructive testing methods for composite inspection

Non destructive testing methods deal with the identification and characterization of damages without altering (destroying) in any way the component inspected, whether they show inner or external visibility. Due to their characteristics, they provide a cost effective approach to investigate condition of a single component or for the in service inspections of complex systems [32]. In the field of composites, numerous techniques are adopted, including ultrasonic testing [33], thermographic testing [34], infrared thermography testing [35], radiographic testing [36], visual testing [37], acoustic emission testing [38], acousto-ultrasonic [39], shearography testing [40] and electromagnetic testing [41].

Visual Testing (VT) is the most basic type of NDT, used in most cases because it is the cheapest and fastest way to inspect a component, limiting the use of other types of testing techniques. The high affordability in the process is also introduced by the absence of any equipment as well. However this method has intrinsic disadvantages in the way in which it is performed, limiting the analysis to external manifestations of damage (surface braking defects) missing all internal defects which are hardly visible at surface.

Ultrasonic Testing (UT) evaluates information carried by an ultrasonic signal transmitted and received by specific transducers and usually post processed on display devices. Based on complex analysis, crack location, flaw size, its orientation and other characteristics could be achieved with good resolution, high flaw detecting capabilities, but at the cost of a difficult set up. Test samples are usually needed for calibration purpose to insure accurate testing of possibly damaged coupons. Such methods are used with manual or automated systems and are useful for both manufacturing and in

service situation. The most commonly used indicators of properties are wave propagation velocity and amplitude (or energy) loss. Some of the testing methods address one property, while others include multi parameter analysis [42]. Generally, small discontinuities can be detected from scattering analysis depending on the frequency range of the system. Different approaches based on high frequency sound waves propagating in solids can be generally exploited; pulse echo and through transmission, bondtester and phased-array. Analyzing the echo of a pulsed wave, the first approach exploits the transit time of the wave and the energy loss due to attenuation and wave scattering on flaws. It is widely used in damage detection during manufacturing and in service inspections and it is incorporated in aircraft manufacturer procedures to detect subsurface impact induced damages. Instead, the through transmission ultrasonic method uses separately a transducer and a receiver kept in contact or far from surface and at a fixed distance to analyze the direct propagation. It is really indicate for automated systems, however it requires accessibility from both sides of the product and does not return any information about the depth of the defect detected. Furthermore, such type of investigation is less practical for on-site in service inspections. The *bondtester* ultrasonic testing includes special equipments for detecting delamination and disbondings in composite laminates using different techniques (e.g. pitch-catch and resonance) designed for local and manual inspections. Phased array ultrasonic testing is mostly used for composites and allows to increase the track width using multiple probe elements [43]. Systems based on this technique are useful for both manufacturing and in-service inspections and when combined with post processing softwares, they are able to provide in plane and sectional reconstructions with pulse echo information for each scanned point. Furthermore, the phased array techniques can be used to optimized the focusing of the signal creating a propagating beam. The stat of the art of this technology includes probes in different shapes to optimize focusing and or surface contour.

Thermography testing (TT) exploits the thermal conductivity of a material which may change by the presence of defects. It is usually able to detect defects that have a diameter greater than their depth in the part. A flaw, such as a delamination or impact damage causes a change in the thermal radiation of the area [44]. Of particular interest is the Infrared Thermography Testing (IRT) where the thermal radiation emitted by a surface of a specimen is recorded with an infrared camera [45]. The active approach is mostly used for NDI of composites. A heat input is used for changing the temperature of the specimen and then the presence of the flaw is detected due to the different conductivity in that location. Advanced active thermography approaches use controlled heat input creating a progressive heat in the material. The camera images are synchronized with the input to analyze the speed of changes in the surface

temperatures, achieving better detection of defects and depth information. Different techniques are available including flash, pulsed, lock-in and transient thermography. In this way it is possible to inspect large area of a component without any couple or contact, but simply acquiring thermal images of one side of the specimen. It is suitable for manufacturing and maintenance application but requires high skilled operators for the post processing of data.

Radiographic Testing (RT) is able to detect delamination when its orientation is not perpendicular to the x-ray beam. Different types of RT techniques are used for several applications. Conventional radiography is the most useful when the parts are neither too thick nor too thin, low voltage radiography is used with parts showing a thickness between 1mm to 5mm, while γ-rays radiography is used for thick parts. Penetrant-enhanced radiography is instead employed specifically to detect small matrix cracks and delaminations in a sample [46]. Furthermore, different methods have been developed covering several applications; film radiography, computed radiography, computed tomography, and digital radiography. The latter is able to differentiate organic and inorganic substances by taking x-rays at various energy levels and comparing density. An interesting consequence is in the ability to distinguish water in honeycomb sandwich structures from resin and filler. Instead, the X-ray Computed Tomography (XCT), is able to provide the 3-D visualized image of the structure, achieving really reliable results [47]. However, XCT approaches are usually really expensive or limited to laboratory applications.

Electromagnetic Testing (ET) methods induce electric currents and/or magnetic fields inside the object of investigation to evaluate different faults observing the electromagnetic response of the material. Also in this case different methods are available to cover all applications including Eddy Current testing, Remote Field Testing, Magnetic Flux Leakage and Alternating Current Field Measurement.

Acoustic Emission (AE) exploits the stress waves generated by material defects; propagating from the location where the damage is emerging, they are detected by an array of highly sensitive piezoelectrics. As a matter of facts, it is a passive approach; analyzing the sound emitted by the energy released during fracture rather than interrogate the structure in some way. The resulting sensitivity is very high, the process of investigation is relatively fast and, using several sensors permanently adopted, it is not necessary the disassembling and preparation of the specimen. For their characteristics, AE techniques are particularly suitable for detecting fatigue damages. However, the complex analysis which is behind this techniques requires skilled operators to correlate data to specific damages.

Acousto-Ultrasonic (AU) methods combine acoustic and ultrasonic testing mostly to assess severity of internal imperfections in composites. Such class of testing provides

not expensive tools, flexibility and sensitivity but not yet enough reliability. It is useful to detect emerging flaws and indicate accumulated damage in a structure due to fatigue or impacts. However it requires detail calibration before any testing.

Shearography testing is a laser optical method using coherent light or coherent soundwaves to provide information about failure in composites by analyzing stress concentration typically distributed around critical defects [40]. The deformation of the surface caused by stress/loading is measured and the defects are detected only by their mechanical response, making not simple the interpretation of results. In addition, it requires special inspection condition (surface condition and illumination) and the loading of the specimen which may be further damaged. As a consequence, it is extremely difficult to characterize defect and it can be adopted mostly for the fast identification of certain flaws. On the other hand shearography provides large area testing capabilities, non-contact properties and good performance on honeycomb materials, which is a big challenge for traditional nondestructive testing methods. In addition its relative insensitivity to environmental disturbances makes this method suitable for less skilled users (less training needed). Finally it is applicable for a large range of applications including detection of delamination in sandwich panels.

Usually all NDT techniques can be divided and grouped in different way, depending on several common characteristics or applications. As suggested in [48], it is possible to broadly divide NDT approaches in contact and non contact methods, having both specific applications in composites. According to such identification, contact methods are traditional ultrasonic testing, eddy current testing, magnetic testing, electromagnetic testing, and penetrant testing. Instead, typical noncontact methods are through transmission ultrasonic, radiography testing, thermography, shearography and visual inspection. This way to group such testing approaches is really crucial because it cannot to be neglected that eliminating any contact between sensor and structure the investigation becomes faster. That is the reason for which although there are so many NDE techniques commonly used in the aerospace industry for composites, visual inspection is still one of the most widely used, due to its simplicity and low cost. However, the requirement, not always possible, of accessibility, and the need of visualizing internal damages lead to the adoption of more sophisticated technologies exploiting the wide variety of physics principles explained. As a matter of facts, practical applications for damage assessment on composite material in the aerospace field include mostly ultrasonic testing, thermographic and vibration methods [49], acoustic approaches [50], infrared thermography [51], shearography [52], and X-rays computer tomography [53].

As described above, each one of these methods has advantages and drawbacks, addressing specific problems in several types of flaw to be detected and different parts.

As a consequence, although the great potentialities of several NDT techniques, some of their inherent limitations still persist. First of all, NDI/NDE inspection sensitivity and reliability while inspecting actual airframes are far from the standards within laboratory tests which include simpler coupons. However, the major concern of current NDI/NDE practices is that they cannot provide a continuous assessment of the structural condition. To practically perform NDI/NDE inspections, the aircraft has to be taken off line, disassembled in some parts and scanned. This process is time-consuming and expensive, making necessary a detailed scheduling and preveting on demand inspections. The implementation of a SHM system could improve such situation due to the permanently attached transducers allowing structure interrogations as often as needed even when and where the accessibility is not possible. The potential benefits introduced by operating SHM within aircraft inspections are detailed in the next section, where specific examples are given to justify the cost benefits achievable by introducing condition-based monitoring with integrated structures.

1.3.2 Benefits introducing SHM in aircraft inspections

Unlike NDE inspections, the on-demand interrogations of a SHM system based on permanently attached sensors are done always in the same way, making possible to build an historical database and acquire change information to assist in the system reasoning process. Advanced signal processing methods can be used to detect characteristic changes in the material state and make that state-change information available to the prognosis reasoning system. The concept of change detection can be used to characterize the material state by identifying critical features that show changes with respect to a reference state that is stored in the information database and updated periodically. When this is performed in coordination with existing NDI/NDE practices, the structural health monitoring information performed between current inspection intervals can provide supplementary data that would have a densifying effect on the historical information database. Another advantage of implementing SHM systems is related to the nonlinear aspects of structural crack propagation. Most of the current life prognosis techniques are indeed based on linear assumptions rooted in laboratory tests performed under well-defined conditions. However, actual operational conditions are far from ideal, and incorporate a number of unknown factors such as constraint effects, load spectrum variation, and overloads. These effects are within the nonlinear fracture mechanics and make the prediction very difficult. However, the dense data that can be collected by an SHM system could be used as feedback information about the crack-growth rate, and could allow the adjustment of the basic assumptions to improve the crack-growth prediction laws.

Structural health monitoring could have a major contribution to the structural

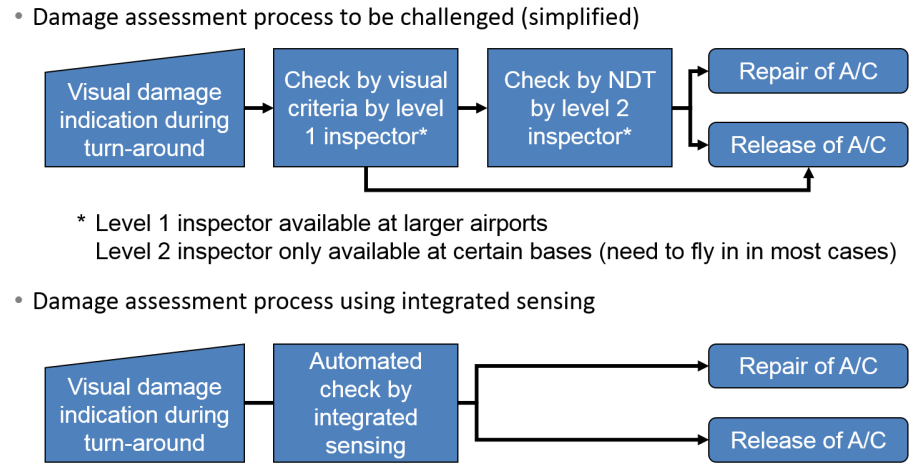

Figure 1.8: Damage assessment processes based on NDE and SHM capabilities.

diagnosis and prognosis not only increasing the safety by introducing a continuous monitoring. As a matter of facts, the introduction of an effective SHM system may completely change the maintenance strategies increasing safety level of operations. The damage assessment process is really complicated by the necessity of inspections targeted to ensure safety according to the damage tolerance design criteria. The complex environment in which aircrafts work, driven by the business of the operator, lead to the necessity of scheduled inspections between several flights which minimize the downtime. Actually the damage assessment process is based on different levels of inspection, as depicted in Figure 1.8, and oriented to release the aircraft or to require its repair. The turn-around operated by the aircraft captain is the first way to detect damages by visual inspection. However the first detailed inspection is operated by the *Level 1* inspectors according to rigorous visual inspection criteria and it is usually available at larger airports. When the release is not obtained during this phase, the inspection operated using sophisticated NDT approaches is required to obtain the release or repair response. However, the *Level 2* inspectors, in charge of such type of inspections, are available only in certain bases and it is necessary to move he aircraft in most cases. As a matter of facts, the inspection procedures are complicated and introduce often relevant downtime. In this context the principal aim of SHM is to reduce operative costs moving from the actual maintenance approach based on two different levels of inspection towards a *condition-based* philosophy exploiting an autonomous and integrated sensing system for achieving the release of the aircraft or its repair request. According to the IATA benchmark for direct operating costs per flight depicted in Figure 1.9, the 17% of the operative costs of a recent aircraft are

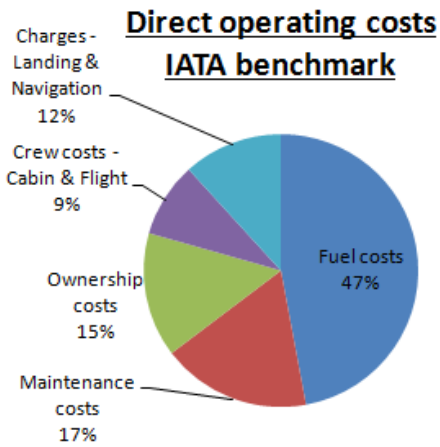

Figure 1.9: IATA benchmark airlines costs share for direct operating costs of a recent aircraft.

Check Type	Frequency	Man hours
A	500-800 FH	20-50
B	4-6 months	150
C	20-24 months	6000
D	6 years	50000

Table 1.2: Scheduled maintenance levels for a commercial aircraft.

demanded to maintenance tasks and they can increase up to 25% for aging vehicles. The scheduled maintenance levels for a commercial aircraft are reported in Table 1.2 with typical frequency and man hours required for each of them. This summary explains easily the complexity of maintenance procedures, step by step more heavy, to ensure safety of aircraft lightweight structures. The *check A* is usually performed overnight every 500-800 flight hours (FH) at an airport gate while the *check B* requires 1 to 3 days at an airport hangar to be completed. More complex but very crucial is the *Check C*, usually performed less than every 2 years requiring 1 to 2 weeks of work in a maintenance base. Instead the *check D* is operated usually every 6 years, where the paint may needed to be completely removed for further inspection on the fuselage skin. For this reason it requires a suitable maintenance base and about 2 months of work. Such data are variable and depend indeed on how much the aircraft is devoted to maintenance, as reported in Table 1.3 for the check C. The cost of a check C depends on the maintenance required (it may be light or heavy) starting from 60k$ for a small narrow body aircraft up to 1M$ for a wide body aircraft [54].

Starting from these considerations, to reduce such costs it is possible to limit non destructive inspections and disassembly of aircraft just in case of negative response

A/C Type	Interval	C-Light cost ($)	C-Heavy cost ($)
B737-800	20 months	120k – 160k	220k – 320k
B747-400	18 months	600k – 800k	1.0M – 1.2M
B767-300ER	16-18 months	450k – 550k	600k – 700k
B777-300ER	16-20 months	375k – 475k	550k – 650k
A320-200	18 months	150k – 180k	250k – 350k
A330-300	18 months	375k – 475k	550k – 650k
E190	6000 FH	70k – 90k	110k – 180k
CRJ-700	4000-6000 FH	60k – 80k	100k – 170k

Table 1.3: Estimation of C-type maintenance costs for aging commercial aircrafts.

claimed by a SHM system. It is indeed estimated that in this way SHM allows to reduce a relevant percentage (up to $3-4\%$) of operative costs for airlines by modifying the damage assessment process (short-time perspective). As a consequence of such aspects, the introduction of a reliable SHM system can increase the safety (continuous monitoring) reducing costs (maintenance just in time). About the latter perspective, it is possible to quantify such reduction estimating inspection costs and SHM system benefits instrumenting the door surrounds of a passenger airplane with 4 doors. The area under investigation is about $7m^2$ and the design flight goal of the fuselage is about 100k FH . The costs of inspection and instrumentation can be divided in NDT inspections, SHM weight, sensor installation and sensors cost. The former is demanded for actual maintenance operation and consists of inspection for barely visible damages (BVID) and visible damages (VID) operated by L2 level inspector. Each inspection may cost around 40k$. The other costs are demanded for SHM based maintenance by avoiding any NDT inspection. For instrumenting one door surround are need about 3kg of sensors, 7kg of electronic parts and 16kg of cables and miscellaneous, for a total mass of 26kg per door. The operational cost derived by further introducing 1kg is about 0.07$ per each FH. The sensor installation cost depends on how the sensor are bonded: (i) bonded on the cured structure or (ii) co-cured. In the first case the cost is about 26k$ per each door surround ensuring 200M FH of durability while it decreases to about 8k$ for a cobonded installation. This means 104k$ or 32k$ for instrumenting all door surrounds of the fuselage. the sensors will cost approximately 12k$ per door, with a total cost of 48k$. For an aging airplane is estimated that 10^3 damages will occur on the fusolage operating for 500k FH. About 75% of these damages occur at door surround and 80% of these damages have a dent depth within 0.3mm and 1.3mm and they require inspection. The resulting cost for inspecting door surrounds is about 4.8M$ per 100k FH. According to the estimation given above, a sensorized fuselage will cost in the worst case about 0.876M$ with a benefit of 3.9M$ if no inspection is

carried out while continuous monitoring the structure. The impressive benefit obtained based on certain assumptions [54] and affected by an uncertainty of 10% does not account the cost for SHM maintenance and the inspections required for clarifying some system responses (combined NDE-SHM). However, also including scatter factors, the promising benefits introduced by integrating SHM during damage assessment process (short-time perspective) are remarkable and not negligible. In addition, SHM must be considered during the structural design: monitoring, inspection and damage detection become an integral part of structures at the design level reducing the knockdown factors introduced by actual damage tolerance approach (long-term perspective) for further decrease operational costs. As a matter of facts, actually SHM appears the only way to design safe and lighter structures.

Given the benefits may be achieved, the next section is dedicated to introduce several outputs demanded to a possible SHM system in terms of diagnostic and prognosis of integrated structures.

1.4 Structural Health Monitoring: diagnosis for structural prognosis

A SHM system provides an effective, continuous, and low-cost integrated framework for detection of damages in structures to avoid catastrophic failure. It can provide significant improvement in cost reduction for both aging and modern lightweight defect-critical structures. The first key role of SHM systems is to replace the traditional scheduled maintenance approach with the on condition maintenance concept, helping to significantly reduce the percentage of the life cycle costs associated with inspection and maintenance operations. Furthermore, a system integrated with structure capable to provide structural diagnostic every time and everywhere as a part of the structure itself can lead to the composite design optimization. The damage tolerance approach operated by large commercial aircraft manufacturers which are increasingly using composites restricts the effective benefits resulting from its adoption and only the integration of a system capable to detect any possible emerging flaw can improve the design.

As aforementioned, a condition-based approach could be able to relax the maintenance strategy minimizing aircraft downtime as well [55]. Moreover the design constraints would be avoided further increasing the structural performance with a more ecological friendly aircraft. The European Union itself is deeply involved in research programs dedicated to mature, validate and demonstrate the technologies that best suit the environmental goals set for regional aircrafts, that will enter service from

2020 onwards, performing low-weight aircraft configurations in which the continuous monitoring is a key concept. The “Green regional Aircraft (GRA)" project [56] recently funded within “Clean SKY" platform under the FP7 program, is indeed aimed to reduce CO_2 and NOx emissions through lightweight architecture, efficient energy management and increased aircraft availability through more efficient maintenance (repair, longer lifetime etc.). However, a crucial aspect emphasized by the recently funded project “Smart Intelligent Aircraft Structures (SARISTU)" under the FP7 program [57], is to limit the integration cost of SHM systems by moving the system integration as far forward in the manufacturing chain as possible. In this manner, SHM integration becomes a feasible concept to enable in-service inspection cost reductions of up to 1% .

Structural Health Monitoring deals with the analysis of structural performances in view of on condition maintenance as well as integrated oriented design. However, an health management system is a *complex environment* in which the diagnosis is the crucial but not the only critical task to perform. Different stages can be identified and likewise different methodologies can be exploited to perform different tasks. The underlying concept is to record the response of a structure when excited by a diagnostic or ambient input, process and analyze the response to extract features affected by defect and relate such parameters to defect characteristics. A typical SHM system consists of transducers for actuation and sensing. The actuator is usually excited by a signal generator for generation of diagnostic input while the sensors acquire data to be transmitted to a data acquisition system. In few cases the ambient excitations replace the diagnostic input and all transducers are used to detect the response of the structure to such external loads. From this distinction, it is possible to broadly group several methods in:

- active SHM;
- passive SHM.

In both cases the data are analyzed by a post-processing unit to predict and estimate damage. Therefore, an efficient SHM system requires transducers, signal processing for several purpose and algorithm providing damage reconstruction/information. Generally, a SHM system may provide a multi-level diagnostic, depending upon the information collected and the algorithm adopted to interpret test data sets. It mainly deals with diagnostic phase and should be supported by a prognosis tool predicting the remaining life span of the structure to obtain a self-sensing smart structure with a condition based lifetime strategy. The health management system can be broadly divided in four different steps [58]:

- damage detection, oriented to identify mostly the presence of the damage when a certain metric overcomes a defined health threshold (decision making output);
- damage localization, which deals with the identification of the more probable location of the detected damage (position output);
- damage dimension assessment, aimed to provide the extension and/or severity of the flaw (severity output);
- remaining life, which deals with the prognosis of the current expected lifetime of the component considering the dimension of damage and the prescribed load history (prognosis output).

The first three outputs constitute the diagnosis of a comprehensive SHM system while the last one is the prognosis demanded as input for the management of the monitored component in order to deliver aircraft release or repair (see Figure 1.8). From this breakdown, it is possible to define the multi-level diagnostic necessary for condition monitoring approach.

The crucial issue is the damage detection, whose reliability affects the remaining steps. The target of the system, i.e. the minimum detectable size with a defined confidence level (usually approached extending to SHM the *Probability of detection* analysis [31]) is crucial for application purpose. Regardless the detection capability of the metric, the quantification of a SHM system [59] is strongly affected by the decision level adopted for the identification which needs a careful unsupervised [60, 61] or supervised [62] analysis of data and it should be optimized in view of the aircraft lifetime management [63]. Moreover, the relation between signal response and flaw size can be primarily assessed approaching a statistical analysis to correlate the specific feature to the damage dimension and/or severity [31, 64]. Thus the system provides simultaneously the presence and the severity of damage scenario. To finally assess the location of hidden flaw, a dedicated algorithm should analyze the (non-censured) data sets available after decision making.

As a matter of facts, a comprehensive diagnostic output may be simply achieved but it is crucial to: (i) chose a signal response that is sensitive to such a hidden flaw as well as increasing with the severity of damage and (ii) estimate at least the position of damage as a spatial point using a reconstruction algorithm. However, a critical point in the context of this work is in the type of damage scenario induced by low velocity impacts which may be different depending on the impact location. Typically, delaminations mostly arise between adjacent layers of flat multilayered composites while disbondigs appear in stiffened composites between thin walled structure (skin) and stringer. Consequently, a SHM methodology aiming to discover and characterize impact induced damages should be able to monitor both events.

Using permanently distributed sensors, several approaches may be used to interrogate or extract sensitive data from the integrated structure and classic SHM systems designed in the last decades can be broadly divided in three groups:

- vibration based techniques;
- wave propagation based techniques;
- electromechanical impedance (EMI) techniques.

The former approaches are both using the dynamic behavior of the structure to collect useful information about its condition. The global vibration approach aims to detect presence and location of damage by analyzing the frequency response functions (FRF) of the structure. Damage mechanisms like delamination and disbondingsl change the dynamic response of the structure that may be used to identify damage. In particular variations on the stiffness, mass or energy dissipation properties of the structure due to such a failure will alter dynamic response characteristics such as mode shapes and natural frequencies. Vibration based techniques are widely used and several comprehensive review can be found in literature [65, 66, 67]. However when the defects are small compared to the dimensions of the structure, it is not easy to distinguish the differences in the vibration response from the noise level and correctly relate changes to damages. Although several techniques have been developed to amplify the differences and eliminate noise, actually the vibration approach is mostly useful to detect widespread or extensive damage.

Wave propagation or guided ultrasonic waves (GUWs) techniques are based on the assumption that a hidden flaw in the structure alters the behavior of the waves travelling in the structure and exploit the propagation and reflection of elastic ultrasonic waves in solids [68]. Typical ultrasonic methods include pitch-catch and pulse-echo techniques. For pitch-catch techniques, elastic waves are generated using an actuating transducer at one location on the structure (pitch), and the response is recorded using a sensing transducer at a different location (catch). Damage and its severity along the wave propagation path is detected by examining such response in terms of wave characteristics. Wave attenuation, dispersion and energy content can be extracted opportunely processing the signal. Pulse-echo techniques exploits the same transducer used to excite the elastic wave also to measure the response after the transducer has finished exciting the structure. Damage is detected by investigating echoes in the measured response due to wave reflections off damaged regions. The time of flight (TOF) can be used to locate the damage and the amplitude of the reflected signal can be used to assess the severity of the damage.

Finally, the EMI techniques exploits the electromechanical impedance response of a piezoceramic (PZT) sensor bonded or embedded into the structure to detect damage in

the near-field [69]. Excited by a sinusoidal voltage sweep with low amplitude from low frequencies up to ultrasounds, the PZT induces the surrounding structure to vibrate due to the bonding and the presence of a fault can be detected observing changes in the electromechanical signature (real and imaginary part of the impedance and admittance). Although the good sensitivity of this method increased by many signal processing techniques to reset the environmental effects [70] and compact devices for data processing [71], this method is usually limited to near field damage detection, making it mostly useful for monitoring the confined damages such as bolts and joints.

Other countless non-conventional approaches are also available and usually characterized by non contact techniques. Among them, vision-based SHM using computer vision techniques are succesfully adopted for developing accurate and low-cost bridge monitoring systems that can identify and quantify irregular behaviors in bridge safety by simply employing single or sparse cameras and image processing techniques [72, 73]. The most important advantages deal with non contact capabilities and the wide area that may be potentially monitored. However, this cost-effective SHM system is hardly adopted for small defects detection and it is limited to fixed targets, such as bridges and other deteriorating civil structures. A similar discussion can be organized considering global positioning system (GPS) as monitoring technology with the aim to develop a reliable and effective method of global displacement sensing [74]. However, from this point of view, both approaches may be considered a further development of classic vibration-based techniques.

Another emerging technology consists of remote interrogation of structures at microwave frequencies so that any parameter affecting the reflected wave is a function of its structural condition [75]. Damage can be detected in composite materials as well demonstrating the feasibility of microwave sensor elements for detecting damage in composite structures. The advantages of having a damage-sensitive structure with permanently embedded sensors that can be interrogated remotely are here found together. As suggested in [76], the unique properties of millimeter wave radiation allows penetrating through many non-conducting materials. Mechanical vibrations are rarely measured with Laser-Doppler-vibrometry (LDV) in practical SHM applications, due to the high costs. Instead, the low cost radar technology represents a promising new approach towards in-situ SHM-scenarios with permanently installed sensors [77]. Furthermore, the low attenuation enables long distance measurements, making this radar-based approahes even an enhancement of vibration-based techniques being able to detect displacements [78] and mechanical vibration (Moll20141802) but with novel and promising capabilities [79].

Among various techniques, GUWs have been extensively investigated in the last decades due to several advantages: (i) the transducers required are light, cheap and

can be easily bonded or integrated in the structure, (ii) they can travel long distances with loss attenuation requiring a limited number of transducers to scan large areas, (iii) the high frequency excitation returns small wavelength allowing to detect minute damages unlike low-frequency vibration technique, (iv) the low frequency ambient vibration does not affect the wave characteristics, (v) the multi-modal controllable behavior allows to detect a wide variety of damages and (vi) the transient nature of the physics is not particularly affected by structural damping. On the other hand, the propagation phenomena are quite complex, especially when dealing with composite structures and dispersive waves.

The possibilities and challenges offered by such techniques pushed the present research, oriented to the detection and characterization of typical impact induced damage in composites using GUWs. Furthermore, the aim to achieve smart and reliable techniques spreaded the scenario to the investigation of EMI potentialities for sensor self-diagnostic. To cover all this aspects, the remaining part of this book is organized as follows: the second chapter is dedicated to a brief overview of GUWs and related SHM approach including key aspects in its development such as design of diagnostic input, signal processing and piezoelectricity. The third chapter is the core of the work and it is dedicated to the methodologies developed for damage detection using direct propagating waves and reflections to ensure the highest level of sensitivity. Large experimental campaigns have been conducted and the results obtained instrumenting panels designed for aircraft wing as well as a real scale outer wing of a commercial aircraft are reported and discussed. The results usually match with classic non-desctructive tests based on ultrasonic phased-array technique and compared with benchmarks when present in the literature. Furthermore, several graphic user interfaces have been developed employing the direct propagation approach for relatively fast and easy data processing . The fourth chapter is dedicated to a wide variety of numerical simulations carried out. All methodologies developed and presented, even when non specified, have been supported by finite element modeling (FEM), introducing new perspectives for effective simulation of wave propagation as well as quantification of GUW based SHM system. A final multi-side validation is indeed presented in view of a signal response correlation for global damage detection approaches unable to deterministically size the damage. The latest aspect spreads out the perspectives for an effective model assisted probability of detection (MAPOD). In the fifth chapter, an experimental investigation carried out at *Fraunhofer Institute for Structural Durability and System Reliability LBF* is presented to discuss few criticalities of GUWs while dealing with sensor failure. Analyzing wave signal it is quite complex to distinguish damage of the structure from sensor fault. To overcome this weakness, the EMI response of typically adopted PZTs is studied to find a possible candidate for a self-diagnostic tool directly

linked with the coded softwares. Finally, few conclusions are reported summarizing the promising results obtained and the further investigation possibilities.

Chapter 2

Guided Ultrasonic Waves

Contents

GUWs based SHM techniques have been increasingly adopted to provide information about damage type, severity and location. Basically, from the measured time histories of the propagating waves, several features are extracted and used as damage identification variables. However mathematical formulation, experiments and simulation demonstrated how challenging is to intercept and exploit the physical phenomenon mostly due to dispersive, multi-modal and multi point reflection behavior of waves complicating the post processing of data. In this context, the present chapter details few aspects of wave propagation, from theory to application, in order to introduce the structural health monitoring methodologies described in Chapter 3.

2.1 Elastic waves in solid media

Waves can be defined as disturbances that travel, or propagate, from one region of space to another. Different types of waves follow the same underlying phenomenon.

Wave type	Particle motion, main assumptions
Pressure (a.k.a. longitudinal; compressional; dilatational; P-waves, axial waves)	Parallel to the direction of wave propagation
Shear (a.k.a., transverse waves; distortional waves; S-waves)	Perpendicular to the direction of wave propagation
Flexural (a.k.a., bending waves)	Elliptical, plane sections remain plane
Rayleigh (a.k.a., surface acoustic) waves, SAW	Elliptical, amplitude decays quickly with depth
Lamb (a.k.a., guided plate waves)	Elliptical, free-surface conditions satisfied at the upper and lower plate surface

Table 2.1: Waves in elastic solids.

The Table 2.1 shows some waves possibly propagating in elastic solid media. Axial waves in bars are the simplest conceptualization of elastic wave motion (1D phenomena) while the equation is complicating when complex structures are considered and an analytical solution is not always available.

Guided waves are mostly important for structural health monitoring. They indeed remain confined inside the walls of the structure, and hence can travel over large distances *guided* by the structure which is also called *waveguide*. Furthermore the high frequency involved leads to little amplitude loss. Finally they can be simply excited with a concentrated source. Thus, they enable the SHM of large areas from a single location. In addition, guided waves can also travel inside curved walls. These properties make them well suited for the ultrasonic inspection of complex systems such as aircrafts, missiles, pressure vessels, oil tanks and pipelines. Examples of guided waves are Rayleigh waves, Shear-Horizontal waves and Lamb waves. Rayleigh waves are found in thick solids that contain a free surface. They travel close to the free surface with very little penetration in the depth of the solid. Rayleigh waves have the property of propagating close to the body surface, with the motion amplitude decreasing rapidly with depth. The polarization of Rayleigh waves lies in a plane perpendicular to the surface. The effective depth of penetration is less than a wavelength. For this reason, Rayleigh waves are also known as surface-guided waves.

In plate like structures, ultrasonic guided waves travel as Lamb waves or shear horizontal (SH) waves. Lamb waves are vertically polarized, whereas SH waves are horizontally polarized. This means that the particle motion of SH waves is polarized parallel to the plate surface and perpendicular to the direction of wave propagation.

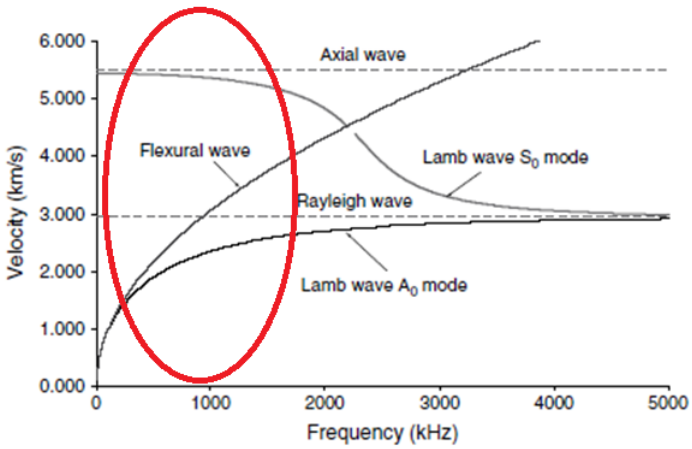

Figure 2.1: Degeneration of fundamental lamb wave modes. The ring includes typical range of frequencies used here in GUWs based SHM [80].

The SH waves can be symmetric and antisymmetric, depending on how the excited particle is moving respect to the motion of the same particle on the opposite side of the neutral plane. With the exception of the very fundamental mode, the SH wave modes are all dispersive, which means that the velocity changes with frequency and consequently the phase velocity is different than the group velocity. This phenomenon complicates the propagation because exciting a wave packet its waveform changes while travelling in the structure. On the contrary, Lamb waves are guided plate waves with the motion polarized along the normal axis of the plate. They can propagate showing a symmetric (S_i) or antisymmetric (A_i) motion of the solid particles. Both modes are quite dispersive and may exist in an infinite number. This means that at any given value of the thickness frequency (product of excitation frequency and plate thickness - fd), a multitude of symmetric and antisymmetric Lamb waves may exist. The higher the thickness frequency, the larger the number of Lamb-wave modes that can simultaneously exist. For relatively small values of fd (below the so-called *cut-off*) frequencies), only the fundamental symmetric and antisymmetric Lamb-wave modes (S_0 and A_0) exist. As the fd product approaches zero, the S_0 and A_0 modes degenerate in the basic axial and flexural plate modes. At the other extreme, while increase fd to highest values, the S_0 and A_0 Lamb-wave modes degenerate into Rayleigh waves confined to the plate surface (Figure 2.1). Guided waves also exist in other thin-wall structures, such as rods, tubes, and shells. Though the underlying physical principles of guided-wave propagation still apply, their study is more elaborate.

As a matter of facts, the physical phenomena of several guided waves are strictly connected, especially while dealing with Rayleigh and Lamb waves (which have the

same polarization direction). They can indeed merely converse one in each other while encountering an abrupt change of the structure like step discontinuities or delamination in thick solids [81, 82]. How much thick or thin the solid should be to allow Rayleigh rather than Lamb waves to propagate depends on the wavelength. In the ultrasound range, when the wavelength is much greater than the thickness of the plate/solid, it is easy to imagine that solid particles are all affected by the motion, which generates Lamb waves. That is the reason for which usually Lamb waves propagation is associated to plate-like structures. Otherwise, while the wavelength is much smaller than the characteristic thickness of the plate/solid, the motion is confined to the boundary of the structure where the disturbance is generated, penetrating for a depth comparable with the wavelength. That is the reason leading to the association between Rayleigh waves and thick solids.

Ultrasonic guided waves in flat plates have been firstly mathematically described in [83] and several comprehensive analysis of Lamb wave propagation are also available in the literature [68, 84, 85, 86, 87, 88, 89]. For many advantages given in the field of application, such as easy excitation and suitable wavelength, Lamb waves are selected for the SHM methodologies developed in this work. For this reason, the next section is dedicated to a brief introduction of their mathematical background in order to justify some physical aspects such as multimodal behavior. However, for a detailed study the author suggests the previous cited works.

2.2 Lamb waves in plates

Lamb waves are elastic guided waves propagating in thin-wall structures along directions contained by the plate's plane and with frequencies mostly in the range of ultrasound. They can exist in two basic types: symmetric and antisymmetric (Figure 2.2), and, for each of these types, infinite modes appear as solutions of the Rayleigh-Lamb equations (Eq. (2.9)). A finite body can support an infinite number of different Lamb wave modes. These modes exist for a specific plate thickness and frequency and they are identified by their respective velocities. In general, elastic waves in solid materials are guided by the boundaries of the media in which they propagate. The mathematical problem can be approached seeking sinusoidal solutions to the wave equation for linear elastic waves subjected to boundary conditions representing the structural geometry: this is a classic eigenvalue problem. The three dimensional wave equation describing the propagation of elastic waves in an isotropic solid media without external forces is defined as follows [88]:

$$(\lambda + \mu)\underline{\nabla}(\underline{\nabla} \cdot \underline{u}) + \mu\nabla^2\underline{u} = \rho\ddot{u} \tag{2.1}$$

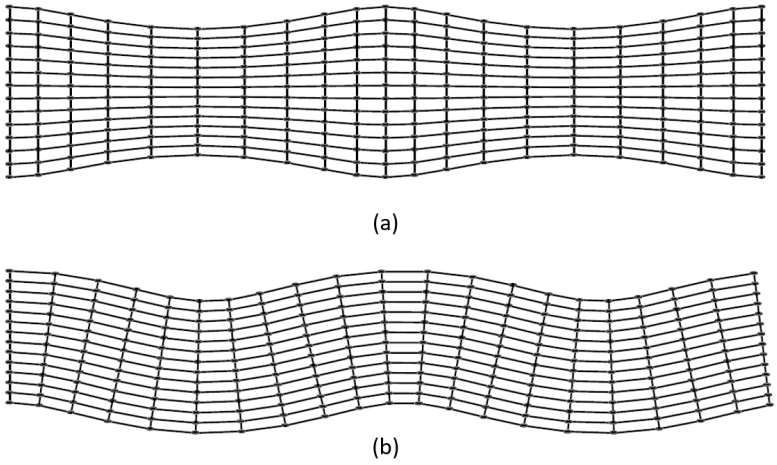

Figure 2.2: Lamb wave mode shapes; symmetric (a), anti-symmetric (b) [87].

where $\underline{u}$ is the displacements vector, λ and μ are the *Lamè constants* and ρ is the density of the isotropic material. Through the Helmoltz theorem the vector $\underline{u}$ can be decomposed using two potentials, one scalar φ and one vecctorial $\underline{\psi}$:

$$\underline{u} = \underline{\nabla}\varphi + \underline{\nabla} \times \underline{\psi} \tag{2.2}$$

By combining Eq. (2.1) and Eq. (2.2) the following equations are obtained:

$$\begin{cases} c_p^2 \nabla^2 \varphi = \ddot{\varphi} \\ c_s \nabla^2 \underline{\psi} = \underline{\ddot{\psi}} \end{cases} \tag{2.3}$$

and then

$$c_p = \sqrt{\frac{\lambda + 2\mu}{\rho}}, \quad c_s = \sqrt{\frac{\mu}{\rho}} \tag{2.4}$$

with c_p and c_s respectively pressure and shear waves velocities. For harmonic propagation in the x_1 direction, $e^{i(\xi x_1 - \omega t)}$, the Eqs. (2.3) become:

$$\begin{cases} \frac{d^2\phi}{dx_3^2} + p^2\phi = 0 \\ \\ \frac{d^2\psi}{dx_3^2} + q^2\psi = 0 \end{cases} ; \qquad \begin{cases} p^2 = \frac{\omega^2}{c_p^2} - \xi^2 \\ q^2 = \frac{\omega^2}{c_s^2} - \xi^2 \\ \xi = \frac{\omega}{c} \end{cases} \tag{2.5}$$

with ω circular frequency and ξ wave number, having general solution:

$$\begin{cases} \phi = A_1 \sin(px_3) + A_2 \cos(px_3) \\ \psi = B_1 \sin(qx_3) + B_2 \cos(qx_3) \end{cases} \tag{2.6}$$

From Eq. (2.5) and Eq. (2.6), by assuming zero displacement in the x_2 direction ($u_2 = 0$), the general form of components of the displacements vector can be derived, grouped into symmetric and antisymmetric components:

$$\begin{cases} u_1 = (A_2 i\xi \cos(px_3) + B_1 q \cos(qx_3)) + (A_1 i\xi \cos(px_3) - B_2 q \cos(qx_3)) \\ u_3 = -(A_2 p \cos(px_3) + B_1 i\xi \cos(qx_3)) + (A_1 p \cos(px_3) - B_2 i\xi \cos(qx_3)) \end{cases} \tag{2.7}$$

The stresses can be then connected to both the scalar and vectorial potentials, and, by applying the conditions of free surfaces on the plate's top and bottom, the resulting system of equations is:

$$\begin{cases} \tau_{33|_{x_3=d}} = \tau_{33}(\varphi, \underline{\psi})|_{x_3=d} = 0 \\ \tau_{33|_{x_3=-d}} = \tau_{33}(\varphi, \underline{\psi})|_{x_3=-d} = 0 \\ \tau_{13|_{x_3=d}} = \tau_{13}(\varphi, \underline{\psi})|_{x_3=d} = 0 \\ \tau_{13|_{x_3=-d}} = \tau_{13}(\varphi, \underline{\psi})|_{x_3=-d} = 0 \end{cases} \tag{2.8}$$

By requiring the system (2.8) to have non-trivial solutions (determinant equal to zero), two transcendental implicit equations are derived; one for symmetric modes and one for antisymmetric ones, called *Rayleigh-Lamb equations* (d is the plate half-thickness, c_{ph} is the wave speed, $\xi = \omega / c_{ph}$ is the wave number):

$$\begin{cases} \frac{\tanh(pd)}{\tanh(qd)} = -\frac{\left(\xi^2 - q^2\right)^2}{4\xi^2 pq} & , \quad symmetric \quad mode \quad (S) \\ \frac{\tanh(pd)}{\tanh(qd)} = -\frac{4\xi^2 pq}{(\xi^2 - q^2)^2} & , \quad antisymmetric \quad mode \quad (A) \end{cases} \tag{2.9}$$

The solutions of Eqs. (2.9) represent the phase velocities c_{ph} of the various Lamb waves modes: these curves do not exist in a closed form, so numerical algorithms are needed in this case. Each one of the two Rayleigh-Lamb equations presents a number of solution curves defining more than one relation between wave number and frequency, or even wave velocity and frequency: several orders are present for both symmetric and antisymmetric modes. By considering the velocity of Lamb waves packets traveling in the plate, it is possible to introduce the group velocity c_g which is linked to phase velocity through the relation:

$$c_g = \frac{\partial \omega}{\partial c_{ph}} \quad or \quad c_g = \frac{c_{ph}}{1 - \frac{\omega}{c_{ph}} \frac{\partial c_{ph}}{\partial \omega}} \tag{2.10}$$

Typical trends of symmetric and antisymmetric Lamb wave modes for an aluminum plate are represented in Figure 2.3. It is evident how (i) the phase and group velocity differ in the dispersive ranges, (ii) the highest modes are characterized by a cut-off frequency below which they cannot exist, and (iii) all modes tend to have the same

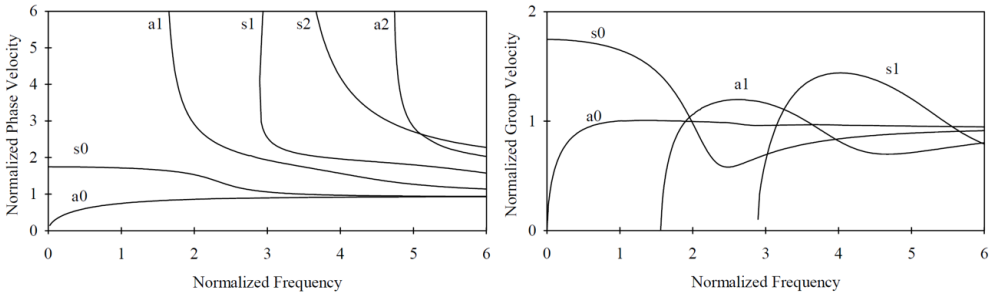

Figure 2.3: Dispersion curves for an aluminum plate, lowest order solutions. Normalizing velocity: shear velocity c_S; normalizing frequency: $\xi_S \cdot d$, with $\xi_S = \omega / c_S$ [87].

velocity strongly increasing the frequency (i.e. they tend to became surface waves).

Although the relatively simple formulation obtained, it is necessary to emphasize that Lamb waves propagation behavior is much more complex than that of classic bulk waves. First of all, they have dispersive characteristics (i.e., the wave velocity changes with frequency, modes, and plate thickness); then, in relation to composite laminates, wave propagation is complicated by the heterogeneous nature of material, its inherent anisotropy and the multi-layered construction leading the wave mode velocity to be macroscopically dependent on the laminate layup, the direction of wave propagation and interface conditions. As a matter of facts, dealing with guided waves for structural monitoring requires analysis of propagating waves making extensive use of signal processing techniques, dedicated algorithms for damage detection, propagation models based on theoretical aspects and correct selection of interrogation and monitoring parameters affected by the complex physics of Lamb waves. A first overview of SHM based on GUWs is presented in the next sections including the description of principal aspects to account for the methodology definition. Such guidelines are reported in order to simplify many technical aspects while approaching the Chapter 3. They are mostly derived from bibliographic study when reported otherwise they are directly moving from the knowledge gained through the experiments carried out.

2.3 GUWs based Structural Health Monitoring

GUWs have been extensively investigated in the last decades due to several advantages aforementioned. A feature making Lamb waves so interesting and advantageous for damage detection is the typical wavelength of the order of centimeters or even millimeters (depending on frequency and mode considered) which makes them able to interact with very small obstacles, e.g. through thickness damages in plates induced by low energy impacts on composites. Furthermore, Lamb waves can be both excited

and sensed by means of small, lightweight and inexpensive transducers such as Piezoelectric Wafer Active Sensors (PWAS) that require low power. PWAS transducers can be produced in different geometries and dimensions so that they can be adapted for the various cases, furthermore they can be directly integrated (bonded or embedded) becoming part of the final structure. This means that Lamb waves can be used to continuously interrogate the structure using permanently integrated sensors in order to detect small damage inside structures from their very early stage of development (i.e. the aim of a SHM system).

2.3.1 Diagnostic wave

The goal of SHM research is to develop a monitoring methodology that is capable of detecting and identifying, with minimal human intervention, various damage types during the lifespan of the structure. Active SHM systems using interrogating Lamb waves are able to achieve such results because different types of damages may interact differently with several waves. Lamb wave based SHM techniques have been proved to provide information about damage type, severity and location. Based on the measured time history of the propagated wave, the traveling time, group speed reduction, and wave attenuation, several parameters can be extracted and used as the damage identification variables. Further processing of the measured signals (e.g., using Short-Time Fourier transform, Hilbert transform, Wavelet transform, Hilbert-Huang transform, etc.) helps damage recognition.

However, the success of the interrogation mostly depends on the interrogation feature used as damage indicator. The incident Lamb waves depend upon the excitation signal parameters (pulse shape, amplitude, frequency and number of cycles to be sent during each pulse period) and may have significant impact on damage detection. For instance, the fundamental anti-symmetric Lamb mode A_0 can be generated at frequencies below 50kHz where is much slower than the symmetric S_0 mode and thus showing a smaller wavelength making it more sensitive to damage detection. In the field of NDE, a common understanding is indeed that the ultrasonic scanning technique can usually detect damage with a characteristic size larger than half wavelength of the employed ultrasonic wave. For this reason, the fundamental antisymmetric mode A_0 is preferable and more sensitive to damage in the low-ultrasound range (i.e. its wavelength is shorter than that of the S_0 mode at the same frequency). Furthermore, the A_0 mode exhibits more severe dispersion at low frequencies. As a consequence, it is simply possible detect delamination evaluating the time of flight (i.e. the thickness frequency decreases in that location affecting the time of arrival [90] or the overall wave behaviour [81]) but more stringent experimental configurations are normally required to prevent energy leakage for its substantial out-of-plane vibrations (i.e.: the leakage

introduces complexities in catching and correctly processing the signal while the wave is travelling). In contrast, the mode shape of the S_0 mode is simple and the stresses are almost uniform throughout the thickness of the plate at low thickness frequency values.

As a matter of facts, while activating diagnostic waves it is crucial to define the *appropriate* mode, the *appropriate* signal and the *appropriate* frequency in order to achieve the most effective identification of damage. Generically, the optimal characteristics of an interrogating wave would be: (i) low dispersion, (ii) low attenuation, (iii) high sensitivity, (iv) easy activation, and (v) easy sensing. Usually, the S_0 mode is selected for damage identification due to, in contrast to the A_0 mode, its:

- lower attenuation (A_0 mode usually presents higher attenuation during propagation because of the dominant out-of- plane movement of particles in the mode shape, which leaks partial energy to the surrounding medium; whereas the S_0 mode has mostly in-plane displacement and its energy is confined within the plate);
- faster propagation velocity which means that complex wave reflection from the boundary can sometimes be avoided;
- lower dispersion in the low frequency range, benefiting signal interpretation.

On the other hand, there has been increasing awareness of using the A_0 mode for damage identification. Its merits, in comparison with the S_0 mode, include:

- shorter wavelength at a given excitation frequency (in recognition of the fact that the half wavelength of a selected wave mode must be shorter than or equal to the damage size to allow the wave to interact with the damage);
- larger signal magnitude in lower ultrasound range (the A_0 mode in a wave signal is usually much stronger than the S_0 mode if two modes are activated simultaneously, giving a signal with high signal-to-noise ratio (SNR), though it attenuates more quickly);
- easier means of activation (the out-of-plane motion of particles in a plate can more easily be activated).

Generally, both the S_0 and A_0 modes are sensitive to structural damage, and both can be used for identifying damage. They are preferable mostly because below the first cutoff frequency it is possible to avoid higher modes preventing more complex interpratation of signals. Although it is feasible to select the preferred interrogating mode, it is indeed not possible to prevent mode conversion at discontinuities and reflections, making preferable exciting fewer modes possible.

To excite primarily the desired mode for interrogating the structure, it is possible to exploit the *wave mode tuning* techniques. While using PWAS is not possible to automatically select the mode because it generates both symmetric and anti-symmetric modes simultaneously, but different methods are effective to isolate one of these. First of all, a desired wave mode can be enhanced while other undesired modes can be cancelled or minimized in a resultant signal, after mutual interaction of various Lamb wave modes generated by a series of appropriately placed PWASs. This mode selection technique is often termed a *multi-sensor mode tuning technique* [91]. Due to the behavior of PWASs, explained afterwards, while exciting thin plates, it is also possible to simply superimpose the effect of two sensors paced on the opposite faces of the structure and synchronize the excitation to remark one mode while suppressing the other one. Both possibilities are effective but practically difficult to be applied requiring more sensors working simultaneously and the accessibility on both sides for the second approach (infeasible for real structures). However even though both modes are present using unique actuator, tuning Lamb waves with PWAS leads to either of symmetric and antisymmetric modes. Their amplitude indeed strongly depends on the frequency, the most important parameter for Lamb waves tuning with sensor. It is possible to excite different modes simply by opportunely changing the frequency because there are ranges in which only one mode is really visible (dominant), due to the much greater amplitude than the other.

To realize how Lamb wave amplitude depends upon frequency, it is useful to consider the so called *tuning curves*, representation of *amplitude vs. frequency* of wave modes. It has been proved that the PWASs could activate the S_0 and A_0 modes of different energy intensities at different excitation frequencies. The concept of a 'sweet spot' has been established, referring to the central frequency of the excitation signal, at which the maximum wave peak magnitude ratio of the S_0 to A_0 (or the A_0 to S_0) modes is reached, so as to minimise the inherent interference between the two wave modes and thus benefit signal interpretation. It is noteworthy that such a PWAS-based tuning technique must be customised for plates of different thicknesses, since plate thickness influences the dispersive properties of wave modes, as does the size of PWASs. There is indeed a common practical guide about the maximization of wave amplitude while changing the wavelength. Using circular PWAS it has been found also by the author that the amplitude increases while approaching a wavelength two times the diameter of the sensor. Furthermore the wavelength depends on the thickness frequency making PWAS dimension and plate thickness the key parameters while tuning wave with PWAS by means of frequency selection.

To better understand such phenomena, typical curves obtained in the context of this research for a composite plate are presented in Figure 2.4. The results are part of

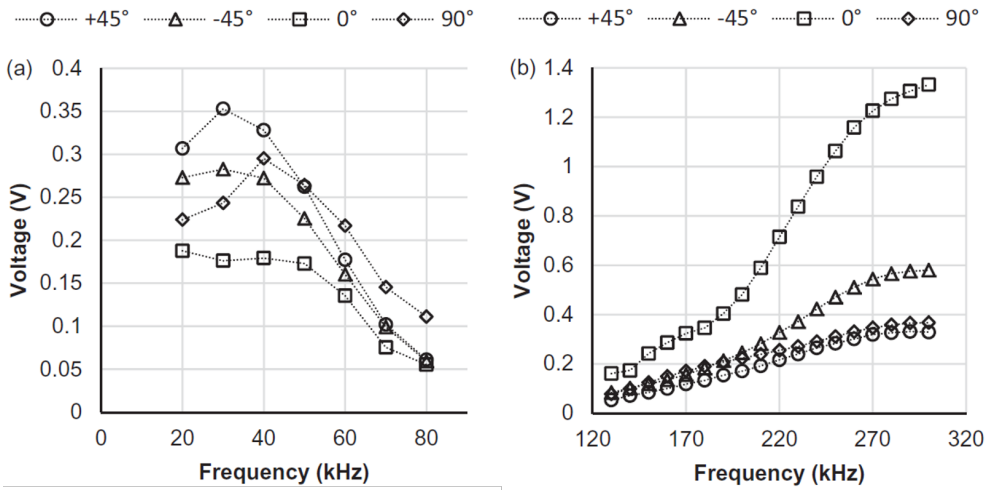

Figure 2.4: Lamb waves response for a composite plate of thickness 1.6 mm, using a PWAS disk of diameter 10mm.

the experiments described in detail in Sec. 4.1.2, involving dispersion measurements in different directions of a quasi-isotropic plate. Due to the strong dependence of the Lamb waves amplitude on the frequency, tests have been carried out in the frequency range from 10kHz to 70kHz to define the dispersive wave mode A_0. Otherwise, the S_0 mode is investigated in the frequency range from 130kHz to 300kHz. In the frequency range considered, the presence of both A_0 and S_0 is evident from the receivers output even though with different amplitudes depending on the central excitation frequency. The extensional waves are negligible in the lower range, due to their smaller amplitude where the A_0 mode is clearly identified. Increasing the frequency, the amplitude of the extensional waves increases while the antisymmetric mode decays in intensity making the S_0 mode clearly visible. The A_0 mode is not analyzed beyond 80kHz because it is indeed not longer clearly identified. The tuning curves allow to precisely define the wave mode amplitude trend with the excitation frequency. Beyond the frequency of maximum tuning, the A_0 mode rapidly decreases in amplitude no matter the direction of propagation is (see Figure 2.4 (a)). Instead, results obtained in the higher frequency range show the increasing amplitude of the symmetric wave mode with the maximum tuning around 300kHz (see Figure 2.4 (b)). On the basis of such evidence, the opportune investigation frequency range can be selected for both modes. However, it is worth emphasizing that all the aforementioned mode tuning approaches can more or less enhance a specific Lamb mode at a given frequency and meanwhile suppress the others modes, but they cannot cancel a wave mode in a signal completely. That point supports the choice to excite fewer modes possible remaining below the first cutoff frequency where possible.

Summarizing the discussion, it is possible to point out that the choice of the excitation frequency is a very important aspect and may account the following considerations:

- minimum number of wave modes, to limit received signal complexity;
- interrogating mode as non-dispersive as possible, to obtain a waveform independent from the propagation distance;
- wavelength according to the damage dimension.

About the last item, in a real application, the size of the damage is one of the things to be evaluated, and therefore it is unknown. Nevertheless, the target of the SHM system is usually known and it is possible to relate the minimum damage to be detected to that fix that point. Another practical issue found by the author while exciting fundamental modes together regards the possibility to select the frequency that minimizes their overlap in the time histories captured by the sensors, improving the detection capability and avoiding misleading interpratation of signals. Hence, according to the wavelength requested for a critical damage dimension and to the most suitable mode, the most effective way to select the frequency is a matter of weighting mode tuning and time shift between different modes. In this way the mode which is primarily excited is clearly sensed and the other one may be exploited as well for damage detection but without any complex interaction with the former. However, this item is mostly connected with the signal waveform, which should be optimized as suggested in the next section, and to the features to be extracted, whose characteristics are reported in Sec. 2.3.3.

To correctly operate the monitoring of the structure, the identification of the wave features affected by a specific damage to investigate is really crucial. No matter what the parameter selected is, when guided waves are propagating in stiffened composites, it is quite challenging and often time consuming to consider the theoretical behavior of wave propagation as reference (model-based approaches). Although promising results have been sometimes obtained with such approaches [92], the post processing of ultrasonic data appears to become further challenging when complex structures are considered, activating multimodal behavior, multi-point reflection and damage interaction when present It is indeed often preferable to directly compare wave signals interrogating the structure different times to detect possible changes respect to a starting baseline. For the latter demand, a parameter representative of the wave behavior is extracted from signals at fixed time intervals, or after fixed load cycles, and compared to a "pristine (or healthy) configuration". If no change is currently present in the structure, the current feature should be very close to that evaluated on the pristine

structure, resulting in a non-identification response. Otherwise, if such a change is present, the feature should increasingly change with severity of damage. No matter what the compared parameter is, a possible metric is the Damage Index (DI) defined as follows:

$$DI = \frac{|f_{CS} - f_{BS}|}{f_{BS}} \tag{2.11}$$

where f_{CS} and f_{BS} are scalar features extracted respectively interrogated the pristine (baseline signal) and current (current signal) structure. With a DI close to zero, the structure is in a healthy state; when the DI exceeds a certain threshold, this means that damage appears; the greater the index, the more serious the damage should be. As a matter of facts, the DI value becomes the signal response.

This approach, defined hereinafter as damage index approach, is extensively used in this research for damage detection and detailed described in Chapter 3. However it is easy to imagine how the identification depends mostly on the wave capability to interact with damage and the sensitivity of the selected feature to that interaction. That is the case when the damage indicator will return valuable information about structural condition. For the first demand the correct design of the interrogating signal is vital for a correct sensing of the propagating wave as briefly described in the next section.

2.3.2 Optimal design of signal waveform

The selection of a Lamb wave mode as the diagnostic wave interacting with possible damage requires to be correctly addressed. The bandwidth, cycle number, frequency and magnitude of this mode are key parameters while operating with dispersive curves to enhance or impair the capability of damage identification to a certain extent. The dispersion primarily prevents the correct identification because the guided wave spreads out and changes shape as it travels long distances, making its analysis a major concern. To reduce this effect, a narrow bandwidth can minimizes the spectral leakage preventing wave dispersion. Windowed toneburst signals with a certain number of cycles rather than a single pulse are used for activating diagnostic wave signals in practice, although a pulse signal may offer higher and more concentrated incident energy. In particular, the *Hanning function*, is the most widely adopted window function, defined as follows:

$$h(n) = \frac{1}{2}\left[1 - \cos\left(2\pi\frac{n}{N-1}\right)\right] \qquad (n = 1, 2, \ldots, N) \tag{2.12}$$

where $h(n)$ is discretised using N samples. Applying the *Hanning* window on a 4.5 sine-cycles signal performing a 1s burst with a central frequency of 40kHz, the mod-

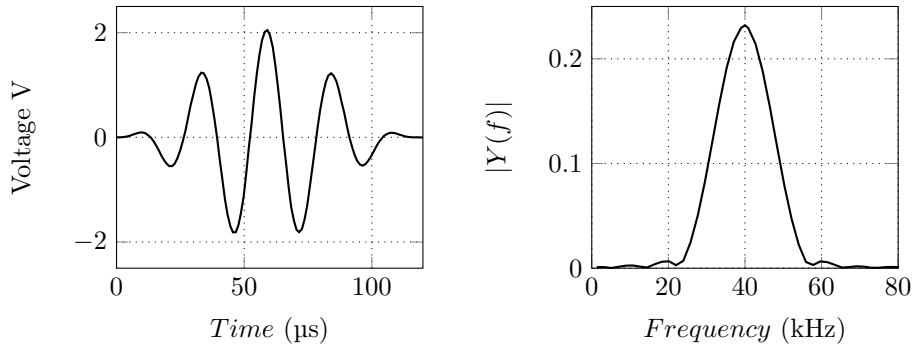

(a) Signal in Time (b) Signal in Frequency

Figure 2.5: Diagnostic wave obtained windowing a 4.5 sine cycles burst with *Hanning* function: time doman history (a) and frequency domain spectrum (b) employing fast Fourier transform (Carrier frequency: 40kHz).

ulated signal and its energy spectrum obtained by Fourier transform are displayed in Figure 2.5. The energy of the modulated wave signal is observed to be concentrated within a very narrow frequency range (centralised at 40kHz in that example), reducing wave dispersion considerably and according with the reduced leakage. For such diagnostic signals, the relationships between the excitation frequency bandwidth $[f_{min}, f_{max}]$, the toneburst cycle number n , and the central excitation frequency f_0 can be formulated by:

$$f_{min} = f_0 \cdot (1 - k/n), \quad f_{max} = f_0 \cdot (1 + k/n) \tag{2.13}$$

where k is a constant depending on the selected window. The Eq. (2.13) hints that, as the cycle number of tonebursts increases, the wave bandwidth is reduced, the signal energy is more concentrated near the central excitation frequency, the peak amplitude increases, and accordingly wave dispersion is minimised. However the number of cycles cannot be further increased without any threshold because the duration of the overall signal increases accordingly and the received signal is the accumulation of input waves, scattered and converted waves altered by the dispersion; a large cycle number may result in a pronounced overlap among the different wave components preventing a correct interpretation of signals.

As a matter of facts, a compromise between the cycle number of the diagnostic wave signal and its duration must be considered case by case to achieve a valuable interrogation. However, as suggested in [91], the most suitable cycle number and frequency of a diagnostic Lamb wave signal can be determined in terms of the minimum

resolvable distance (MRD), which is defined as:

$$MRD = \frac{v_0}{d}\left[l \cdot \left(\frac{1}{v_{min} - \frac{1}{v_{max}}}\right) + T_{initial}\right]_{min} \tag{2.14}$$

where l and d are the wave propagation distance and plate thickness; v_0,v_{min} and v_{max} are the group velocity at the central frequency of the input wave-packet, and the minimum and maximum velocities of the wave-packet to travel the distance of l , respectively, $T_{initial}$ is the initial time duration of the wave-packet. It has been found that the lower a MRD value, the better the resolution, and the more suitable the current frequency and cycle number for damage identification. From this evaluation, S_0 and A_0 have been found to possess very low MRD values and accordingly are often selected for damage identification.

Finally, about the magnitude of the signal adopted to excite the diagnostic wave, while increasing its voltage and keeping fixed the frequency the magnitude of the diagnostic Lamb wave and that of the sensed wave increase accordingly. The amplitude values reported in Figure 2.4 are refferred to a generated signal of 80V peak to peak and a distance between actuator and sensor of 150mm, demonstrating that the attenuation of the output signal due to the bonded PWAS efficiency and the travelling distance in composite can be also affected by the noise if not correctly addressed. Increasing the magnitude of the signal can increase the signal to noise ratio, leading to an explicit response signal with less noise, though at the cost of higher energy consumption. However, in a practical application two different aspects should be accounted. First of all the excessive voltage can depolarise PWAS elements, whose maximum working electrical loading is about $250 - 300\text{V}\,\text{mm}^{-1}$ in the element thickness. Then, the amplitude and the frequency of the signal cannot be simultaneously increased above a defined limit according to the digital to analog and analog to digital conversion capabilities of the hardware used to excite and sense guided waves. The latter demand is perhaps one the most critical issues while practically dealing with the implementation of GUWs based SHM systems.

When the wave mode selected for diagnostic signal is optimized, several signal processing techniques may be required to correctly identify and characterize the propagation behaviour and extract features able to detect possible anomalies in the waveguide. The next section is dedicated to such aspects, which closes the overview of several guidelines for effective GUWs SHM.

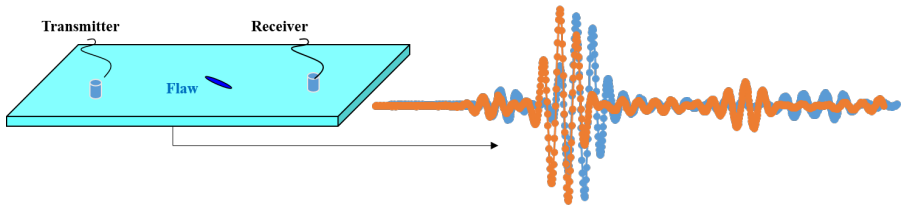

Figure 2.6: Lamb waves response sensed using pitch catch approach as a synthesis of wave propagation.

2.3.3 Signal processing

For the sake of the simplicity, it can be asserted that the propagation changes when a detectable damage is encountered, making possible the structural diagnosis. However, the complexities of wave propagation while traveling in non-isotropic media [93, 94] make quite difficult to relate time histories caught in few single sensing points to how the wave is propagating and eventually interacting with such a hidden flaw. As highlighted in Figure 2.6 for a pitch catch approach, the acquired signals are merely a synthesis of the wave propagation, which is reflected in the time history of the high frequency vibration affecting the receiver. Hence, the ultrasonic propagation has to be related to specific parameters (signal responses) which may be affected by unforeseen failure. Signal processing and computation are crucial elements in the implementation and operation of any damage identification system. The generic system requires appropriate signal processing technology to extract features from different types of sensors and to translate this information into a diagnosis of location and severity of damage [95].

As a matter of facts, the accuracy and precision of a GUWs-based damage identification approach depends on the signals captured by several sensors and it is largely subject to their processing and interpretation. Captured Lamb wave signals carry comprehensive information as to interference existing in the path of wave propagation, such as damage in the medium inducing some changes in the captured signals. The key is to correctly tease out these changes and then associate them with particular variations in damage parameters (e.g., presence, location, size and severity). The existence of multiple wave modes, dispersion, mode conversion, superposition of scattered waves from structural boundaries or irregularities (e.g., joints, stiffeners and openings), broadband noise and other features make challenging this process. Even using a DI approach, it is vital for damage identification to use appropriate signal processing to extract appropriate features. Efficient signal processing is expected to

extract essential yet concise characteristics (e.g., magnitude, frequency, energy, wave speed and travelling time) from raw signals, to assist in assessment of damage parameters in conjunction with appropriate data fusion algorithms. The latter demand deals with the algorithms capable to relate signal responses to damage parameters and it is remarked in the Chapter 3 where the signal processing techniques described below are extensively adopted.

Digital signal processing (DSP) is the study of any signals in digital representation and several approaches are available. It is common to broadly group these approaches is in terms of the domain where the processing is conducted, i.e., time domain, frequency domain and joint time-frequency domain analyses. Wave signals are normally digitized in time domain, whether they are obtained from measurements or models. Then, digitized data is normally transformed both for the frequency and time domain for a better understanding of the dynamic response of the structure.

Typically DSP techniques in time domain involve the Hilbert transform, correlation, integration, time reversal, exponential smoothing, regression (curve-fitting), extrapolation, differencing and decomposition. All of these approaches can globally or locally extract the aforementioned characteristics from a time-series Lamb wave signal. Instead, DSP in the frequency domain is typified by the Fourier Transform (FT), Fast Fourier Transform (FFT), Digital Signal Filter, Two-dimensional FT and FFT (2D-FT/FFT). However it is common to combine the analyses in the sole time and sole frequency domains avoiding any potential loss of information. That is where the joint time-frequency domain analysis differs from the previous DSP approaches. Short-time Fourier transform (STFT), Wigner-Ville distribution (WVD) and wavelet transform (WT) are typically adopted for the latter demand.

A typical problem while processing guided waves is to extract their dispersive behavior by plotting the wave velocity of the selected mode versus the frequency. Such curves, called *dispersion curves*, are mostly adopted to characterize the material, to detect possible anomalies and also to validate numerical models correlating simulation and experimental outcomes (see Chapter 4). A typical approach to define the trend of group velocity while increasing the frequency is based on the *time of flight* method, where the distance between a couple of sensor is fixed and the group velocity is referred to the time shift of excited and sensed wave. Due to the importance of this aspect in the present work, two types of signal processing techniques are considered detailed hereinafter:

- short-time Fourier transform (STFT) technique;
- combined cross correlation and Hilbert transform (HT) technique

The basic idea of the short-time Fourier transform is to divide the time signal in

small segments (*short time*) and perform the Fourier analysis (*fourier transform*) on each time segment to confirm that certain frequencies exist or occur in that segment. The constant time-window is transformed by the fast Fourier transform (FFT) in the frequency domain. This time window is then shifted to a new position in time usually adopting a fixed overlap and the transform is repeated. Since the constant time-window STFT don't due to a high resolution both in time and in frequency, but only in one of them, STFT applies the basic FT on a small signal segment about time moment t , by multiplying a time window function (commonly a *Hanning* or *Gaussian* window) and neglecting the rest of the signal. This operation is then continued by moving the short time window along the entire time axis, to obtain the energy spectrum of the full signal. Given a signal $s(t)$, to study the signal properties at time t_0, windowing processing is applied to emphasize the signal at that instant and suppress those at other time. The window, indicated by a function $h(t)$, is centered at t. The windowing process will produce a modified signal:

$$S_t(\tau) = s(\tau)h(\tau - t) \tag{2.15}$$

This modified signal is a function of the fixed time, t, and the varying time τ. The corresponding Fourier transform of signal $S_t(\tau)$ is:

$$S_t(\omega) = \frac{1}{2\pi}\int e^{-j\omega t}s_t(\tau)\,d\tau = \frac{1}{2\pi}\int e^{-j\omega t}s(\tau)h(\tau - t)\,d\tau \tag{2.16}$$

The energy density spectrum at time t is:

$$P_{SP}(t,\omega) =\mid S_t(\omega)\mid^2 \tag{2.17}$$

For each different time, a different spectrum is available and the totality of these spectra is the time-frequency distribution P_{SP}, called *spectrogram*. Contour plot is applied in the spectrogram to represent the amplitude of each point in the time-frequency space and it is possible to characterize the characteristic time of the wave both considering the carrier frequency of the signal or the maximum amplitude. The correct time windowing returns indeed the maximum P_{SP} while the central frequency is considered.

Satisfactory precision cannot be obtained along the time- and frequency-axes synchronously because is not possible to divide the signal into finer and finer part due to the uncertainty principle:

$$\Delta\omega \cdot \Delta t \geq \frac{1}{2} \tag{2.18}$$

which states that the product of the standard deviation in time and frequency (time

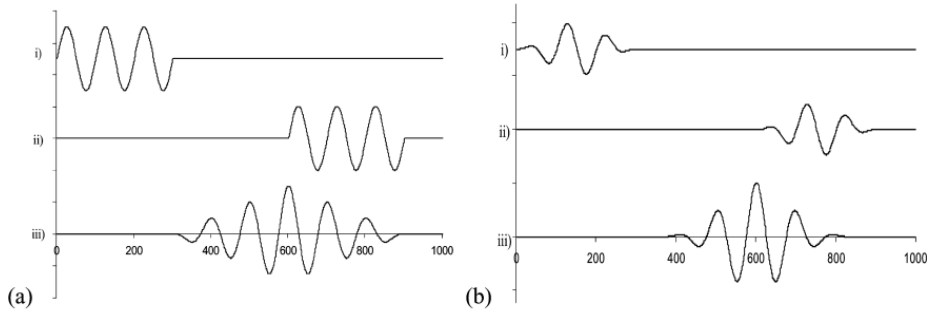

Figure 2.7: Cross-correlation of simulated tone-burst signals: (a) 3-count sine signal: (b) 3-count Hanning-window smoothed signal. Note: (i) transmitted signal $x(t)$; (ii) received signal $y(t)$; (iii) cross-correlation of $x(t)$ and $y(t)$.

and frequency resolutions) is limited. The decrease (increase) in frequency resolution results in an increase (decrease) in time resolution and vice versa.

About the second approach, the cross correlation is used for time delay assessment due to its capability to detect similarities in two signals [96, 97]. The cross correlation $R_{xy}(t)$ of two signals $x(t)$ and $y(t)$ is defined by:

$$R_{xy}(t) = \int_{-\infty}^{\infty} x(\tau)y(\tau + t)\, d\tau \tag{2.19}$$

or in case of discrete-time signals, by:

$$R_{XY}(m) = \frac{1}{N}\sum_{n=0}^{N-1} x(n)y(n-m) \tag{2.20}$$

The principle is based on the fact that the time delay can be found simply by maximizing the cross correlation function. However, due to the oscillating trend of the latter function (Figure 2.7), its maximum can be more effectively found resorting to the envelope of the signal [98]. The envelope of the signal is simply extracted by applying Hilbert transform (again in time domain) to the cross correlation signal. The Hilbert transform is defined as:

$$H(x(t)) = -\frac{1}{\pi}\int_{-\infty}^{+\infty} \frac{x(\tau)}{t-\tau}\, d\tau \tag{2.21}$$

It can also be defined in terms of convolution theory:

$$H(x(t)) = x(t) * \frac{1}{\pi t} \tag{2.22}$$

It is worth noting that in the applications considered in this work, the results obtained using both methods are always comparable. No matter what the DSP technique is used, from the arrival time assessment, the group velocity is then directly evaluated as:

$$v_g = \frac{d_s}{ToF} \tag{2.23}$$

where v_g is the group velocity of the wave, d_s is the distance between actuator and receiver sensors and the ToF is the time of flight. The difficulty consists in the fact that the signals transmitted and received with the PWAS transducers are much weaker than the signals typically encountered in conventional ultrasonics. Furthermore, the signal are quite complex due to several modes and interactions involved within time series. These makes indeed the signal processing more challenging and demanding.

Moving to the specific application of damage detection, several signal processing techniques can be exploited in relation to the wave feature selected. Such selection depends primarily upon the type of damage to investigate while interrogating the structure. Summarizing the aspects mentioned in Sec. 1.2.2, an impact induced damage can be indeed idealized as a complex discontinuity distributed through the thickness changing the waveguide characteristics [99]. The dispersion behavior of Lamb waves can be exploited because the interaction with local damage may result in a different arrival time of the propagating wave packet. The group velocity is very sensitive to such damages modifying the structural waveguide characteristic thickness while the dispersion curve shows a gradient towards the section thickness. The group velocity results directly from the *Time of Flight (ToF)* estimating the characteristic time of the sensed ($\bar{t}_s$) and excited ($\bar{t}_e$) waves, respectively.

$$ToF = \bar{t}_s - \bar{t}_e \tag{2.24}$$

However, this effect may be effective only for some combinations of wave modes, thicknesses variations and actuation frequencies. A discontinuity in a waveguide may results in an abrupt change of the local mechanical impedance [100], which defines the transmitted and received portions of the energy content of the propagating wave. Using a pitch catch approach, an hidden flaw can be detected monitoring such a *Transmission Factor (TF)*, here defined as a ratio between an energy parameter $\overline{E}$ of sensed and excited signal:

$$TF = \frac{\overline{E}_s}{\overline{E}_e} \tag{2.25}$$

Both energy parameter and characteristic time are computed by means of *Short Time*

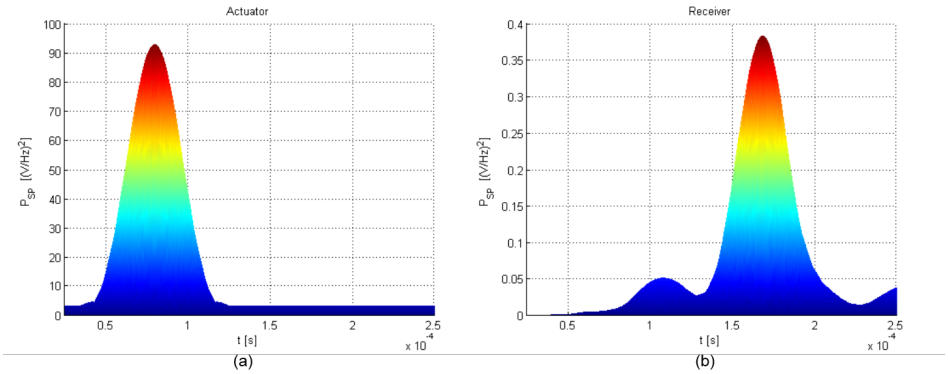

Figure 2.8: P_{SP} distribution in time domain highlighting the characteristic energy content of the excited (a) and sensed (b) wave around the central frequency. The peak is associated to the most tuned mode.

Fourier Transform (STFT) of the digitized signal (see Eq. 2.26)

$$STFT\left\{x\left(t\right)\right\}\left(t,\omega\right)=X\left(\omega,t\right)=\sum_{t\rightarrow-\infty}^{+\infty}X\left(t\right)\omega\left(t-\tau\right)e^{j\omega t} \tag{2.26}$$

where $x(t)$ is the discrete signal and $\omega(t)$ is the window function, chosen here as *Hanning* function, typically used in digital signal processing to select a subset of a series of samples to be processed with Fourier transform [101]. The advantage of such function is very low aliasing, at the cost of slightly decreased resolution (widening of the main lobe) . From the spectrogram analysis, the maximum amplitude of P_{SP} is used to characterize the energy content of the wave mode exploited in Eq. 2.25 and the characteristic time exploited in Eq. (2.24) as depicted respectively in Figure 2.8 and Figure 2.9. It is worth noting that the ratio between excited and sensed wave in Eq. 2.25 is proposed to neglect every dependence upon discrete transformation included in Eq. (2.26) (e.g.: $\omega(t)$ and τ). About arrival time, the STFT approach is usually preferred because of the double feature obtained preventing further processing for cross correlation analysis which has been proved to lead to quite close results.

When the damage occurs, the wave transmitted over the flaw is the result of a very complex interaction resulting in scattering of the incident guided mode into a finite number of propagating modes and infinite non propagating evanescent modes [102] which may include mode conversion. As a matter of facts, to account every change into the complex wave packet sensed rather than the interrogating mode selected, the parameter should account the entire diagnostic signal. For the latter demand, a useful feature is the wave energy E, which can be derived from the generalized sense of signal

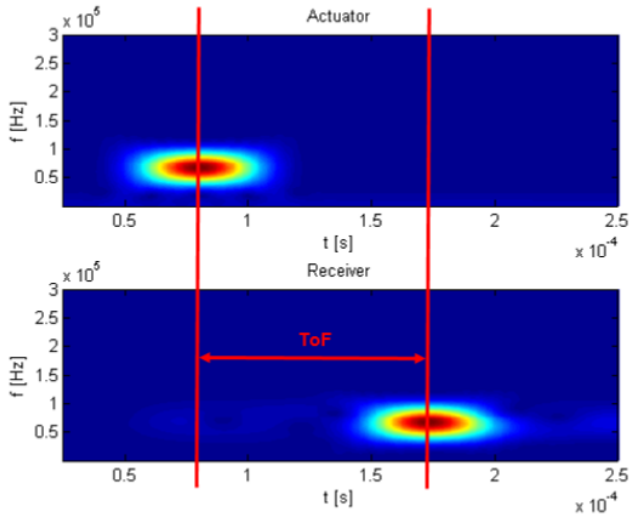

Figure 2.9: P_{SP} distribution in frequency-time domain highlighting the characteristic time of the most tuned excited (a) and sensed (b) wave mode.

processing [103] analyzing the time or spectral domain following the Eq. (2.27).

$$E = \sum_{-\infty}^{+\infty} x\left(t\right)^2 = \sum_{-\infty}^{+\infty} \left|X\left(\omega\right)\right|^2 \tag{2.27}$$

It has to be pointed out that the time analysis is here preferred to maximize the resolution. Moreover, the signal is typically sensed from t_0 (trigger time) to t_{fin} (final observation time) and every dependency upon time limited analysis is here neglected because the damage index approach provides merely a comparative analysis avoiding such criticality.

Such metric can be finally computed following Eq. (2.28), where the extracted feature f (scalar quantity), chosen among Eqs. (2.24), (2.25), (2.27) or others, is respectively evaluated on pristine (f_B) or currently operating (f_C) structure to assess the damage indicator.

$$DI(f) = \frac{|f_C - f_B|}{f_B} \tag{2.28}$$

Another way to detect every change in two waveforms consists to statistically compare them computing a classical correlation index on concurrent measurements. Specifically, the *Pearson Correlation Coefficient* ρ is considered in Eq. (2.29), where $x_1 = x_1(t)$ and $x_2 = x_2(t)$ are the digitized signals to compare, N_{sp} is the number of digitized samples so that x_{1i} is the $i-th$ sample of $x_1(t)$, and the over-line provides

the sample set mean.

$$\rho = \frac{\left|\sum_{i=1}^{N_{sp}} \left(x_{1i} - \overline{x}_1\right)\left(x_{2i} - \overline{x}_2\right)\right|}{\sqrt[2]{\sum_{i=1}^{N_{sp}} \left(x_{1i} - \overline{x}_1\right)^2 \sum_{i=1}^{N_{sp}} \left(x_{2i} - \overline{x}_2\right)^2}} \tag{2.29}$$

Correlating the same signal sensed on healthy and damaged configuration provides directly a damage metric, resulting unnecessary to create a percent index. In detail, two perfectly correlated signals resulting in a unit value of ρ are expected when no damage occurs. Otherwise, a decreasing value of ρ is expected when such a damage is present. For that reason the damage (metric) index is computed as:

$$DI\left(\rho\right) = 1 - \rho \tag{2.30}$$

The signal processing techniques are widely adopted for estimation of damage in investigate composite structures. However, before moving further into the detail of SHM methodologies based on the processing of the aforementioned features, the next section is dedicated to a briefly introduction of piezoelectricity and PWAS principles that are exploited to correctly set up measurements and realistically model a GUWs-based SHM system.

2.4 Piezoelectric principles

The success of GUWs for damage monitoring is certainly due to their countless damage detection capabilities. However every methodology is suited for application if leads to the best trade-off between effectiveness and practical applicability. For the latter demand, the further development of PWAS technologies enhanced the perspective of GUWs techniques, allowing easy activation and sensing of waves with low power and good affordability. The piezoelectricity is the phenomenon allowing the interrogation of the structure and it is the argument of this section before moving to the actual capabilities of modern sensor technologies. As suggested in [91], Lamb waves can be excited and collected by a wide variety of transducers. However, typically used are the piezoelectric lead zirconate titanate (PZT); they have very good performance in Lamb wave generation and are an interesting solution for integration in the structures under test.

For these reasons, in this research 10mm diameter and 0.25mm thickness PZT disks made of ferroelectric soft piezo material (PIC255) by *Physik Instrumente* (PI Ceramic) are usually bonded to the structure for several purposes. Thus, the actuation equations of this materials (crucial while modeling PZT elements) and the working mode (crucial

while modeling the effect of such transducers) are detailed in the following sections.

2.4.1 Piezoelectricity

Piezoelectricity describes the physical phenomena underlying the possibility to generate an electric field when the material is subjected to a mechanical deformation (direct piezoelectric effect), or, produce a mechanical strain while applying an electric field (converse piezoelectric effect) [104]. The direct piezoelectric effect predicts how much electric field is generated by a given mechanical stress and it is exploited for sensing purpose (piezoelectric sensors). The converse piezoelectric effect predicts how much mechanical strain is generated by a given electric field and it is succesfully emplyed for actuation purpose (piezoelectric induced-strain actuators).

For linear piezoelectric materials, the interaction between the electrical and mechanical variables can be described by linear relations in the tensorial form [80]:

$$S_{ij} = s^E_{ijkl} T_{kl} + d_{kij} E_k + \delta_{ij} \alpha^E_i \theta \tag{2.31}$$

$$D_i = d_{ikl} T_{kl} + \epsilon_i k^T E_k + \overline{D}_i \theta \tag{2.32}$$

where S_{ij} and T_{ij} are the strain and stress, E_k and D_i are the electric field and electric displacement, and θ is the temperature. The stress and strain variables are second-order tensors, whereas the electric field and the electric displacement are first-order tensors. The coefficient s_{ijkl} is the compliance, which signifies the strain per unit stress. The coefficients d_{ikl} and d_{kij} signify the coupling between the electrical and the mechanical variables, i.e., the charge per unit stress and the strain per unit electric field. The coefficient α_i is the coefficient of thermal expansion. The coefficient $\overline{D}_i$ is the electric displacement temperature coefficient. Because thermal effects influence only the diagonal terms, the respective coefficients, α_i and $\overline{D}_i$, have single subscripts. The term δ_{ij} is the Kroneker symbol.

Piezoelectric ceramics are perovskite varieties in which the linear piezoelectric response dominates. Commercially available piezoelectric ceramics formulations are internally biased and optimized to finally provide a quasi-linear behavior. At low electric fields, such materials are indeed well described by the linear piezoelectric equations [80]:

$$S_{ij} = s^E_{ijkl} T_{kl} + \bar{d}_{ijk} \cdot E_k \tag{2.33}$$

$$D_m = \bar{d}_{mkl} \cdot T_{kl} + \epsilon^T_{mn} E_n \tag{2.34}$$

where $\bar{d}_{ijk}$ differs from those in the previous equations due to the linearization process. On these principle are operating the PWAS and in the specific case, PZT disks, which

(a) PWAS disk transducer.

(b) Conventional ultrasonic transducers

Figure 2.10: Examples of PWAS disk transducer and conventional ultrasonic trasducers [104].

are briefly presented in the next section.

2.4.2 Piezoelectric wafer active sensors

The successful experiments performed in NDT and SHM applications based on propagating waves, combined with their minimal invasiveness and inexpensiveness have positioned PWAS as the highly established technology for the development and implementation of active SHM systems. Unlike conventional ultrasonic transducers (Figure 2.10 (b), PWAS (Figure 2.10 (a)) can be surface mounted or inserted inside layered materials such as composites, thus becoming integral part of the structure where they are installedon. Although the considerable advantages in using PWAS, there are some difficulties related mostly to the nonlinear behaviour involving electrical and mechanical variables and the interaction with the hosting structure.

Practically, PWAS are inexpensive transducers that operate on the piezoelectric principle, whose coupling between the electrical and mechanical effects (mechanical strain S_{ij} , mechanical stress T_{kl}, electrical field E_k, and electrical displacement D_j can be expressed from the tensorial piezoelectric constitutive equations as [104]:

$$S_{ij} = s^E_{ijkl} T_{kl} + d_{kij} E_k \tag{2.35}$$

$$D_j = d_{jkl} T_{kl} + \epsilon^T_{jk} E_k \tag{2.36}$$

where s^E_{ijkl} is the mechanical compliance of the material measured at zero electric field ($E = 0$), ϵ^T_{jk} is the dielectric permittivity measured at zero mechanical stress ($T = 0$), and d_{kij} represents the piezoelectric coupling effect. The coupling effects make the underlying physics much more complex than conventional strain sensors (e.g. strain gauge devices). However, unlike those classic sensors, exploiting the converse

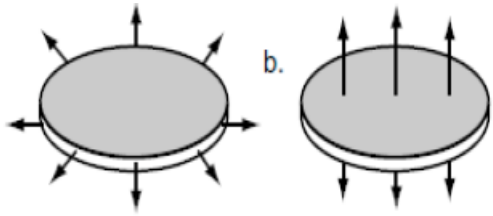

Figure 2.11: Deformation modes of a PWAS disk under electrical voltage [104].

piezoelectric effect, PWAS are active devices as well and they can interrogate the structure even addressing high-frequency applications (order of kHz and MHz).

In detail, PWAS transducer can be used as: (i) high-bandwidth strain sensors, (ii) high-bandwidth strain exciters, and (iii) resonators. In the first case, PWAS convert directly mechanical energy to electrical energy. The conversion constant is linearly dependent on the signal frequency. In the kHz range, signals of the order of hundreds of mV are easily obtained. No conditioning amplifiers are needed; the PWAS can be directly connected to a high-impedance measuring instrument, such as a digitizing oscilloscope. In te second application, PWAS converts directly the electrical energy into mechanical energy. Thus, it can easily induce vibrations and waves in the substrate material. PWAS acts very well as an embedded generator of waves and vibration. High frequency waves and vibrations are easily excited adopting input signals around 10V. Finally, PWAS can perform resonant mechanical vibration under direct electrical excitation. Thus, very precise frequency standards can be created with a simple setup consisting of the PWAS and the signal generator. When working as resonators, PWASs can be used to excite and sense Lamb-waves. Under alternating electric voltage, the free PWAS acts indeed as an electromechanical resonator. The characteristics deformation modes shown in Figure 2.11 are indeed able to correctly excite S_i and A_i behaviour. Following Eq. (2.36), an oscillatory voltage produces indeed an oscillatory mechanical behavior (excitation) while an oscillatory expansion and contraction produces an alternating voltage at PWAS terminal leads (sensing). Particularly, the in-plane motion is coupled with the particle motion generated on the material surface by the elastic waves. Otherwise, the in-plane motion is excited by the applied oscillatory voltage through the d_{31} piezoelectric coupling. Itis worth noting that unlike conventional ultrasonic transducers which act through surface tapping, applying vibrational pressure to the object's surface, PWASs act through surface pinching and are strain coupled with the hosting surface. This coupling between PWAS and hosting structure provides better efficiency while transmitting and receiving propagating waves and tuning capabilities maximizing the coupling when the characteristic length matches an half wavelength of the exited elastic wave.

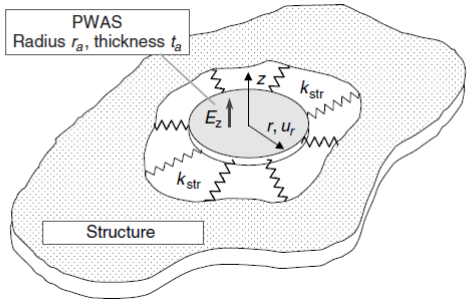

Figure 2.12: Circular PWAS constrained by structural stiffness, $k_{str}(\omega)$ [104].

From a practical standpoint, rectangular shaped PWAS with high in-plane aspect ratio can generate unidirectional waves. while circular PWAS excite omnidirectional waves that propagate in circular wave fronts unless material anisotropy. Due to this characteristic, the latter type, referred also as piezoelectric *disk*, is exploited in this work to characterize the material anisotropy of composites as well as interrogate the structure preventing any preferred direction. To model the PWAS disk, the piezoelectric constitutive equations can be considered in cylindrical coordinates considering a circular piezoelectric element of radius r, thickness t and width b, excited by the thickness polarization electric field, E_z and constrained on a bidimensional structure (see Figure 2.12). The scalar constitutive equations become:

$$\begin{cases} S_{rr} = s_{11}^E T_{rr} + s_{12}^E T_{\theta\theta} + d_{31} E_z \\ S_{\theta\theta} = s_{12}^E T_{rr} + s_{11}^E T_{\theta\theta} + d_{31} E_z \\ D_z = d_{31}(T_{rr} + T_{\theta\theta}) \epsilon_{33}^T E_z \end{cases} \tag{2.37}$$

where S_{rr} and $S_{\theta\theta}$ are the mechanical strains, T_{rr} and $T_{\theta\theta}$ the mechanical stresses, E_z the electrical field, D_z the electrical displacement, s_{11}^E and s_{12}^E the mechanical compliances at zero electric field ($E = 0$), ϵ_{33}^T the dielectric permittivity at zero mechanical stress ($T = 0$), and d_{31} the piezoelectric coupling between the electrical and mechanical variables. For axisymmetric motion (ideal PWAS without any wrap around electrodes), the problem is θ-independent and the space variation is in r only and d_{31} is the fundamental coupling parameter.

Chapter 3

Structural Health monitoring methodologies

Contents

It is worth noting that the complex propagation behavior makes quite difficult to reconstruct the real wavefield from limited resources, namely the few single sensing points. Thus, damage detection requires the analysis of wave parameters (signal responses) which may be affected by hidden changes in structural characteristics (i.e.: damage scenario). A possible failure would be detected directly comparing one or more of such parameters with scheduled intervals towards a "pristine (healthy) configuration". While no change is present in the structure, the feature currently computed should be very close to that evaluated on the pristine structure, resulting in a non-identification response. Otherwise, if such a damage is occurred, the selected signal response should increasingly change according with the severity of damage. While dealing with GUWs, the measurements consist of broadband signals due to the ul-

trasonic waves propagating in the structure [91], whose comparative analysis provides information about hidden flaws by means of damage indicators as assessment metrics. Practically, while such a damage index is close to zero, the structure can be considered undamaged/healthy. Otherwise, if the metric exceeds a certain threshold, such a damage is really appearing. Common changes in wave propagation characteristics are correlated to potential anomalies in the waveguide by means of one or more damage metrics. However, measurements of ultrasonic dynamic responses are quite challenging although such techniques are well addressed by many years. As a matter of facts, even data acquisition is crucial to achieve the desired performances and reliability of the system. Consequently, the first step towards such a detailed analysis improving the effectiveness of a SHM system should be to define how measurements, feature extraction and techniques used to relate damage features affect the final diagnosis. Several features may show different sensibilities to various types of damages. As aforementioned, when the response of the structure cannot be simply predicted (e.g. impact on composites [13]), different features can be extracted as signal response to track changes within the waveguide with increasingly efficiency [105]. Likewise, many algorithms [106, 107] and signal processing techniques [108, 109] working under different operative conditions [110] and temperatures [111] may be implemented in a SHM system, whose key comparison criteria is mostly the *Probability of Detection* [31, 99].

The crucial issue is thus to define an algorithm to relate one or more wave features (signal response) to damage features (diagnosis) in relation to the desired level of inspection. In this context, this chapter is dedicated to the algorithms developed using GUWs-based SHM resorting to a distributed array of ultrasonic sensors to detect and localize damages analyzing direct propagating waves [112] or scattering as well [113]. All relevant aspects are here detailed and few results obtained are reported to highlight critical points, improvements and capabilities of the resulting methodologies, which have been widely validated on several real scale structures with different damage scenarios.

3.1 Flaw detection using direct propagating waves

The identification and localization procedure adopted here requires the ultrasonic interrogation in “pitch catch" mode in different operative conditions dealing with many steps whose processes are schematically described in Figure 3.1 and explained afterwards. The main activities involved in this process can be grouped in:

- data acquisition, where the guided waves are recorded according to the interrogation mode and stored for analysis;

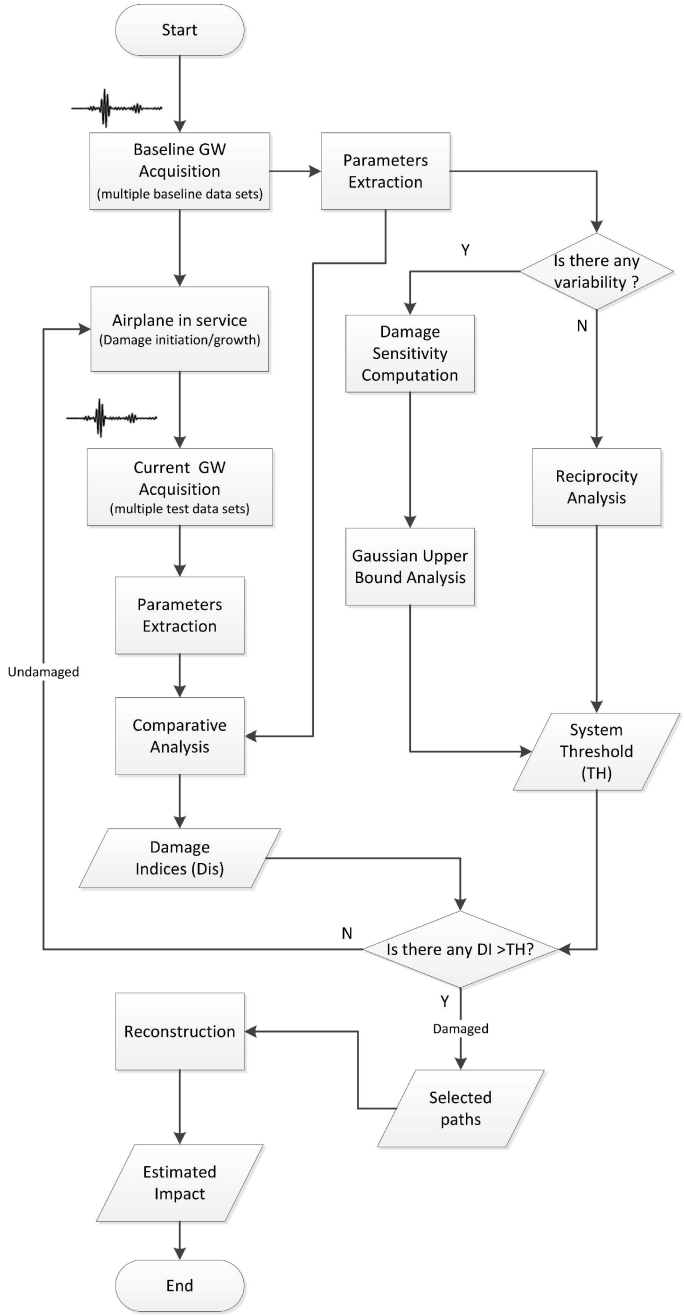

Figure 3.1: Overall processes within the proposed GW based monitoring system. DI and TR denote here the damage index referred to a specific signal response and the respective threshold.

- data processing, which deals with the analysis of stored data to extract features possibly affected by the damage (signal response);
- decision-making process, where the minimum metric associated to a damage with a reasonable confidence is established;
- damage reconstruction, which deals with all algorithms aimed at a certain diagnosis, no matter the level of the estimation.

The data acquisition is not discussed in detail in the present work unless the description of the measurement setup. However, it is worth noting that the critical issue is the correct sampling of the guided waves related to the acquisition and analog to digital (receivers) and digital to analog (transmitter) conversion. As a matter of facts, a poor resolution of time histories reduces the system capabilities. The second item is related to several signal processing techniques to establish characteristic features of propagating wave which reveal the interaction with damage (this topic has been previously addressed in Sec. 2.3.3). Instead, the latter items are crucial to select all useful data among those processed and to correctly relate the signal responses to damage features (e.g.: occurrence, position, severity, dimension), as described hereinafter.

3.1.1 Multi-path reconstruction principles

The Figure 3.1 shows that a key procedure regards the decision making approach, consisting in different processes. Moving from the necessity of a threshold assessment aforementioned, it can be asserted that an autonomous damage detection consists itself in the determination of a threshold level warning the presence of a damage. Consequently, the censure of results should be achieved with a non-arbitrary decision procedure and should not lie to the operator expertise.

The detection approach is based on a multi path analysis in which the paths between every actuator-receiver pair are exploited to achieve an independent interrogation, whose analysis provides one or more parameters among those presented in Sec. 2.3.3. Using a cluster with a limited number of sources, it is indeed possible do define a set of paths affected by the structural condition of the included and surrounding area as depicted in Figure 3.2 (a). When at least one damage index exceeds the threshold, the system identify that path as affected by damage. Considering every possible combination of paths, only few *selected paths* are identified by the system through the decisional phase and used for the localization presented in Sec. 3.1.1. It is expected that most paths crossing the damage are affected by stiffness variation and the different vibration response affects the signals. Otherwise, when no such damage occurs, several paths are not affected by any stiffness variation. That procedure

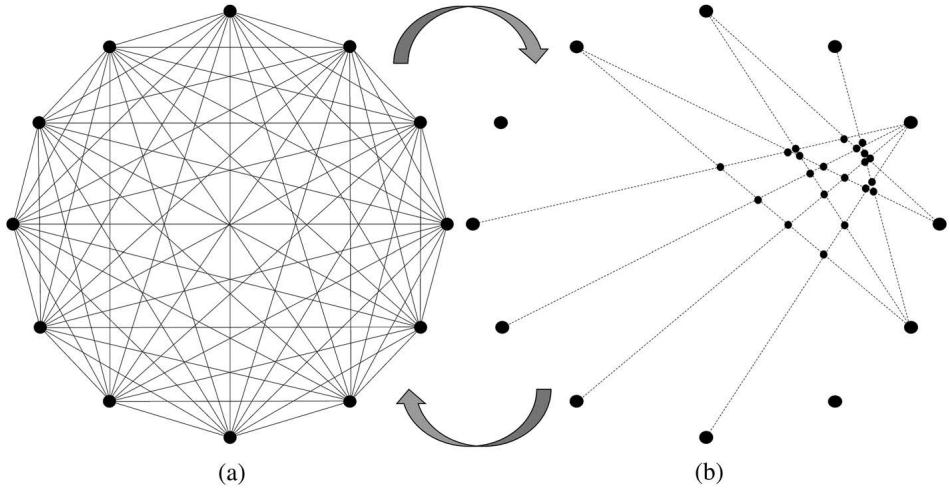

Figure 3.2: Transmitter receiver paths for circular transducer array configuration (a)and selected paths affected by a possible damage (b).

provides the selection of paths as qualitatively depicted in Figure 3.2 (b). As a consequence, the damage index should vanish when resulting from the comparison of signals sensed on the same health status. However, repeating measurements leads to slightly different results with nonzero value of DI, especially when a time domain parameter is considered. That demands a decision tool using prediction techniques to define the minimum indicator value warning a damage indeed present.

Decision-making approach

Random and systematic variability in measurements requires a statistical approach to avoid that changes in the dynamic response are misinterpreted. Statistics allows indeed to classify the extracted features and to achieve damage diagnosis. Several approaches are available in the literature to define a discriminating threshold. Many of the SHM techniques involve thresholds based on the hypothesis of Gaussian distribution for the damage parameters in the "unsupervised learning" mode. For this purpose, some form of outlier detection is typically employed [114], in which the central statistics is the key aspect of the investigation. Alternatively, statistical process control procedures may be used to indicate abnormalities in the signal response. They are typically implemented in the form of control charts that are the most commonly used statistical process control technique for outlier analysis, and they are also suitable for automated continuous system monitoring [115, 116, 117]. Another interesting approach implements the extreme value statistics to define the tail of the statistical distribution for the extracted features [60]. The main issue is to ensure that the extreme values are

properly estimated because here the intact condition and the altered state are very close. Generally, threshold determination can be obtained by using previous observations or simulations. In many investigations, the effects of disturbances, such as inputs and environmental variation, are simulated in order to achieve the estimated threshold value in the next measurements. In this context, the Monte Carlo method can be efficiently adopted [118] even to estimate the statistical confidence intervals of characteristic parameters from measurements [119]. The same approach is also suited for outlier detection procedures in order to arrive at the threshold value [62]. However, to achieve the desired effectiveness, a large sample is needed making this approach often computationally intensive. When a large number of signals is measured or a large number of complex simulations is required to reconstruct the damage, it is not generally feasible to use a Monte Carlo approach [118].

As a matter of facts, decision is a matter of weighting knowledge and uncertainties. To account such a variability due to the non repeatability and noise of measurements, here a prediction interval is defined according to the specific feature considered and using an unsupervised analysis Coupling an opportune hypothesis test proving the normal distribution of a particular signal response and the Gauss bound definition, an effective discrimination of sensitive signals can be indeed reached even with few samples and less effort [61]. The decision-making procedure that allows to define the damaged paths is based on the fact that the damage identification can be treated as a statistical event; the damage is detected if some damage metrics evaluated from measurements overcome a threshold value for a given confidence level. A rigorous parametric statistics allows to define the damage threshold in an unsupervised learning mode if the normal distribution of signal response noise is demonstrated via a rigorous hypothesis test, such as a Kolmogorov and Smirnov test [120].

The DI is defined from the measured signals representing the ultrasonic waves propagating through the structure related to different structural configurations (see Eq. (2.11)). Otherwise, the noise in signal response preventing the correct diagnosis can be statistically evaluated defining a damage sensitivity (DS) indicator. It takes its foundation from DI formulation, considering another baseline signal rather than the current signal for the comparison in unsupervised learning mode:

$$DI = \frac{\left| f_{Bi} - f_{Bj} \right|}{f_{Bi}} \tag{3.1}$$

where f_{Bi} and f_{Bj} are the $i-th$ and $j-th$ signal response extracted from the same dataset. Considering a dataset of n samples (i.e. n baseline signals), the statistical noise population from the DS analysis can be parametrically defined as depicted in

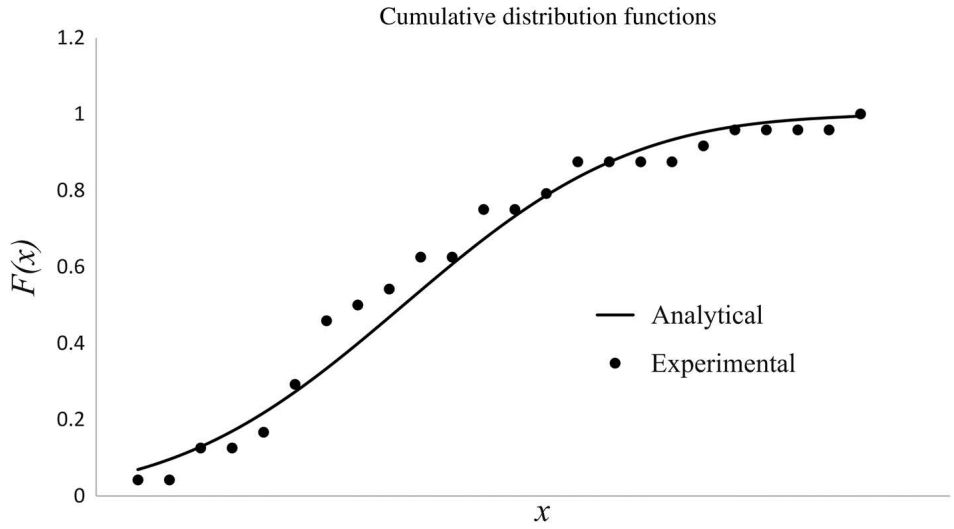

Figure 3.3: Kolmogorov and Smirnov testing. Comparison between analytical and experimental cumulative distribution functions of DS population monitoring the energy level of signals in a composite panel without defect.

Figure 3.3 and the detection threshold level is defined as:

$$I_{th} = \mu + k \cdot \sigma \tag{3.2}$$

where μ is the estimated mean value and σ is the estimated standard deviation of the DS population. The k factor defines the bounds of the prediction interval and it depends on the significance level chosen in accordance with normal distribution. With the probability of $1 - \alpha$ every sample x_i of the population X (i.e., DS population) is in the range defined by statistical bounds. Thus, considering the upper bound only, the noise is included within the threshold defined with the probability:

$$Pr\left(x_i \in X \leq \mu + k \cdot \sigma\right) = 1 - \left(\frac{\alpha}{2}\right) \tag{3.3}$$

For instance, for a normally distributed DS, the threshold level fixed as $\mu + 1.96 \cdot \sigma$ provides a 97.5% prediction interval. If the value of DI lies below this limit, then there is 97.5% confidence in stating that there is no damage. Similarly, if the value of DI is greater than this limit, then there is a 97.5% confidence in stating that there is damage.

Unfortunately, such analysis may return a correct threshold only when such a variability in signal response is present. As a matter of facts, this condition does not appear when a discrete transformation is carried out (see Eq. (2.26)) mostly because the coarse frequency discretization hides measurement uncertainties. To overcome the

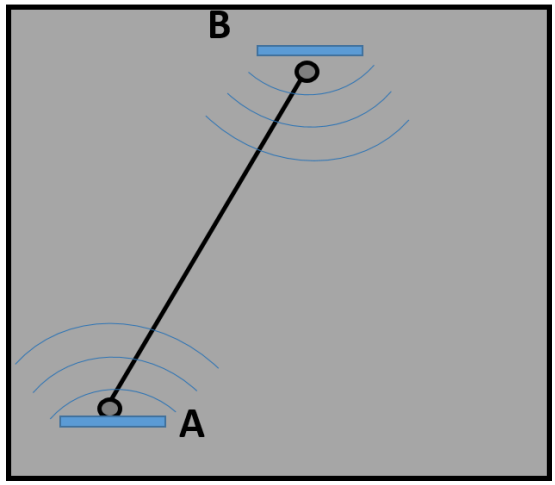

Figure 3.4: According to Betti reciprocal theorem applied to direct wavefield, the same relative influence is found considering A-B and B-A pairs.

latter evidence, the *Acoustic Reciprocity Theorem* is successfully adopted to discern noise from signal response. Although concurrent measurements demonstrate in such cases a nearly repeatability of extracted features, they show otherwise a lack of agreement respect to *Betti* reciprocal theorem [3], which suggests that the signal response related to the direct wave should not be dependent upon the direction of wave propagation when any damage does not appear. Looking to the Figure 3.4, this means that exciting Lamb wave with a transducer in A and sensing the wave propagation in B returns a feature that is equal to that extracted from signal recorded by sensor in A while exciting propagation in B. Measurements and data processing show that this principle is not satisfied even when not any damage is indeed present in the structure. Thus, the mismatch is considered here due to such uncertainties affecting damage detection as well, and it simply provides the decision value as the maximum difference observed in the related feature merely changing the propagation direction.

Reconstruction algorithm

The identification of damage is the first diagnostic output achievable with a SHM system, warning the presence of a damage. With a statistical correlation, the signal response can be related to the severity of damage [31], but it does not provide any information about its location. Using several signal processing techniques proposed in Sec. 2.3.3, the detection approach described in Sec. 3.1.1 aims to select that paths affected by such a damage. The last result can be used to locate the damage using an opportune reconstruction scheme aimed to assess the risk to have a damage in a

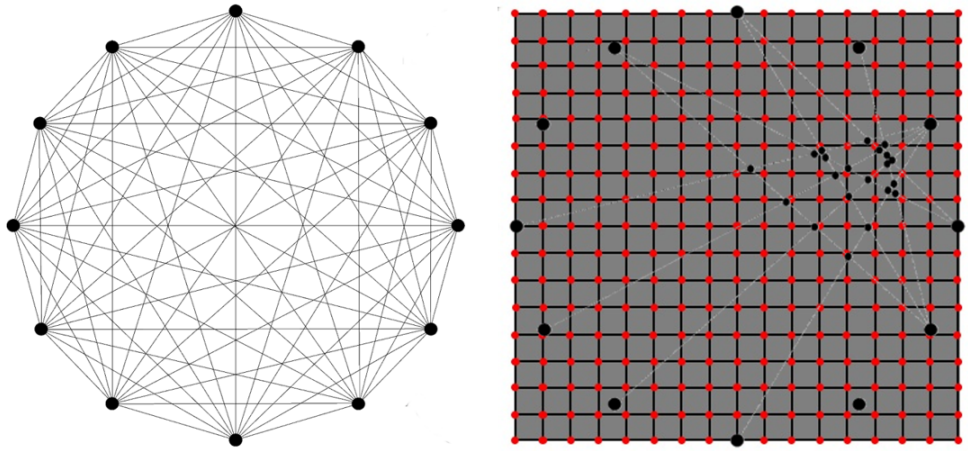

Figure 3.5: Sensors cluster with all interrogating paths (a). Representation of a typical bi-parametric structural mesh (b). Selected paths (light grey lines) and their intersections (sparse black points) are highlighted in the background.

specific location. Since the identification is provided with threshold definition, the location of damage is estimated as the location with the highest risk. The information contained after data processing is related to the paths and it is necessary to get that knowledge on the structure via developing an image depicting the position of damage. Many image techniques to investigate the region surrounded by an array of transducers have been developed in the past years in this field as reported in [121]. One of such techniques is guided wave based tomography where certain features of a wave mode or of a sensed signal are used as input to create an image of the area for damage detection. Discretizing the structure to be monitored in finite elements (see Figure 3.5), it is possible to define two different types of mesh: (i) the structural mesh, where the health information is desired, and (ii) the SHM mesh, where that information is primarily known. Depending on the relation between them, it is possible to differentiate two different approaches:

- mesh-based approaches, where SHM data are directly obtained on the structural mesh (i.e. the SHM mesh corresponds to the structural mesh [108]);
- meshless approaches, where the SHM data are obtained in points not previously known and interpolated on the structural mesh (i.e. the SHM mesh does not match with the structural mesh [122, 112])

With the first approach, explained in detail at the end of Sec. 3.1.2, the computational effort is often heavy accounting for each point the effect of all possible paths resorting to a decreasing probability far from their line of sight [106].

To reduce the efforts demanded by a mesh-based probabilistic formulation, the effect of selected paths is here considered in a different way. From their intersection few emerging points create the *SHM mesh* on which the structural condition is assessed (parametrized) by averaging the DI values respectively obtained along intersecting lines of sight. The coordinates of such resulting nodes, whose weight is the resulting DI, can be passed on to an algorithm providing the estimated impact point for localization of hidden flaw through such a tomographic representation of damaged area. To perform such process, displayed in Figure 3.1 as *Reconstruction*, different image processing techniques can be exploited. Mainly three different approaches can be followed to portray the health status from scattered data points obtained:

- discrete approach;
- spatial interpolation;
- nodal density.

With the former approach, scattered data constitutes a discrete system, whose barycentric coordinates are calculated to estimate the impact point by means of weighted mean algorithms. The weight of every discrete point is mainly the DI which returns at the emerging node. Otherwise, the more classic spatial interpolation exploits scattered data to smooth a surface on a supporting (structural) mesh using an interpolating scheme to evaluate the risk to have a damage in a specific location. Instead, the latter approach enables the density of the SHM mesh as key parameter for evaluating such risk. It mainly accounts that the greater the number of points, the higher the probability to have a damage in the concerned area should be. Returning a sort of damage risk map, both of the last two approaches provide such a global reconstruction rather than merely the localization of hidden flaw. The following assumptions provide the main concepts of the reconstruction to obtain a rapidly decreasing risk moving away from the SHM mesh:

1. the area in which the methodology estimates the damage risk is limited to that enclosed by the sensors, which provide an absorbing boundary condition for the interpolating scheme;
2. the algorithm assigns risk values to unknown points (structural mesh) of the monitored area accounting only scattered set of points that the damage decision approach returns (SHM mesh);
3. the information gathered from a transmitter-receiver pair contributes to the localization only when its line of sight intersect at least another path selected via decision-making approach;

4. the maximum value of the interpolating function is the most probable position of damage and it is assumed to be the impact location.

About the last item, it can be pointed out that the dimension of damage can be estimated as well from interpolated data, but a preliminary assessment of POD for the specific system is required [99, 31]. With regard to the third point, it is instead crucial to note that a specific scattered point affects only the surrounding area according to the specific scheme adopted for the interpolation. Although different approaches are available and characterized for interpolation purpose [123], the imaging is carried out using spline-based algorithm, typically suited for image processing when few data are supposed to be available. Such interpolation is then improved weighting the effect of DIs with the nodal density approach to remove shadows in the images as described afterwards. Finally the outcome of the discrete approach is reported as secondary information on the same image to achieve a more reliable localization.

The results obtained with this approach to detect impact induced delamination in real scale structures are discussed in the next sections. The criticalities of the reconstruction are focused in Sec. 3.1.2 and investigated by means of numerical simulations to exclude any connection with experimental uncertainties. The improvement is obtained resorting to a normalization and further fusion of data finally resorting to a multi-path and multi-parameter approach called MP^2 and based on meshless reconstruction. The results are finally compared with those obtained using literature mesh based "benchmarks" coded by author and improved as well resorting to the same multi-parameter approach. After validating the reliability and efficiency of MP^2 system, a real aircraft structure is investigated in Sec. 3.1.3, where several graphic user interfaces developed for user-friendly data storage and analysis with MP^2 approach are described as well.

3.1.2 Delamination detection within composites

The experimental setup employed to perform laboratory tests is first presented in this section to describe the remaining (data sets acquisition) processes involved in a possible airplane lifetime supported by a condition-based maintenance strategy. It is worth noting that this chapter provides a depth in the methodology development of a SHM systems and based mainly on tests using laboratory equipments or dedicated acquisition systems and numerical simulations. However, the generality of the exploited investigation does not affect the results moving towards a more practical on-board hardware. The discussion involves indeed ultrasonic data no matter how the data acquisition is performed.

The first test specimen investigated is a CFRP tapered panel designed for a lower

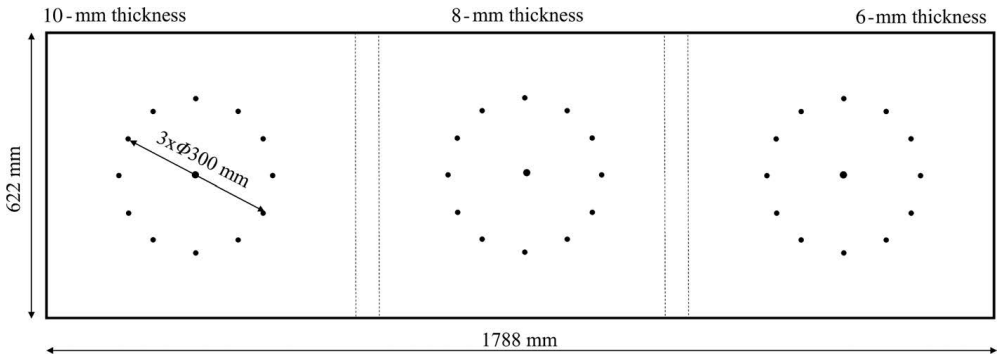

Figure 3.6: Configuration of the tapered wing panel.

wing box of commercial aircrafts. The external plies are made of carbon-epoxy 5-Harness Satin Weave (5HS), a woven fabric in which the filling yarn floats over four warp yarns and under another one. Uniaxial and biaxial carbon-epoxy plies are then combined within the two 5HS layers, resulting in a 16 plies laminated bay with 6mm thickness, a 22 plies laminated bay with 8mm thickness and a 28 plies laminated bay with 10mm thickness respectively. An array of 13 PZT disks made of ferroelectric soft piezo material (PIC255) by *Physik Instrumente* (PI) is bonded onto the surface of each bay through a vacuum-based secondary bonding procedure commonly used by aircraft industries. A circular pattern constituted of 12 PZT disks is adopted to maximize the ray path density while the remaining sensor is bonded onto the network center for dispersion assessment purpose. The thickness variation is obtained through two ramp links between the three bays with constant thickness resulting in the structure sketched in Figure 3.6. In detail, measurements have been taken in an typical laboratory without controlling any external parameter. An arbitrary waveform generator (HP/Agilent 33120A) is used to burst a 4.5 sine-cycle signal with 10V peak to peak amplitude in order to polarize the material. The Hanning function is adopted to window the sine-cycles to reduce the frequency leakage which provides undesired effects caused by dispersion. A 60kHz carrier frequency is excited to obtain the best compromise between tuning A_0 mode and detaching $A_0 - S_0$ in the time domain. An amplifier is finally adopted to boost the voltage up to 80V peak to peak, mainly to increase the signal to noise ratio for the longest distances. For every interrogation, a PZT disk is excited with a burst period of 1s. Lamb waves, generated by means of the converse piezoelectric effect, travel in the structure and are sensed by remaining transducers exploiting the direct piezoelectric effect. For the latter demand an Agilent DSO7104A 4 channels digital oscilloscope is employed to digitize ultrasonic signals with up to 1GHz sampling rate. Finally the signals are post-processed for the parameters extraction described in Sec. 2.3.3 directly on a workstation.

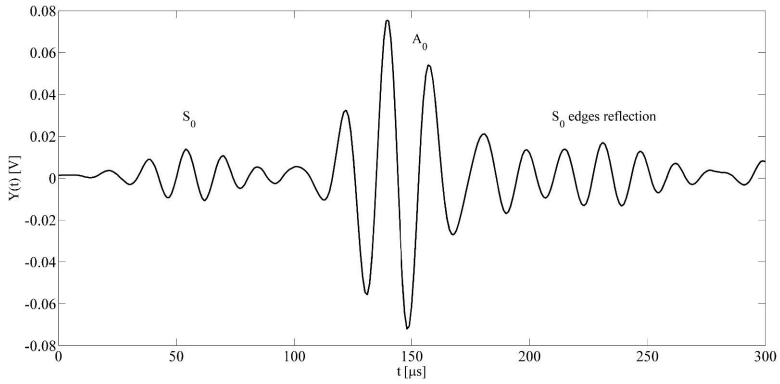

Figure 3.7: Typically recorded ultrasonic signal with several modes.

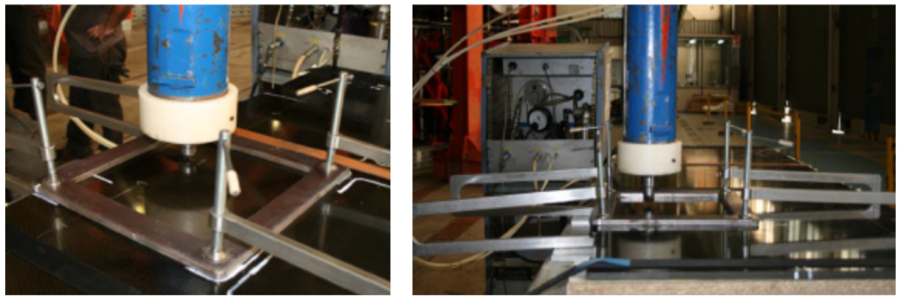

(a) (b)

Figure 3.8: Overall setup for impact test under impact weight machine with 1 inch tip. Impact test setup (a) and drop weight impact machine (b).

Using the defined setup, the baseline GUWs acquisition is performed interrogating the pristine structure through 10 concurrent measurements aimed to create a multiple baseline data set containing enough samples for decision making approach. A typical signal recorded is depicted in Figure 3.7, where several modes and echoes are evident. The “Airplane in service" process (see Figure 3.1) expected to suddenly provide a damage initiation is simulated directly with an impact testing providing a barely visible damage with an hidden critical flaw. For the latter demand, a drop weight impact test machine is employed with a 1 inch diameter tip. An overall configuration of the impact test and a representation of the drop weight machine are reported in Figure 3.8. To induce an acceptable damage level, the three bays of 6, 8, and 10mm are loaded with calibrated energies of 85, 110, and 150J, respectively. The appearance of damage is assessed via classic ultrasonic phased array NDT around the impact locations where the indentation is always slightly visible. The performed C-scan images reported in Figure 3.9 clearly show the appearance of barely visible damages due to hidden delamination always greater than 20mm diameter while the external visibility is quite

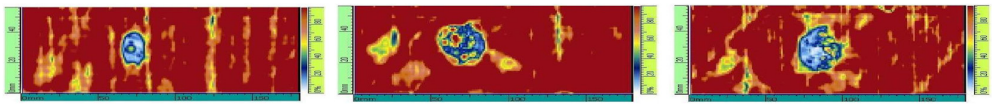

(a) (b) (c)

Figure 3.9: Calibrated impact longitudinal C-scan performed on (a) 10mm-thick, (b) 8mm-thick, and (c) 6mm-thick bays. Scan length, 162mm.

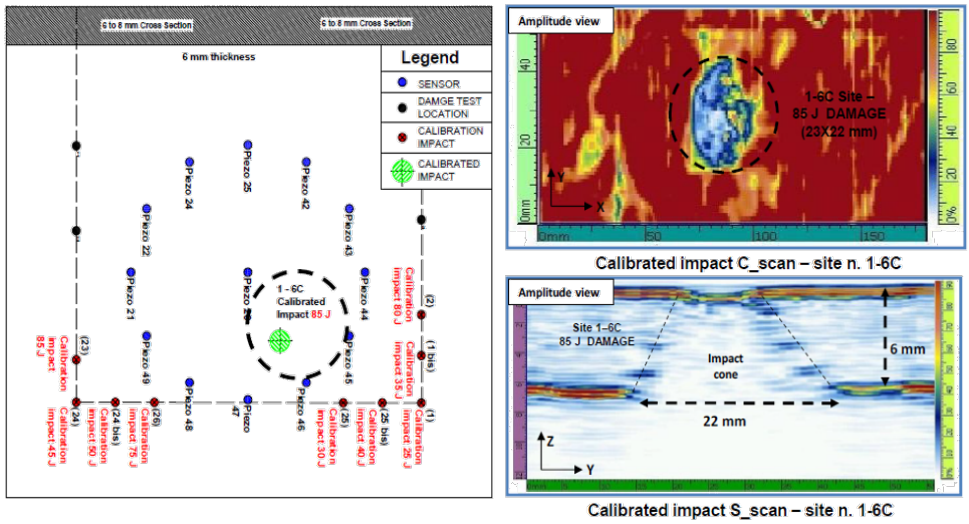

Figure 3.10: Calibrated impact longitudinal C-scan performed on 6-mm-thick bay with in plane and sectional views.

complex. The NDI result obtained for 6mm thickness bay is detailed in Figure 3.10, where the S-scan image (section view) allows to better show the evidence of the barely visible damage. The impact cone, due to several delaminations among several adjacent layer is strongly affecting the local stiffness of the structure while the indent depth is slightly appreciable.

The decision-making outputs are thus summarized in Table 3.1, 3.2 and 3.3 estimating the prediction interval while processing the signal energy and the mismatch of reciprocity (Betti) theorem while considering the transmission factor and time of flight. The same measurements aforementioned are repeated on damaged structure to achieve the multiple test data set and a database is built to storage parameters as well as metrics useful for health monitoring purpose. The signal processing described in Sec. 2.3.3 is carried out with the aim to extract successful information on the flaw appearance. It is important to remind that only fundamental Lamb wave modes are excited in low ultrasound. Whereas antisymmetric mode appears more tuned, group velocity and transmission factor of the A_0 mode are evaluated by processing recorded

Parameter	Process	Threshold (TH)	α
E	Gaussian	0.39	0.5
ToF	Betti	0.24	n.a.
TF	Betti	0.025	n.a.

Table 3.1: Making-decision outputs obtained for the 6mm-thick bay.

Parameter	Process	Threshold (TH)	α
E	Gaussian	0.42	0.5
ToF	Betti	0.20	n.a.
TF	Betti	0.025	n.a.

Table 3.2: Making-decision outputs obtained for the 8mm bay.

signals. Instead, the energy content integrated over the time allows to account the effect of the damage on several propagating modes. From the comparison of signals recorded along all lines of sight defined by all possible pairs of sensors, only few paths are selected as those affected by the damage. For several features, only the DIs higher than the respective threshold currently suggest the presence of the damage. The associated paths are displayed resorting to a mixed arrow-space graphical representation in Figure 3.11 processing the energy content of the signals. It is possible to observe

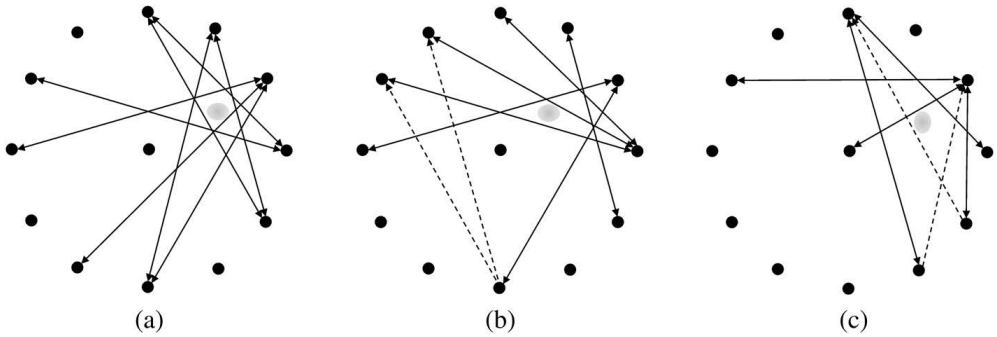

Figure 3.11: Paths selected through decision making procedure processing energy content of the signal. 6mm-thick bay (a), 8mm-thick bay (b), and 10mm-thick bay (c).

Parameter	Process	Threshold (TH)	α
E	Gaussian	0.26	0.5
ToF	Betti	0.18	n.a.
TF	Betti	0.021	n.a.

Table 3.3: Making-decision outputs obtained for the 10mm-thick bay.

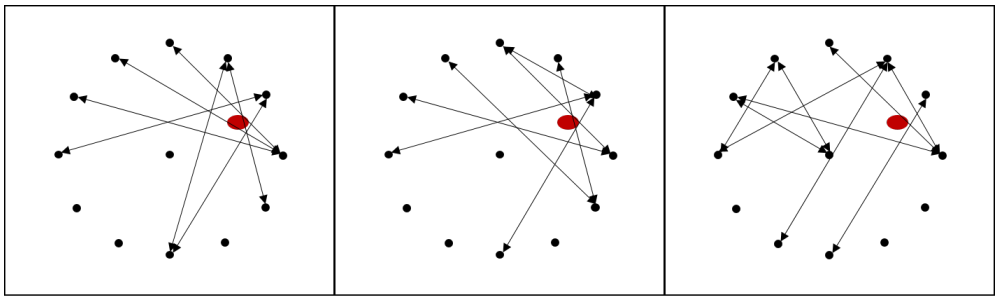

Figure 3.12: Paths selected through decision making procedure for extracted features. Signal energy (a), A_0 mode transmission factor (b), and A_0 mode time of flight (c).

that the damage, qualitatively identified by the depicted spot, appears in the region with the maximum number of selected paths even when few line of sights suggest the presence of such a damage (c).

To compare the ability to locate the damage using several features, the same representation is reported for the central bay in Figure 3.12 and used for the tomographic reconstruction. With the exception of ToF based selection, images suggest again that the damage appears in the region with the maximum number of selected paths. From other investigations and simulations, the ambiguity of ToF-based result is confirmed when low dispersive waves are tuned by combination of frequency and thickness. In such cases the local variation of wave propagation velocity due to such flaw is commendable and hidden from the noise, as better explained in the following investigations.

Even though the mixed arrow-space graphic representation allows to detect the damage, the innovative tomographic reconstruction aforementioned provides the damage localization without ambiguity with a slight computational effort. The decision-making procedure leads to the definition of emerging intersection points (SHM mesh); each node contains information about the surrounding structural condition according to the several DIs extracted from intersecting paths. To locate the damage, a surface is fitted on the scattered data using a triangulation-based cubic interpolation (Spline), obtaining a color-mapped two-dimensional image extracted from the surface. Then, the damage location is estimated considering the centroid of the SHM mesh using DIs as weight factor (discrete approach). The centroid is estimated first via a geometric weighted averaging algorithm and then considering its arithmetic definition. Accordingly, the damage location is then defined as the point $CG = (x_{CG}; y_{CG})$ in the Cartesian reference. The geometric extrapolation of the coordinates (CG_G) is carried

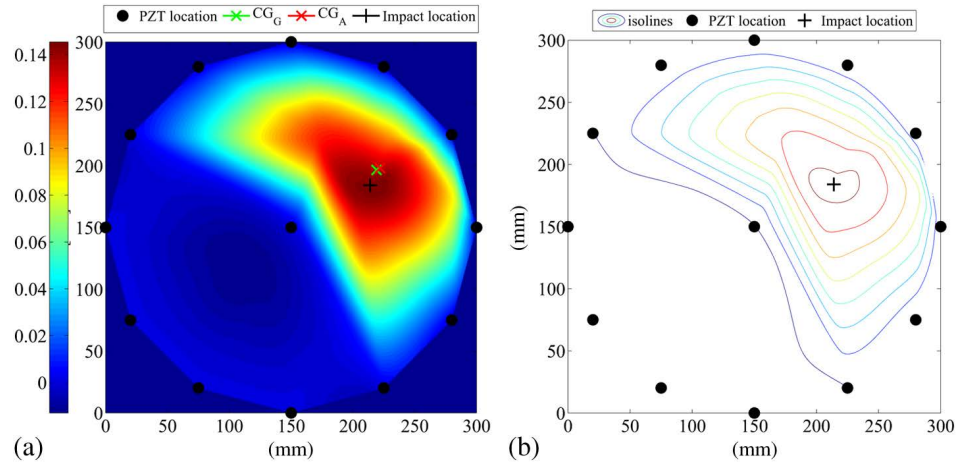

Figure 3.13: Tomographic analysis of the 10mm-thick bay. (a) Map of damage and (b) contour of isolevel.

out as follows:

$$x_G = \sqrt[\Sigma_{i=1}^{n} f_i]{\prod_{i=1}^{n} x_i^{f_i}}, \quad y_G = \sqrt[\Sigma_{i=1}^{n} f_i]{\prod_{i=1}^{n} y_i^{f_i}} \tag{3.4}$$

while the arithmetic coordinates (CG_A) are given by:

$$x_G = \frac{\sum_{i=1}^{n} x_i \cdot f_i}{\sum_{i=1}^{n} f_i}, \quad y_G = \frac{\sum_{i=1}^{n} y_i \cdot f_i}{\sum_{i=1}^{n} f_i} \tag{3.5}$$

where f_i is the weight of the $i-th$ node, namely the DI. A typical result obtained using such approaches is reported in Figure 3.13 (a), where although a minimum number of emerging nodes results from making-decision approach (see Figure 3.11 (c)), the impact location is predicted with a negligible error compared to the actual size of the damage. The contour plot of the isolevel curves showed in Figure 3.13 (b), highlighting areas with equal risk of damage occurrence, demonstrates that the impact location falls exactly in the area with greater probability of damage appearance. Furthermore, slightly changing the threshold level does not affect the reconstruction using discrete approach and spatial interpolation. With regards to the central bay, a similar reasonable result can be found processing signal energy (see Figure 3.14) and transmission factor of A_0 mode. In both cases the impact is estimated with a negligible error no matter the mathematical formulation is and the reconstruction is able to depict the damaged area. Otherwise, a slight uncertainty in damage localization is obtained while processing the time of flight of the A_0 mode. Although the image processing returns a well assessed damage risk, the Figure 3.15 shows that the presence of emerging nodes far from the failure location introduces an error in impact

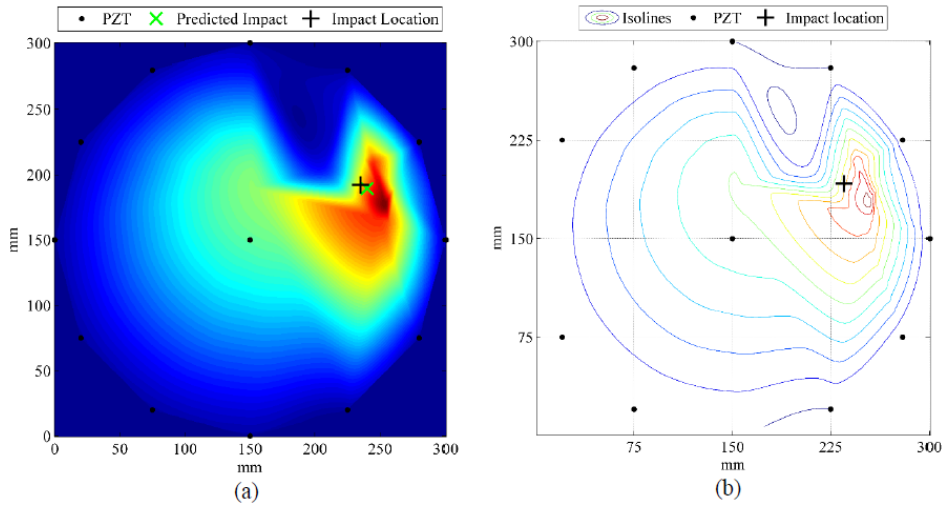

Figure 3.14: Tomographic analysis of the 8mm-thick bay. Map of damage (a) and isolevel curves (b) processing signal energy.

localization using the discrete approach and the result indeed does not match with the spatial interpolation.

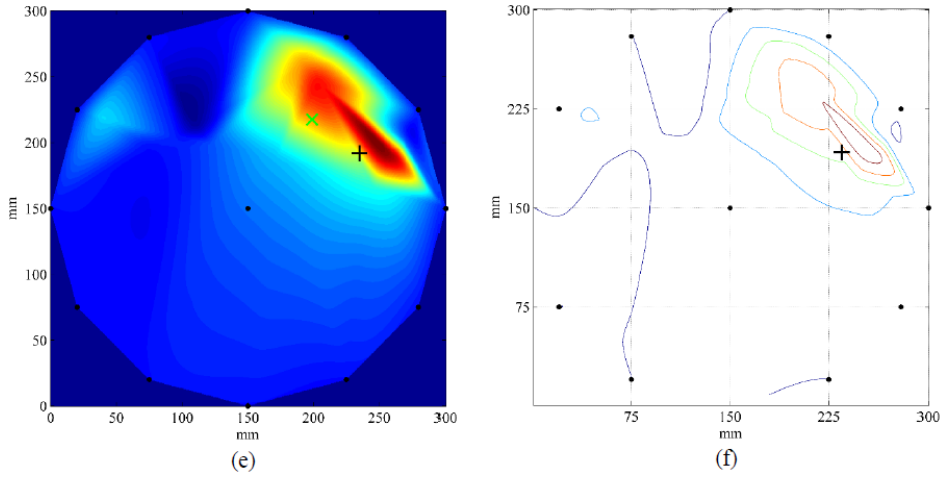

Figure 3.15: Tomographic analysis of the 8mm-thick bay. Map of damage (a) and isolevel curves (b) processing time of flight of A_0 mode.

Although a very simple, faster (compared with other image reconstruction algorithms) and effective approach has been obtained including discrete analysis and spatial interpolation to improve hidden flaw localization after a making decision approach, few criticality aspects have been detected with the aid of numerical simulations as well:

- phantom damages; several spots in the image may suggest damage where no

failure is present. This event happens when few nodes in the SHM mesh are emerging far from the damage due to the intersection of most affected paths among those selected. The high DI level associated to those paths induces a high risk to a single node which is indeed far from damage location.

- feature sensitivity; due to the complex behavior of wave propagation and the statistical making-decision approach, it happens that some paths that are indeed affected by the damage do not show a response suggesting any change in the structure. Otherwise, relevant changes in signal response can be detected even when no such a damage indeed affects the correspondent line of sight. This happens especially when Time of flight associated with low dispersivity of A_0 mode is adopted to detect changes in the waveguide;

About the first item, it is worth noting that the most critical area (damage) corresponds always to the area with the largest number of neighboring nodes in the SHM mesh. This remark suggests to resort to such a nodal density as damage metric; the greater the number of nodes, the higher the risk of damage occurrence in the concerned area. This consideration relies on the fact that the occurrence of an isolated spot with a high DI may originate a false alarm of the health monitoring system. Conversely, the presence of a large number of points with certain DI values provides a higher system response reliability. The output of a numerical simulation, whose validation is described in the Chapter 4, is considered hereinafter to establish a reliable solution. The Figure 3.16 (a) shows that the phantom damages are located in a sparsely populated area as well. This means that the hypothesis is well founded. Regardless of the parameter considered, the problem of ghost damages appearing during the reconstruction is well addressed even resorting to numerical results (less affected by uncertainties), being a lack of reconstruction technique. The SHM mesh consists indeed of nodes emerging from the intersection of those paths affected by the damage occurrence according to the making-decision output. It may happen that two selected paths strongly affected by the hidden failure (i.e., they have a high DI) intersect each other in an area far away from the real damage location. Thus an isolated spot arises around that location, generating a lack of reliability. To reduce the probability that the damage prediction may be affected by this sort of false alarm, the density of the SHM mesh can be calculated for each node resorting to the distance between that node and the others as follows:

$$\frac{1}{f_i} = \frac{\sum_{j=1}^{n} \sqrt{(x_i - x_j)^2 + (y_i - y_j)^2}}{n-1}, \quad i \neq j \quad and \quad i,j = 1,2,\ldots,n \tag{3.6}$$

where f_i is the density parameter of the $i-th$ node and and n is the number of SHM

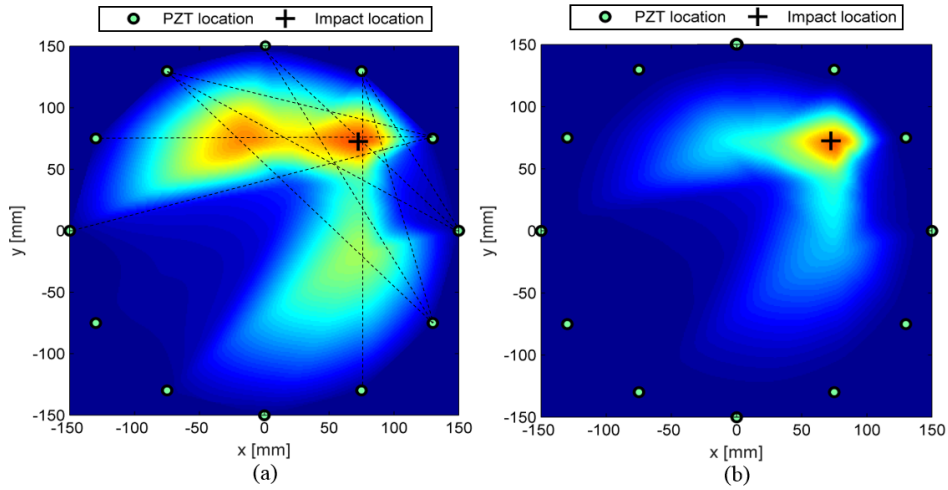

Figure 3.16: Tomographic analysis of the numerical test-case. Map of damage based on energy level (a) and weighted energy level (b).

nodes. Then the parameter is normalized in order to do not affect the DI scale as follows:

$$\bar{f}_i = \frac{f_i}{(f_i)_{max}}, \quad i = 1, 2, \ldots, n \tag{3.7}$$

Such a densification factor is preferred here rather than a classic density definition because it allows to address such a weight for each node; the higher is the inverse of the average distance obtained, the greater the number of nodes in the surrounding area. Instead to construct another image, a new damage index is formulated as:

$$DI_{iw} = \bar{f}_i \cdot DI_i \tag{3.8}$$

where DI_i is the damage index value assigned to the $i-th$ node after decision making phase. The DI_{iw} is thus preferred because it incorporates the severity of damage (DI_i) with the density of emerging nodes in the surrounding area (f_i). The ability to eliminate phantom damages is depicted in Figure 3.16 (b), where any indecision in the damage reconstruction is overcome, without giving up the information about the gravity of damage. In this case, the probability of a false alarm due to the occurrence of phantom damage may rapidly decrease.

The second item regards the sensitivity of the specific feature to a specific damage. Due to the wide range of variables involved (frequency, thickness, multimode, dispersion, damage scenarios, etc.), it is often complex to well establish the relation between a classified damage and the effectiveness of a single feature. Other results, not reported here for sake of the conciseness, confirm that every parameter is affected by its own

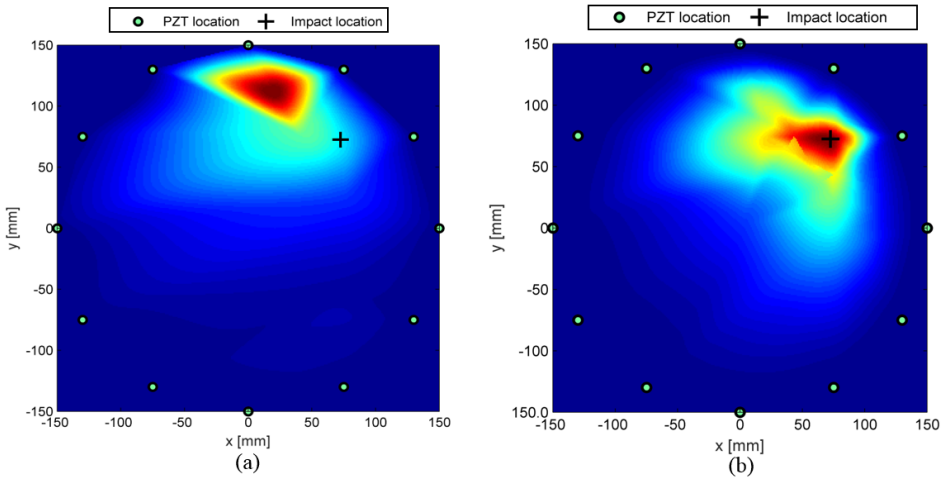

Figure 3.17: Tomographic analysis of the numerical test-case. Map of damage based on single ToF (a) and multi-parameter(b) approach.

sensitivity to the specific damage considered. Summarizing such investigation, it is possible to point out that damage indicators based on wave energy content analysis in time domain is really effective for detection and localization but it is mostly affected by noise resulting in a very high threshold which may censure also useful data. Even the transmission factor based damage index is effective for damage reconstruction but it appears to be affected by reflections and echoes appearing in the signal and distorting the wave spectrum. Finally, time of flight parameter effectiveness is strictly related to the dispersive behavior of selected lamb wave mode. This feature appears indeed effective while decreasing the thickness of the structure and the efficiency is strongly reduced with thicker solids. Furthermore, it has to be mentioned that the measurements are carried out on defined paths and the local effect of damage on propagating waves is also averaged by the distance between pairs of sensors.

The most relevant result regards such dispersive behavior, which affects the localization of damage using ToF single-parameter representation. The Figure 3.17 (a) shows indeed the lack of agreement processing the ToF weighted damage index even when propagating waves are simulated, remarking that the incorrect result obtained in Figure 3.15 (a) is due to the parameter selection rather than to uncertainties in measurements. The red region, which represents the most probable position of the hidden failure is indeed quite far from the damaged region ($20\times20\text{mm}^2$ around black cross). As a matter of facts, the optimization of the reconstruction cannot be oriented to find the most suitable parameter for the specific case otherwise the methodology effectiveness could be strictly related to such conditions. Furthermore it is not envisioned to change the decision level to improve the result. Decisional procedure indeed affects and tightly

correlates the POD with the probability of false alarm (PFA). More specifically, with respect to the specific target of the system, safety is indeed directly connected with POD and the downtime (operative costs) decrease according with PFA [63]. Thus, while increasing threshold the PFA decreases (desirable) and the probability of missed detection increases which means a decreasing POD (undesirable). This means that the only way to improve the system is to change or improve the system response. Without altering the making decision approach, several parameters can be weighted and combined in order to reduce wrong effects due to the presence of a parameter which may not be effective and to increase the robustness of the system. Although probabilistic reconstruction is a consolidated approach for GUWs-based damage detection [106], there is a limited number of studies in which resulting reconstruction images for the same structural state are fused to improve damage localization and background noise [110]. The data fusion here is carried out resorting to the following steps: (i) weighting procedure according to Eq. (3.8) for each parameter extracted from travelling waves and selected by decision making step, (ii) interpolation of damage according to each feature on the structural mesh (single parameter approach), (iii) normalization of data obtained on that mesh, and (iv) data fusion for the multi-parameter representation of damage. The result obtained with data fusion of normalized weighted DIs is depicted in Figure 3.17 where the wrong effect of the ToF based reconstruction (a) is clearly smoothed by introducing the multi-parameter approach (b) including all of the three features considered.

To establish the effectiveness of the MP^2 meshless methodology, the results obtained are compared with a classic mesh-based approach where the damage index is evaluated in the same way for every path depicted in Figure 3.18 (a). Then, the damage probability index (DPI) is calculated in every point of structural mesh shown in Figure 3.18 (b) resorting to a decreasing probability function based on a nonlinear definition of a distance Index (dI) which establish the effect of the path on its surrounding area. The effect induced by the $i-th$ path to the specific point P of the structural mesh is addressed as follows:

$$DPI_i(P) = dI_i(P) \cdot DI_i \tag{3.9}$$

where DI_i is the damage index of $i-th$ path and $dI_i(P)$ is the distance index between that path and point P calculated according to enable a specific decreasing probability. To obtain the classic elliptical reconstruction [108], for each point P the distance $\delta_i(P)$ is calculated from the distances between that node and the sensors connected by the $i-th$ path. The distance index is then evaluated following Eq. 3.10 where β is a scale parameter (i.e. it defines the farther influence of a path) usually calibrated on known

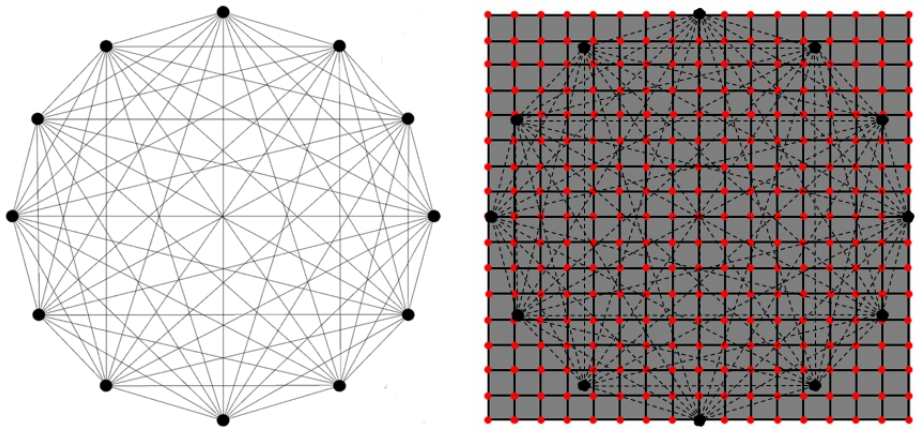

Figure 3.18: Cluster of sensor with all passible propagation paths (a) and typical mesh for mesh-based reconstruction approach (b).

condition to improve the reconstruction. Finally, the DPI of the point P is evaluated accounting the effects of every selected path induced on the point P and normalizing such overall value for further data fusion according to the multi-parameter approach.

$$\begin{cases} dI_i(P) = \frac{\beta - \delta_i(P)}{\beta - 1}, & \delta_i(P) \leq \beta \\ \\ dI_i(P) = 0, & \delta_i(P) \geq \beta \end{cases} \tag{3.10}$$

The results obtained with mesh based and meshless multi-parameter (MP^2) approach are reported in Figure 3.19. The former (a) based on a mesh defined reconstruction is able to identify and localize the damage without uncertainties. The same conclusion can be drawn from the latter reconstruction (b) based on the meshless approach, where the density weight is able to restrict the localization quite around the damage location. From the comparison it is possible to define how the same reasonable result can be obtained with the meshless approach with fewer computational cost needed.

Another interesting approach deals with the beamforming techniques applied to guided waves excited and sensed through a cluster of sensors. They are indeed signal processing techniques used in sensor arrays for directional signal transmission or reception [124] and used in wave-based structural health monitoring to specifically address the propagation. Such algorithms sum signals received by sensors to form the beamforming output and they can be exploited for acoustic source localization [125] as well as in the situation where one or a group of receiving array elements is also used as a source of Lamb waves.[126]. Although these techniques have been demonstrated

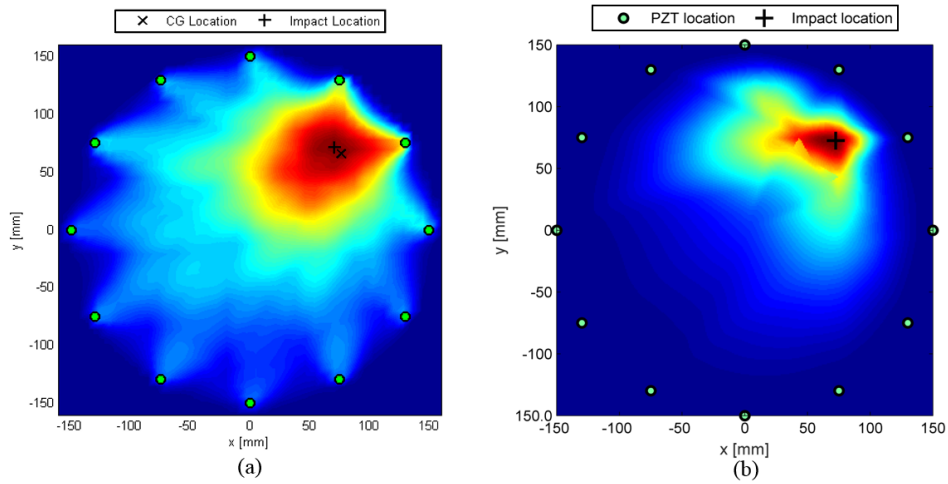

Figure 3.19: Tomographic analysis of the numerical test-case. Mesh based multi-parameter approach (a) and MP^2 meshless image reconstruction (b).

to be really effective in several cases, when an anisotropic material is considered in a real scale complex structure (see Sec. 3.1.3), various reflections may really complicate the reconstruction with a non reasonable detection [127].

3.1.3 Damage detection in complex structures using MP^2 methodology

The methodology described in the previous section is employed and validated on a real scale lower wing panel designed for the outer wing box of a commercial aircraft. The same material and similar thicknesses of the previously analyzed panel are designed with the addition of several stringers for stiffening the thin walled structure. The Figure 3.20 shows 5 different groups of sensors which are monitoring 7 critical bays for possible delaminations or stringers debondings induced by impact loads. A dedicated cabling and data acquisition system has been designed for autonomous ultrasonic interrogation and signal acquisition in order to perform similar interrogations to those described in Sec. 3.1.2. As depicted in Figure 3.21, several bays of the structure are sensorized with clusters of PZTs bonded on the inner surface to perform condition monitoring when the wing box is correctly assembled and mounted on the aircraft. Totally, 133 flexible disks (DuraAct™P-876K025) with external protective film are installed using again a controlled bonding procedure based on vacuum bags and heat curing. Nine impacts are performed on the outer surface of the wing panel when assembled in the wing box using a drop weight machine; few impact positions are chosen in the middle of some bays while the remaining locations are selected under the stringers feet to reproduce a stiffener debonding. The panel is characterized by

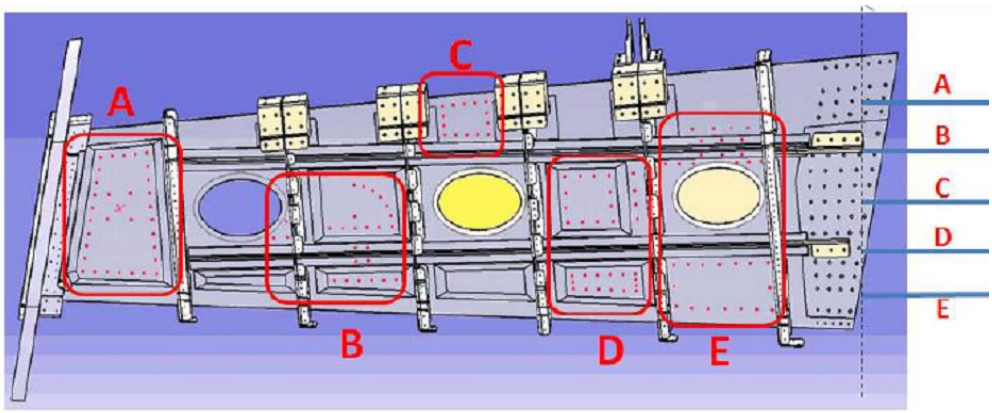

Figure 3.20: Sketch of the lower wing panel designed for the outer wing box of a commercial aircraft with several instrumented area.

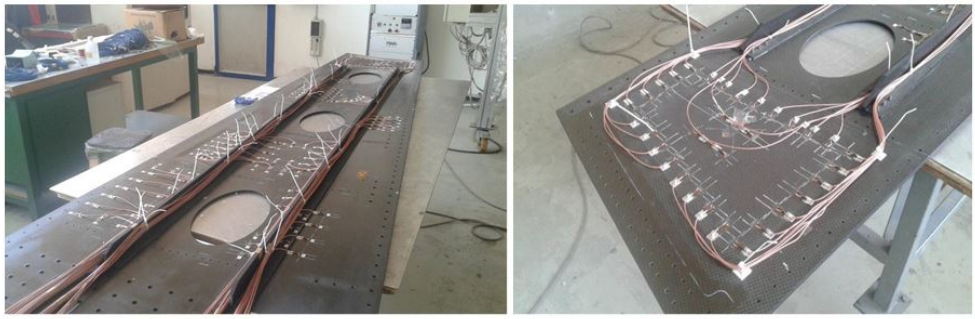

Figure 3.21: Lower wing panel instrumented for GUWs interrogation (a) and typical monitored area (b).

varying thicknesses and layups in each bay and for this reason a preliminary activity of calibration of the impact energy is carried out in order to find the minimum impact energy producing the minimum delamination dimension corresponding to each selected impact position. In order to calibrate the impact energy, it is raised up from 20J at 5J steps until the first delamination has been identified by ultrasonic NDI.

The damage identification is here strongly challenging due to the complex wave propagation behaviour in real composite aerostructures characterized by thickness variation, stiffener and holes. From Figure 3.22 the noisy introduced in the signals and the several modes and echoes recorded are quite evident. A 4.5 sine-cycles windowed burst with a frequency of 60kHz is adopted again as diagnostic wave to achieve a trade off between tuning of A_0 mode and time shift between fundamental modes. Although the complex operative conditions in which the system worked, the damage reconstruction approach appears able to determine the damage location, even though

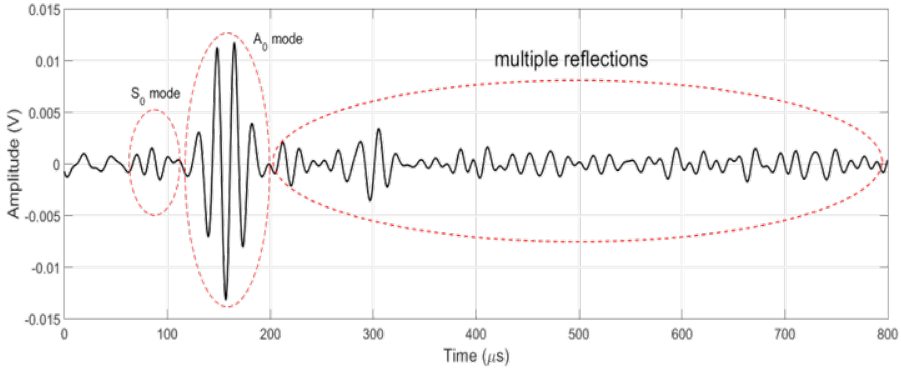

Figure 3.22: Typical time history of the propagating wave captured at sensor location. Several modes and reflections propagating at frequency of 60kHz.

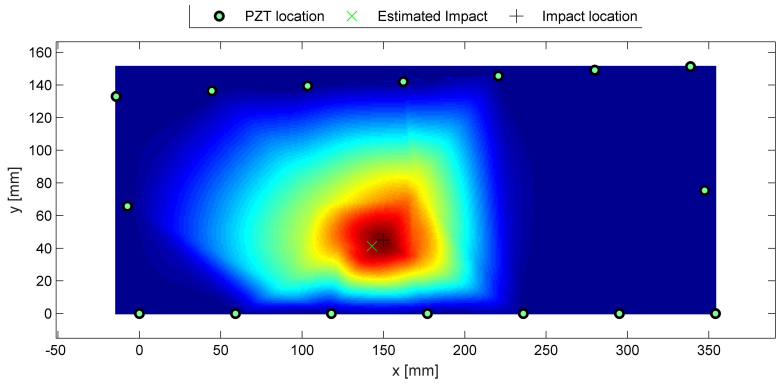

Figure 3.23: MP^2 damage detection of flat area included in the section E of the lower wing panel.

some ghost areas (phantom damages) are often present, especially processing a single parameter without accounting the density of emerging nodes in the SHM mesh. However, the introduction of the density parameter to weight damage indicators highly reduces the presence of those areas and increases the reliability of the system. In addition, the results can be enhanced with the multi-parameter analysis by performing the image fusion of the various damage reconstructions using the same supporting mesh grid. It is worth noting that the best results are always achieved by the image fusion of all different reconstructions derived from the three different damage parameters (i.e. signal energy level, time of flight and transmission factor) as reported in Figure 3.23, where the diagnosis of the flat area included in the section E is depicted. Good results are obtained even while reconstructing damaged area where thickness ramps are present. Despite of the different and less regular geometry, the tomographic method based on unsupervised threshold definition and multi-parameter processing have not

found any indecision in detecting and locating the impact damages.

As a matter of facts, all consideration made in the previous section investigating the tapered panel and numerical results can be here confirmed, demonstrating the effectiveness of the implemented approach combining mesh-less reconstruction from statistical selection of propagation paths with multi-parameter analysis and image fusion techniques in order to provide higher levels of probability of detection for all the investigated damage scenarios (a more detailed description of the disbonding detection is reported in the next section). Furthermore, the result is often even more promising than that of conventional mesh-based approaches with fewer computational costs possible.

The methodologies are actually implemented in a a modular analysis software including all the algorithms developed to extract from the wave signals some metrics representing the damage level, as well as to graphically interpolate and superimpose the indicator levels in order to present damage positions and dimensions according to the MP^2 paradigms. The workflow of a condition monitoring system is quite complex due to the several stages depicted in Figure 3.1. When different parameters have to be extracted, the related damage detection has to be targeted within appropriate decision making framework and the results have to be manipulated to reconstruct damages; many inputs and information should be indeed declared. Hence, an interactive graphic user interface (GUI) for structural health monitoring including various methodologies described is developed within MATLAB® environment in order to provide an easy accessible platform to execute the various processing tasks for feature extraction, making decision and damage reconstruction. The front panel of the modular software is depicted in Figure 3.24, where it is possible to download the diagnosis performed with the several integrated sensor clusters on the overall structure. The global geometry tool indeed provide the comprehensive health overview of the structure and it is supported by a dispersive tool for material characterization. The front panel allows to approach several modules for SHM analysis and preliminary characterization of the material using the embedded buttons which start several tools. The analysis front panel of the GUI framework is depicted in Figure 3.25. Geometric information and specific signal options, settings for several parameters analysis and threshold assessment are operated using the panels on the left. Damage risk functions are reconstructed on structural mesh considering (from left to right) damage index, density index and weighted damage index. It is possible to process a single feature or the fusion of several combinations for the multi-parameter option. In detail (from top to bottom) the contour plot, three dimensional distribution and isolines of interpolating surface are respectively depicted for online monitoring. No limitation in term of geometry is present because the algorithms, once provided the plate geometry and the transducers

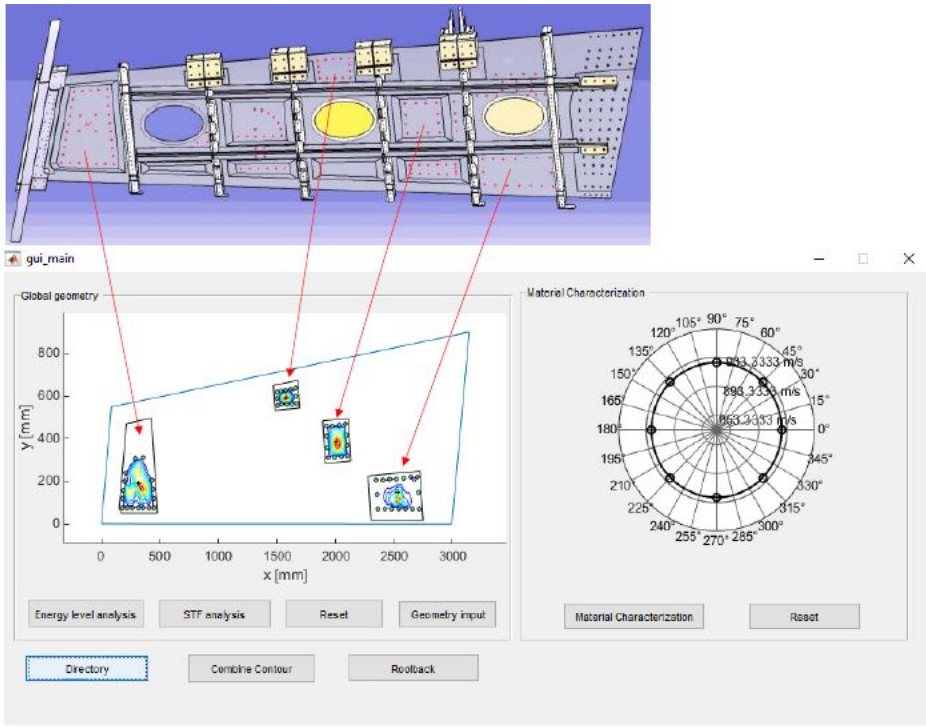

Figure 3.24: Main front panel of the MP^2 modular software. Few results of the lower wing panel are displayed in the global geometry tool.

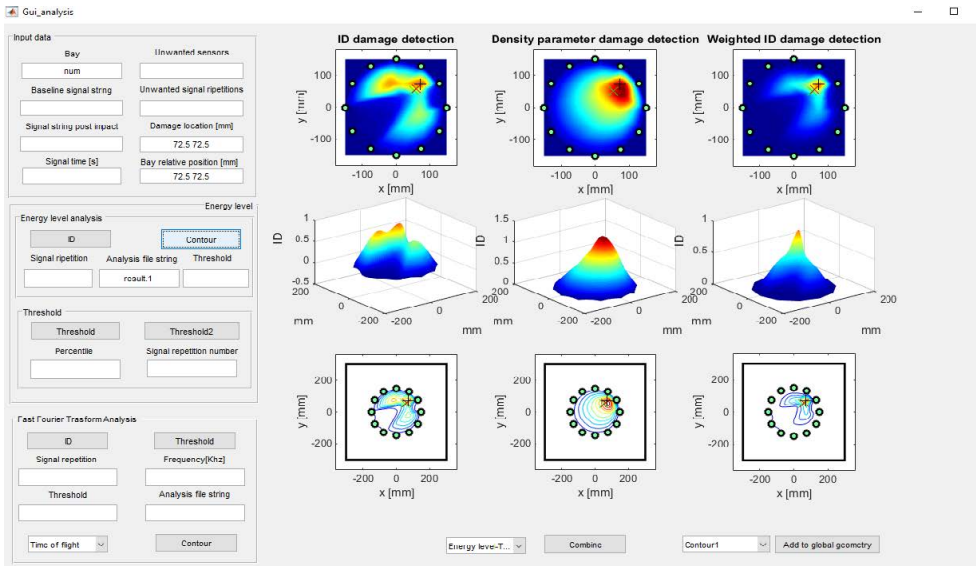

Figure 3.25: Analysis tool panel of the MP^2 modular software. Overall energy based damage detection of numerical test case reported in Figure 3.16.

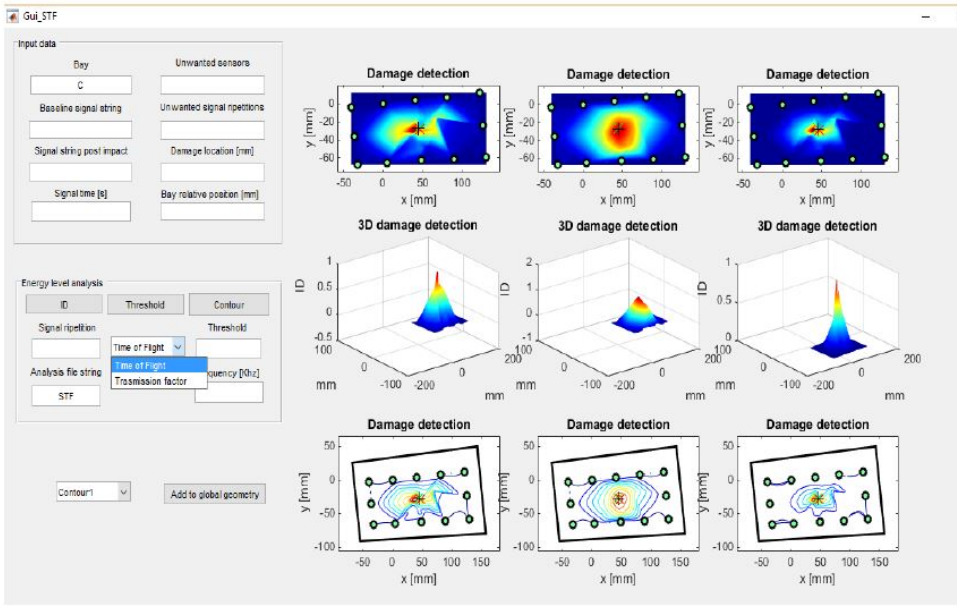

Figure 3.26: Analysis tool panel of the MP^2 modular software. Overall ToF based damage detection of section C of the lower wing panel.

location, are able to analyze data without any further input. The user may also exclude several data connected to a specific sensor. This feature is particularly useful in such cases where the robustness of a specific system has to be investigated while reducing the number of sensors and for self-diagnostic purpose (see Chapter 5). The threshold is assessed from a statistical investigation of the specific parameter considered, swithcing the suitable making decision framework for that feature. Three different methods are opportunely addressed to such cases for evaluating the signal noise from concurrent measurements. The upper bound level of normal distribution, its mean value when high noisy is present, and the acoustical reciprocal theorem where not any variability is present are respectively implemented and able to address the wide variety of cases investigated until now. The software is finally capable to elaborate a database with all features extracted by current and baseline interrogation useful for data post-processing (damage index and threshold) and image reconstruction (single or multi-parameter). An example of the diagnosis obtained for the bay C of the lower wing panel using the modular software implemented is also depicted in Figure 3.26, demostrating again the capability to correctly detect and locate the induced damage.

The GUI analysis panel is strongly linked to a preliminary analysis panel used for material characterization purpose, as depicted in Figure 3.27. The polar plot of the propagation velocities as well as the dispersion and tuning curves of the selected wave

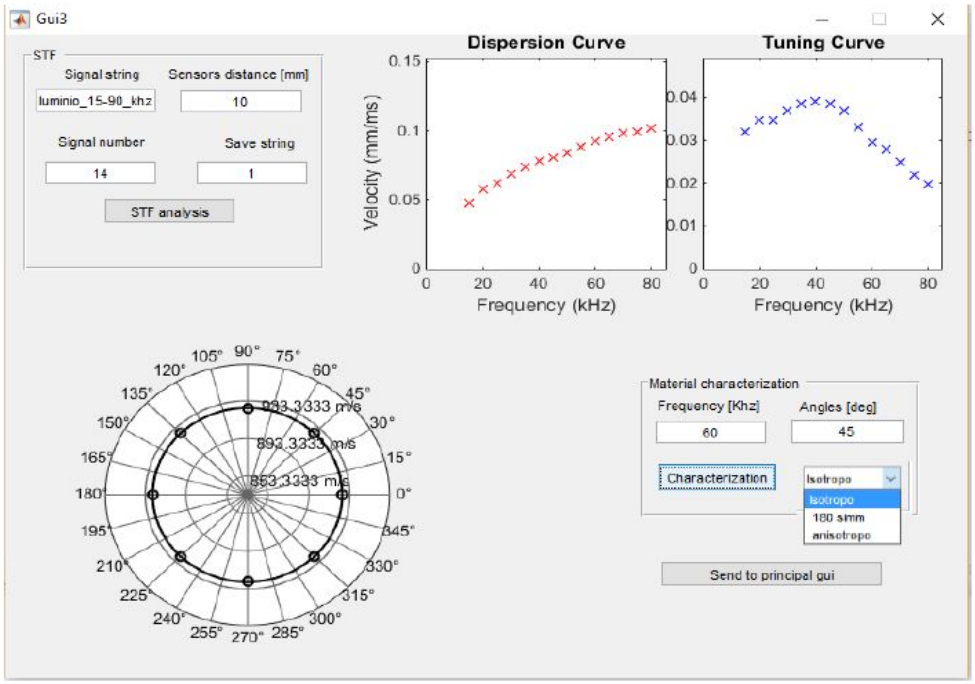

Figure 3.27: Preliminary analysis tool panel of the MP^2 modular software. Dispersive characterization of an isotropic aluminum plate.

mode are reconstructed here from available data according to the dispersive characterization provided in Chapter 4. Such results obtained are indeed useful to define few working settings for measurements or simulations (i.e.: most suited frequency for interrogation) and can be indeed reported in the front panel (see Figure 3.24).

Finally, the software is linked to an external tool providing an interactive platform which has been developed within MATLAB® environment as well and supporting the mesh-based reconstruction. Also this graphic user interface is capable to simultaneously analyze several wave features affected by damage and various probabilistic algorithm based on linear and nonlinear reconstruction techniques. The designed main panel is depicted in Figure 3.28 and it is divided in three specific sections. The former on the left allows to define all inputs and settings, including an external window to interactively exclude sensors. Selecting data files, the software is able to elaborate a database with all features extracted by current and baseline configuration useful for data post-processing and damage reconstruction. The second section on the top level provides the definition of the reconstruction method selecting from the horizontal bar the damage index, decreasing probability and features to be considered or combined for a multi-parameter approach). Finally, the central window provides the resulting

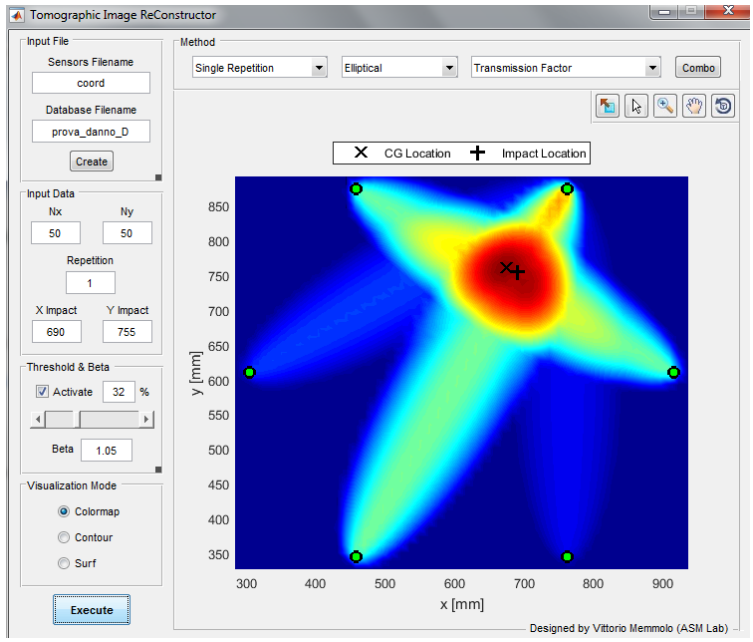

Figure 3.28: Analysis tool panel for mesh-based reconstruction. Elliptical detection of a small mass added to an aluminum panel.

tomographic image (colormap, contour of isolines or surface of probabilistic function depending upon the visualization mode selected) and the comparison between impact position (if known) and its estimation.

The results reported here are limited to those necessary to explain the methodologies and softwares developed as well as their effectiveness. However they are covering only few investigations among those succesfully performed. Moreover they are mostly referred to the localization of impact induced delamination. The case of stringer disbonding, which is more complex and critical, is approached as well in this work but reported in the next section where a new methodology to define the size of disbonding is also described and compared to the actual MP^2 system capabilities.

3.1.4 Disbonding detection in complex structures

As aforementioned, using a distributed cluster of sensors, the propagating wave can be detected through pitch-catch approach; namely one sensor is actuated to excite an elastic wave (pitch) and remaining sensors are exploited to sense propagating field (catch). This means that the sensor used to excite propagation is not used to sense any wavefield. However every PZT used to sense the propagation (receiver) excited by the previous one (transmitter) is able to catch the direct propagation but also every other echo redirected by discontinuities towards that location. Starting from this

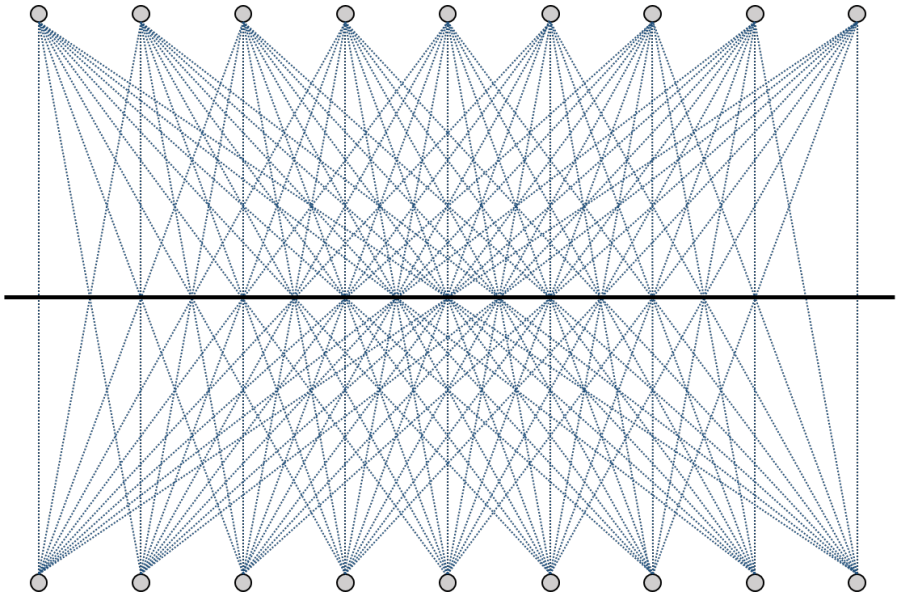

Figure 3.29: Sensor cluster and interrogating patterns obtained using direct waves propagation.

consideration, for the specific case of a disbonding between stringer and thin walled composite structure, sensor configurations can be broadly divided in:

- *Closed Pattern* or *sensor matrix*, where the sensors constitute a polygonal geometry and the wave directly propagating along every line of sight is recorded exploiting every possible couple of sensors located on opposite sides of the stringer (see Figure 3.29). Every change involving the structure, the stringer and their interface is thus expected to affect those paths crossing the defect.

- *Open Pattern* or *sensor vector*, with which a linear distribution of sensors is instrumented alongside the stringer, which is exploited as a reflector (see Figure 3.30). Every change at the stiffener interface can be detected with the pitch catch approach analyzing the reflections scattered by the stringer.

The first configuration allows to detect and locate the damage using the making decision step to select the paths affected by the hidden flaw and a dedicated algorithm to localize the damage from DI datasets, namely exploiting the paradigms of the MP^2 approaches. As aforementioned, they can be broadly grouped in *mesh-based* and *meshless* approaches depending how the risk to have a damage is computed for a specific location. The former prescribes a cloud of points (mesh) where the risk is achieved accounting the effect of every selected path with a decreasing probability [128, 129]. Using a meshless approach, the SHM mesh is defined after making decision restoring DI datasets on the intersections of selected paths. Then the results are

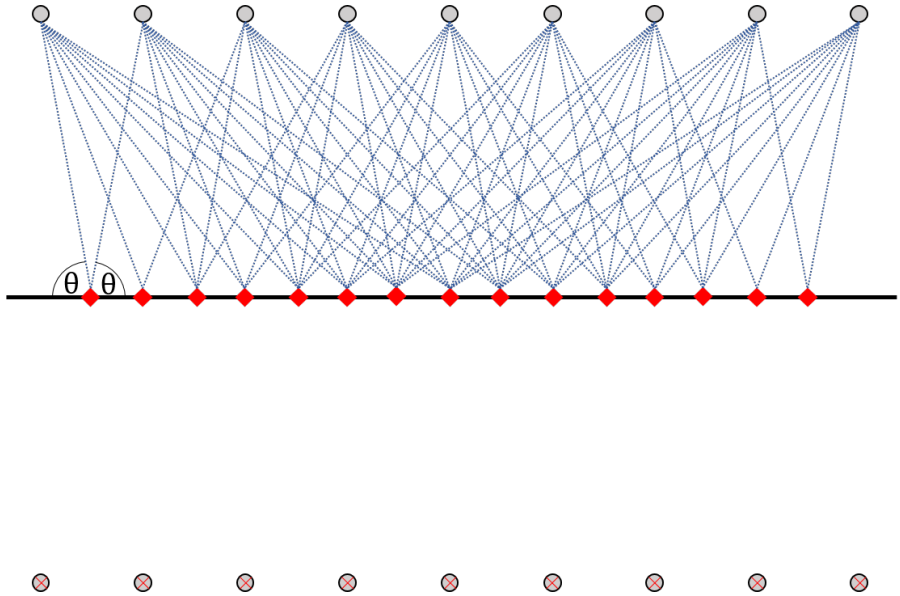

Figure 3.30: Sensor cluster and interrogating patterns obtained exploiting the stringer as a Lamb waves reflector.

interpolated over the predefined structural mesh according to the resolution required [112] and exploiting different schemes [123]. The latter approach, proposed in the previous sections for detecting damage scenario in flat plates, is extended to stiffened panels for disbonding detection. A typical result is reported in Figure 3.31, where the diagnosis obtained with meshless approach to detect an impact induced disbonding is depicted. The complex geometry (left) is part of the real scale wingbox designed in carbon-epoxy material for a commercial aircraft (see section B in Figure 3.20). The thin walled structure has a 6mm thickness and shows a ramp connection towards the stringer leg where the baseline thickness is 8mm and the thickness of leg and web is 8mm as well. The reconstruction is based on the energy content of first antisymmetric mode (A_0) of propagating Lamb waves using the density of emerging points as resolution parameter [130]. The paths are selected resorting to the statistical prediction interval estimated for that feature according to Sec. 3.1.1. The centroid of the discrete system constituted by emerging nodes is computed as well to estimate impact location, showing the very marginal error obtained. As depicted in the figure (right), the map shows an increasing risk around the disbonded area allowing to detect and localize the perturbed zone. No matter what the mathematical formulation is used, the centroid is able to locate the impact with a negligible error compared to the disbonding extent which appears to be about 35mm when assessed with classic ultrasonic NDT.

Although the failure is correctly localized, this approach provides a damage recon-

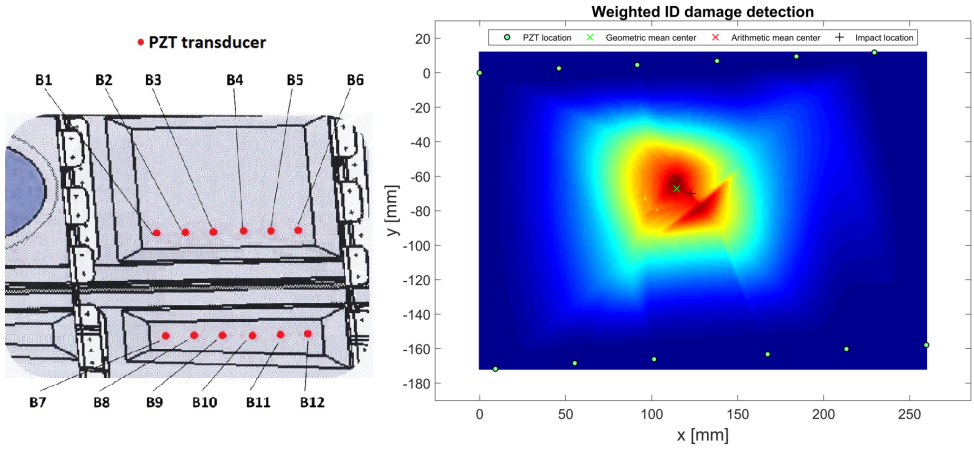

Figure 3.31: Diagnosis of a stringer disbonding using global approach. Geometry of the monitored area and sensor configuration (left) and map of risk obtained with meshless approach (right).

struction that is not focused on the disbonding scenario and thus hereinafter mentioned as *global approach*. Furthermore, the stringer prevents to insert lateral sensors, reducing the capabilities of the MP^2 approach because part of the stiffened area is not correctly scanned. Finally, the deterministic assessment of damage size is not achievable. Hence, nevertheless the fast and reasonable result obtained again, the diagnosis provided by using the global approach based on the MP^2 method is not comprehensive and detailed for the specific case of the disbonding.

With the aim to focus the monitoring on the disbonding scenario above all else and to overcome geometrical constraints induced by stringer, the second approach appears to be promising. In this case each sensor is actuated to excite Lamb wave propagation which is sensed by all other sensors along the line. Such receivers are able to primarily detect the direct waves propagating parallel to the stringer and then that reflected from the stringer. This is where there is a clear difference between such approaches. Analyzing the reflected part of the signal it is possible to gather information about the health of the stringer in a specific point, which is the *check* (or *control*) *point* of a *local approach* as referred to further in this work. The local approach is described in detail in the next section, from theoretical issues and modeling to experimental application.

3.2 Disbonding assessment from wave scattering analysis

In the case of disbonding, particular conditions connected to the impact event practically lead to the separation between the stringer and the hosting structure preventing the collaboration between parts with a dangerous drawback for loading absorbing. As

mentioned in Chapter 1, usually disbonding stoppers are included into the design to avoid separations between stiffeners and skin above the maximum size ensuring collaboration [29]. Moving towards a condition based approach, it appears crucial the deterministic diagnosis of damage in terms of size and severity.

Although the analysis of direct waves propagating is able to return the detection and position of disbonding as widely demonstrated also in [131], size and severity of damage is not directly assessed even when ultrasonic features are sensitive to such a hidden flaw [130]. On the other hand, multiple ultrasonic echoes caused by reflections from the plate's boundaries can be leveraged to enhance imaging performance [92], complex structures may be used to redirect lamb waves to ensure the monitoring of a specific area [132] exploiting its scattering capabilities or ray path models can be assessed to locate and size the damage [133]. Hence, the reflections of wave interacting with stiffeners can be analyzed to improve the diagnostic or design new strategies. Regardless the post processing of data, both global and local approaches exploit a metric defined following Eq. (2.11). That is much easier to imagine when the global approach is used due to the damage affecting the direct wave propagation whether it is a disbonding or not. The valuable information which can be further derived analyzing the wave portion reflected from the stiffener is related to the physical problem of scattering when interacting with discontinuities. The stiffener region is an area characterized by a strong mismatch of structural impedance. When the stringer is bonded to the surface, the excited wave propagating within the plate is partially reflected from the stringer while another amount of energy is transmitted allowing the wave mostly to penetrate into the stringer web. That is where the propagation behavior can be exploited for damage detection. A sensor bonded beyond the stringer cannot clearly detect any propagating wave due to the presence of the stringer. Instead, when the disbonding creates a perfect separation between stringer and structure, it precludes the wave to propagate into the stringer. A sensor beyond the stiffened area senses a propagating wave, while no such an amount of energy is reflected [134].

Anyway, this behavior suggests the effectiveness of a DI approach whether the receivers are used to sense direct wave or reflected wave. In the former, when the actuator is excited on the pristine structure, a receiver located beyond the stringer is unable or marginally able to sense the propagating wave with a little amplitude. When the measurement is repeated on a damaged structure, the transmitted signal, whose amplitude is not negligible anymore, is sensed by the receiver. Thus, a metric based on DI formulation appreciates the increasing energy transmitted when disbonding is present. This is the principle adopted by the global approach, which is effective for identification no matter the type of damage is, but it is unable to characterize it. In the latter case, the stringer is merely a reflector so that exciting the wave from a

single location in the pristine structure, a receiver bonded on the same side senses the amount of energy reflected from the stringer. When a disbonding occurs, the same receiver senses a reflection scattered by the stiffened area whose energy is strongly reduced depending upon the severity of damage. Consequently, focusing the analysis on the expected portion of energy reflected from stringer, the DI is a valuable metric for assessing local health condition close to the specific scattering point. In addition, the information gathered from direct wave allows to correctly identify that portion without resorting to complex theoretic models but simply modeling the propagation behavior as defined in the next section.

Within the last demands, the present section deals with the scattering of propagating waves for identification, localization and size and severity assessment of disbondings in stiffened composites, which are rarely investigated in the literature. Due to the complexities involved, a simple geometrical reduction is used to describe the propagation of the first antisymmetric Lamb wave mode (A_0) using the object of investigation itself as scatterer. Including boundary reflections into the reconstruction model provides high performance diagnostic reducing transducers and pattern complexities of conventional techniques.

3.2.1 Propagation model

The multipath propagation model described hereinafter estimates patterns of multiple echoes in scattered guided ultrasonic waves (GUWs) from a reflector, namely the stringer to be monitored. This approach calculates the propagation path of each echo to estimate its arrival time and evaluate the energy content of the GUW packet reflected from the scatterer. The paths along GUWs may travel can be broadly divided into one direct path and multiple indirect paths. It is necessary to distinguish the wave packets traveling along the useful indirect (reflected) path from that propagating along the direct path. The former one generally consists of a first segment between actuator and scatterer and a second segment between scatterer and receiver. Otherwise, the direct path is merely the segment between actuator and receiver. To exploit the information gathered from wave packets reflected by the scatterer, the reconstruction method can be broadly divided in two steps: (i) ray tracking and (ii) damage estimation. In the following sections the hypothesis for ray tracking and the related optimal design configuration are discussed towards the experimental application.

Working hypothesis and assumptions

When the actuator is pitched, the excited Lamb wave modes are propagating in several direction depending upon the composite properties [94] and reach the stringer and

the receiver in different time depending upon the geometrical configuration as well. The ray tracking is concentrated to two different propagation paths which are referred hereinafter as *direct path* and *reflected path*. About the latter one, it is constituted by an incident segment and a reflected segment for which certain assumptions are considered in developing the ray tracking. Linear elastic material behavior is considered. The excitation frequency is selected below the first cutoff frequency, so that only fundamental modes, anti-symmetric (A_0) and symmetric (S_0), can propagate. The fundamental shear horizontal (SH_0) mode is indeed negligible because the adopted PZTs are insensitive to that mode.

When the wave interacts with the stringer, the behavior is quite complex and it is challenging to recognize evanescent and/converted modes. Moreover, since the non isotropic mechanics of composite, the path followed by the scattered wave is not certainly defined. Thus, looking to the Figure 3.32, the two modes are reflected by the stringer in such a way that can be simplified as follows. The strongest hypothesis is that incident A_0 mode is reflected as A_0 only, and the S_0 mode is reflected as S_0 only. The propagation direction of the reflected waves is governed by Snell's law [135]:

$$k_i \cdot \sin(\theta_i) = k_r \cdot \sin(\theta_r) \tag{3.11}$$

where k_i and θ_i are the wavenumber and angle of the incidence wave, respectively, while k_r and θ_r are the wavenumber and angle of the reflected wave (see Figure 3.32). Since no mode conversion occurs, the wavenumber remains the same if the pattern velocity is not much affected by propagation direction, as usually happens for composite structures designed for real application [43]. Therefore, the incident and reflected angles are also the same:

$$\theta_i = \theta_r \tag{3.12}$$

For such assumptions the wave is reflected from the scatterer with the same properties of the incident wave. This means that considering a multi-modal wave, if one incident mode is dominant, that is primarily propagating along reflected path and sensed by receiver. This behavior can be easily investigated tuning the frequency with the desired mode [94] and enabling the simple windowing for DI computation.

In other words, similarly to a free-edge, the stringer is supposed to act as mirror and the path taken from a source to the scatterer and then to a receiver can be simply traced by connecting the receiver to the mirrored location of the source with respect to the boundary. This means that the Eq. 3.12 uniquely returns the interrogating point for damage detection, namely the mirroring point. With those assumptions every couple of sensors interrogates a specific point like depicted in Figure 3.30. Thus, the

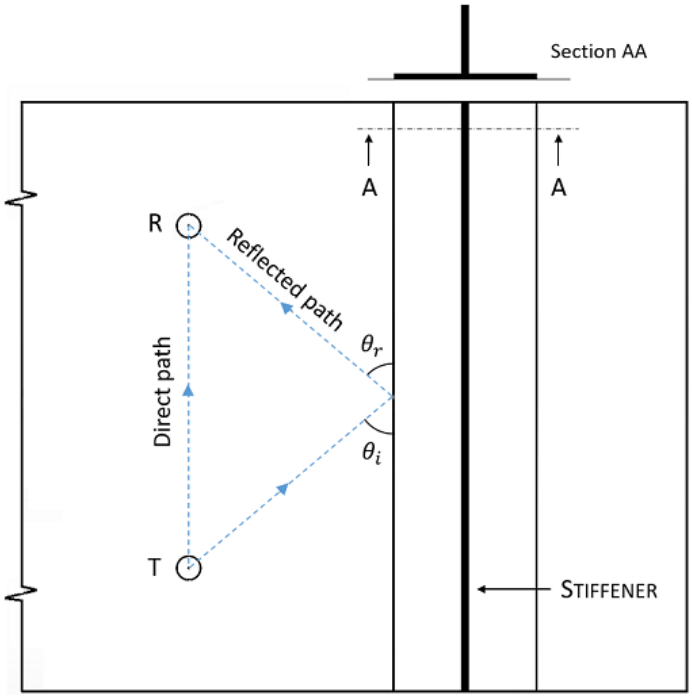

Figure 3.32: Geometric configuration for a sensor pair exploited for local approach.

maximum number of check points or control points is:

$$M = 2 \cdot (N - 1) - 1 \tag{3.13}$$

where M is the number of check points and N the number of sensors. It is possible to interrogate the same point with different couple of sensors creating redundancy as well.

It is worth noting that the method is based on the properties of wavemode packet interacting with the scatterer and redirected towards the receiver. For the latter demand, it is necessary to correctly visualize that portion of signal using a specific actuator-receiver pair. Accordingly, geometrical constraints have to be accounted as explained in the next section.

3.2.2 Optimal design configuration

When excited from a single location (see T in Figure 3.33) the wave propagates along different directions and guided by the structure. When the stringer is perfectly bonded, R senses the direct wave and that one reflected from the mirroring point. The amplitude of the latter one is smaller than that of the direct wave and requires to be

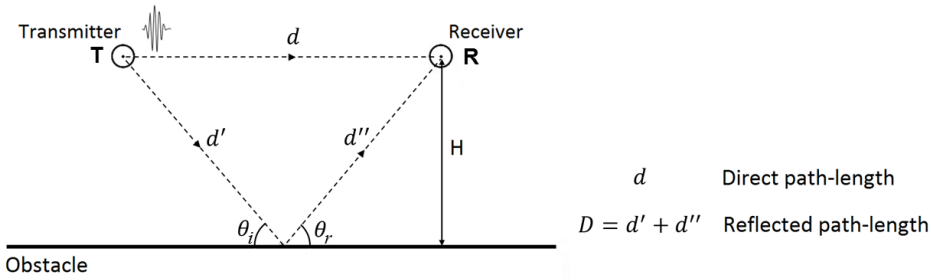

Figure 3.33: Schematic representation of sensors pair distribution for carrier frequency calculation f_C following Eq. (3.17).

isolated from the former to be analyzed and gather correct information about stringer condition. The relative position of T, R and stringer is thus crucial to distinguish signals associated to different propagating waves sensed by R. The sensor R records the direct wave in a time which depends upon excited characteristics. This means that wave propagation and location of sensors should be accordingly set. The duration of the wave is indeed affected by various parameters usually chosen to accommodate signal conditioning, namely to reduce the dispersive behavior and tune the wave mode exploited for damage detection. The carrier frequency should maximize the amplitude of the mode respect to coexisting modes [94], which is affecting the velocity of wave and signal duration. On the other hand, the dispersive behavior modifies the waveform while traveling in the structure due to the different velocity of the particles and it is usually accommodated exciting various windowed sine cycles to minimize the leakage and the bandwidth, affecting the duration of the wave packet. The geometrical design of the sensorized structure is finally crucial to define the time of flight necessary to travel along direct path and reflected path respectively; it is merely dependent upon the distances d and H shown in Figure 3.33.

Theoretically, if t_D and t_R are the time of flight referred to the direct wave and reflection from stringer respectively recorded in R, the Eqs. (3.14) return their values assuming that the two wave-packets propagate with the same group velocity v_g.

$$t_D = \frac{d}{v_g}, \qquad t_R = \frac{D}{v_g} \tag{3.14}$$

The carrier frequency f_C enabling the time separation of direct and reflected wave can

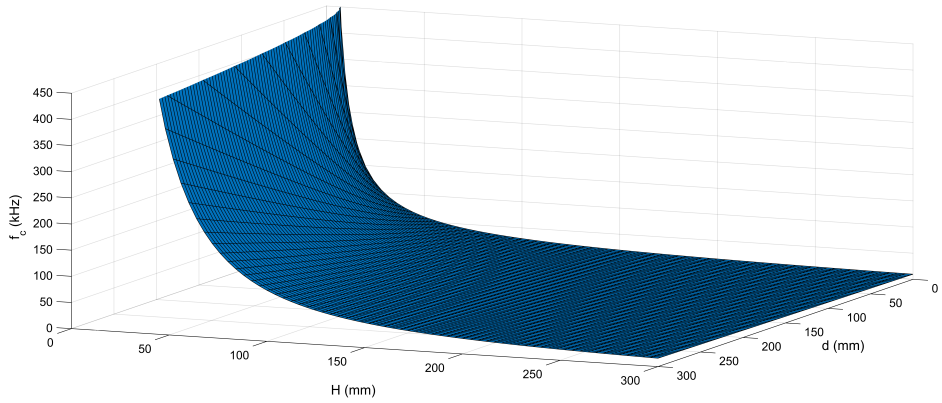

Figure 3.34: Distribution of the carrier frequency f_C in $d-H$ space which ensures a correct visualization of the reflected wave. The group velocity $v_g = 1311.7$m/s is estimated processing signals acquired from test case presented in Sec. 3.2.3.

be derived from the following relationship:

$$\Delta T = t_R - t_D = \tau = n \cdot \frac{1}{f_C} \tag{3.15}$$

where τ and n are the overall duration and the number of sine-cycles of the excited signal respectively . Thus, the carrier frequency can be defined as:

$$f_C = \frac{n \cdot v_g}{D - d} \tag{3.16}$$

where d and D are the direct and indirect path length (see Figure 3.33). Finally, in term of distance between pair and stringer (H), the frequency can be rewritten as:

$$f_C = \frac{n \cdot v_g}{2 \cdot \sqrt[2]{[H^2 + (d/2)^2]} - d} \tag{3.17}$$

Practically, the relation proposed in Eq. 3.17 returns the combination of geometrical and excitation parameters which allows to correctly visualize the reflected wave and exploit the reflection-based method which is discussed in Section 3.2.1.

The representative surface which satisfies such a working constraint derived in the Eq. 3.17 is depicted in Figure 3.34 and detailed for fixed values of pair distance d in Figure 3.35 to emphasize the distribution of carrier frequency respect to geometric parameters. Basically, if the combination of parameters returns a point that is above the depicted surface, such combination is appropriate. Otherwise, it may be unable to ensure a correct visualization of reflected wave corrupting the expected information.

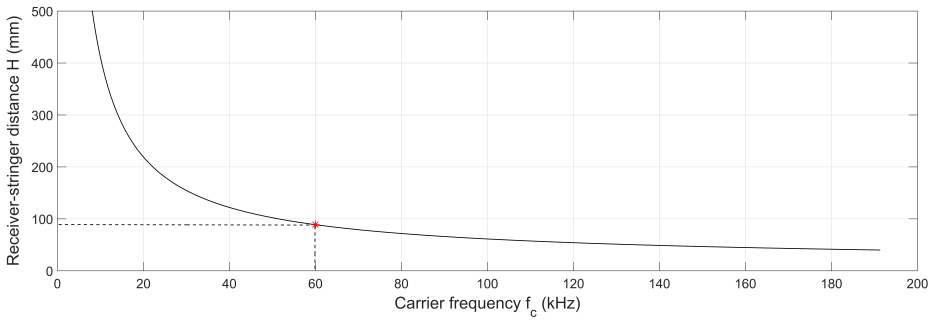

Figure 3.35: Distribution of carrier frequency f_C vs. distance H following Eq. (3.17). The group velocity $v_g = 1311.7$m/s is estimated processing signals acquired from test case presented in Sec. 3.2.3.

This conclusion is motivated by the fact that a frequency bigger than f_C returns a shorter signal representing the direct wave sensed by R which ensures a conservative design. On the other hand, looking to the curve depicted in Figure 3.35, the minimum distance required between sensors line and reflector (H) can be picked entering with the value of the carrier frequency in the graph obtained by the definition of a specific pair distance d. Again, if the combination of design parameters returns a point that is above the depicted curve, then the design is conservative. Otherwise, it is not appropriate to correctly select the reflection. Basically, a greater value of H returns a greater difference between direct and reflected path lengths, ensuring more time separation of waves which are traveling along.

A critical parameter for a correct design is the group velocity, which defines the arrival time of the direct wave and can be estimated directly from the signal or from theoretical side whether if it is function of frequency or not. The last aspect is crucial for a correct design, defining the non-linearity of the Eq. (3.17) when a dispersive behavior is intercepted. In that case the depicted distributions are correct only around the frequency chosen to calculate the velocity. Increasing the frequency, the velocity may change modifying the output resulting from the Eq. (3.17) in a non linear way. In that case and without thereby affecting the general purpose, the relationship between geometrical and signal parameters can be exploited merely to verify the correctness of the design as follows:

$$f_C \geq f_c = \frac{n \cdot v_g}{2 \cdot \sqrt[2]{[H^2 + (d/2)^2]} - d} \tag{3.18}$$

where f_c is defined as *control frequency*, namely the minimum carrier frequency which ensures to isolate a reflection from direct wave. If the combination of geometrical and signal parameters verifies the Eq. (3.18), the design can be considered appropriate.

Otherwise, it is necessary to accommodate the geometrical parameters and/or the signal parameters to satisfy that relation. Furthermore, if the frequency changes, the velocity has to be merely updated as well to check again if the Eq. (3.18) is verified.

The Eq. (3.18) is proposed here for validating working parameters and it can be neglected that the group velocity is a function of frequency whether it is or not. Basically, if the chosen working frequency f_C is below the control frequency, the proposed method may be unable to correctly work. Otherwise, if f_C is greater than f_c, that is the case where the reflected wave is isolated. Curves and surface reported in the previous figures are referred to a fixed value of group velocity, experimentally evaluated at a 60 kHz on the composite panel investigated afterwards. Although such simplification, it is possible to understand how geometrical parameters (d and H) and signal waveform parameter (n) affect the control frequency guiding the design amendments. Such trends allow indeed to primarily design the experimental set-up, taking into account that a final validation should be always carried out when every parameter changes. Finally, if the purpose is to define rather than to verify the proper working frequency, a nonlinear analysis has to be performed by considering that the group velocity is a function of frequency.

It has to be pointed out that the group velocity is assumed to be equal along different paths, which is not generally verified when a composite structure is considered, even with a quasi isotropic layup [94]. However, depending on the wave propagation properties, this issue can be faced with a conservative design. It is indeed crucial that uncertainties affecting measurements and calculation (when v_g is evaluated directly from signal processing of direct wave) [136] and lacks of agreement with theoretical propagation (when v_g is theoretically assessed) do not affect the approach corrupting the reflection visualization. This means that the velocity should be merely underestimated considering the conservative value v_c following Eq. (3.19) when it is calculated with Time of Flight (ToF) approach or Eq. (3.20) when it is theoretically assessed.

$$v_c = \frac{ToF - \epsilon(t)}{d} \tag{3.19}$$

$$v_c = v_g - \epsilon(v) \tag{3.20}$$

The value used to accommodate the velocity depends upon the uncertainties mentioned above and it is suggested to account at least 5% error in the estimation of v_g. This approach is adopted to ensure a conservative design as well as for correctly windowing the reflection as explained in Sec. 3.2.3. However, if the discrepancy between control frequency and carrier frequency is relaxed, using whether v_c or v_g does not change the feasibility of the design, as showed in Sec. 3.2.3.

3.2.3 Disbonding reconstruction

In this section the results obtained monitoring a composite stiffened panel designed for a wing box are presented. A first investigation on design parameters and scattering capability of the stringer is carried out and discussed in Sec. 3.2.3, validating the theoretical aspects discussed in the previous section. Then, the damage detection approach is exploited to identify, localize and quantify a complex damage scenario as well as to reveal the the multi-level diagnostic provided by the system and discussed in Sec. 3.2.3.

Preliminary investigation

The monitored structure is depicted in Figure 3.36. The specimen is a composite panel fully made of carbon/epoxy material and designed for the lower part of a regional aircraft wing box. The thin walled structure is stiffened with five *C-type* stringers made of the same material and bonded together with the plate during the manufacturing process to ensure structural continuity without any other splice. The panel dimensions are 1200mm × 900mm × 25mm and the stringers are placed with an equal spacing of 200mm along the long side. The outer bay of the structure (A) delimited by the stiffener and the free edge is exploited for the preliminary investigation aimed to verify what is theorized in Sec. 3.2.1 and check the optimal design formula discussed in Sec. 3.2.2. The outer bay ensures to investigate the wave interaction with the stringer and compare it with scattering from free edge, which is an ideal mirror. Following the discussed propagation model, the pitch catch approach allows to detect the presence of the stringer as well as of the free-edge by windowing in the recorded signal and analyzing the reflection redirected from that location.

Four lead zirconate-titanate (PZT) disks made of ferroelectric soft piezo material (PIC255) by *Physik Instrumente* (PI), 10mm diameter and 0.25mm thickness, are bonded on the plate surface through a vacuum-based secondary bonding procedure commonly used by aircraft industries. Thus, the rectangular network depicted in Figure 3.36 is obtained and sketched in Figure 3.37 together with the possible working modes discussed afterwards. The diagnostic signal is emitted by an arbitrary waveform generator (HP/Agilent 33120A), as a 4.5 sine-cycles burst with 10V peak-to-peak tension and windowed using Hanning function to obtain a narrow-bend curve in the spectral domain. The carrier frequency of 60kHz is chosen to obtain an excitation ensuring the best compromise between tuning of the first antisymmetric Lamb wave mode A_0, A_0/S_0 amplitude and optimal design geometrically constrained by the bay dimension. An amplifier is used to boost the voltage with up to 80V eak to peak increasing the signal to noise ratio. The ultrasonic signal is then digitalized and recorded

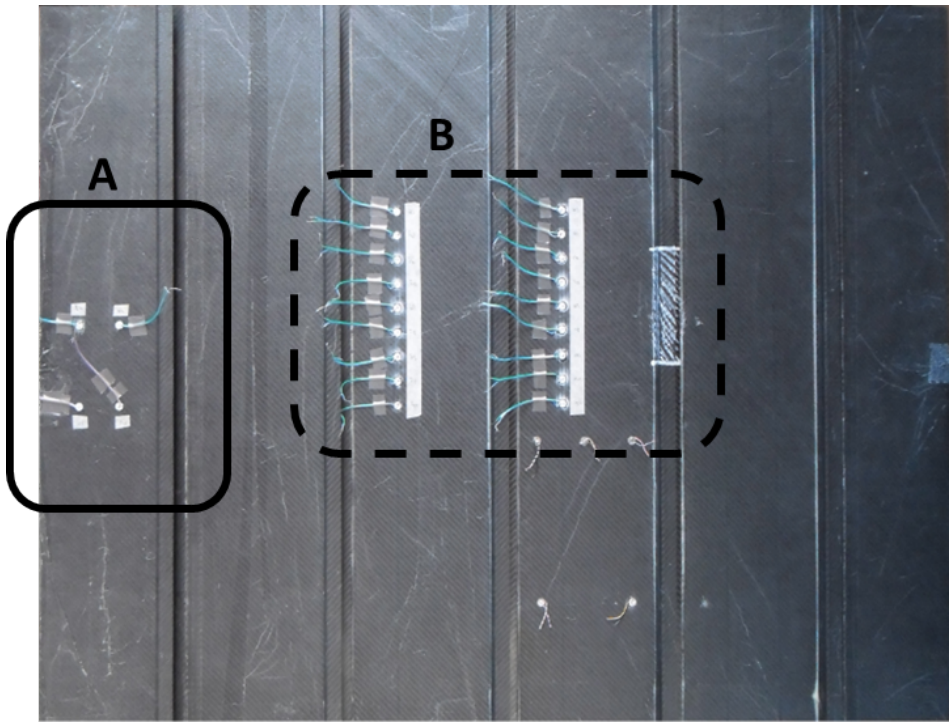

Figure 3.36: Composite panel made by carbon/epoxy material and stiffened with five C-type stringers uniformly spaced. The outer bay (A) is exploited for preliminary study and the central area (B) is instrumented for SHM application.

with a four channel digital oscilloscope with up to 1GHz sampling rate (Agilent InfiniiVision DSO7104A). Finally, the digitized ultrasonic signals are downloaded to a personal computer for data post processing.

Hence, for each actuator-receiver pair, the group velocity of the A_0 mode and the ToF of the reflected waves can be estimated from direct wave in the measured signals. Two different reflected paths are generated by the model for each sensors pair, as schematically shown in Figure 3.37. The sensor pairs ideally divide the bay in order to have a specular design whether to detect the presence of the stringer or the free edge position. This means that the distances between the stringer and sensor pairs #1-#2 and #3-#4 are equal to the distances between the free edge and sensor pairs #3-#4 and #1-#2, respectively. This sensor distribution is exploited to compare the analysis of stringer detectability with the free edge (ideal reflector) merely fixing the H parameter.

The results obtained for the above-mentioned reflected paths are illustrated in Table 3.4 and in Table 3.5 for actuator-receiver pairs #1–#2 and #3–#4 respectively. The outcomes of pairs #2–#1 and #4–#3 are omitted for the sake of the conciseness

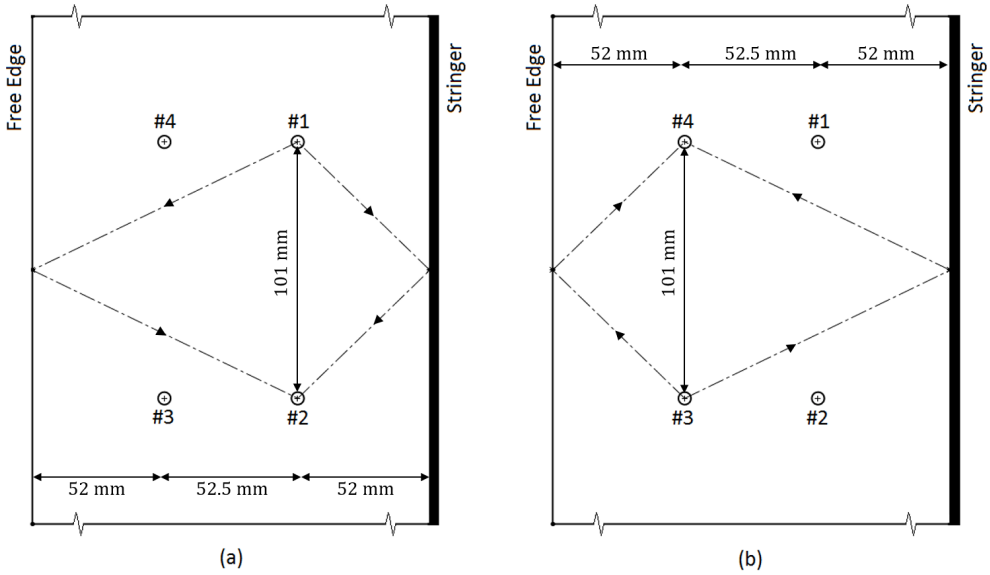

Figure 3.37: Schematic diagram of design and direct and reflected paths considering the stringer as well as the free edge for (a) actuator #1 – receiver #2 and (b) actuator #3 – receiver #4.

because they are comparable with and merely support the results discussed in the following. The expected time of flight along reflected path is evaluated from the estimation of group velocity v_g of the direct wave propagation using the STFT approach and it is referred as ToF hereinafter. Then, the time of flight is evaluated directly from reflected wave, i.e. comparing the reflection recorded at receiver location and that of the excited wave. The latter value is referred as $\overline{ToF}$ and it is expected to be close to ToF value when the reflected wave is correctly identified from the signal, namely when the working hypothesis are verified. The comparison shows indeed an excellent agreement when the reflection from the farther obstacle (i.e., the longest reflected path) is considered. Conversely, when the reflection from the closer obstacle is assessed, a certain discrepancy appears evident from comparison. As shown in Figure 3.38 exciting sensor #1, the direct wave-packet sensed by sensor #2 (A_0 mode which follows a small S_0 mode) merges with the first echo (stringer), making harder the signal processing and the correct features extraction. Instead, the echo from the edge can be perfectly recognized.

In other words, the combination of geometry parameters and the diagnostic excitation signal does not ensure that the reflection coming from the closer obstacle is sensed after that the direct wave completely propagates through the receiver. This result is in accordance with the design constraints theorized in Sec. 3.2.2 with the Eq. (3.18),

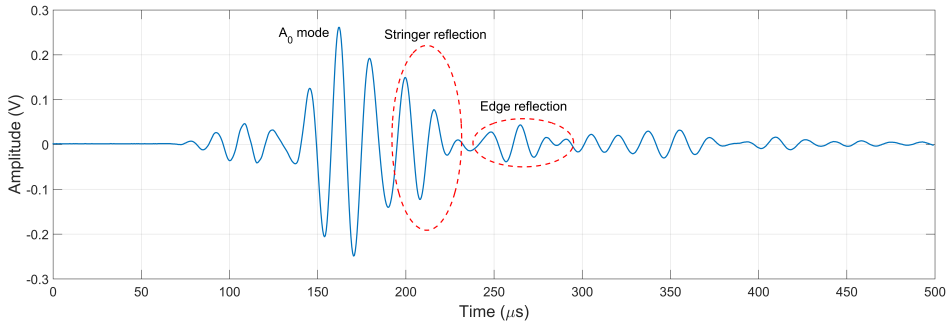

Figure 3.38: Signal recorded by sensor #2 while exciting sensor #1.

Reflector	d' (mm)	v_g(m/s)	ToF $\mu(s)$	$\overline{ToF}$ (μs)	ΔToF (μs)
Free-edge	116.06	1311.70	176.96	177.75	-0.79
Stringer	77.49	1311.70	110.52	128.0	-17.48

Table 3.4: Path #1-#2. Results obtained estimating v_g and ToF from direct wave propagation.

which is indeed here verified only for the farther reflector. This means that when the pair #1-#2 is exploited, the free-edge is correctly detected while the presence of the stringer cannot be detected from reflection analysis. On the contrary , when the pair #3-#4 is used, the free-edge is not detected while the presence of the stringer can be correctly identified from reflection analysis. This trend is thus confirmed whether the reflector is the free edge or the stringer, demonstrating the feasibility of exploiting the stringer as a scatterer. Furthermore the propagating waves actually adhere to Snell's law which can be applied to model the reflected paths from structural features like stiffener or free-edge. The agreement resulting from comparison finally suggests that the mode conversion is indeed negligible because the lack of agreement is only due to the "non-correct" design when present.

The last conclusion can be confirmed remarking the criticality aspect of the optimal design configuration. Referring to the previous case of actuator-receiver pairs #1 – #2, the Figure 3.39 shows the numerical trends of the control frequency f_c needed to isolate the reflected wave versus the receiver-obstacle distance H for different values

Reflector	d' (mm)	v_g(m/s)	ToF (μs)	$\overline{ToF}$ (μs)	ΔToF (μs)
Free-edge	77.49	1286.60	112.68	129.75	17.07
Stringer	116.06	1286.60	180.41	181.0	-0.59

Table 3.5: Path #3-#4. Results obtained estimating v_g and ToF from direct wave propagation.

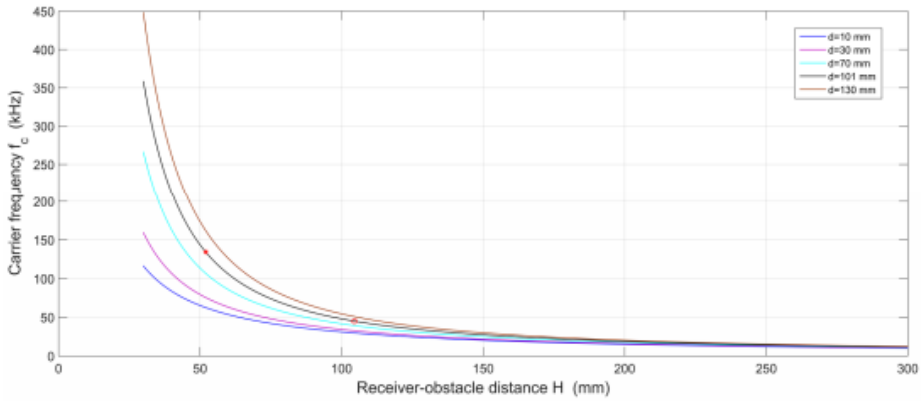

Figure 3.39: Numerical trend of the control frequency f_c needed to isolate the reflected wave with respect to the receiver obstacle distance H for different values of the sensors distance d (with $n = 4.5$ and $v_g = 1311.7$m/s).

of the sensors distance d and fixed group velocity ($v_g = 1311.7$m/s) and the number of sine cycles ($n = 4.5$). It can be noted how, for the current sensors configuration ($d = 101$mm) and sine-cycles number ($n = 4.5$), the chosen excitation frequency allows to isolate the reflection from the farther obstacle ($H = 104.5$mm), being greater than the control frequency ($f_c = 45.02$kHz). The last one is identified by vertical coordinate of the circle picked in Figure 3.39 approaching the graph with the current value of H. Otherwise, in order to isolate the stringer reflection ($H = 52$mm) and considering the estimated velocity, the central frequency of the excited wave should be greater than $f_c = 134.24$kHz (see diamond in Figure 3.39). This means that the configuration does not respect the optimal design formula merely because the carrier frequency f_C is smaller than the control frequency f_c. It has to be mentioned that the control frequency can be here calculated also considering v_c rather than v_g without thereby affecting the conclusions because the discrepancy between f_c and f_C is quite large.

Summarizing the preliminary investigation, it is possible to point out that the working hypothesis about incident reflection behavior (Snell's Law and conversion) can be accepted whether the obstacle to be detected for monitoring purpose is a perfect reflector (free-edge) or not (stringer). Moreover, the optimal design approach proposed is able to correctly assess the feasibility of a possible interrogation/geometry configuration merely estimating the propagation velocity of the wave mode selected for interrogating the structure. Starting from such consideration, in the next section the damage detection approach is proposed and the results are discussed.

Damage detection

Following the previous results, a further investigation has been conducted on the inner bay of the same specimen (see dotted area named B in Figure 3.36) with the aim to detect and locate stiffener disbonding through the proposed signal reflections based method. The damaged bay has been instrumented with a linear array of nine PZT sensors equally spaced with $d = 30\ mm$ and permanently installed on the structure surface. As described and verified above, it is assumed that:

- the wave signal is reflected by the stringer web with the same incident angle (Snell's law);
- the incident A_0 mode is reflected as A_0 mode only (i.e. the A_0 to S_0 conversion is negligible).

The interrogated wave is excited again with 60kHz carrier frequency and using a windowed 4.5 sine-cycles train for the above discussed reasons. On the basis of this parameters, the investigation for optimal sensor design is conducted looking for an appropriate distance H between the array of sensors and the stiffener. To have an optimum isolation of the reflections from the stiffener for at least two pairs of sensors for each actuator (i.e. considering $d = 60$mm) that distance is chosen to be $H = 120$mm .

The overall configuration of the instrumented specimen is sketched in Figure 3.40. Each sensor is individually actuated and the wave propagating in the structure is sensed by two following sensors exploiting the simple pitch-catch approach supplying the current damaged state according to the approach proposed in Figure 3.30. The design actuated enables the maximum number of checking points according to Eq. (3.13) without any redundancy to minimize the computational time. A first ultrasonic interrogation is carried out to define the baseline data set, namely the record of the propagation behavior in the pristine structure. Basically, the interrogation should be performed with the same sensor pattern used to currently monitor the structure. However, to make more challenging the post processing and verify the robustness of the reflection based method, the baseline data set is provided interrogating an undamaged adjacent bay of the same panel (identically instrumented for such purpose). The damage is manually induced to conveniently define the dimensions of procured disbonding and several severities of damage, which are assessed with a classical non-destructive evaluation which shows the presence of a fully disbonded area with a central region of additional skin-thickness reduction, as illustrated in Figure (3.41). The collected reference signals are first processed in order to verify the validity of previous assumptions describing the reflected propagating waves. Even in this case, good agreement is found in the comparison between ToF and $\overline{ToF}$. Two different reflections can be

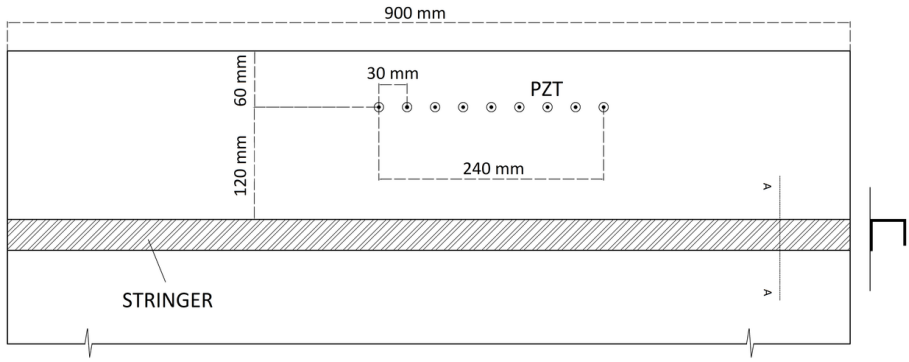

Figure 3.40: SHM system configuration designed to monitor the disbonding of the stringer with the maximum resolution of check points.

detected in the sensed signals due to the presence of two stringers delimiting the bay. It is also confirmed that only which one is following the optimal design configuration (i.e. the farer stringer) can be detected correctly.

A damage localization approach is then implemented exploiting information gathered by the waves redirected from the stringer to be monitored. The basic idea relies on the fact that the occurrence of damage substantially modifies the wave-paths of stiffener reflections as follows:

- when the stringer is perfectly bonded to the panel, the wave is reflected by the stringer and it can be captured by a sensor appropriately located;
- the presence of a disbonded region induces the wave to be transmitted beyond the stringer so that the reflection appears strongly attenuated in the acquired signal.

Knowing the reflected paths, control points are identified as the mirroring points and they generate the scanning line along the skin-stringer interface. Therefore, the damage index is defined for each control point by comparing the reflection redirected from that location to provide information about damage detection, location and severity. Two indirect paths are geometrically constructed when each sensor is excited (e.g.: #1-#2, #1-#3, #2-#3, #2-#4 and so on) obtaining a monitoring mesh with 15mm spaced control points so that 15 nodes result as represented in Figure 3.42. Starting from the expected ToF values, the stringer reflections are time windowed from digitized signals for each considered reflected path. The window size is that ensures to totally include the portion of signal redirected by the stringer. For the latter demand,

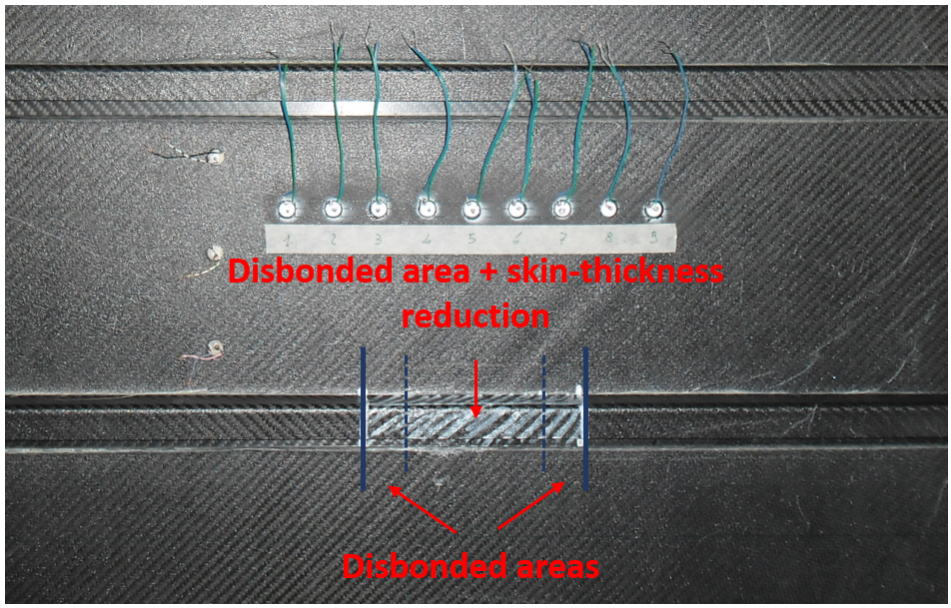

Figure 3.41: Inner bay of the panel investigated for SHM purpose. The disbonding induced is highlighted evidencing a central region which shows an additional skin-thickness reduction.

it is defined by the following time interval:

$$[t_i; t_f] = [ToF - \epsilon; ToF + \tau + \epsilon] \tag{3.21}$$

where ToF is the time of flight expected for the reflected path, τ is the overall duration of the excited signal and ϵ is a small percentage error used to accommodate the uncertainties aforementioned. In addition to those aspects, it has to be considered that the duration of the signal may slightly change due to dispersive behavior. In this case such behaviour is slightly intercepted by the A_0 mode for the combination of material properties and excitation frequency chosen. However, when the dispersion is strongly appearing, it is reasonable to relax the window dimension increasing the right bound.

Thus, the DI formulation proposed in Eq. (2.11) is computed to monitor each control point on the base of generalized energy contained by the wave supposed to be reflected from that point. The feature is extracted from current and baseline signal as follows:

$$f_{BS} = \int_{t_i}^{t_f} s_{BS}(t)^2 dt; \qquad f_{CS} = \int_{t_i}^{t_f} s_{CS}(t)^2 dt \tag{3.22}$$

where t_i and t_f are evaluated according to Eq. (3.21) and $s(t)$ is the digitized signal.

The results obtained performing the discussed post-processing are depicted in Figure 3.43, where the damage index is plotted versus the coordinate of the scanning

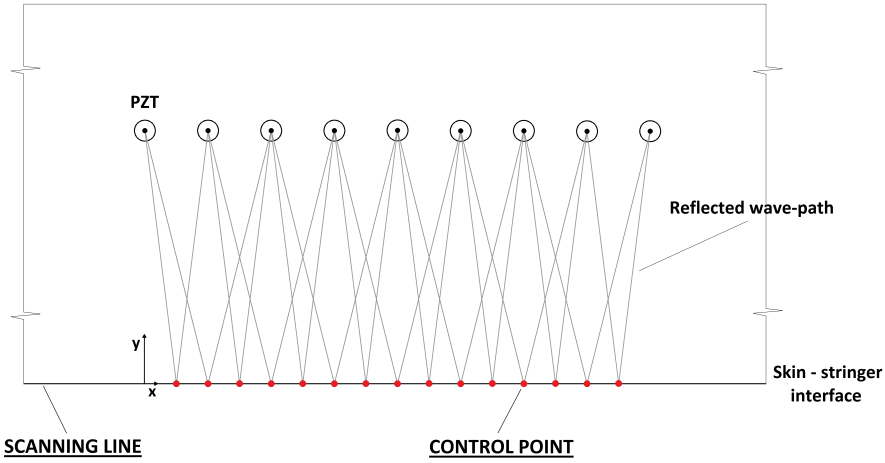

Figure 3.42: Scanning line along skin-stringer interface otained maximizing the density of nodes to monitor the interested area for disbonding detection.

line X. The coordinate with $X = 0$ corresponds to that of the first PZT and it is the reference for the scanning direction of the non destructive evaluation performed with a classic ultrasonic phased array probe to evidence the disbonded area with 1mm uncertainty [43] and reported in Figure 3.44.

From NDE it is possible to define three different characteristic regions. Starting from the left ($X = 0$), it is possible to detect a first undamaged region where the through thickness phased array investigation correctly returns the plate interface (blue regions) and the stiffener interface (i.e. the central red region). Then a first damaged area (A) can be assessed between $X = 55$mm and $X = 100$mm, where the disboding is increasingly evident due to the central area that returns a different echo amplitude confirmed by the mixed orange and dark blue area. From $X = 100$mm to about $X = 160$mm the echo response changes and defines the dark blue and orange big spots, according to the increasing severity of damage which characterizes the third region (B). In this area it is indeed present a skin thickness reduction which is confirmed by visual inspection and due to the forced manual disbonding which pulled part of the skin. Following, the region (C) between $X = 160$mm and $X = 190$mm is quite similar to the first damaged area observed. Finally another undamaged area is correctly detected after $X = 190$mm.

It is worth noting how the proposed approach appears to be able to detect (DI values above zero) and accurately locate the damage, using a limited number of sensors. Moreover, the distribution of control points along the skin-stringer interface allows to outline the extent of the disbonded region and thus to assess the damage size. It is

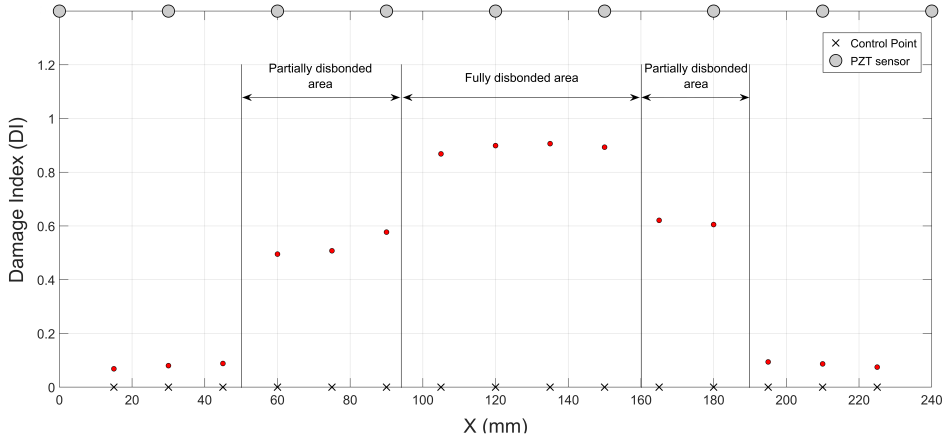

Figure 3.43: Distribution of Damage Index DI vs. X, which provides control points coordinate along the scanning line (skin-stringer interface). C-scan report is shown for comparison in Figure 3.44.

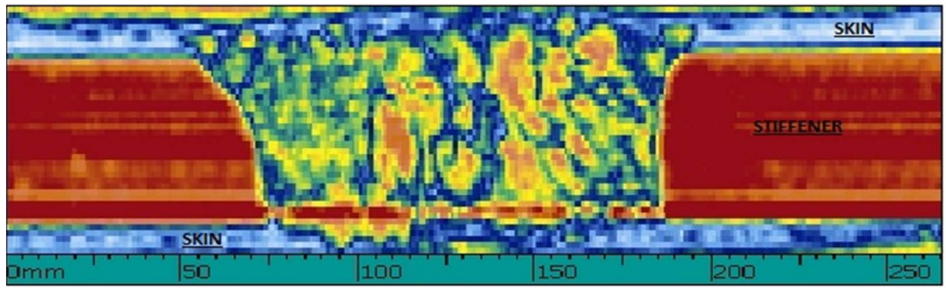

Figure 3.44: C-scan report obtained with ultrasonic phased array method. The X coordinate is in accordance with Figure 3.43 for comparison.

also interesting to observe that the results show an increasing value of damage index according with the severity of damage where the disbonded area is accompanied by a skin-thickness reduction. The thickness variation causes a reduction of material acoustic impedance, increasing the mismatch of impedance already provided by the disbonding. Therefore, the method enables to accomplish a multi-level diagnostic system in which different functions of monitoring are implemented.

Summarizing the results which are reported in Table 3.6, the system is able to clearly detect a disbonding of 135mm with an uncertainty of 15mm provided by 7.5mm (half pitch) of uncertainty for both right and left sides. On the contrary, the NDE analysis returns a disbonding not greater than 135mm with 1mm of uncertainty. Furthermore, the system is able to localize the position of the damage, correctly identifying the tips of disbonding. Finally it is able to correctly localize the position and extension of the three different damaged area, named *partially disbonded* and *fully disbonded* re-

Inspection	Overall (mm)	A (mm)	B (mm)	C (mm)
SHM	135 ± 15	45 ± 15	60 ± 15	30 ± 15
NDE	135 ± 1	45 ± 1	60 ± 1	30 ± 1

Table 3.6: Damage assessment obtained with proposed SHM and classic ultrasonic NDE.

gion respectively in Figure 3.43. Also in this case the dimensions of the three regions assessed to be 45mm, 60mm and 30mm are quite close to that assessed via NDE unless the uncertainty that is much greater. About the latter aspect, it is envisioned that the accuracy of damage assessment can be improved enhancing the control points density on the scanning line. This could be carried out by reducing the distance between adjacent transducers and increasing the number of sensors. Nevertheless, in this case, additional weight and cost of the system have to be evaluated.

It is remarkable that baseline and current signals are acquired in the same time neglecting possibly different mechanical and bonding properties as well as position uncertainties. Two important conclusions can be pointed out considering that (i) environmental effects (neglected) are not affecting the damage assessment, and (ii) mechanical properties and installation uncertainties are affecting damage index. However, the results shown in Figure 3.43 demonstrate that effect of uncertainties on DI are not remarkable due to the much more increasing level with disbonding, ensuring robustness of the system while replacing sensors during lifetime. In addition, environmental aspects would not affect the detection except for small values of DI, which is not the actual case. Temperature effets, even neglected in this stage, can be instead addressed resorting to available strategies [111].

About system capabilities, the proposed local method can simultaneously monitor two adjacent and parallel stringers using different values of H. The latter demand is needed because a central pattern provides the overlap of the wave-packets reflected by scatterers making impossible to assess what stringer may be damaged. Changing the frequency according to H value, it is possible whether to focus the analysis of both stringers or to select a specific scanning line. In this way, it is possible to reduce the numer of sensors and related costs for analog to digital converters, signal processing and transducers. Furthermore, integrated solutions with layers containing array of sensors ready to be interrogated can be adopted due to simple and linear geometry needed [137]. Finally, this local approach is only needed where a comprehensive and detailed diagnosis is required, limiting a countless increase of sensors.

Ti conclude this discussion, it is worth noting that the propagation model is based on the assumption of uniform group velocity pattern. Even though this seems an hard assumption while dealing with composite materials (e.g. see results for unidirectional

composite laminate in Sec. 4.1.2), the lamination sequences adopted in real scale aircraft structures have not strict anisotropic properties, such as the structure under investigation and that considered in Sec. 4.2.1. That is the reason for which this approach is really well suited for aerospace composites. Furthermore such method, based on the aforementioned propagation model, does not need any theroretical or simulation modeling to be actuated on different materials. The velocity prediction needed to estimate the energy portion of the wave redirected by the stringer is indeed performed resorting to the direct propagation analysis preventing any complex aiding tool.

Chapter 4

Numerical approaches for GUWs propagation in structural health monitoring systems

Contents

From the results discussed in the previous chapter, the efficient damage detection obtained employing guided ultrasonic waves is quite clear and further promising due to the feasibility of its application. However, the complexities introduced by wave propagation, scattering and defect interaction make really challenging to deal with the measurements and sometimes experiments become also expensive and time consuming. As a matter of facts, many aspects should be accounted while dealing with Lamb waves starting from material dependencies. For this reason, the entire chapter is dedicated to numerical approaches used in combination with theoretical aspects to better understand the physics of wave propagation and support the development of the methodologies as well as their assessment.

In detail, a first section is dedicated to finite element (FE) modeling for guided

wave propagation with the aim to find an efficient approach among those available in commercial softwares. The attention is first given to the A_0 Lamb wave mode propagating in quasi-isotropic laminates which are widely adopted with the attempt to obtain an isotropic-like material with low coupling effects when loaded. The particular behavior of the antisymmetric mode is correctly intercepted resorting to simplified plate theories achieving the best compromise between efficiency and accuracy. Then the attention is moved on the possibility to reproduce the damage detection approach within simulated environment to support the development stage, whose results have been disclosed in the previous chapter demonstrating the remarkable support provided by numerical simulation to fix the paradigms of the MP^2 approach. A multi-side validation is proposed to verify the correct reproduction of the experimental conditions and a brief overview about further perspective based on model assisted investigation is finally provided.

4.1 GUWs propagating in composite laminates

Wave propagation in composite structures is more complex respect to the case of isotropic ones. The material inhomogeneity, the anisotropy and the multi-layered construction lead to the significant dependence of wave modes on laminate layup configurations, direction of wave propagation, frequency and interface conditions. In addition to the dispersive behaviour and quite complex interaction with discontinuities, such characteristics make prohibitive a comprehensive knowledge. Hence, theoretical investigations and numerical simulations targeted to study the guided waves behavior in the composite laminates are useful for supporting the experimental activities in order to better understand the physics of the phenomena involved. Theoretical aspects of wave propagation in plates have been presented by several authors [68, 83, 84, 85, 88, 86]. Analytically this problem can be studied through resolving equation of motion [138, 139, 140]. The exact solution of three-dimensional problems consisting of multilayered, angleply laminates of finite thickness and large lateral dimensions subjected to various types of surface loads are also available [141, 142] Approximate thin-plate theories have also been developed to obtain the analytical solutions for the response of thin isotropic and anisotropic plates to surface loads [143]. Nevertheless for complex structures this problem became analytically intractable. In such cases the most efficient way to investigate the problem deals with the modeling of the problem resorting to numerical schemes to solve its characteristic equations like in the case of finite element approaches, whose capabilities are depicted in the next section.

4.1.1 Finite elements approaches

The finite element method (FEM) is considered as one of the well-established and convenient techniques for computer approximate solution of complex problems in different fields of engineering. It is indeed a versatile tool to analyze this class of problems [144], where a comprehensive investigation including experimental and numerical (finite element) methods can be used to determine the interaction of ultrasonic guided waves with structures and discontinuities.

Generally, in an environment based on FE modeling, two different approaches can be adopted to investigate the propagation of guided waves in the laminate composite structures: (i) the equivalent single-layer approach (ESL), which treats the whole laminate as an equivalent homogenous plate, and (ii) the tridimensional approach (3D) that requires the modeling of each ply constituting the laminate. Due to the accuracy needed for simulation of wave propagation in laminated composites, numerical researches mostly focused on 3D finite element models [145]. In a 3D approach each layer is discretized using brick-type elements. This technique is indicated especially when transverse shear deformation effect is not negligible, because it can predict accurately local effects. Using this approach Zhao et al. [146] verified the dispersion results by the finite element method and studied the directivity characteristics of Lamb waves numerically in laminates. However 3D approach introduces a number of degree of freedoms (DOFs) that depends even on the number of layers constituting the laminate. Furthermore dynamic explicit analysis to simulate wave propagation requires great attention in spatial and temporal discretization. In order to have a good resolution of the captured waves, element dimension should be very small compared to the minimum wavelength and the time step used to integrate the dynamic equations must be smaller than the time that the dilatation wave takes to cross a single element. Thus the numerical problem quickly becomes too expensive. To improve computational efficiency, ESL approach is very useful to obtain solutions of Lamb waves in composites. The ESL plate theories are derived by making suitable assumptions about the displacement through the thickness of the laminate [147]. The composite stack is represented as a single layer, whose stiffness properties are "equivalent" to the multilayered structure. The number of DOFs is thus independent from the number of layers constituting the laminate. Furthermore ESL description is easily embedded into standard element formulations by simply declaring a composite cross-section. Thus a good compromise between efficiency and accuracy is often reached.

Among those approaches, classical laminated plate theory (CLPT) is the simplest one where the shear deformation effects are neglected according to Love-Kirchhoff plate theory extended to laminates. However, due to their low transverse shear stiffness, composite laminates often exhibit significant transverse shear deformation. As a

consequence, CLPT is not always able to predict guided waves propagation characteristics when wavelength is near the laminate thickness [148]. Prosser investigated the propagation of plate waves in several graphite/epoxy composite laminates of different ply layups [149]. Comparison of the measured flexural dispersion with theoretical predictions based on CLPT showed indeed a lack of agreement. He determined that the effects of shear deformation and rotatory inertia, neglected in CLPT, are the cause for such discrepancy. Therefore, CLPT is only valid when the wavelength is much greater than the plate thickness (very low ultrasounds).

Unlike CLPT, the first shear deformation theory (FSDT), based on Reissner–Mindlin displacement fields [150], includes transverse shear deformation and rotary inertia. However, the theory is developed on the assumption of constant transverse shear7strain through the thickness and this simplification does not satisfy the boundary conditions at the lower and upper surfaces of the plate. In addition, the distribution of transverse shear stresses in a layered cross section is non-uniform and the transverse shear strains are distributed nonuniformly as well. Therefore it is necessary to smooth this contradiction introducing a shear correction factor (SCF) to match the effect of such constant distribution with that introduced in the reality. Thus an additional effort to obtain SCFs is also required when this approximate plate theory is used. Furthermore, even though is well suited for the simulation of the antisymmetric mode [93], FSDT cannot describe accurately higher modes of wave propagation [151, 152]. Finally, the combination of shell elements and ESL theory cannot be used to simulate the symmetric wave mode characterized by the thickness bulging and contracting. In the latter case, three-dimensional modeling is mandatory [94].

In order to overcome the problem of SCF evaluation, many researchers implemented improved FSDTs or higher-order shear deformation theories (HSDT) in which higher expansion of displacement field along the laminate thickness is considered [153, 154, 155, 156, 157]. Unlike the above mentioned work which do not deal with wave propagation, in [158] the authors implemented second and third order theories in order to predict symmetric and antisymmetric lamb wave modes respectively, obtaining a good agreement with 3D-Elasticity theory. Zhao et Al. calculated dispersive curves of Lamb waves with a third order plate theory that respects the stress free boundary condition obtaining results close to exact solutions [159]. However, it is worth noting that using higher order plate theories complicates the equations and reduce the benefits when compared with 3D theories. Furthermore in commercial FEA codes, HSDT theories are never implemented, limiting their use to very simple cases.

An investigation of different finite element models with explicit dynamic analysis for Lamb wave simulation in isotropic plate and quasi-isotropic laminated composite is presented in [160]. They considered two kinds of FE models using different 3-D

ρ [kg/m^3]	E_1 [MPa]	$E_2 = E_3$ [MPa]	$G_{12} = G_{13}$ [MPa]	G_{23} [MPa]	$\nu_{12} = \nu_{13}$	ν_{23}
1520	175000	6900	4970	2374	0.2542	0.4689

Table 4.1: Elastic properties of *graphite-epoxy* lamina.

Stacking sequence	Dimensions
$[0°]_s$	600x600x3.2 [mm^3]
$[\pm 45°/0°/90°]_s$	600x600x1.6 [mm^3]
$[\pm 45°/0°/90°/90°/0°/\pm 45°]$	600x600x1.6 [mm^3]

Table 4.2: Properties of laminates.

finite elements: (i)continuum elements (3D-solid brick type element) and (ii) structural elements (3D shell element). Nevertheless for the former, the effective material properties of the whole composite plate are considered, resulting in an isotropic- like plate rather than a multilayered laminate. For the latter, based on ESL (FSDT) approach, the problem of transverse shear is not considered and addressed. However, from the following investigation focused on the modeling of the first antisymmetric Lamb waves mode (A_0), this aspect appears really crucial to correctly intercept its dispersive behavior. Numerical (FEM) and experimental analysis are carried out using both 3D and ESL approaches and employing ABAQUS/Explicit® FEM Code. The main goal of the first investigation is to establish the validity of using the FE method based on approximate first order plate theory to represent the physic of guided wave propagation as a first step towards a simulated damage detection system.

4.1.2 Experimental observation

The first part of the investigation consists of several measurements carried out to characterize the dispersive behavior of A_0 mode propagating in composite laminates analyzing three different cases: (i) unidirectional plate, (ii) quasi isotropic plate with symmetric and (iii) non-symmetric stacking sequence. The panels are made of carbon-epoxy unidirectional lamina whose mechanical properties have been obtained through mechanical tests and reported in Table 4.1. Property of plates are shown in Table 4.2, where it is evident that the non-symmetric plate is equal to the symmetric plate unless the last two wrapped plies.

The measurements are performed exciting and sensing the waves using 10mm diameter and 0.25mm thickness PZT disks made of PIC-255 soft material by *Physik Instrumente* (PI) and bonded to the surface of the plates with cyanoacrylate glue.

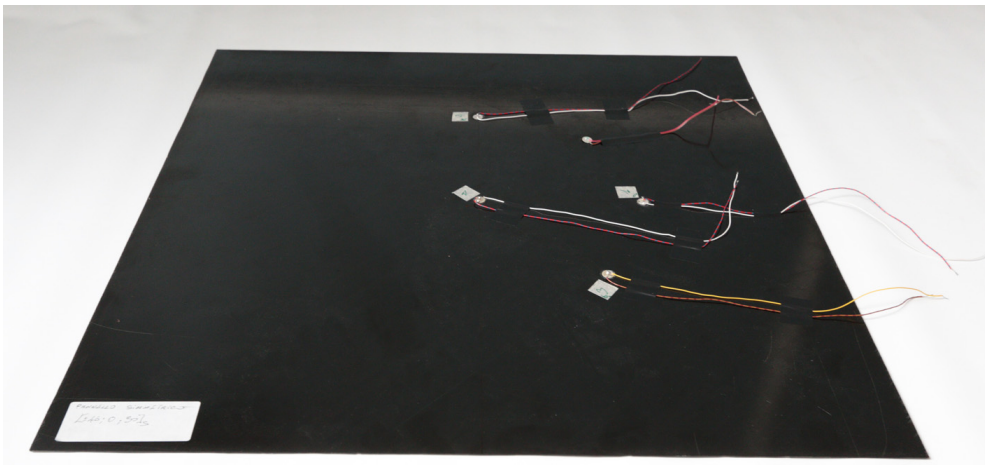

Figure 4.1: Experimental setup. Instrumented carbon/epoxy panel with bonded PZTs.

The pitch-catch approach is used to obtain the data exciting a burst signal as that used to interrogate the structure. To characterize the propagation behaviour in several directions, the actuator is located at the center of the plate and the sensors are bonded along the characteristic directions of the plate at a fixed distance as depicted in Figure 4.1 The excitation signal is generated as a voltage signal by a waveform generator HP/Agilent 33120A, amplified and applied to the transducer, where it is converted into deformation. The vibration imposed by the actuator travels in the structure with a wave front that depends mostly on the mechanical properties along the propagation directions. Once the sensors turn the mechanical vibrations imposed by plate in electrical signals, the acquisition is performed by using an oscilloscope Agilent InfiniiVision DSO7104A. To minimize dispersive effects distorting the waveform, a low leakage excitation is used again, as described in Sec. 2.3.2. When voltage is applied to the piezoelectric transducer with a frequency below the cutoff frequency only A_0 and S_0 are energized and their time of flight can be calculated performing signal processing according to Sec. 2.3.3. In this way the velocity of the wave in several direction can be plotted as a function of frequency (dispersion curves) or orientation (polar pattern).

Tests on several plates are carried out in the frequency range from 10kHz to 300kHz to define the dispersive wave modes A_0 and S_0. However, due to the crucial application of the former mode for damage detection, the relative results obtained up to $70 - 80kHz$ are only discussed hereinafter. As disclosed in Sec. 2.3.1, it is indeed possible to excite the different modes separately by simply tuning the frequency. Dispersion curves obtained by experimental tests on unidirectional plate are shown in Figure 4.2. Tests on unidirectional plate involved frequencies from 10kHz to 60kHz, with step of

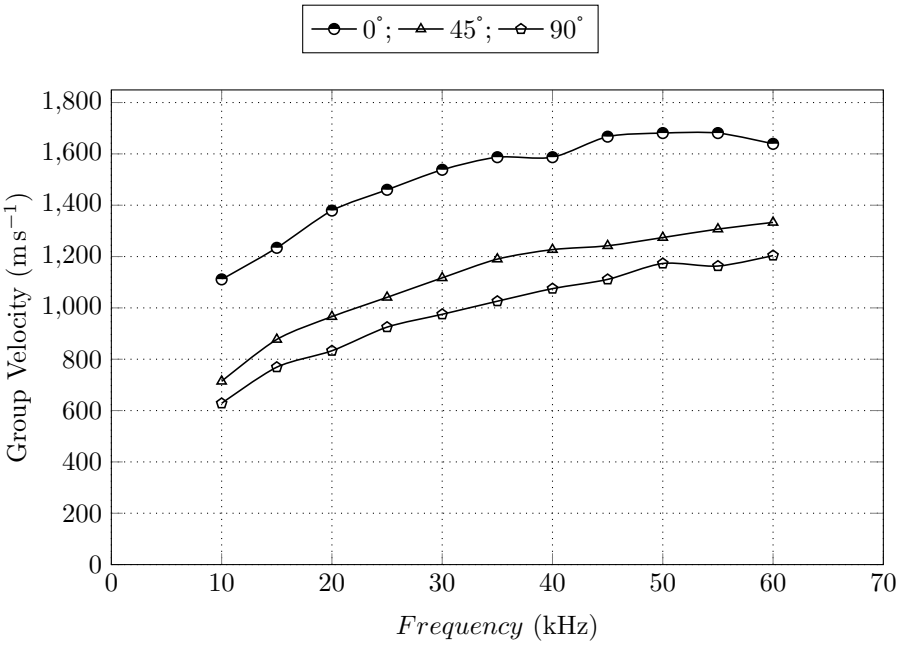

Figure 4.2: Experimental group velocities ontained on UD plate in several direction of propagation

5kHz. Amplitudes of A_0 mode are evaluated from output signals registered through PWASs and then processed in time domain using cross correlation approach with Hilbert transform (see Sec. 2.3.3). Results show the presence of a direction along which the A_0 *Lamb wave* mode propagates faster. This effect is due to the fact that the velocity of waves propagating in the structures is directly dependent on the stiffness of the media. Due to the anisotropy of composite laminae, the direction of fiber reinforces (0°) of an unidirectional plate is associated with a much greater stiffness. As a consequence, contrary to what happens in a isotropic material, Lamb waves propagation in composites depends strongly on direction of propagation. Polar diagram in Figure 4.3, obtained with spline interpolation of experimental data, shows the polar pattern of group velocity at a work frequency of 40kHz and it highlights the greatest A_0 mode velocity along fiber direction (0°) indicating that this lowest order mode behaves quite distinctly in different propagation directions with regard to the 0° fibre.

Such a mechanism is very important while dealing with Lamb waves in composite structures. Even though is less evident, while considering quasi isotropic structures the discrepancy along several directions may remain as demonstrated by measurements performed on the both pates. Dispersion curves obtained by experimental tests on quasi-isotropic plate are shown in Figure 4.4. Tests on symmetric quasi-isotropic plate

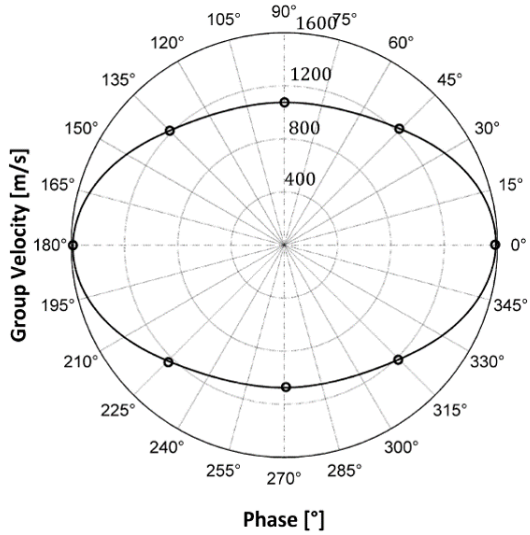

Figure 4.3: Polar pattern of A_0 mode propagating in unidirectional plate: frequency 50kHz. Markers depict experimental outcomes.

involve frequencies from 10kHz to 70kHz with 10kHz step. The results obtained with the same aforementioned procedure show the presence of a direction around 45° along which the A_0 mode propagates faster. Otherwise, the nonsymmetric panel exhibits two directions (±45°) with a greater propagation velocity, as demonstrated by dispersion curves depicted in Figure 4.5 and obtained by experimental tests on quasi-isotropic plate involving frequencies from 10kHz to 80kHz with 10kHz step. As a consequence, contrary to what happens in a isotropic material, Lamb waves propagation depends on direction of propagation also in quasi-isotropic composite laminates. Polar Diagrams in Figure 4.6 show the polar group velocities at different frequencies, evidencing the greater propagation velocity along 45° direction. However, by comparing this polar trend with that obtained for unidirectional plate, the radial variation appears less evident.

The problem can be more specifically addressed resorting to the classical lamination plate theory, whose mathematical formulation for predicting the macromechanic behavior of a laminate is based on an arbitrary assembly of homogenous orthotropic laminae which leads to the ABD matrix definition. It indeed directly relates the forces and moments for unit width, $\{N\}$ and $\{M\}$, respectively, to the midplane strains $\{\epsilon\}$ and curvatures $\{\kappa\}$:

$$\begin{Bmatrix} \{N\} \\ \{M\} \end{Bmatrix} = \begin{bmatrix} [A] & [B] \\ [B] & [D] \end{bmatrix} \begin{Bmatrix} \{\epsilon\} \\ \{\kappa\} \end{Bmatrix} \tag{4.1}$$

Even though the in-plane extensional stiffness $[N]$ of a quasi-isotropic plate is not

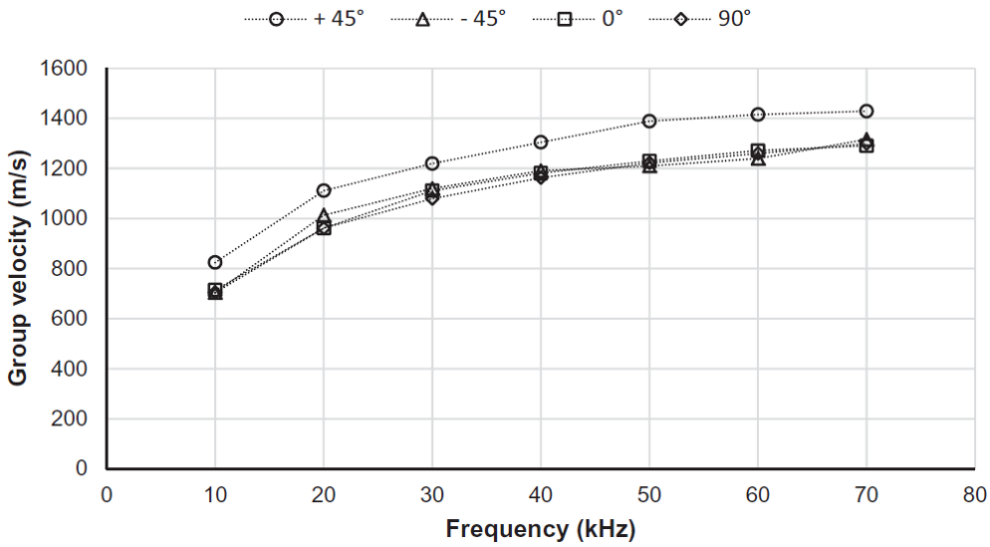

Figure 4.4: Experimental dispersion curves of the A_0 mode for symmetric quasi-isotropic plate.

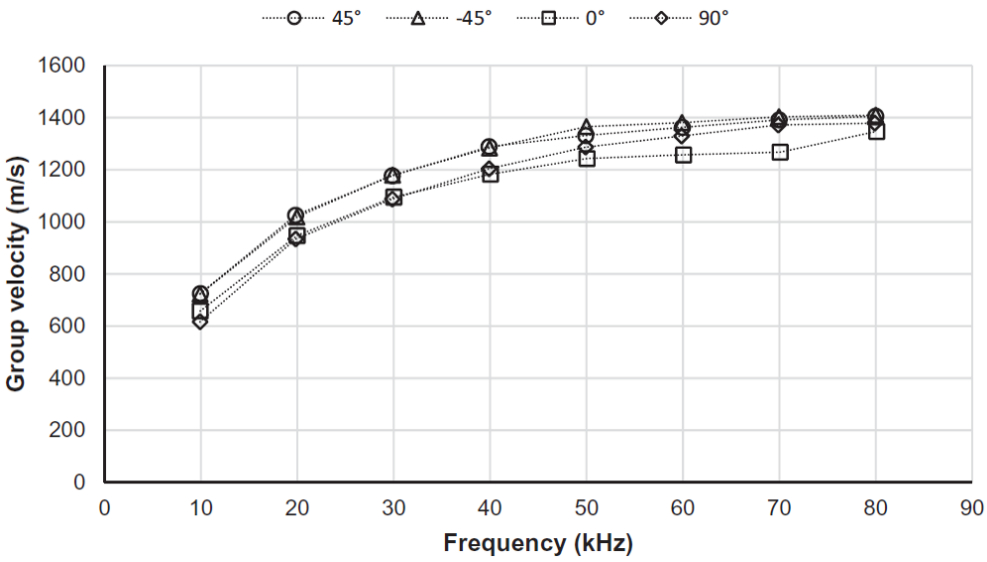

Figure 4.5: Experimental dispersion curves of the A_0 mode for nonsymmetric quasi-isotropic plate.

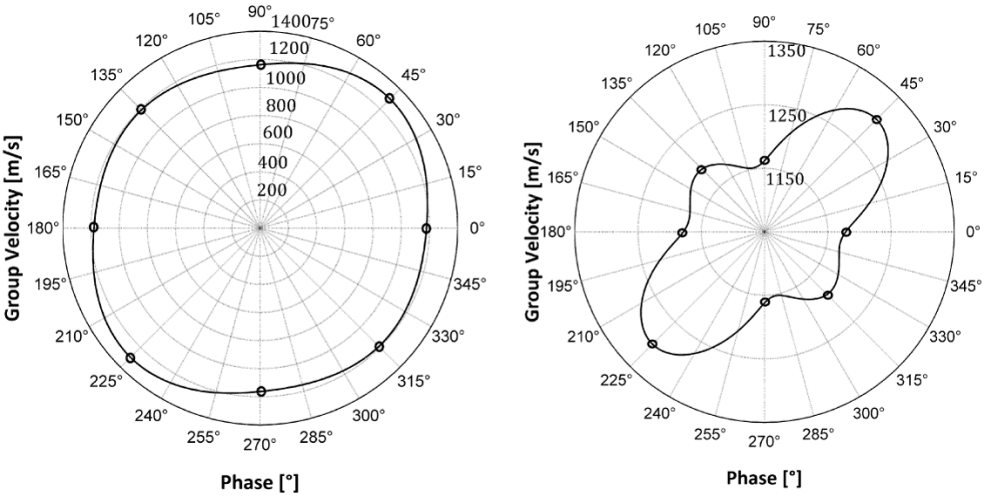

Figure 4.6: A_0 mode propagating in symmetric quasi-isotropic plate at 40kHz: polar pattern (left) and radial variation (right). Markers depict experimental outcomes.

changing while varying the direction, there is a stacking effect on bending stiffness due to the anisotropy of the composite laminae; i.e. its apparent laminate stiffness properties are dependent on stacking sequence. Since its formulation in accordance with the classical laminated plate theory, flexural stiffness varies in radial directions due to orientation and stacking sequence of laminate. The generic term of Flexural stiffness matrix D_ij is defined as

$$D_{ij} = \frac{1}{3}\sum_{k=1}^{N} \bar{Q}_{ij}^{(k)}(z_{k+1}^3 - z_k^3) \tag{4.2}$$

where N is the number of plies, $\bar{Q}_{ij}^{(k)}$ is the generic term of $\sigma - \epsilon$ relation of *k-th* ply under in-plane rotation and z_k is the distance between *k-th* ply and neutral plane of laminate. The radial variation of D_{11} of quasi-isotropic laminates is shown in a polar diagram (Figure 4.7), where is evident its greatest amplitude around 45° direction. Comparing the result obtained here in term of D_{11} for the symmetric plate with the radial pattern of group velocity enlarged in Figure 4.6 (b), it is quite clear the relation between flexural stiffness and radial variation of group velocity. The same conclusion can be carried out for the nonsymmetric panel, where the inversion of the external plies returns the same flexural stiffness considering ±45° directions, namely the directions associated with higher velocity of A_0 mode (see Figure 4.5). Therefore, radial flexural stiffness variations due to stacking sequence effects in continuous quasi-isotropic laminates are significant. It is worth noting that due to the third order dependence of flexural stiffness, this effect is usually much more evident in those

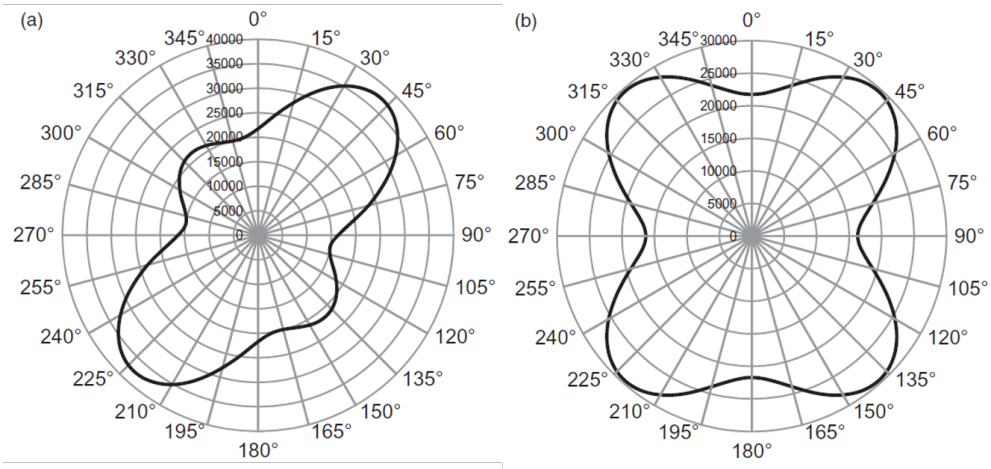

Figure 4.7: Stiffness polar diagramm for symmetric (a) and nonsymmetric (b) quasi-isotropic plate

directions associated with reinforcements of external plies.

The investigation of the S_0 mode, discussed in [94] and not reported here for the sake of the conciseness, leads to completely different remarks. The outcomes on quasi-isotropic plates do not allow to significantly identify one or more directions along which the wave mode propagates faster. As expected, the previous conclusion concerning the bending stiffness for the A_0 mode cannot be asserted when a symmetric mode is considered. Given the quasi-isotropic nature of the laminate, the change in velocity with the considered direction is not appreciable. Therefore, only the flexural modes are strongly affected by the flexural stiffness of the plate. Otherwise, symmetric modes, which are characterized by a primary extensional motion of the particles, appear to be indeed not affected.

Two considerations can be remarked from such results: (i) a detailed material characterization is desirable even when a quasi-isotropic composite plate is considered and (ii) the numerical approach used to simulate guided waves propagation must be able to intercept the dispersive behaviour along characteristic directions to be appropriate for modeling stage. About the first item, it worth noting that such characterization including dispersive and tuning analysis is suited for discovering the behaviour of the selected interrogation mode for structural health monitoring. That is mostly the reason for which it is proposed as preliminary analysis tool in the MP^2 modular software in Sec. 3.1.3. About the latter demand, a simplified numerical modeling is presented in the next section considering its capability to correctly intercept the dispersive behaviour of A_0 mode as accuracy criterion.

4.1.3 Simplified ESL modeling

In this section transient finite element analysis of wave propagation in ABAQUS® environment is presented. Explicit dynamic procedure is used to solve the problem of wave propagation due to the computational benefits for this type of transient problems. The complete elastic wave propagation in the plate is simulated in order to compare the results with measurements outcomes. To achieve a comprehensive overview, the approaches based on CLPT, FSDT and 3D are employed. Hence, plates are first discretized as a single equivalent layer, assuming both CLPT and FSDT displacement theories, and then as multilayered laminates considering 3D elements to idealize every lamina. To consider 3D approach, $C3D8R$ element (an 8-node linear brick, reduced integration, hourglass control element) is used to discretize each layer according to the material orientation (fiber direction). One element along each lamina thickness is employed to reduce the shape factor effects on wave propagation. Instead, to consider CLPT and FSDT theories, $S4R$ element (a 4-node, reduced integration, hourglass control finite element) is adopted to idealize the structure. Relatively large transverse shear stiffnesses are introduced to simulate the infinite transverse stiffness expected with classical lamination plate theory. Otherwise, to consider FSDT theory, the crucial aspect is to define the appropriate shear correction factor (SCF). From energy assumptions, in isotropic plates it is possible to define easily the SCF value $\frac{5}{6}$, due to the continuum transverse shear quadratic distribution along the thickness. In multilayered sections, the real issue is the dependence of SCF by lamination, geometric parameters, but also on the loading and boundary conditions. Unfortunately the exact values of SCF are well known a priori only for few cases [161]. To predict SCF values Burton and Noor [162] and Sze et al. [163] found a solution in the development of iterative predictor–corrector techniques in which value $\frac{5}{6}$ is often used as a starting value in iterative processes. Many approaches for obtaining the SCF in composite laminates are based on matching characteristics obtained by the first order theory with those obtained from the three-dimensional elasticity theory or experimental ones. The characteristics used for the matching include the transverse shear strain energy, the propagation velocity of a flexural wave, the natural frequency of the thickness shear vibration mode or the cut-off frequency of wave modes [164, 165, 166, 167, 168]. A general derivation and interpretation of SCFs independent by loads and boundary conditions can be derived by matching the shear stress resultants and shear strain energy of a layerwise higher-order shear theory with those of the equivalent first-order shear theory [169]. Other formulations of SCFs are available in [170, 171, 172], where values close to $\frac{5}{6}$ are obtained for orthotropic laminates with a large number of plies.

In order to consider FSDT in Abaqus, $S4R$ element is employed introducing transverse shear stiffnesses in the shell section definition. They are evaluated considering

the FSDT theory and using a shear correction factor obtained according to the procedure proposed in [172] and based on what is theorized in [171]. As expected for a quasi-isotropic plate, a value of $\frac{5}{6}$ is calculated, which is very close with the other obtained values of 0.802 [161] and $\frac{\pi}{12}$ [168].

In order to appropriately simulate the propagation up to 80kHz carrier frequency, a 1mm$\times$1mm mesh is adopted. To correctly catch the waveform, spatial discretization must be indeed opportunely chosen as follows:

$$d_{el} \leq \frac{\lambda_{min}}{(10-20)} \tag{4.3}$$

where λ_{min} is the minimum wavelength and d_{el} is the element dimension in the direction of propagation considered. For A_0 mode λ_{min} occurs at maximum work frequency due to the monotonically increasing velocity. Due to the in plane geometric definition of elements (quadrilateral), dimension considered to satisfy the Eq. (4.3) is the along diagonal (maximum) dimension. Another important aspect of numerical simulation is how modeling PZT sensors. They turn the electrical field in deformation field, imposing a vibration in plate and they have indeed relatively small dimensions respect to plates. For such reasons, PZT sensors are discretized as single nodes (namely the disk center) and (i) on the actuator is imposed an out of plane displacement employing the same waveform of electrical signal considered in experiments while (ii) the out of plane displacements is extracted during time integration at sensing nodes (namely the disk center) to evaluate the arrival time in several directions. In this way only the A_0 mode is primarily excited and sensed in the range from 10kHz to 80kHz. As made for processing experimental results, time of flight is always calculated using cross-correlation technique and employing Hilbert transform to determine the envelope of cross-correlated signal.

For the sake of the conciseness, the results obtained for the symmetric quasi isotropic plate are discussed hereinafter making possible to generalize the conclusions because confirmed by other test cases. Considering CLPT, based on Kirchhoff displacement field, transverse shear deformation is neglected and there is a great lack of agreement comparing numerical and experimental results. The former outcomes indeed overestimate the group velocity in the whole frequency range analyzed as depicted in Figure 4.8. On the contrary, FSDT (shell elements with specified transverse shear stiffness) and 3D approach (brick elements) return results in agreement with the experiments.

To detail the reasonable response obtained while modeling with FSDT based FE approach, the comparison of numerical and experimental dispersion curves is reported for all investigated directions from Figure 4.9 to Figure 4.12. The modified Mindlin

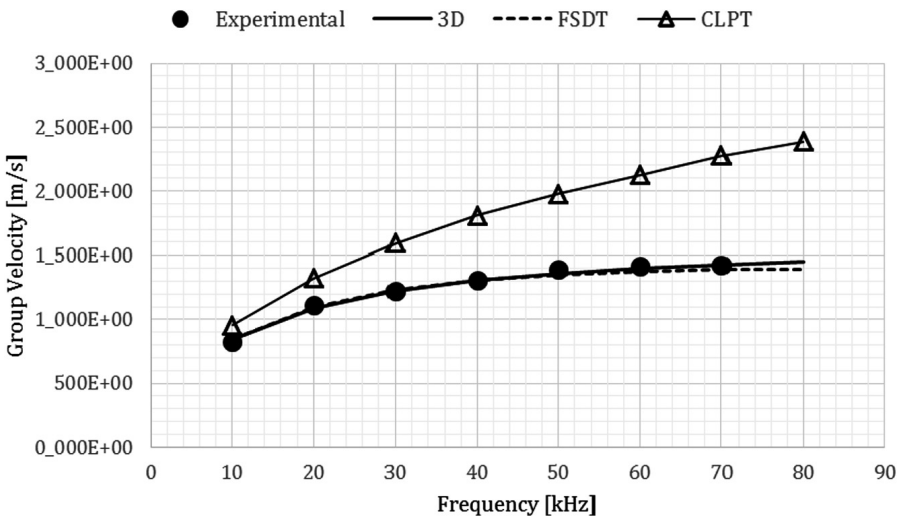

Figure 4.8: Dispersive curves of A_0 mode propagating in symmetric quasi isotropic panel along $+45°$ direction. Comparison of several numerical approaches with measurements.

	$3D$				$FSDT$			
θ	$+45°$	$-45°$	$0°$	$90°$	$+45°$	$-45°$	$0°$	$90°$
$\epsilon_{\%}$	3.2	3.5	4.7	2.6	3.2	5	7.9	1.7
Freq.	50	40	60	30	50	50	50	60

Table 4.3: Percentage error of numerical group velocities on quasi isotropic plate respect to experimental ones.

plate theory for laminated structure accurately predicts the lowest anti-symmetric wave mode in the whole frequency range correctly detecting the presence of a faster propagation direction as well. The agreement obtained also for the other panels demonstrates that the shear correction employed is generally adequate for simulation and few discrepancies can be found with respect to the 3D approach, as demonstrated by the percentage error obtained in numerical testing respect to experimental results reported in Table 4.3 for the symmetric quasi-isotropic plate. Finally it should be emphasized that using the same in plane size of the elements, the ESL approach with FSDT formulation improves computational efficiency compared to brick modeling which is more expensive given the greatest number of nodes: 825s are required instead of 14325s for running one process.

Thus, it is worth noting that the first-order shear deformation theories provide a higher computational efficiency at the cost of a slightly reduced accuracy for the global structural behavior in antysimmetric wave propagation problems. Furthermore, to correctly address the shear effects is simpler while increasing the number of plies with

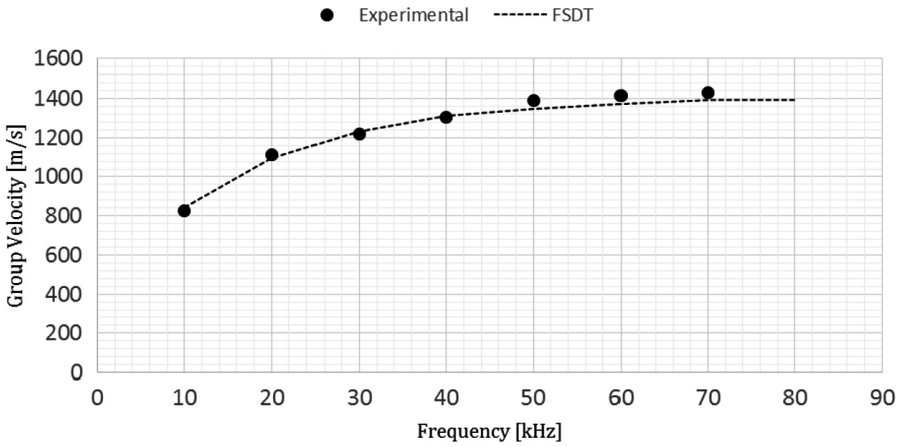

Figure 4.9: Dispersive curves of A_0 mode propagating in symmetric quasi isotropic panel along $+45°$ direction: numerical FSDT and experimental comparison.

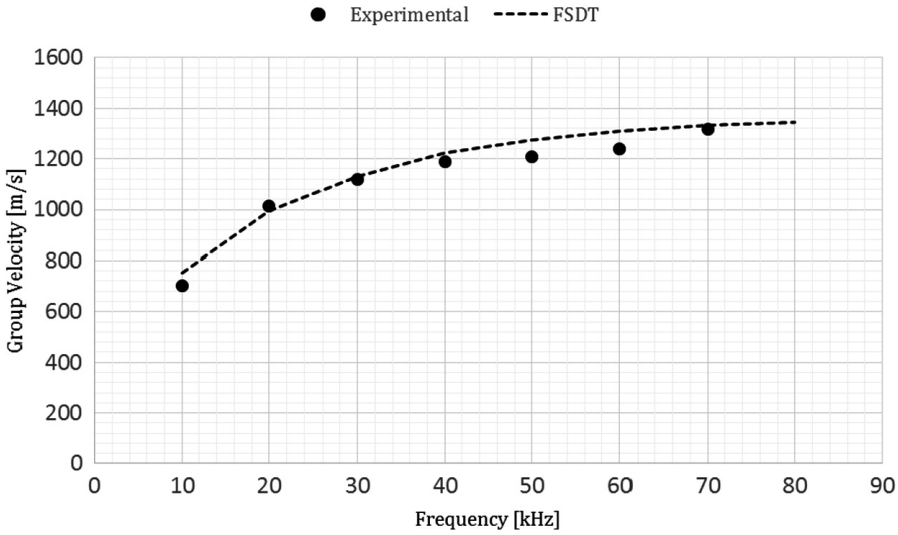

Figure 4.10: Dispersive curves of A_0 mode propagating in symmetric quasi isotropic panel along $-45°$ direction: numerical FSDT and experimental comparison.

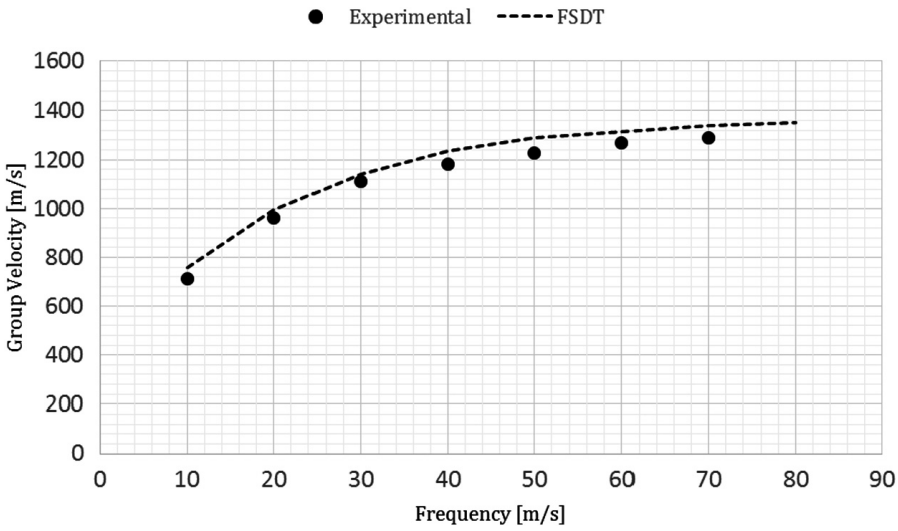

Figure 4.11: Dispersive curves of A_0 mode propagating in symmetric quasi isotropic panel along 0° direction: numerical FSDT and experimental comparison.

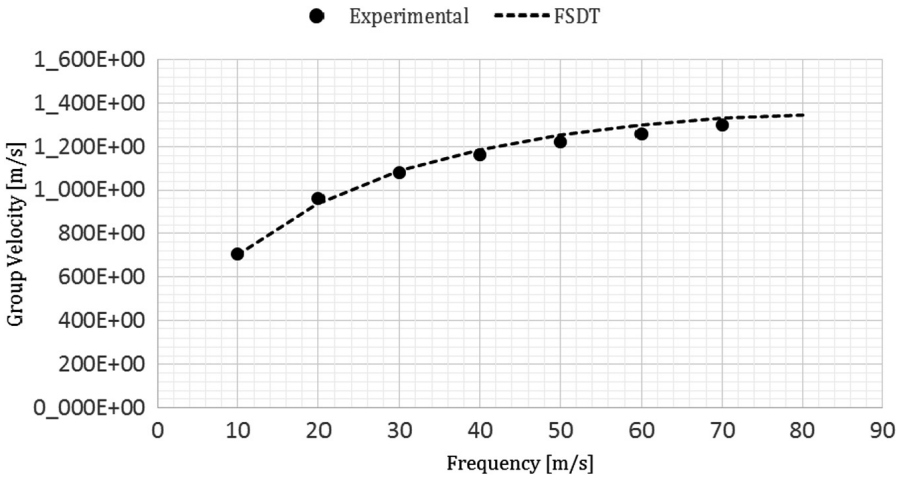

Figure 4.12: Dispersive curves of A_0 mode propagating in symmetric quasi isotropic panel along 90° direction: numerical FSDT and experimental comparison.

multiple orientations. For these reasons this approach is proposed in the next section for the multi-side validation of a model assisted damage detection system

4.2 Multi-side validation for global damage detection

Damage detection using GUWs is really promising but the complexities involved during ultrasonic measurements cannot be faced without resort to theoretical aspects and modeling. In this context the introduction of simulations can aid the research and development because they are suited to:

- remove uncertainties related to measurements which prevent to clarify methodology criticalities (consider the case of phantom damage or dispersion effect on ToF analysis);
- introduce parametric investigations which cannot be experimentally conducted (i.e. effects of location, dimension and severity of damage);
- set new strategies based on the system characteristics revealed by simulations;
- reduce costs and time of experimental campaigns;
- quantify the performances of the system under variable conditions.

However to fulfill the whole range of aiding purpose while dealing with simulated environments for GUWs-based SHM implementation and verification, it is desirable to have:

- a reasonable propagation simulation of the selected Lamb wave mode;
- a damage interaction simulation in line with experiments while oriented to similar flaw identification (i.e. reasonable results in terms of DI);
- a rigorous replication of the operating environment in which the structure is monitored.

Such requirements define the multi-side validation required to release an effective and efficient modeling environment suited for reproducing the experiment peculiarities and to improve the methodologies.

With regards to the global SHM approach using direct propagating waves, the first requirement can be verified through a wave field analysis in order to intercept the correct behavior of A_0 mode propagating in the structure, such as the characterization proposed in Sec. 4.1 based on considering dispersive and pattern behaviour as comparative items and verification criteria. The second condition implies that the damage

has to be appropriately simulated looking at: (i) the conformation of damage induced by impact on the structure and (ii) the sensitivity to damage dimension in terms of extracted features.

Regardless the former aspects, investigated in detail in the following sections, the third requirement is crucial for the reproducibility of the damage detection system within simulated environments. Although the proposed global SHM approach leads to a reliable identification, measurements carried out both on the undamaged and damaged structures show that the same structural configuration interrogated at different times returns non zero values of damage indicators. The noise in the signal response does not allow to clearly distinguish between noisy and significant response. As a consequence, it happens that some paths that are indeed affected by the damage do not show a response suggesting the presence of such damage. Moreover, in such cases the change in signal response can be relevant even if no changes occur. In the first case, the decision-making strategy leads to a non-correct censure of the signal response. Instead, a false alarm occurs in the second case. From a practical point of view, the operating environment in which the structure is monitored may be very variable and it appears to be very difficult to keep repeatability at small values. Slightly different measurement conditions could lead to significant changes in the signal response with a misinterpretation of results. From the experimental standpoint, these events can be analyzed using a statistical approach, namely the decision making framework to select the paths indeed affected by the damage. Instead, when a simulated environment is considered, no such variations can be appreciated due to repeatability and reproducibility of the simulations. Indeed, the SHM algorithm should be able to gather correct information in each type of monitoring condition, and a correct model assisted analysis should take in consideration this aspect.

To account for the uncertainties of environmental conditions, two different strategies can be followed:

- introduce appropriate variability in the source model achieving a multiple dataset by multiple simulations;
- introduce appropriate variability in the output of a single simulated interrogation;

For saving time considerably, the second approach is pursued and the generic recorded signal $s(t)$ is modeled as filtered Gaussian white noise adding white Gaussian noise $\eta(t)$ to the simulated time history:

$$y(t) = s(t) + \eta(t) \tag{4.4}$$

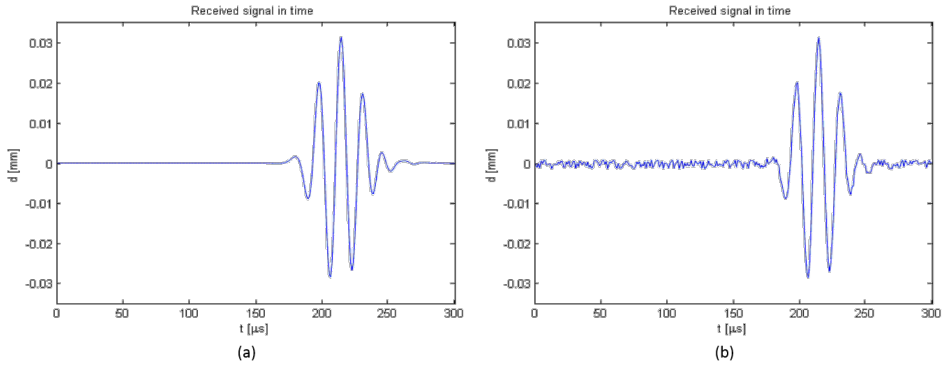

Figure 4.13: Numerical time histories of A_0 mode without (a) and with (b) added noise.

The pseudo experimental data generation is focused on the energy of the captured signal. The random noise $\eta(t)$ is added looking for the same sensitivity index. According to the decision-making procedure, once the system noise is characterized in term of mean and variance of the normal distribution fitted on that index, random numbers are generated to obtain the same variability with the same number of samples and the simulated experimental noise is added with numerical signals. An example of the effect of noise introduction is showed in Figure 4.13. In this way, different simulated *measurements* are obtained for each couple of PZTs and for each structural condition, as in the experimental case. Then the making decision procedure can be employed as well as after a measurement stage.

About the other validation items, generally, in addition to their inherent simplicity and low computational cost, ESL models often provide a sufficiently accurate description of global response for thin and moderately thick laminates. Among these theories, the FSDT provides the best compromise between solution accuracy, economy and simplicity, as demonstrated in Sec. 4.1. However, the ESL models have limitations that prevent them from being used to solve the whole spectrum of composite laminate problems:

- the accuracy of the global response predicted by the ESL models deteriorates as the laminate becomes thicker;
- the ESL models are often incapable of accurately describing the state of stress and strain at the ply level near geometric and material discontinuities or near regions of intense loading (which are the areas where accurate evaluations are mostly needed).

In the next sections the other numerical aspects are explained in detail looking at verify the aforementioned conditions to avoid any lack of agreement with measurements.

Stacking sequence	Dimensions
$[5H/B45/U/B/U/B45/U/B]_s$	$600 \times 600 \times 1.6[\text{mm}^3]$

Table 4.4: Lamination sequence of the 6mm-thick bay of the tapered wing panel presented in Sec. 3.1.2.

Properties	Biaxial	Uniaxial	5Harness
ρ [kg/m^3]	1790	1790	1770
E_1 [MPa]	81000	152000	158420
$E_2 = E_3$ [MPa]	8800	8800	8800
$G_{12} = G_{13} = G_{23}$ [MPa]	4100	4100	3600
$\nu_{12} = \nu_{13} = \nu_{23}$	0.31	0.31	0.31

Table 4.5: Elastic properties of *graphite-epoxy* laminae adopted for the 6mm-thick bay of the tapered wing panel presented in Sec. 3.1.2.

4.2.1 Wavefield simulation

The 6mm-thick bay of the tapered wing panel presented in Sec. 3.1.2 is discretized resorting to a 600mm × 600mm × 6mm layered composite plate on which 12 PZT transducers are mounted and arranged in a circular network. The plate is laminated using unidirectional laminae with fibers along 0° (UD) and biaxial laminae with orientation 0°/90° (B) and ±45° (B45) which are stacked between $5Harness$ (5H) external plies according to Table 4.4. The plies are discretized as single layers modeling the material properties reported in Table 4.5 and material orientation according to the stacking sequence. The behavior of laminates respect to the wave propagation shows many complexities. From a practical point of view, propagating waves result in signals acquired through an array of sensors distributed over a structure. They are indeed affected by the material characteristics, including the level of anisotropy, the layered stacking through the thickness and geometric discontinuities (such as thickness variation), frequency of excitation and boundaries, generating scattering, diffraction and reflection of the waves. A congruent request is that the numerical modeling assumptions allow to respect the discussed dependencies. According to the characterization carried out in Sec. 4.1, the dispersive behavior is indeed a key validation tool if the direct waves are considered for damage detection.

The ESL approach is here again adopted for transient finite element analysis of wave propagation. The ABAQUS/Explicit® code is used to integrate the dynamic problem to evaluate the group velocity of the first antisymmetric Lamb wave mode in order to compare the observed response with the calculated one. In detail, the

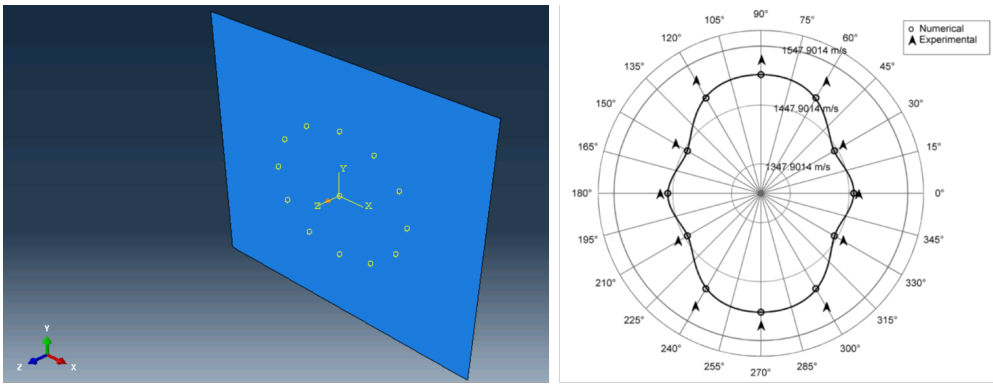

Figure 4.14: Overall scheme adopted in the simulation environment for the arrival time correlation (a) and group velocity comparison along several directions at 60kHz (b). Maximum percentage error, 5%.

FSDT is used to idealize the structure with an equivalent layer. To this purpose, the $S4R$ element available in the ABAQUS/Explicit® is adopted again correcting the transverse shear inconsistency of FSDT introducing an SCF equal to $\frac{5}{6}$, according to the evidence shown in [170, 171, 172] when a large number of plies are considered. About the plate idealization, the mesh density is chosen to be sufficiently small to resolve the characteristic wavelength and correctly capture the desired 60kHz wavefield (i.e.: the interrogation frequency) response resulting in a 1mm×1mm mesh. All sensors are discretized as single nodes because they have very small size when compared to the distance between sensors, and their local effect on the global wavefield behavior can be neglected. The central PZT actuator is constrained with an out of plane displacement using a windwed 4.5 cycles sine burst in time domain. The out of plane displacements in the 12 PZT receivers located on the circular pattern (ϕ = 300mm) is registered to evaluate the arrival time in several directions, as depicted in Figure 4.14 (a). The STFT method is adopted to calculate the arrival time and thus group velocity, whose comparison with measurement outcomes in Figure 4.14 (b) highlights the reasonable result obtained. Indeed, the maximum percentage error of 5% is obtained.

Again the FSDT-based ESL approach, with which the laminate is idealized as a single layer with the same stiffness properties of the pristine structure, provides a good balance between computational efficiency and accuracy for the global structural behavior in wave propagation problems if the transverse shear effects are correctly addressed. Then, the final crucial aspect deals with the damage idealization, as explained in the next section.

4.2.2 Damage modeling

It is worth noting that the modeling stage for monitoring purpose needs the prediction of the wave-damage interaction, whose characteristics depend upon the idealization approach as well. Obviously, the unknown nature of the hidden flaw requires a comprehensive analysis of the specific type of damage in the reality. In the case of impact induced damage, it is very difficult to imagine the material degradation when a barely visible damage (BVID) appears. From a theoretical standpoint, it can be seen as a complex discontinuity through the thickness. By definition, a discontinuity in a waveguide is an abrupt change of the guide's characteristics along its propagation direction. Composite panels can be characterized by the presence of inner discontinuities related to the local change of cross-section along the panel length. As aforementioned, at these discontinuities are called "delaminations" to indicate the separation between plies in a composite laminated panel. However the induced damage is not simply a unique separation between adjacent layers. In order to understand what really happens within the multilayered plate due to the impact load, a comprehensive non destructive evaluation (NDE) is performed through Olympus® Omniscan MX1 on the panel upper side. The C-scan image in Figure 4.15 shows the overall extension of the hidden flaws in the x-y plane but does not gather information on the flaw severity trough the thickness. Instead, the B-scan and S-scan images reveal the complex discontinuity. Although the indentation is barely visible, the whole thickness appears to be affected by delaminations and intralaminar cracks, in a completely non continuous stacking through the thickness. A similar result is obtained performing the NDE on the plate lower side, confirming the "tapered-conical" defect. Due to such NDI results, the damage is simulated via local stiffness degradation in the finite element formulation. Indeed, the stiffness matrix of a structural system depends upon the material properties, geometry and boundary condition. Even if from a theoretical point of view a single delamination do not leads to a high global stiffness reduction, the through thickness complex discontinuity shown in Figure 4.15 as a combination of intralaminar and interlaminar damages justifies the stiffness reduction approach, already proposed in the literature for several purposes [173] and here simulated adopting degraded elements within ABAQUS® environment. In specific, the structure is divided in a set of finite areas discretized into a set of finite elements categorized into undamaged or damaged states with different degradation levels through the thickness. The damage parameters available are the in plane extension and depth of the damage, the degradation level of the finite elements, and the shape and conformity of the damage. For validation purpose, a quadrilateral region with degraded stiffness is discretized to idealize the damage, keeping a structured mesh as well. Then, the experimental methodology is replicated with few efforts in the simulated environment and the DIs are evaluated

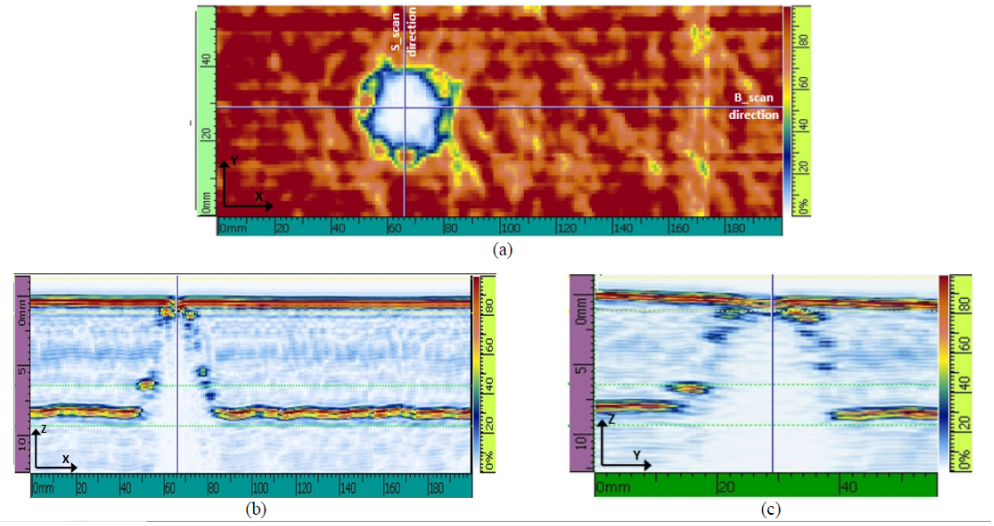

Figure 4.15: Non destructive evaluation of the impact induced damage. C-scan (a), B-scan (b) and S-scan (c) of the impacted region. Scan length, 200mm.

d[mm]	t[mm]	DI [%]
10	2.25	5
15	3.0	13
20	3.75	22
20	4.5	25
25	3.75	25
25	4.5	42

Table 4.6: Damage indicators obtained in the simulated environment for different damage dimensions.

along damaged and undamaged lines of sight under several conditions. Considering the in-plane dimensions of the hidden flaw set to $d \times d\text{mm}^2$ and a given depth of t[mm] along the thickness, few results obtained along a damaged path are reported in Table 4.6. The severity of the damage is well appreciated and both the in-plane dimension and depth of the damage appear to be parameters which can be evaluated from propagation analysis. The results obtained are again reasonable, correctly showing an effective change when such damage is simulated along the corresponded line of sight and no change when the damage is far from the line of sight (i.e. before the introduction of a noisy level).

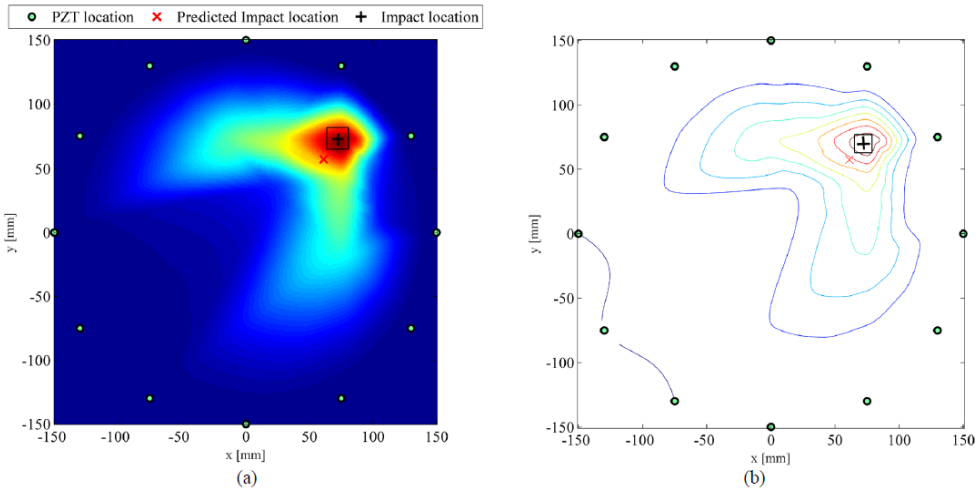

Figure 4.16: Tomographic analysis of the investigated panel in the simulated environment. Map of damage (a) and contour of isolevel curves (b).

4.3 Monitoring and model assisted perspectives

In this section, the results obtained for the last case in Table 4.6 are reported, as it is that closest to the experiments. The signals are evaluated as discussed in Sec. 3.1.2, repeating the simulation actuating individually every PZT on the circular array. In order to consider unexpected errors in the measured displacements, the effects of random noise is introduced by adding Gaussian noise directly to the signals acquired after simulation. From this point of view, the response depends upon two groups of parameters: the standard deviation of the noise and the parameters describing the flaw, explained in Sec. 4.2.2. Thus, as redundant measurements are an effective way to reduce the effect of noise, redundant disturbed signals are selected to reduce the effect of simulated noise. Given 10 time series for each response, and a 20% decision level defined respect to the computed damage index, Figure 4.16 depicts the results obtained for the investigated case. The map of damage, which represents the estimated risk to have a damage, and the related isolevel curves highlight the reasonable result respect to similar experimental investigation reported in Sec. 3.1.2 as well as the good agreement between simulated damage and its prevised location. It is useful to emphasize that this result is obtained accounting both the severity of calculated DIs and the density of intersection points defined by the decision making procedure.

The interaction of the propagating A_0 mode with through thickness delaminations provides important information on the damage location. The Finite Element simulations carried out adopting FSDT based equivalent single layer approach provide an

effective idealization of the damage scenario. Moreover, a good agreement between simulations and experimental results can be achieved in terms of wave propagation, wave-defect interaction and damage detection. Furthermore, the noise simulation allows to achieve a reasonable replication of experimental uncertainties and to simulate the decision making procedure as well. Finally the early results show the sensitivity of proposed DI respect to the in plane dimension and depth of damage, according with the sensitivity of damage indicators respect to flaw severity. Such results allowed to insert simulation stages in the development of methodologies revealing phenomena hardly visible by measurements. Furthermore, both the latter aspects introduce the possibility of a reliability assessment of the system using simulated environments. Although few aspects, which typically appear during experimentation (i.e. repeatability and reproducibility of measurements) cannot be reproduced via simulated environment, when a rigorous numerical correlation is adopted, model assisted probability of detection (MAPOD) is indeed an efficient alternative to classic methods [31], reducing time and costs. MAPOD uses models to minimize the empirical samples needed to achieve statistically meaningful characterization results. To this end, much efforts and several protocols have been proposed to obtain methodologies incorporating empirical data, models, and simulations for characterizing SHM methods in terms of the proposed statistical metrics of reliability for damage detection, localization, and sizing [174]. Regardless the necessity for efficiently addressing a wide range of damage and operational conditions, and effective methods for evaluating the appropriate metrics of reliability depending on the SHM system type and function, a critical aspect is the "non-idealization" of the experiment in the simulated environment, achieving correct impact of the occurring parameters and their influences for flaw detection as well as efficiently addressing variability in the model. The main issue is the feasibility to adopt experimental data in order to only assess the modeling stage. Then, the large amount of data required for statistical assessment could be extracted from simulated environment with few efforts. From this standpoint, the multiple validation provided here, accounting vibrational as well as damage interaction properties revealed during experimentations, confirms the well addressed modeling.

In detail, two different techniques are available for the probability of detection assessment, the n/N and the more sophisticated "$\bar{a}$ versus a" method. The former, based on the classic hit-miss approach, requires data including the real size of damage and the corresponding Probability of Detection estimated by the diagnostic algorithm. Given N different cases for the same flaw size, and n is the number of hit response, the related POD value is directly extracted for that flaw dimension and plotted accordingly into an histogram. However, the hit condition has to be declared, in order to achieve a non-arbitrary evaluation of the hit or miss detection. Regardless damage

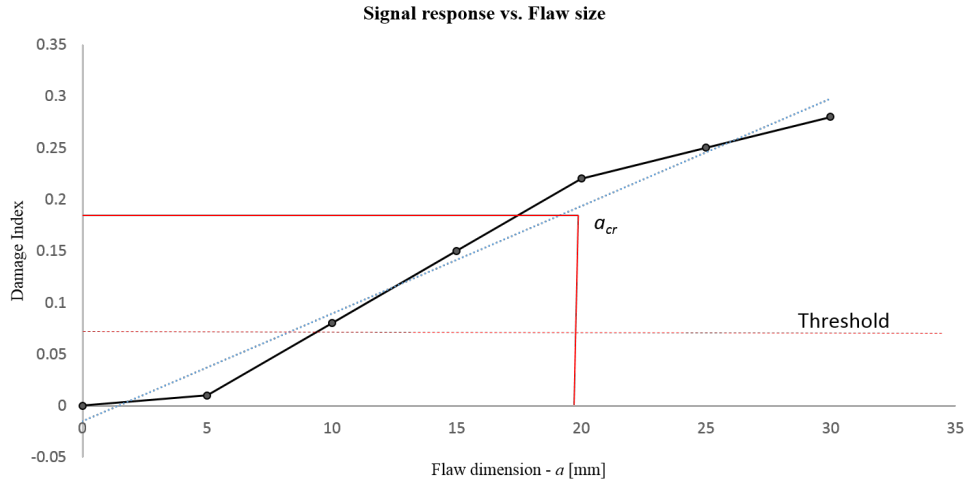

Figure 4.17: Damage Index Profile evaluated along a damaged line of sight omitting noise effect (b). Damage depth t = 3.75 mm.

dimension, in order to achieve statistically meaningful characterization results, a set of deterministic factors has to be chosen including for instance position, shape, orientation, conformation and depth of damage while other random factors are neglected and included in the noisy level. According to such approach in model assisted framework, the related outputs should be calculated in the simulated environment and the detection algorithm employed to achieve the (model assisted) POD dataset.

Otherwise, in view of a more detailed analysis in order to accurately assess the system performance, an indicative trend of the damage index profile has to be defined versus flaw size accounting all deterministic parameters and random variability. The damage indicator is indeed the signal response which should classify the estimated size of damage, when the system (i.e. that based on global approach) does not return any size information. The linear prediction is then adopted to construct the POD curve in order to define the reliability assessment of the SHM system with the $a_{90/95}$ parameter. It is indeed a significant output identifying the flaw size detectable with a probability of 90% and a confidence of 95% and thus a valuable definition of the system target. In order to provide an overview of the feasibility of the proposed framework for characterizing the developed active hotspot monitoring system, the obtained DI profile is reported in Figure 4.17. There, the model is limited to a single explanatory variable (flaw size) and the linear prediction between the possibly transformed signal response (damage index - DI), and the flaw characteristic is plotted neglecting the noisy effect. It is worth noting that DI is evaluated along a path crossing the damage and all other deterministic parameters are fixed while increasing its dimension. The

trend line depicts that the signal response is approximately linear respect to the flaw size; that is indeed a basic assumption using the $\bar{a}$ versus a method. Furthermore, it is worth noting that the definition of this profile introducing all relevant deterministic and random factors in the simulation aids the introduction of a statistical characterization of the signal response for flaw size assessment. Where the system does not return any damage dimension output, such as using the global approach, this allows the possibility to directly correlate the flaw dimension with the current signal response (namely the damage index). Fixed the threshold, and given a final characterization, it is indeed possible to identify a critical dimension of damage (a_{cr} associated with the necessity to repair or further inspect the component) from DI assessment.

Chapter 5

Methodologies for system self diagnostic

Contents

The final part of the work is dedicated to a preliminary investigation for piezoelectric sensor self-diagnostic procedure, aimed to in-situ monitoring of the sensors and actuators used in the structural health monitoring (SHM) methodologies presented. Due to the large number of distributed PZTs needed to correctly interrogate the structure, the self-diagnostic procedure, where the sensors/actuators are confirmed to be functioning properly during operation, is a crucial process to minimize false alarms in the diagnosis. The procedure verified here and already performed in a wide range of similar applications is based on the capacitive analysis of piezoelectric sensors, which is manifested in the imaginary part of the measured electrical admittance. Furthermore, through the analytical and experimental investigation, it is confirmed that possible failures (debonding and partial breakage) affects the ultrasonic propagation warning damage where no change in the structure is indeed present. Therefore, by monitoring the dynamic response of the structure resulting in the wave propagation is not possible to discern structural and sensor contribution to damage indicators. Otherwise, by

separately monitoring the imaginary part of the admittances, it is possible to assess the degradation level of the PZT and its attachment to a host structure rather than structural failure. This chapter introduces the effect of an unknown sensor failure, reports few investigations carried out and concludes with an experimental example to demonstrate the feasibility of the proposed sensor-diagnostic procedure together with an automatic tool to remove the sensor related outputs from data processing.

5.1 Self-diagnostic

As a matter of facts, ultrasonic measurements are point by point signal records which may be affected by structural efficiency (desirable) and sensor condition (undesirable). Even though emerging techniques based on wave analysis are available in the literature [175], unfortunately, as showed afterwards, is quite complex to discern when a signal changes due to a (i) structural failure, (ii) PZT degradation or (iii) combination of the previous events. From the sensor diagnostic standpoint, the total failure of a PZT can be easily identified because any voltage output is not produced while receiving and any excitation is not applied while actuating. However, if only a partial fracture occurs due to impact loads, PZTs are often still able to produce sufficient performance but introducing or sensing distorted signals potentially leading to a false indication and a misleading diagnosis. The degradation of bonding integrity and sensor quality is thus problematic when the PZTs are demanded to interrogate the structure during lifetime and under hazard conditions. It is indeed crucial to detect possible anomalies in the sensor performances to identify when it is necessary to replace the transducer or the entire network.

The effect is indeed remarkable when a cluster of sensor is adopted to have a global reconstruction of the damage. The propagation path, whose sensor is degraded, may warn the presence of a damage where no such flaw is indeed present. From this point of view, looking at the damage detection as a statistical event, this means that the noise is enlarging the area of interest inducing a further probability of false alarm. Discerning the signal response from the noise (see Figure 5.1), it is indeed possible to define different compound probabilities. To assess the system capabilities the probability of detection is really crucial; it indeed means safety because the system is able to detect a prescribed damage with that defined probability of success. On the contrary, the definition of the probability of false alarm is crucial to account the possible downtime. Such probabilities are strictly related with the system threshold, which is defined accounting the signal response variability while transducers are properly working. When a sensor is partially damaged, the mean and/or variance of the related noise distribution increase and the probability of false alarm increases accordingly.

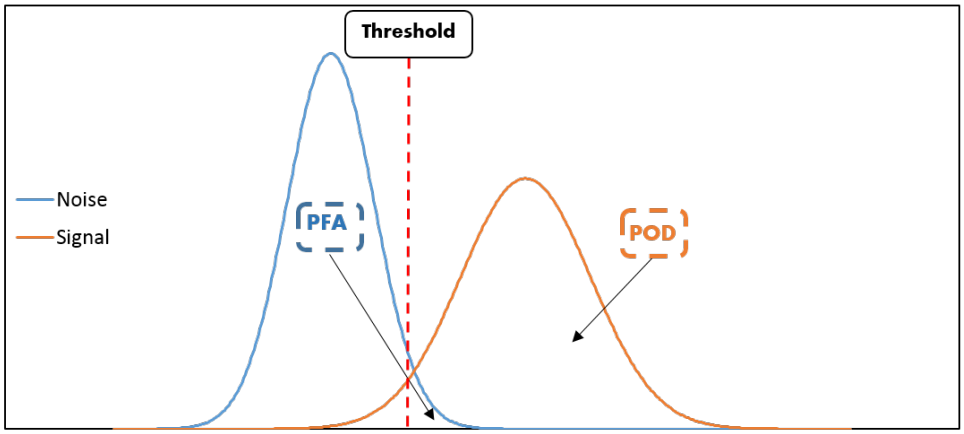

Figure 5.1: Typical overlap between noise and effective signal response. Threshold definition affects both distributions.

This is really undesirable in an autonomous monitoring system, inducing the repair of the structure where the sensor cluster is compromised rather than the structure itself. To avoid that corrupted results induce false alarms in the diagnostic, two strategies can be pursued:

- detect the anomalies in the signal response due to the sensor fault to compensate that effect on damage indicators;
- detect the sensor currently broken to neglect related information during data processing;

The second approach is indeed the most effective solution, avoiding misleading interpretation of corrupted signals at the cost of a little reduction of the system target, which remains at least well defined as suggested in the concluding remarks of Sec. 5.2.3.

5.1.1 Overview

A piezoelectric sensor self-diagnostic procedure based on electrical impedance measurements can be used to judge the quality of the bond between transducer and structure as described in several works [176, 177, 178]. The susceptance spectrum which is the imaginary part of the admittance spectrum can also be used to judge the quality of the bond between transducers and structure in SHM systems. It has been found that the effects are significant, modifying the phase and amplitude of propagated waves and changing the measured impedance spectrum [179]. Several studies have been carried out to characterize the effects induced on Lamb wave propagation revealing

dependencies on the shape of debonding [180], making really hard the application of compensation algorithms to exploit the response of a sensor when partially fault (namely the first strategy aforementioned). As a consequence, these changes could lead to false indications on the structural conditions without an efficient sensor-diagnostic process, also addressed as self-diagnostic.

From this standpoint, different variables can be measured to diagnose PZT debonding in the structure including not only admittance measurement, but also impedance measurement with temperature effect on the sensors [179], reciprocity between time response of PZT sensors using Lamb waves [181], electrical properties of PZT sensors [182] and maximum amplitude analysis [183]. As a mater of facts, the transducer dimensions play an important role in determining the frequency at which the peak sensor response occurs, leading to exploit the relation between sensing dimension and wave tuning with PZT as a parameter to detect a debond [175]. However, wavefield generated by a PZT is quite complex even using circular sensors. As already mentioned in[184], it is indeed not symmetric for all frequencies in the case of a fully bonded transducer, due to the wrap-around electrode which interrupts the axisymmetry. That wrap is indeed necessary to correctly bond together disk and structure exploiting one side of the PZT. In addition the effects caused by debonding highly depend on the chosen actuation frequency and exhibit a strong angular dependency [185]. The shape of the maximum velocity polar plot changes due to the debonding and the maximum velocity can even be higher than for the case of the fully bonded transducer. Hence, it is really complex to discern the fault of a transducer in an array of sensors by monitoring the wave response only.

From a very brief statement of the problem, it can be concluded that the different PWAS faults have a significant effect on the wave propagation. The changed wave propagation leads to changes in the SHM system diagnostic, based on active acousto-ultrasonics where PWAS are employed for actuation and sensing purposes. Depending on the method used for acousto-ultrasonics-based SHM, these effects have an impact on the statement about the health of the structure and might lead to false alarms, as not the structure but the PWAS is defective. It is therefore highly recommended to check the transducers to ensure the reliability of the SHM system. For the detection of PWAS faults, the suscpetance as imaginary part of the admittance has proven to be sensitive. Furthermore it is indeed possible to select the analysis of a single PZT, instead of resort to a probabilistic analysis of wave responses to detect the transducer which is not properly working among those are working. Due to such considerations, in this work, the effect on wave propagation when PZT is not correctly operating is slightly remarked in term of damage indices compared with typical values encountered when a structure is damaged. Then an algorithm capable to compare the status of

piezo with the baseline condition is developed comparing the slope of the susceptance for any acquired measurement to the values given by the healthy condition. In this way, if the sensor is found to be defective, it is excluded from any further damage detection use with a dedicated tool within the SHM interface, in order to achieve an algorithm to simultaneously sort sensors and detect damage in the structure.

5.1.2 Electromechanical impedance

The electrical impedance of a PZT can be expressed as the relation of the input voltage and the resulting current in the piezo. The inverse is called admittance. Due to the presence of the electromechanical coupling in the piezoelectric transducer, its electrical impedance when bonded depends upon the mechanical properties of the host structure and it is named ElectroMechanical Impedance (EMI). Due to this reason it is often used for damage detection assessment. When the PZT is bonded to an hosting structure, the complex electromechanical impedance can be computed according to the following formula [186, 187, 188]:

$$Z(\omega) = \left[i\omega C \left(1 - \kappa_{31}^2 \frac{Z_S(\omega)}{Z_S(\omega) + Z_P(\omega)} \right) \right]^{-1} \tag{5.1}$$

where Z is the electrical impedance measured at the piezo coupled to the host structure, C is the zero-load capacitance, κ is the electromechanical cross coupling coefficient, Z_S and Z_P are the mechanical impedance of the host structure and that of the un-bonded piezo respectively. Instead, according to [70], the complex electromechanical admittance can be addressed with the following decomposition:

$$Y(\omega) = \left[i\omega \frac{A_P}{t_P} \left(\epsilon_{33} - d_{31}^2 E_P \frac{Z_S(\omega)}{Z_S(\omega) + Z_P(\omega)} \right) \right]^{-1} \tag{5.2}$$

where the zero load capacitance is described in term of geometrical properties of the PZT (Contact surface (A_P) and thickness (t_P)), ϵ_{33} is the permittivity, E_p is the Young modulus and d_{31} is the piezoelectric load constant. Due to the higher sensitivity to structural changes, the real part of the complex electrical impedance is usually taken into account for monitoring purposes. Instead, due to the second decomposition, it appears evident how the admittance is primarily affected by the PZT properties. This short overview on physical modeling of the EMI shows why faults have an impact on this quantity, which includes electrical and mechanical parameters. Geometrical, electrical and mechanical properties are indeed affecting such formulation, with emerging dependencies upon PZT characteristics as detailed in Table 5.1 Otherwise, the next section is dedicated to measurements carried out to practically exploit and verify such

Geometry	PZT Electrical Properties	Mechanical Properties	Structure Mechanical Properties
A_P	ϵ_{33}	E_p	Z_S
t_P	d_{31}	Z_p	Z_S

Table 5.1: Several PZT and structure properties afecting admittance response.

ρ [kg/m^3]	E_1 [MPa]	$E_2 = E_3$ [MPa]	$G_{12} = G_{13}$ [MPa]	G_{23} [MPa]	$\nu_{12} = \nu_{13}$	ν_{23}
1500	134500	9951	4556	3772	0.284	0.319

Table 5.2: Elastic properties of *graphite-epoxy* lamina.

impacts including ultrasound and electromechanical impedance investigations.

5.2 Experimental results

To investigate the effects of transuducer faults on wave propagation and the feasibility of a EMI-based self-diagnostic technique, a composite plate is manufactured using high tensile carbon fibers and epoxy resin to made unidirectional laminae, whose mechanical properties are depicted in Table 5.2. The several layers are stacked with hand layup technology resulting in a quasi-isotropic plate described in Table 5.3 from which several coupons of 250mm×40mm are cut and equipped with PZTs with different bonding conditions. The PZT is the usually adopted piezoceramic disk made of PIC-255 soft material by *Physik Instrumente* (PI) depicted in Figure 5.2 (a) where it appears attached on the composite surface with a double component epoxy glue. The EMI measurements are firstly performed on unbonded PZTs to detect any variability in the measured signature and then on coupled PZTs, i.e. attached to 6 different specimens as shown in Figure 5.2 (b). On the same specimens, the wave propagation is analyzed considering different damage scenarios, in order to simulate damages induced by impact on the structure (delamination and internal discontinuities) and on the transducer (partial debonding and partial breakage). Given the variability from ten unbounded PZTs (addressed in the next section employing again such an unsupervised

Stacking sequence	Dimensions
$[\pm 45°/0°/90°]_s$	$600 \times 600 \times 2.0[\text{mm}^3]$

Table 5.3: Properties of laminated plate.

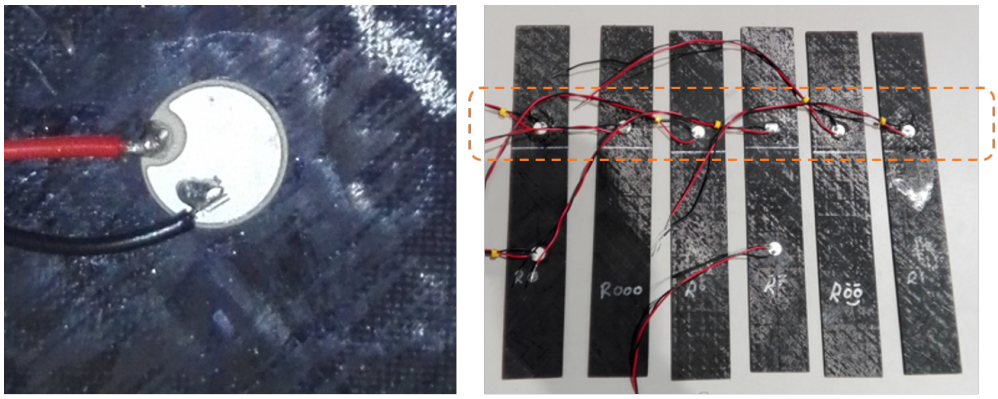

(a) (b)

Figure 5.2: Experimental setup. Detail of PZT (a) and specimens (b) adopted for measurements.

Healthy	PZT		Structure		
No damage	Debond (25%)	Debond (30%)	Breakage	Delamination	Insert
SP_1	SP_2	SP_3	SP_4	SP_5	SP_6

Table 5.4: Several specimens with different damage scenarios involving PZT faults and structure failures.

analysis), only one specimen (SP_1) is instrumented to establish the healthy condition (i.e.: the baseline status for EMI and ultrasounds measurements). Typical PZT faults due to unforeseen impacts are: (i) the debonding of the PZT, where a part of the transducer is locally detached due to bond yielding, and (ii) the breakage of the PWAS, where a part of the transducer is detached from the remaining part which is completely attached to the structure. The former case is simulated in the experiments with different disbonding levels (SP_2 and SP_3) while the breakage is obtained removing a part of the PZT before starting the bonding procedure (SP_4). Although those damages may appear similar, the breakage reduces the zero load capacitance of the PZT while the debonding changes only the relative effect between transducer and structure leading to different effects on susceptance signature. Finally, two different failure conditions are simulated for the structure: (i) a delamination near the sensor location is induced by removing the connection between two adjacent layers (SP_5) and (ii) a discontinuity along the line of sight is obtained inserting an external body ($SP6$). The comparison of several specimens characteristics is summarized in Table 5.4. The ultrasound investigation and eletromechanical impedance assessment are conducted using the experimental setup shown in Figure 5.3.

The details of measurements campaign are briefly described in the next sections

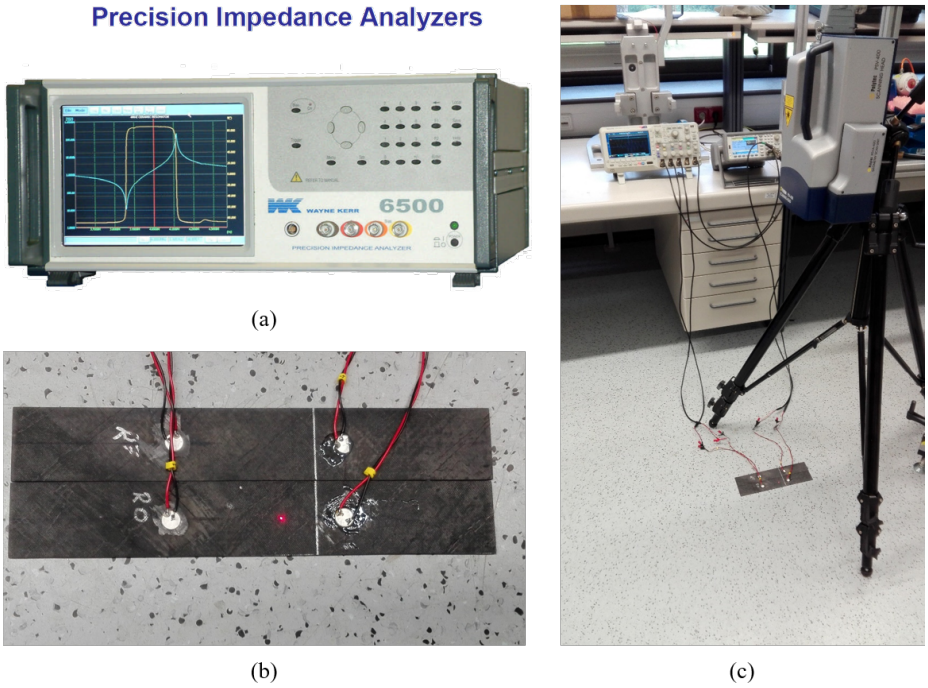

Figure 5.3: Experimental setup. Detail of EMI analyzer (a), specimens configuration (b) and instruments adopted for ultrasonic inspection.

where the revealed results are discussed before moving to a possible self-diagnostic approach and future improvements to increase the overall system reliability.

5.2.1 Ultrasound investigation

The ultrasonic investigation is carried out exciting wave propagation in the range between 10kHz and 60kHz, where the A_0 is more tuned as widely demonstrated for these types of structures. Healthy and corrupted PZTs are excited with a 4.5 sine cycles burst windowed with Hanning function. The signal is simultaneously boosted up to 18volt peak to peak with an arbitrary generator by Keysight Technologies® to be conveyed to PZTs and to a digital oscilloscope by Tektronix®. The latter is used to digitalize and syncronize all signals recorded at PZTs location with that used for excitation. Although the sensing is mostly operated catching the out of plane velocity with Laser doppler velocimetry, the propagating wave is indeed also captured by means of other healthy PZTs. For the sake of conciseness only few outcomes are reported here due to the redundancy of results. The ultrasonic propagation (40kHz) obtained exciting the PZTs bonded respectively on specimens SP_1 and SP_3 is shown in Figure 5.4. The PZT debonding induces a slight variation on the time of flight

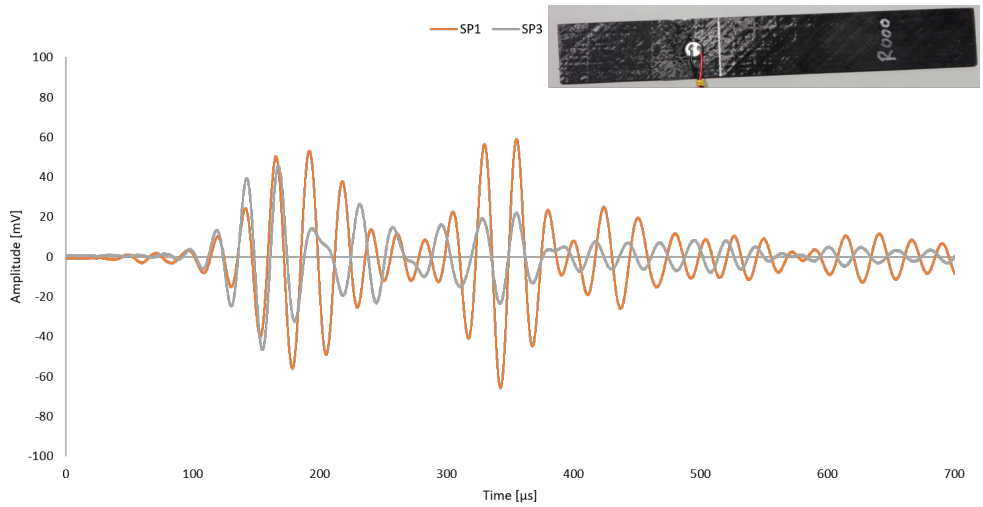

Figure 5.4: Ultrasound investigation exciting heathy and disbonded PZT (PIC 255): frequency 40kHz.

of the direct waves while the waveform is completely distorted and the reflections appear weaker due to the non effective contraction of the transmitting transducer. A similar result can be observed comparing the ultrasonic propagation (40kHz) while exciting the PZT bonded on specimen SP_4 shown in Figure 5.5. Here, the direct wave is weaker and slower due to the breakage and the wave is not correctly propagating in the structure as demonstrated by various echoes which are still slightly emerging. In both cases damage indicators return a value above the threshold as defined in Sec. 3.1.1, warning a damage where the sensor fault is instead present. A similar result is obtained while interrogating the specimen SP_2 or exciting different frequencies. Likewise, by comparing the ultrasonic response of a damaged specimen (SP_6) it is possible to observe how the insert affects the propagation, the different thickness frequency around that location induces changes in wave amplitude and velocity. As depicted in Figure 5.6, the number and amplitude of reflections is still varying but in this case they are amplified by the scattering at damage location rather than damped by the sensor fault. In this case the SHM system returns a diagnosis in line with the damage appearance. The investigation is carried out also using broken PZTs to sense wave propagation excited by properly working transmitters, leading to similar results with damage indicators warning damage where sensor deterioration is indeed present. Hence, as a matter of facts, it is complex to distinguish sensor fault by failure of the structure in terms of DIs and a further sensor diagnostic is confirmed to be crucial.

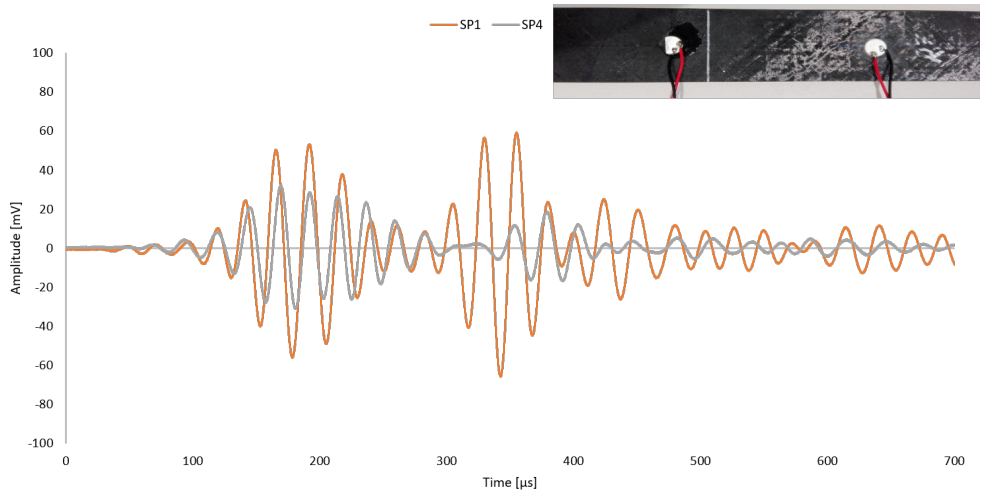

Figure 5.5: Ultrasound investigation exciting heathy and partially broken PZT (PIC 255): frequency 40kHz.

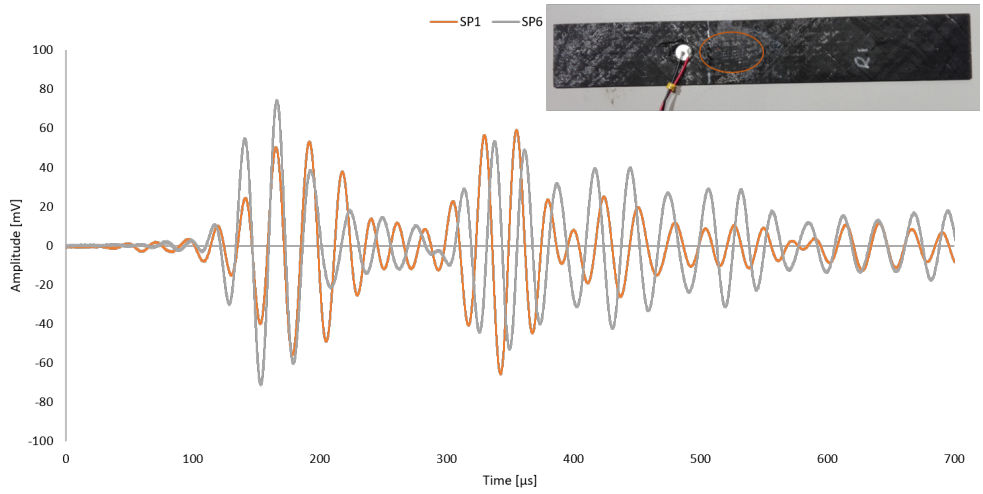

Figure 5.6: Ultrasound investigation exciting heathy PZTs (PIC 255) under different structural conditions: frequency 40kHz.

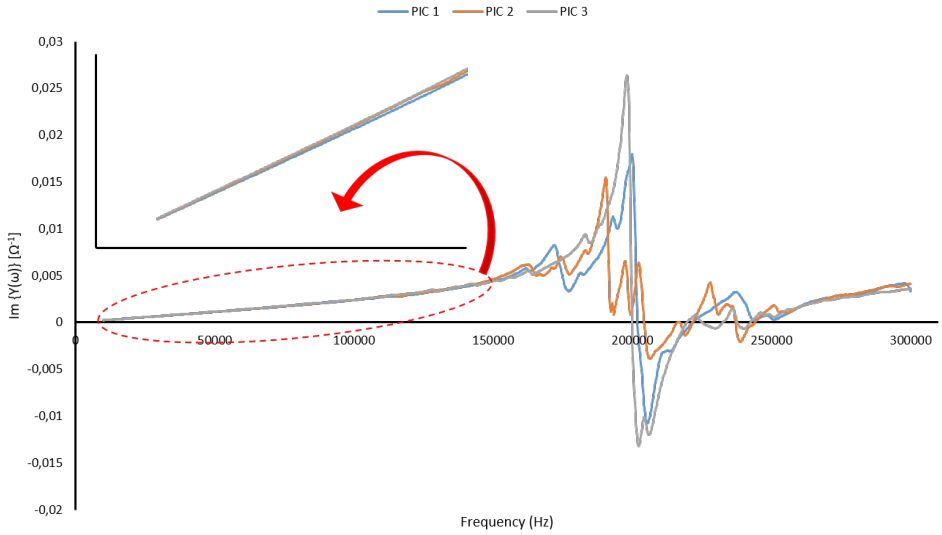

Figure 5.7: Susceptance signature of unbonded PZT (PIC 255) disks.

5.2.2 Electromechanical impedance investigation

The electromechanical impedance analysis is carried out looking for the most suited physical quantity associated to the piezo fault. The precision impedance analyzer Wayne Kerr 6500B (see Figure 5.3 (a)) is employed for the investigation of PZTs in different frequency ranges to maximize the sampling rate. The overall spectra considered is in the range from 10hertz to 300kHz, where the PZT is excited with a frequency sweep and an applied voltage of 1V. In the meantime, the system measures the current flowing through the circuit generated with the measuring leads of the PZT. First of all, a number of 10 PZT disks like that shown in Figure 5.2 (a) are analyzed when unbonded to any structure. The susceptance spectra obtained from three of them is reported in Figure 5.7. The PZT response is measured and the imaginary part of the complex electromechanical admittance is extracted in the range between 10kHz and 300kHz, simply by changing the transducer and the electrical leads soldered with every PZT. As depicted in the plot of susceptance versus frequency, the high spectrum signature around the PZT resonance (i.e. 200kHz) is strongly non linear and affected by simply replicating PZT and its connection. However, unlike other quantities, the susceptance signature at lower frequencies is quite linear and it appears slightly affected by sample uncertainties. The good reproducibility and such a linear behaviour in the large spectrum analysis makes the susceptance a good candidate for assessing changes occurring at PZT level.

Comparing the measurements of unbonded and bonded PZTs in the range from

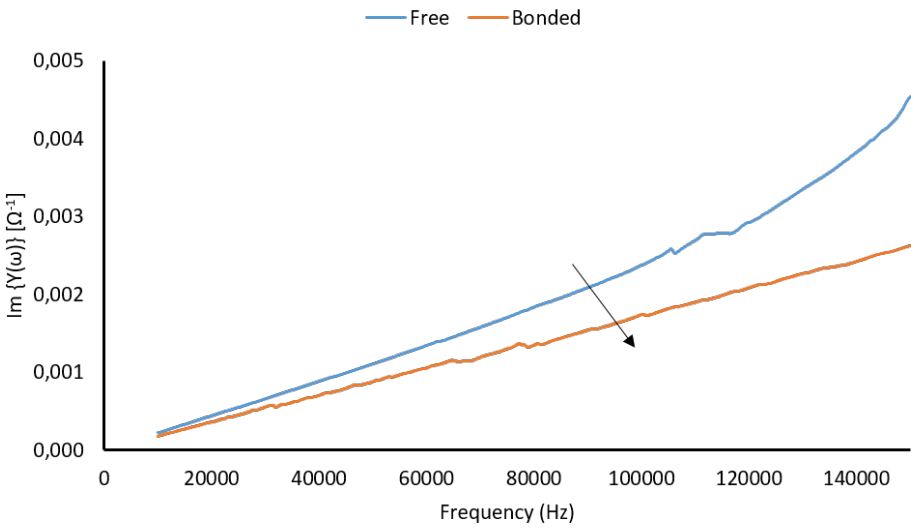

Figure 5.8: Susceptance signature of unbonded and bonded PZT (PIC 255) disks.

10kHz to 150kHz in Figure 5.8, it appears evident how the slope of the signature decreases due to the structural coupling according to Eq. (5.2). Even though the presence of local peaks, the relative influence between PZT and structure can be indeed adopted to verify the health of the sensor, inducing changes in the signature slope. Such evidence is shown in Figure 5.9 (a), where the debonding returns a greater slope of the signature due to reducing influence of the structure on the PZT, which is indeed partially disconnected. Detailing the analysis in the range between 10Hz and 60kHz in Figure 5.9 (b), it is worth noting that local peaks are attenuated and the intercept of the linear trend is not affected. Unless marginal effects, the intercept appears to be not affected even when the breakage of PZT occurs. In this case the remaining part of the transducer is correctly bonded with the hosting structure but its zero load capacity is decreasing according to the ratio $\frac{A_P}{t_P}$. As a direct consequence, the slope of the signature is decreasing as depicted in Figure 5.10 (a) and local peaks are attenuated again according to what depicted in Figure 5.10 (b). Finally, due to the structural failure, the mechanical impedance of the structure is changing and slightly affects the slope of the signature according to Figure 5.11 (a) and no matter what the flaw introduced. Detailing the analysis in the frequency range between 10Hz and 60kHz shown in Figure 5.11 (b), it is evident that local peaks in the signature are still present and a shift in frequency domain can be marked no matter the damage is. Those results suggest that the EMI response of the piezoelectric transducer allows to classify different failures of PZT and structure when the imaginary part of the admittance is

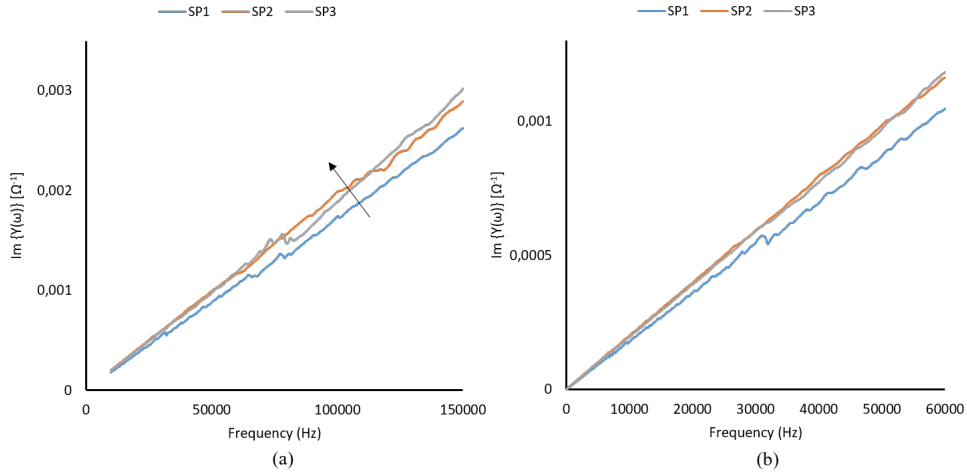

Figure 5.9: Susceptance signatures of heathy and disbonded PZT (PIC 255). Frequency range: 10kHz – 150kHz (a) and 10Hz – 60kHz (b).

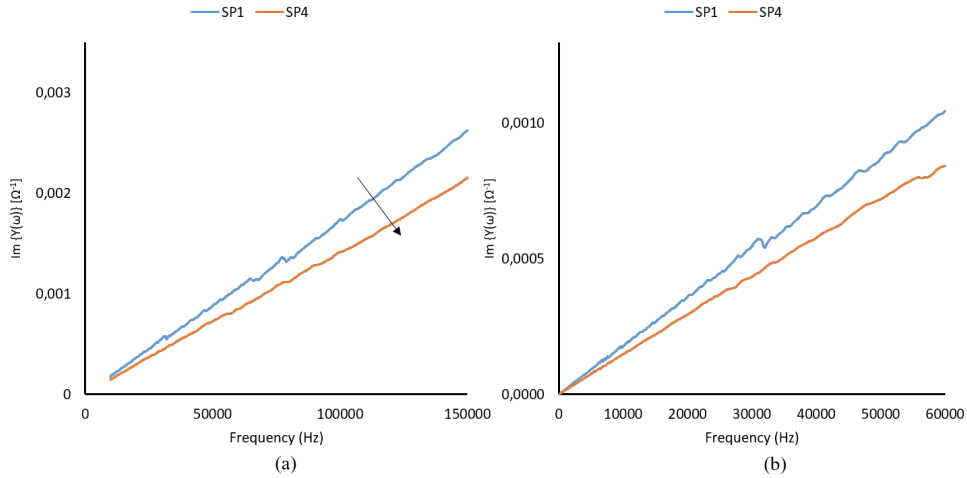

Figure 5.10: Susceptance signatures of heathy and partially broken PZT (PIC 255). Frequency range: 10kHz – 150kHz (a) and 10Hz – 60kHz (b).

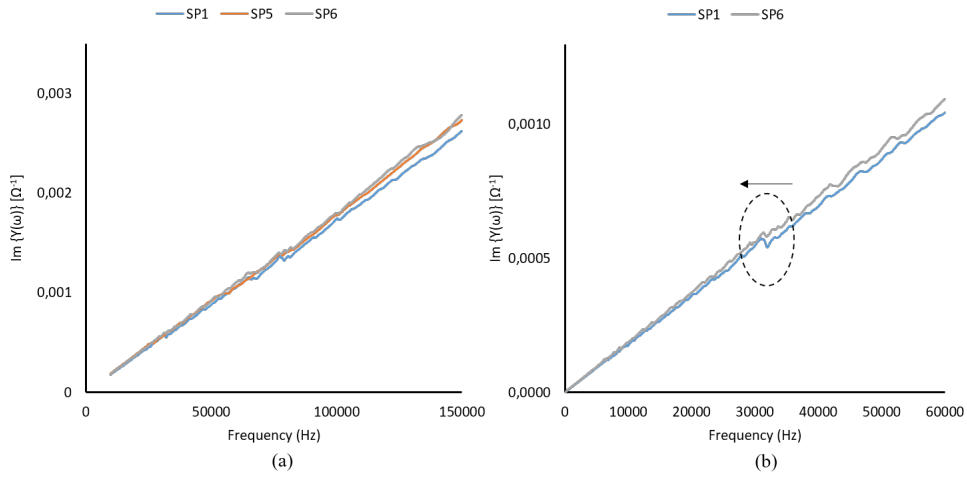

Figure 5.11: Susceptance signatures of heathy PZTs (PIC 255) under different structural condition. Frequency range: 10kHz − 150kHz (a) and 10Hz − 60kHz (b)

monitored. Assessing this physical quantity, the system self-diagnostic may be carried out according the approach proposed in the next section.

5.2.3 Proposed approach and discussion

According to the ultrasound investigation, the effects of the PZT defects are non negligible for the generated wave field. The analysis indicates that these types of failure introduce similar outputs for damage indicators used for SHM systems leading to possible false alarm. However, due to the promising results showing that it is possible to detect PZT faults with the help of the susceptance spectrum, a possible self diagnostic approach may integrate the SHM diagnosis. To achieve this purpose the monitoring of the susceptance slope is proposed here as self-diagnosic feature. The PZT damage indicator is indeed obtained with the same formulation used for structural monitoring in Eq. (2.11), where the baseline and current features are classified looking to the slope of the susceptance signature.

According to the measurements, the linearity of the susceptance may be considered quite valid until 150kHz even though local peaks may slightly alter the trend. In thise range the slope is calculated using a linear least-squares fit and chosing the upper frequency to limit the range of analysis (i.e.: 20−30kHz). In this way the interpolating law will be:

$$Y(f) = m \cdot f + b, \quad 10\text{Hz} \leq f \leq 20\text{kHz} \tag{5.3}$$

where m is the slope of the susceptance and b the y-intercept value. The former represents the feature to be compared for fault indicator. Obviously this equation

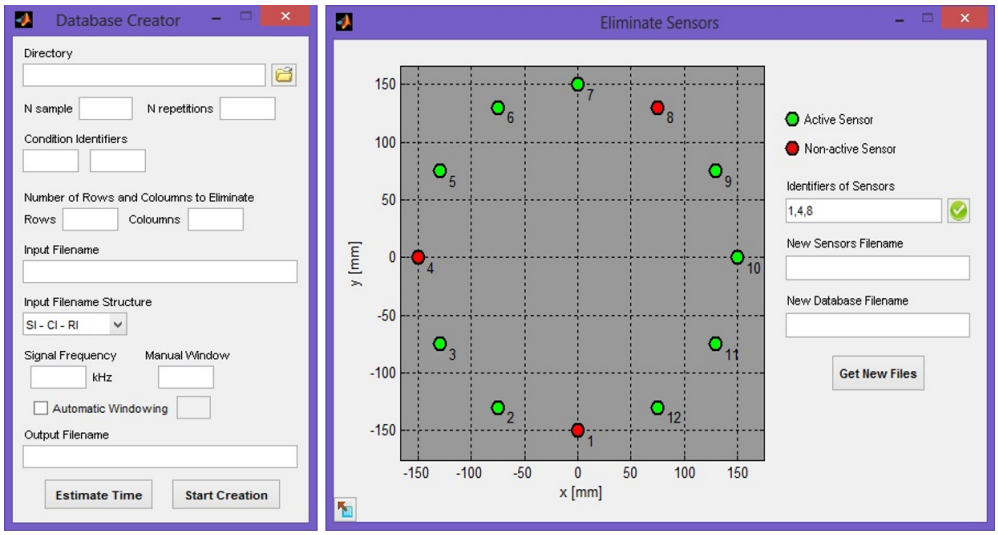

(a) (b)

Figure 5.12: Self-diagnostic tool. Database upadate (a) and transducers removal tool (b).

does not describe the local peaks, but only a straight line describing the expected value within the frequency range. With the expected susceptance slope value for a healthy sensor defined, an expression of an acceptable range for healthy sensors needs to be characterized. A straightforward methods to define the bondaries to discern damage response from noise is based on an unsupervised analysis. In the same way of damage index, a sensitivity indicator is calculated estimating the susceptance slope of several unbonded PZTs. Then the variability is calculated and a bilateral prediction iinterval is estimated according to parametric statistics (see Sec. 3.1.1). All values below this threshold are censured (health status) and namely the sensor is found to be healthy. Otherwise sensor is found to be defective and excluded from any further damage detection use. From the measurements carried out, this approach has been demonstrated to be effective to discern the fault PZTs rather than structural failure which are currently inducing variations comparable with uncertainties and returning damage indicators below the threshold setting.

In order to achieve effective SHM with self-diagnostic procedure, the algorithm used should simultaneously sort sensors and detect damages with information gathered from healthy transducers. To obtain this result, a self diagnostic tool is dedicated to sort the damaged sensors Figure 5.12 and to eliminate the relative data from calculation of the health database (a) or to eliminate diagnostic data from visualization (b).

However the results push two different discussions about methodology and health management scenarios. The former deals with the opposite effect that debonding and

breakage are inducing on the susceptance signnature. It may happens that the effects of the former failure are compensated by a simultaneous (partial) breakage of the debonded part. In this case the sensor damage indicator may falls in the range of healthy response where the sensor is indeed broken. This possibility suggests a further scenario of investigation dealing with peaks attenuation while sensor is damaged and with Lamb wave tuning. The latter is indeed strictly connected to the sensing dimension of the transducer and together with the other indicators may lead to a multi-parameter self diagnostic increasing probability of correct detection as achieved for diagnostic purpose.

About health management, it is necessary to point out that even with a PZT inspection method correctly warning a sensor fault, in the first place it is not possible to establish if it leads to false alarm of the SHM system and if the remaining sensors still provide a reliable diagnostic. For this analysis it is definitely necessary to combine the results of the SHM system with the results of the PZT self diagnostic approach in a performance assessment, where the output of the transducer inspection is related to the effects that PZT faults have on the SHM system. As aforementioned, an interesting perspective is the possibility to identify the target of the system with one or more sensor faults in order to instantaneously assess and update the reliability of the system. This is a valuable advantage while removing rather than compensating distorted signals. It is indeed possible to correctly evaluate the new system target (i.e.: achievable reliability with fewer sensors) and eventually decide about replacing the defected transducers or the entire system (i.e.: if the target is bigger than critical flaw dimension). This scenario appears time consuming and expensive while dealing with measurements but it can be assessed basing the analysis on statistics and (model assisted) probability of detection, as introduced among the final discussions in Sec. 4.3r. For this analysis thresholds and procedures of both methods for structural damage detection and for PWAS inspection have to be taken into account and their framework appears well established in the present work.

Concluding Remarks

A SHM system provides an effective, continuous, and low-cost integrated framework for detection of damages in structures to avoid catastrophic failure. It can provide significant improvement in cost reduction for both aging and modern lightweight defect-critical structures. The first key role of SHM systems is to replace the traditional scheduled maintenance approach with the on condition maintenance concept, helping to significantly reduce the percentage of the life cycle costs associated with inspection and maintenance operations. Furthermore, a system integrated with structure capable to provide structural diagnostic every time and everywhere as a part of the structure itself can lead to the composite design optimization. The damage tolerance approach operated by large commercial aircraft manufacturers which are increasingly using composites restricts the effective benefits resulting from its adoption and only the integration of a system capable to detect any possible emerging flaw can improve the design.

In this work guided ultrasonic waves have been investigated for online monitoring of emerging and barely visible flaws within composite structures subject to low velocity impacts. The experimental campaigns widely supported by theoretical and numerical studies lead to the definition of two different SHM methodologies. The former is based on a global approach, providing fast identification and effective localization of impact induced damages in complex composite structures resorting to a sparse array of transducers capable to excite and sense guided waves interrogating the structure along all possible paths defined by the sensor pairs. A statistical selection of most affected paths and a further image reconstructed by manipulating damage metrics at emerging intersection points (SHM mesh) allow to achieve the global diagnostic, whether the damage is emerging in flat panels (i.e.: multiple delaminations through the thickness) or in stiffened structures (i.e. stringer debondings). This approach is further enhanced improving all criticality aspects achieving a multi-path and multi-parameter

monitoring system, named MP^2. It exploits indeed the capability of different features extracted from ultrasonic signals to discover different types of damages, it classifies for every one of those the SHM mesh warning the presence of the failure weighting the related feature with the density of the emerging nodes and it finally provides the diagnostic image by normalization and data fusion to increase the probability of detection. All algorithms are then implemented in a user-friendly software to perform the structural monitoring without any relevant skill of the operator.

The second methodology is focused on the comprehensive and deterministic diagnosis of debondings. It is developed investigating ultrasonic guided waves propagating and scattering in stiffened composite media. Resorting to a linear array of transducers alongside the structural discontinuity to monitor, the resulting local technique is capable to predict arrival time of guided waves scattering from that location detecting, as a consequence, every possible change in the specific scattering area. The propagation model based on Snell's Law and negligibility of mode conversion is verified by a preliminary experimental investigation. Such model is used for disbonding assessment focusing the analysis on the wave portion scattered by the stringer to detect changes in the reflector itself. From a second investigation, promising results are achieved, exhibiting the capability of the method to accomplish a multi-level diagnostic analysis which represents perhaps one of its most attractive features. An excellent agreement with classic ultrasound non destructive testing is finally obtained. The system is indeed capable to successfully detect and accurately locate the damage as well as to outline the extent and quantify the severity of the disbonding.

It is worth noting that damage detection using GUWs is really promising but the complexities involved during ultrasonic measurements cannot be faced without resorting to theoretical aspects and modeling. About the latter demand, one of the major concerns of this work deals with the definition of a model assisted damage detection system aimed to support experimental investigations and achieve a detailed assessment of system performances. The Finite Element simulations carried out adopting equivalent single layer approach based on first-order shear deformation theory provide an effective idealization of the problem while correctly addressing any relevant aspect of implementation within multilayered structures (i.e. shear effects and damage modeling). It is worth noting that adopted theories provide a higher computational efficiency at the cost of a slightly reduced accuracy for the global structural behavior in antisymmetric wave propagation problems. Hence, a good agreement between simulations and experimental results can be achieved in terms of wave propagation, wave-defect interaction and damage detection. Furthermore, the noise simulation proposed allows to achieve a reasonable replication of experimental uncertainties and to simulate the decision making procedure as well. Finally, the numerical outcomes show

the sensitivity of proposed metrics respect to the in plane dimension and depth of damage, according with the sensitivity of damage indicators respect to flaw severity. Such results allowed to insert simulation stages in the development of methodologies revealing phenomena hardly visible by measurements.

Both the latter aspects introduce the possibility of a reliability assessment of the system using simulated environments, minimizing the empirical samples needed to achieve statistically meaningful characterization results with fewer measurements possible. This is perhaps the most interesting perspective for future investigations. As a matter of facts, the necessity for efficiently addressing a wide range of damage and operational conditions cannot be covered by experimental campaigns. Achieving correct impact of the occurring parameters and their influences for flaw detection as well as efficiently addressing variability in the model, the simulated framework validated in this work can be used for this purpose. For instance, it would be able to assess how the system performances are changing with fewer sensors in order to define when the achievable diagnostic is satisfactory respect to the critical damage size to detect. This aspect is strictly connected with the self-diagnostic tool finally presented in this work and implemented in the SHM software. Even though a further investigation is needed to study more complex sensor fault scenarios, the approach based on the capacitive analysis of piezoelectric sensors, which is manifested in the imaginary part of the measured electrical admittance, is correctly warning the transducer degradation. In order to achieve effective SHM with self-diagnostic procedure, the resulting algorithm simultaneously sort sensors and detect damages with information gathered from healthy transducers. In this way the risk of false alarms induced by broken sensors is minimized or even cancelled enhancing the overall reliability of the SHM system.

Acknowledgements

I would first like to thank the *Italian Ministry of Education, Universities and Research* for financing the scholarship for the fulfillment of the requirements for the degree of Doctor of Philosophy in Industrial Engineering which I got in 2014, November. It is always a bit of a challenge, that moment at the start of a new experience, so my thanks to my advisor, Prof. Fabrizio Ricci, for his guidance and support during the preparation of the research activities since he accepted to supervise my M.Sc. thesis in Aerospace Engineering. My thanks even go to Dr. Leandro Maio for being a mentor and a friend, and for encouraging and exciting my passion for research at any time since he accepted as well to supervise my activities during M.Sc. graduation. I benefit greatly from my daily interactions with both of them. Finally, I would like to thank the coordinators of the Ph.D. course in Industrial Engineering, Prof. Fabio Bozza (former) and Prof. Michele Grassi (currently appointed) for the coordination of courses, seminars and all related activities.

Special acknowledgements go to the *Fraunhofer Institute for Structural Durability and System Reliability* in Darmstadt. I spent in the Institute the last 9 months of my research activities under the supervision of Dr. Andreas Friedmann and Dr. Mihail Lilov, whom I offer my gratitude for guiding me in the daily activities together with Dr. Valerio Carli, who invited me and was my mentor there. The support provided by the Institute headed by Prof. Tobias Melz is highly appreciated, giving me the possibility to achieve one of the aims of my research dealing with a different research scenario where the knowledge shapes very likely into a product.

A special thank is also dedicated to *Aerospace* Journal (MPDI) for the Travel award received for attending and presenting during the 20^{th} International Conference on Composite Structures (ICCS 20) in CNAM, Paris, France, 4–7 September 2017. A similar gratitude is spent for *Composite Structures* journal (Elsevier) for sponsoring me with the Ian Marshall's Award for Best Student Paper during ICCS 20 in CNAM,

Paris, France, 4–7 September 2017.

Finally, I would like to strongly thank Prof. Michele Meo and Dr. Jochen Moll. They kindly accepted to review my thesis, in view of the final discussion of the dissertation during the public defense. Their effort and the detailed and valuable feedback provided are much more than highly appreciated.

Bibliography

[1] D. Raymer, *Aircraft Design: A Conceptual Approach, Fourth Edition (AIAA Education Series)*. AIAA, 2006.

[2] R. Jones, *Mechanics Of Composite Materials*, ser. Materials Science and Engineering Series. Taylor & Francis, 1998.

[3] T. Megson, *Aircraft Structures for Engineering Students (Fifth Edition)*, 5th ed. Boston: Butterworth-Heinemann, 2013.

[4] W. Roeseler, S. Branko, and M. Kismarton, "Composite structures: the first 100 years," in *Proceedings of the* 16^{th} *Incternational Conference on Composite Materials*, 2007.

[5] M. Walz, "The dream of composites: the use of composite material in Boeing's 787 Dreamliner is benefiting manufacturing, the environment, and, ultimately, the entire air travel industry." *R&D Magazine*, 2006.

[6] F. Baylis. Boeing 787 advancements. [Online]. Available: http://aviationknowledge.wikidot.com/aviation:boeing-787-advancements

[7] J. Tomblin, "Overview of composite material trends in aviation manufacturing," University Lecture.

[8] A. A. Jaoude, "Analytic and linear prognostic model for a vehicle suspension system subject to fatigue," *Systems Science & Control Engineering*, vol. 3, no. 1, pp. 81–98, 2015.

[9] *MIL-HDBK 17-3F Composite Materials Handbook*, ser. Department of defense Handbook, USA, 2002.

[10] *JSSG-2006, Aircraft Structures*, ser. Department of Defense joint service specification guide, USA, 1998.

[11] *Aviation Safety: Status of FAA's Actions to Oversee the Safety of Composite Airplanes*, United States Government Accountability Office, USA, 2011.

[12] S. R. Finn and G. Springer, *Composite Plates Impact Damage: An Atlas.* Taylor & Francis, 1991.

[13] S. Abrate, *Impact on Composite Structures:.* Cambridge University Press, 1998.

[14] G. Davies and X. Zhang, "Impact damage prediction in carbon composite structures," *International Journal of Impact Engineering*, vol. 16, no. 1, pp. 149–170, 1995.

[15] H. Choi and F.-K. Chang, "A model for predicting damage in graphite/epoxy laminated composites resulting from low-velocity point impact," *Journal of Composite Materials*, vol. 26, no. 14, pp. 2134–2169, 1992.

[16] S. Finn and G. Springer, "Delaminations in composite plates under transverse static or impact loads - a model," *Composite Structures*, vol. 23, no. 3, pp. 177–190, 1993.

[17] M. de Moura and J. Gonçalves, "Modelling the interaction between matrix cracking and delamination in carbon-epoxy laminates under low velocity impact," *Composites Science and Technology*, vol. 64, no. 7-8, pp. 1021–1027, 2004.

[18] C. Li, N. Hu, Y. Yin, H. Sekine, and H. Fukunaga, "Low-velocity impact-induced damage of continuous fiber-reinforced composite laminates. Part I. a FEM numerical model," *Composites Part A: Applied Science and Manufacturing*, vol. 33, no. 8, pp. 1055–1062, 2002.

[19] E. Kim, M. Rim, I. Lee, and T. Hwang, "Composite damage model based on continuum damage mechanics and low velocity impact analysis of composite plates," *Composite Structures*, vol. 95, pp. 123–134, 2013.

[20] O. Allix and L. Blanchard, "Mesomodeling of delamination: Towards industrial applications," *Composites Science and Technology*, vol. 66, no. 6, pp. 731–744, 2006.

[21] L. Maio, E. Monaco, F. Ricci, and L. Lecce, "Simulation of low velocity impact on composite laminates with progressive failure analysis," *Composite Structures*, vol. 103, pp. 75–85, 2013.

[22] H. Wang and T. vu Khanh, "Fracture mechanics and mechanisms of impact-induced delamination in laminated composites," *Journal of Composite Materials*, vol. 29, no. 2, pp. 156–178, 1995.

[23] J. Hodgkinson, *Mechanical Testing of Advanced Fibre Composites*, ser. Woodhead Publishing Series in Composites Science and Engineering, J. Hodgkinson, Ed. Woodhead Publishing, 2000.

[24] J. Lee and C. Soutis, "Experimental investigation on the behaviour of CFRP laminated composites under impact and compression after impact (CAI)," in *EKC2008 Proceedings of the EU-Korea Conference on Science and Technology*, ser. Springer Proceedings in Physics. Berlin, Heidelberg: Springer, 2008, vol. 124.

[25] H.-Y. T. Wu and G. S. Springer, "Measurements of matrix cracking and delamination caused by impact on composite plates," *Journal of Composite Materials*, vol. 22, no. 6, pp. 518–532, 1988.

[26] E. Guynn and T. O'Brien, in *INFLUENCE OF LAY-UP AND THICKNESS ON COMPOSITE IMPACT DAMAGE AND COMPRESSION STRENGTH.*, no. pt 1, 1985, pp. 187–196.

[27] D. Liu, "Impact-induced delamination—a view of bending stiffness mismatching," *Journal of Composite Materials*, vol. 22, no. 7, pp. 674–692, 1988.

[28] S. Takeda, S. Minakuchi, Y. Okabe, and N. Takeda, "Delamination monitoring of laminated composites subjected to low-velocity impact using small-diameter FBG sensors," *Composites Part A: Applied Science and Manufacturing*, vol. 36, no. 7, pp. 903–908, 2005.

[29] *AC No: 20-107B. Composite Aircraft Structure*, U.S. Department of Transportation - Federal Aviation Administration, USA, 2009.

[30] *AC No:25.571-1D - Damage Tolerance and Fatigue Evaluation of Structure*, U.S. Department of Transportation - Federal Aviation Administration, USA, 2011.

[31] *MIL-HDBK No: 1823A. Non destructive evaluation system reliability assessment*, U.S. Department of Defence, USA, 2009.

[32] C. K. Liew, M. Veidt, N. Rajic, K. Tsoi, D. Rowlands, and H. Morton, "Inspections of helicopter composite airframe structures using conventional and emerging nondestructive testing methods," *Journal of Testing and Evaluation*, vol. 39, pp. 1011–1022, 2011.

[33] W. Peng, Y. Zhang, B. Qiu, and H. Xue, "A brief review of the application and problems in ultrasonic fatigue testing," *AASRI Procedia*, vol. 2, no. Supplement C, pp. 127 – 133, 2012.

[34] T. Kroeger, "Thermographic inspection of composites," *Reinforced Plastics*, vol. 58, no. 4, pp. 42 – 43, 2014.

[35] V. Vavilov, O. Budadin, and A. Kulkov, "Infrared thermographic evaluation of large composite grid parts subjected to axial loading," *Polymer Testing*, vol. 41, no. Supplement C, pp. 55 – 62, 2015.

[36] K. Tan, N. Watanabe, and Y. Iwahori, "X-ray radiography and micro-computed tomography examination of damage characteristics in stitched composites subjected to impact loading," *Composites Part B: Engineering*, vol. 42, no. 4, pp. 874 – 884, 2011.

[37] R. H. Bossi and V. Giurgiutiu, "15 - nondestructive testing of damage in aerospace composites," in *Polymer Composites in the Aerospace Industry*, P. E. Irving and C. Soutis, Eds. Woodhead Publishing, 2015.

[38] F. Sarasini and C. Santulli, "10 - non-destructive testing (NDT) of natural fibre composites: acoustic emission technique," in *Natural Fibre Composites*, A. Hodzic and R. Shanks, Eds. Woodhead Publishing, 2014, pp. 273 – 302.

[39] Z. Su, C. Zhou, M. Hong, L. Cheng, Q. Wang, and X. Qing, "Acousto-ultrasonics-based fatigue damage characterization: Linear versus nonlinear signal features," *Mechanical Systems and Signal Processing*, vol. 45, no. 1, pp. 225 – 239, 2014.

[40] Y. Hung, L. Yang, and Y. Huang, "5 - non-destructive evaluation (NDE) of composites: digital shearography," in *Non-Destructive Evaluation (NDE) of Polymer Matrix Composites*, ser. Woodhead Publishing Series in Composites Science and Engineering, V. M. Karbhari, Ed. Woodhead Publishing, 2013, pp. 84 – 115.

[41] S. H. Yang, K. B. Kim, H. G. Oh, and J. S. Kang, "Non-contact detection of impact damage in cfrp composites using millimeter-wave reflection and considering carbon fiber direction," *NDT & E International*, vol. 57, no. Supplement C, pp. 45 – 51, 2013.

[42] B. Ducharne, D. Guyomar, G. Sébald, and B. Zhang, "10 - modeling energy losses in power ultrasound transducers," in *Power Ultrasonics*, J. A. Gallego-Juárez and K. F. Graff, Eds. Oxford: Woodhead Publishing, 2015, pp. 241 – 256.

[43] L. Maio, V. Memmolo, S. Boccardi, C. Meola, F. Ricci, N. Boffa, and E. Monaco, "Ultrasonic and IR Thermographic Detection of a Defect in a Multilayered Composite Plate," *Procedia Engineering*, vol. 167, pp. 71–79, 2016.

[44] N. Meyendorf, P. Nagy, and S. Rokhlin, *Non-destructive Materials Characterization: With Applications to Aerospace Materials*. Berlin, Heidelberg: Springer, 2013.

[45] R. Mulaveesala and S. Tuli, in *AIP Conference Proceedings*, vol. 1004, 2008.

[46] A. Ataş and C. Soutis, "Subcritical damage mechanisms of bolted joints in cfrp composite laminates," *Composites Part B: Engineering*, vol. 54, no. Supplement C, pp. 20 – 27, 2013.

[47] E. Bayraktar, S. Antolovich, and C. Bathias, "New developments in non-destructive controls of the composite materials and applications in manufacturing engineering," *Journal of Materials Processing Technology*, vol. 206, no. 1, pp. 30 – 44, 2008.

[48] S. Gholizadeh, "A review of non-destructive testing methods of composite materials," *Procedia Structural Integrity*, vol. 1, no. Supplement C, pp. 50 – 57, 2016.

[49] A. Katunin, K. Dragan, and M. Dziendzikowski, "Damage identification in aircraft composite structures: A case study using various non-destructive testing techniques," *Composite Structures*, vol. 127, no. Supplement C, pp. 1 – 9, 2015.

[50] F. Aymerich and W. Staszewski, "Impact damage detection in composite laminates using nonlinear acoustics," *Composites Part A: Applied Science and Manufacturing*, vol. 41, no. 9, pp. 1084 – 1092, 2010.

[51] C. Meola, S. Boccardi, and G. Carlomagno, *Infrared Thermography in the Evaluation of Aerospace Composite Materials: Infrared Thermography to Composites*. Woodhead Publishing, 2016.

[52] R. Růžek, R. Lohonka, and J. Jironč, "Ultrasonic c-scan and shearography NDI techniques evaluation of impact defects identification," *NDT & E International*, vol. 39, no. 2, pp. 132 – 142, 2006.

[53] D. Bull, S. Spearing, I. Sinclair, and L. Helfen, "Three-dimensional assessment of low velocity impact damage in particle toughened composite laminates using micro-focus x-ray computed tomography and synchrotron radiation laminography," *Composites Part A: Applied Science and Manufacturing*, vol. 52, pp. 62 – 69, 2013.

[54] F. Ricci, E. Monaco, L. Maio, N. Boffa, and V. Memmolo, "The role of SHM in the design and maintenance of modern and aging structures," in *Proceedings of International Symposium on Dynamic Response and Failure of Composite Materials*, Island of Ischia, 2016.

[55] L. Cot, Y. Wang, C. Bèts, and C. Gogu, "Scheduled and shm structural airframe maintenance applications using a new probabilistic model," in *Proceedings of 7th European Workshop on Structural Health Monitoring, EWSHM 2014 - 2nd European Conference of the Prognostics and Health Management (PHM) Society*, 2014, pp. 2306–2313.

[56] Clean Sky 1 GRA - Green Regional Aircraft. [Online]. Available: http://www.cleansky.eu/green-regional-aircraft-gra

[57] SARISTU - Smart Intelligent Aircraft Structures. [Online]. Available: http://www.saristu.eu/

[58] A. Rytter, "Vibrational based inspection of civil engineering structures," Ph.D. dissertation, Denmark, 1993.

[59] V. Janapati, F. Kopsaftopoulos, F. Li, S. Lee, and F.-K. Chang, "Damage detection sensitivity characterization of acousto-ultrasound-based structural health monitoring techniques," *Structural Health Monitoring*, vol. 15, no. 2, pp. 143–161, 2016.

[60] K. Worden, D. W. Allen, H. Sohn, and C. R. Farrar, "Damage detection in mechanical structures using extreme value statistics," vol. 4693, 2002, pp. 289–299.

[61] E. Monaco, V. Memmolo, F. Ricci, N. Boffa, and L. Maio, "Guided waves based SHM systems for composites structural elements: Statistical analyses finalized at probability of detection definition and assessment," in *Proceedings of SPIE - The International Society for Optical Engineering*, vol. 9438, 2015.

[62] H. Sohn, C. Farrar, N. Hunter, and K. Worden, "Structural health monitoring using statistical pattern recognition techniques," *Journal of Dynamic Systems, Measurement, and Control*, vol. 133, no. 4, pp. 706–711, 2001.

[63] G. Cottone, S. Gollwitzer, U. Heckenberger, and D. Straub, "Reliability-oriented optimization of replacement strategies for monitored composite panels for aircraft structures," in *Structural Health Monitoring 2013: A Roadmap to Intelligent Structures - Proceedings of the 9th International Workshop on Structural Health Monitoring, IWSHM 2013*, vol. 2, 2013, pp. 2728–2735.

[64] A. Gianneo, M. Carboni, and M. Giglio, "Feasibility study of a multi-parameter probability of detection formulation for a lamb waves based structural health monitoring approach to light alloy aeronautical plates," *Structural Health Monitoring*, vol. 16, no. 2, pp. 225–249, 2017.

[65] W. Fan and P. Qiao, "Vibration-based damage identification methods: A review and comparative study," *Structural Health Monitoring*, vol. 10, no. 1, pp. 83–111, 2011.

[66] A. Deraemaeker and K. Worden, *New Trends in Vibration Based Structural Health Monitoring*, ser. CISM International Centre for Mechanical Sciences. Springer Vienna, 2012.

[67] J. Sinou, "A review of damage detection and health monitoring of mechanical systems from changes in the measurement of linear and non-linear vibrations," in *Mechanical Vibrations: Measurement, Effects and Control*, R. C. Sapri, Ed. Nova Science Publishers, Inc., 2013, pp. 647 – 702.

[68] I. Viktorov, *Rayleigh and Lamb Waves: Physical Theory and Applications*, ser. Ultrasonic Technology. Springer US, 1967.

[69] G. Park and D. J. Inman, "Structural health monitoring using piezoelectric impedance measurements," *Philosophical Transactions of the Royal Society of London A: Mathematical, Physical and Engineering Sciences*, vol. 365, no. 1851, pp. 373–392, 2007.

[70] T. Siebel and M. Lilov, "Experimental investigation on improving electromechanical impedance based damage detection by temperature compensation," *Key Engineering Materials*, vol. 569-570, pp. 1132–1139, 2013.

[71] M. Lilov and T. Siebel, "Emilia - a compact impedance analyzer for local integrity assessment," in *Proceedings of the International Conference on Structural Dynamic , EURODYN*, 2014, pp. 2173–2177.

[72] T. Khuc and F. N. Catbas, "Structural identification using computer vision-based bridge health monitoring," *Journal of Structural Engineering*, vol. 144, no. 2, p. 04017202, 2018.

[73] D. Feng and M. Q. Feng, "Vision-based multipoint displacement measurement for structural health monitoring," *Structural Control and Health Monitoring*, vol. 23, no. 5, pp. 876–890, 2016.

[74] T. Yi, H. Li, and M. Gu, "Recent research and applications of gps based technology for bridge health monitoring," *Science China Technological Sciences*, vol. 53, no. 10, pp. 2597–2610, Oct 2010.

[75] S. Kharkovsky and R. Zoughi, "Microwave and millimeter wave nondestructive testing and evaluation - overview and recent advances," *IEEE Instrumentation Measurement Magazine*, vol. 10, no. 2, pp. 26–38, April 2007.

[76] J. Moll, K. Bechtel, B. Hils, and V. Krozer, "Mechanical vibration sensing for structural health monitoring using a millimeter-wave doppler radar sensor," in 7^{th} *European Workshop on Structural Health Monitoring, EWSHM 2014* - 2^{nd} *European Conference of the Prognostics and Health Management (PHM) Society*, 2014, pp. 1802–1808.

[77] J. Moll and V. Krozer, "Radar-based mechanical vibration sensing for structural health monitoring applications: A comparison of radar transceiver measurements at 24 ghz and 100 ghz," in 8^{th} *European Workshop on Structural Health Monitoring, EWSHM 2016*, vol. 3, 2016, pp. 2128–2133.

[78] C. Li, W. Chen, G. Liu, R. Yan, H. Xu, and Y. Qi, "A noncontact fmcw radar sensor for displacement measurement in structural health monitoring," *Sensors*, vol. 15, 2015.

[79] B^2-Monitor: Millimeter-Waves for Monitoring Bats and Blades. [Online]. Available: http://b2monitor.de/

[80] V. Giurgiutiu, *Structural Health Monitoring with Piezoelectric Wafer Active Sensors*, second edition ed., V. Giurgiutiu, Ed. Oxford: Academic Press, 2014.

[81] C. Schaal, H. Samajder, H. Baid, and A. Mal, "Rayleigh to lamb wave conversion at a delamination-like crack," *Journal of Sound and Vibration*, vol. 353, pp. 150–163, 2015.

[82] C. Schaal, S. Zhang, H. Samajder, and A. Mal, "An analytical study of the scattering of ultrasonic guided waves at a delamination-like discontinuity in a plate," *Proceedings of the Institution of Mechanical Engineers, Part C: Journal of Mechanical Engineering Science*, vol. 231, no. 16, pp. 2947–2960, 2017.

[83] H. Lamb, "On waves in an elastic plate," *Proceedings of the Royal Society of London A: Mathematical, Physical and Engineering Sciences*, vol. 93, no. 648, pp. 114–128, 1917.

[84] J. Achenbach, *Wave Propagation in Elastic Solids*, ser. Applied Mathematics and Mechanics Series. North-Holland Publishing Company, 1973.

[85] K. Graff, *Wave Motion in Elastic Solids*, ser. Dover Books on Physics Series. Dover Publications, 1975.

[86] D. Royer, D. Morgan, and E. Dieulesaint, *Elastic Waves in Solids I: Free and Guided Propagation*, ser. Advanced Texts in Physics. Springer Berlin Heidelberg, 1999.

[87] P. B. Nagy, *Introduction to ultrasounds*, 2001.

[88] J. Rose, *Ultrasonic Waves in Solid Media.* Cambridge University Press, 2004.

[89] J. L. Rose, *Ultrasonic Guided Waves in Solid Media.* Cambridge University Press, 2014.

[90] A. Mal, F. Ricci, H. Samajder, and H. Baid, "NDE of composite structures using ultrasonic guided waves," in *Proceedings of SPIE - The International Society for Optical Engineering*, vol. 8695, no. 86950E, 2013.

[91] Z. Su and L. Ye, *Identification of Damage Using Lamb Waves: From Fundamentals to Applications*, ser. Lecture Notes in Applied and Computational Mechanics. Springer London, 2009.

[92] A. Ebrahimkhanlou, B. Dubuc, and S. Salamone, "Damage localization in metallic plate structures using edge-reflected lamb waves," *Smart Materials and Structures*, vol. 25, no. 8, p. 085035, 2016.

[93] L. Maio, V. Memmolo, F. Ricci, N. Boffa, E. Monaco, and R. Pecora, "Ultrasonic wave propagation in composite laminates by numerical simulation," *Composite Structures*, vol. 121, 2016.

[94] L. Maio, V. Memmolo, F. Ricci, N. Boffa, and E. Monaco, "Investigation on fundamental modes of guided waves propagating in symmetric and nonsymmetric composite laminates," *Proceedings of the Institution of Mechanical Engineers, Part C: Journal of Mechanical Engineering Science*, vol. 231, no. 16, pp. 2988–3000, 2017.

[95] W. Staszewski, C. Boller, and G. Tomlinson, *Health Monitoring of Aerospace Structures: Smart Sensor Technologies and Signal Processing.* Wiley, 2004.

[96] C. Knapp and G. Carter, "The generalized correlation method for estimation of time delay," *IEEE Transactions on Acoustics, Speech, and Signal Processing*, vol. 24, no. 4, Aug 1976.

[97] D. Marioli, C. Narduzzi, C. Offelli, D. Petri, E. Sardini, and A. Taroni, "Digital time-of-flight measurement for ultrasonic sensors," *IEEE Transactions on Instrumentation and Measurement*, vol. 41, no. 1, pp. 93–97, Feb 1992.

[98] G. Hueber, T. Ostermann, T. Bauernfeind, R. Raschhofer, and R. Hagelauer, "New approach of ultrasonic distance measurement technique in robot applications," in *WCC 2000 - ICSP 2000. 2000* 5^{th} *International Conference on Signal Processing Proceedings.* 16^{th} *World Computer Congress 2000*, vol. 3, 2000, pp. 2066–2069.

[99] V. Memmolo, F. Ricci, L. Maio, N. Boffa, and E. Monaco, "Model assisted probability of detection for a guided waves based SHM technique," in *Proceedings of SPIE - The International Society for Optical Engineering*, vol. 9805, 2016.

[100] L. Cremer, M. Heckl, and B. A. T. Petersson, *Structure-borne sound: Structural vibrations and sound radiation at audio frequencies*, 2005.

[101] F. J. Harris, "On the use of windows for harmonic analysis with the discrete fourier transform," *Proceedings of the IEEE*, vol. 66, no. 1, pp. 51–83, Jan 1978.

[102] B. Auld, *Acoustic fields and waves in solids, volumes I and II*, 1975.

[103] A. Oppenheim and G. Verghese, *Signals, Systems and Inference, Global Edition.* Pearson Education, Limited, 2016.

[104] V. Giurgiutiu, "Piezoelectric wafer active sensors - PWAS transducers," in *Structural Health Monitoring with Piezoelectric Wafer Active Sensors*, second edition ed., V. Giurgiutiu, Ed. Oxford: Academic Press, 2014, pp. 357 – 394.

[105] V. Memmolo, M. Cindolo, F. Ricci, N. Boffa, L. Maio, and E. Monaco, "A user interface damage detection technique based on a multi-parameter methodology," *Procedia Engineering*, vol. 167, pp. 39–47, 2016.

[106] T. R. Hay, R. L. Royer, H. Gao, X. Zhao, and J. L. Rose, "A comparison of embedded sensor lamb wave ultrasonic tomography approaches for material loss detection," *Smart Materials and Structures*, vol. 15, no. 4, p. 946, 2006.

[107] N. Testoni, L. De Marchi, and A. Marzani, "Detection and characterization of delaminations in composite plates via air-coupled probes and warped-domain filtering," *Composite Structures*, vol. 153, pp. 773–781, 10 2016.

[108] X. Zhao, R. L. Royer, S. E. Owens, and J. L. Rose, "Ultrasonic lamb wave tomography in structural health monitoring," *Smart Materials and Structures*, vol. 20, no. 10, p. 105002, 2011.

[109] L. De Marchi, A. Marzani, J. Moll, P. Kudela, M. Radzieński, and W. Ostachowicz, "A pulse coding and decoding strategy to perform Lamb wave inspections using simultaneously multiple actuators," *Mechanical Systems and Signal Processing*, vol. 91, pp. 111–121, 2017.

[110] J. E. Michaels and T. E. Michaels, "Guided wave signal processing and image fusion for in situ damage localization in plates," *Wave Motion*, vol. 44, no. 6, pp. 482 – 492, 2007.

[111] A. J. Croxford, J. Moll, P. D. Wilcox, and J. E. Michaels, "Efficient temperature compensation strategies for guided wave structural health monitoring," *Ultrasonics*, vol. 50, no. 4, pp. 517 – 528, 2010.

[112] V. Memmolo, L. Maio, N. Boffa, E. Monaco, and F. Ricci, "Damage detection tomography based on guided waves in composite structures using a distributed sensor network," *Optical Engineering*, vol. 55, no. 1, 2016.

[113] V. Memmolo, E. Monaco, N. Boffa, L. Maio, and F. Ricci, "Guided wave propagation and scattering for structural health monitoring of stiffened composites," *Composite Structures*, pp. –, 2017.

[114] K. Worden, G. Manson, and N. Fieller, "Damage detection using oulier analysis," *Journal of Sound and Vibration*, vol. 229, pp. 647–667, 2000.

[115] M. Fugate, H. Sohn, and C. Farrar, "Vibration-based damage detection using statistical process control," *Mechanical Systems and Signal Processing*, vol. 15, pp. 707–721, 2001.

[116] H. Sohn, J. A. Czarnecki, and C. R. Farrar, "Structural health monitoring using statistical process control," *Journal of Structural Engineering*, vol. 126, no. 11, pp. 1356–1363, 2000.

[117] L. Bornn, C. R. Farrar, G. Park, and K. Farinholt, "Structural health monitoring with autoregressive support vector machines," *Journal of Vibration and Acoustics*, vol. 131, pp. 021 004–021 004–9, 2009.

[118] C. Farrar and K. Worden, *Structural Health Monitoring: A Machine Learning Perspective*. Wiley, 2012.

[119] L. A. N. Laboratory and U. States., *A Comparison Study of Modal Parameter Confidence Intervals Computed Using the Monte Carlo and Bootstrap Techniques*. United States. Department of Energy. Office of the Assistant Secretary, Management and Administration., 1998.

[120] M. Hazewinkel, *Encyclopaedia of Mathematics: Volume 3 Heaps and Semi-Heaps — Moments, Method of (in Probability Theory)*, ser. Encyclopaedia of Mathematics. Springer US, 2013.

[121] M. Mitra and S. Gopalakrishnan, "Guided wave based structural health monitoring: A review," *Smart Materials and Structures*, vol. 25, no. 5, p. 053001, 2016.

[122] J. Moll, R. Schulte, B. Hartmann, C.-P. Fritzen, and O. Nelles, "Multi-site damage localization in anisotropic plate-like structures using an active guided wave structural health monitoring system," *Smart Materials and Structures*, vol. 19, no. 4, 2010.

[123] V. Memmolo, N. Boffa, L. Maio, E. Monaco, F. Ricci, and N. Pasquino, "Experimental characterization of a composite structures health monitoring methodology," in *3rd IEEE International Workshop on Metrology for Aerospace, MetroAeroSpace 2016 - Proceedings*, 2016.

[124] B. D. V. Veen and K. M. Buckley, "Beamforming: a versatile approach to spatial filtering," *IEEE ASSP Magazine*, vol. 5, no. 2, pp. 4–24, April 1988.

[125] G. McLaskey, S. Glaser, and C. Grosse, "Acoustic emission beamforming for enhanced damage detection," in *Proceedings of SPIE, Sensors and Smart Structures Technologies for Civil, Mechanical, and Aerospace Systems 2008.*, vol. 6932, no. 693239, 2008.

[126] T. Stepinski and M. Engholm, "Advanced beamforming of 2d arrays for structural health monitoring using lamb waves," in *Proceedings of the* 5^{th} *European Workshop on Structural Health Monitoring 2010*, 2010, pp. 1011–1016.

[127] P. Wölcken and M. Papadopoulos, *Smart Intelligent Aircraft Structures (SARISTU): Proceedings of the Final Project Conference.* Springer International Publishing, 2015.

[128] J. P. Koduru and J. L. Rose, "Mode controlled guided wave tomography using annular array transducers for shm of water loaded plate like structures," *Smart Materials and Structures*, vol. 22, no. 12, p. 125021, 2013.

[129] V. Memmolo, F. Ricci, N. Boffa, L. Maio, and E. Monaco, "Structural Health Monitoring in Composites Based on Probabilistic Reconstruction Techniques," *Procedia Engineering*, vol. 167, pp. 48–55, 2016.

[130] E. Monaco, V. Memmolo, N. Boffa, L. Maio, and F. Ricci, "Guided waves based SHM systems: parameters selection for better identification and localization of damages in composites stiffened plates," in *Proceedings of* SPIE - *Health monitoring of structural and biological system 2017*, vol. 10170, no. 101701E, 2017.

[131] E. Monaco, N. Boffa, V. Memmolo, F. Ricci, and L. Maio, "Detecting delaminations and disbondings on full-scale wing composite panel by guided waves based SHM system," in *Proceedings of SPIE - The International Society for Optical Engineering*, vol. 9805, 2016.

[132] W. H. Ong and W. K. Chiu, "Redirection of lamb waves for structural health monitoring," *Smart Materials researches*, vol. 2012, no. 718686, p. 9, 2012.

[133] I. Kim and A. Chattopadhyay, "Guided lamb wave-based structural health monitoring using a novel wave packet tracing method for damage localization and size quantification," *Journal of Intelligent Material Systems and Structures*, vol. 26, no. 18, pp. 2515–2530, 2015.

[134] F. Ricci, E. Monaco, L. Maio, N. Boffa, and A. Mal, "Guided waves in a stiffened composite laminate with a delamination," *Structural Health Monitoring*, 2016.

[135] A. Gunawan and S. Hirose, "Reflection of obliquely incident guided waves by an edge of a plate," *MATERIALS TRANSACTIONS*, vol. 48, no. 6, pp. 1236–1243, 2007.

[136] L. Maio, F. Ricci, V. Memmolo, E. Monaco, and N. Boffa, "Application of laser doppler vibrometry for ultrasonic velocity assessment in a composite panel with defect," *Composite Structures*, vol. 184, no. Supplement C, pp. 1030 – 1039, 2018.

[137] SMART Layer® technologies. Built-in sensor network of Structural Health Monitoring. [Online]. Available: http://www.acellent.com/en/products/sensors/

[138] A. H. Nayfeh and D. E. Chimenti, "Free wave propagation in plates of general anisotropic media," *Journal of Applied Mechanics*, vol. 56, 1989.

[139] D. L. Anderson, "Elastic wave propagation in layered anisotropic media," *Journal of Geophysical Research*, vol. 66, no. 9, pp. 2953–2963, 1961.

[140] A. Nayfeh, *Wave Propagation in Layered Anisotropic Media: with Application to Composites*, ser. North-Holland Series in Applied Mathematics and Mechanics. Elsevier Science, 1995.

[141] A. K. Mal and S. Lih, "Elastodynamic response of a unidirectional composite laminate to concentrated surface loads: Part i," *ournal of Applied Mechanics*, vol. 59, pp. 878–886.

[142] S. Lih and A. K. Mal, "Elastodynamic response of a unidirectional composite laminate to concentrated surface loads: Part ii," *ournal of Applied Mechanics*, vol. 59, pp. 887–892.

[143] S.-S. Lih and A. K. Mal, "On the accuracy of approximate plate theories for wave field calculations in composite laminates," *Wave Motion*, vol. 21, no. 1, pp. 17 – 34, 1995, honor and Memory of Julius Miklowitz.

[144] H. Samajder, H. Baid, F. Ricci, and A. Mal, "Lamb waves in a honeycomb composite sandwich plate," pp. 8695 – 8695 – 11, 2013.

[145] F. Moser, L. J. Jacobs, and J. Qu, "Modeling elastic wave propagation in waveguides with the finite element method," *NDT & E International*, vol. 32, no. 4, pp. 225 – 234, 1999.

[146] J. Zhao, J. Qiu, H. Ji, and N. Hu, "Four vectors of lamb waves in composites: Semianalysis and numerical simulation," *Journal of Intelligent Material Systems and Structures*, vol. 24, no. 16, pp. 1985–1994, 2013.

[147] J. Reddy, *Mechanics of Laminated Composite Plates and Shells: Theory and Analysis, Second Edition.* Taylor & Francis, 2004.

[148] J. Ashton and J. Whitney, *Theory of laminated plates*, ser. Progress in materials science series. Technomic, 1970.

[149] W. H. Prosser, "The propagation characteristics of the plate modes of acoustic emission waves in thin aluminum plates and thin graphite/epoxy composite plates and tubes," *The Journal of the Acoustical Society of America*, vol. 92, no. 6, pp. 3441–3442, 1992.

[150] R. Mindlin, "Influence of rotary inertia and shear on flexural motions of isotropic, elastic plates," *Journal of Applied Mechanics*, 1951.

[151] Y. Liu, N. Hu, C. Yan, X. Peng, and B. Yan, "Construction of a mindlin pseudospectral plate element and evaluating efficiency of the element," *Finite Elements in Analysis and Design*, vol. 45, no. 8, pp. 538 – 546, 2009.

[152] A. Żak, "A novel formulation of a spectral plate element for wave propagation in isotropic structures," *Finite Elements in Analysis and Design*, vol. 45, no. 10, pp. 650 – 658, 2009.

[153] J. Whitney and C. Sun, "A higher order theory for extensional motion of laminated composites," *Journal of Sound and Vibration*, vol. 30, no. 1, pp. 85 – 97, 1973.

[154] R. Tanov and A. Tabiei, "A simple correction to the first-order shear deformation shell finite element formulations," *Finite Elements in Analysis and Design*, vol. 35, no. 2, pp. 189 – 197, 2000.

[155] R. Rolfes and K. Rohwer, "Improved transverse shear stresses in composite finite elements based on first order shear deformation theory," *International Journal for Numerical Methods in Engineering*, vol. 40, no. 1, pp. 51–60, 1997.

[156] G. Alfano, F. Auricchio, L. Rosati, and E. Sacco, "Mitc finite elements for laminated composite plates," *International Journal for Numerical Methods in Engineering*, vol. 50, no. 3, pp. 707–738, 2001.

[157] S. S. Ramesh, C. Wang, J. Reddy, and K. Ang, "A higher-order plate element for accurate prediction of interlaminar stresses in laminated composite plates," *Composite Structures*, vol. 91, no. 3, pp. 337 – 357, 2009.

[158] L. Wang and F. G. Yuan, "Lamb wave propagation in composite laminates using a higher-order plate theory," vol. 6531, 2007, pp. 6531 – 6531 – 12.

[159] J. Zhao, H. Ji, and J. Qiu, "Modeling of lamb waves in composites using new third-order plate theories," *Smart Materials and Structures*, vol. 23, no. 4, p. 045017, 2014.

[160] C. Yang, L. Ye, Z. Su, and M. Bannister, "Some aspects of numerical simulation for lamb wave propagation in composite laminates," *Composite Structures*, vol. 75, no. 1, pp. 267 – 275, 2006.

[161] J. Whitney, "Shear correction factors for orthotropic laminates under static load," *Journal of Applied Mechanics, Transactions ASME*, vol. 40, no. 1, pp. 302–304, 1973.

[162] W. Burton and A. K. Noor, "Assessment of computational models for sandwich panels and shells," *Computer Methods in Applied Mechanics and Engineering*, vol. 124, no. 1, pp. 125 – 151, 1995.

[163] K. Sze, L.-W. He, and Y. Cheung, "Predictor–corrector procedures for analysis of laminated plates using standard mindlin finite element models," *Composite Structures*, vol. 50, no. 2, pp. 171 – 182, 2000.

[164] P. Yang, C. H. Norris, and Y. Stavsky, "Elastic wave propagation in heterogeneous plates," *International Journal of Solids and Structures*, vol. 2, no. 4, pp. 665 – 684, 1966.

[165] T. Chow, "On the propagation of flexural waves in an orthotropic laminated plate and its response to an impulsive load," *Journal of Composite Materials*, vol. 5, no. 3, pp. 306–319, 1971.

[166] S. B. Dong and F. K. W. Tso, "On a laminated orthotropic shell theory including transverse shear deformation," *Journal of Applied Mechanics*, vol. 39, pp. 1091–1097, 1972.

[167] C. W. Bert, "Simplified analysis of static shear factors for beams of nonhomogeneous cross section," *Journal of Composite Materials*, vol. 7, no. 4, pp. 525–529, 1973.

[168] L. Wang and F. Yuan, "Group velocity and characteristic wave curves of lamb waves in composites: Modeling and experiments," *Composites Science and Technology*, vol. 67, no. 7, pp. 1370 – 1384, 2007.

[169] P. F. Pai, "A new look at shear correction factors and warping functions of anisotropic laminates," *International Journal of Solids and Structures*, vol. 32, no. 16, pp. 2295 – 2313, 1995.

[170] A. Ramaswamy, F. Barzegar, and G. Z. Voyiadjis, "Study of layering procedures in finite-element analysis of rc flexural and torsional elements," *Journal of Structural Engineering*, vol. 121, no. 12, pp. 1773–1783, 1995.

[171] J. Figueiras, *Ultimate load analysis of anisotropic and reinforced concrete plates and shells*, ser. PhD Thesis. University College of Swansea, 1974.

[172] A. Ferreira, *MATLAB Codes for Finite Element Analysis: Solids and Structures*, ser. Solid Mechanics and Its Applications. Springer Netherlands, 2008.

[173] S.-Y. Lee, G. Rus, and T. Park, "Detection of stiffness degradation in laminated composite plates by filtered noisy impact testing," *Computational Mechanics*, vol. 41, no. 1, pp. 1–15, 2007.

[174] J. Aldrin, E. Medina, E. Lindgren, C. Buynak, and J. Knopp, "Protocol for reliability assessment of structural health monitoring systems incorporating model-assisted probability of detection (MAPOD) approach," in *Structural Health Monitoring 2011: Condition-Based Maintenance and Intelligent Structures - Proceedings of the 8th International Workshop on Structural Health Monitoring*, vol. 2, 2011, pp. 2452–2459.

[175] C. N. Sathyanarayana, U. Ashwin, and S. Raja, "Effect of sensor debonding on lamb wave propagation in plate structure," *ARPN Journal of Engineering and Applied Sciences*, vol. 9, 2014.

[176] I. Mueller, A. Shpak, M. Golub, and C.-P. Fritzen, "Effects of debonding of pwas on the wave propagation and the electro-mechanical impedance spectrum," vol. 3, 2016, pp. 1847–1856.

[177] I. Buethe, B. Eckstein, and C.-P. Fritzen, "Model-based detection of sensor faults under changing temperature conditions," *Structural Health Monitoring*, vol. 13, no. 2, pp. 109–119, 2014.

[178] T. G. Overly, G. Park, K. M. Farinholt, and C. R. Farrar, "Piezoelectric active-sensor diagnostics and validation using instantaneous baseline data," *IEEE Sensors Journal*, vol. 9, no. 11, pp. 1414–1421, Nov 2009.

[179] G. Park, C. R. Farrar, F. L. di Scalea, and S. Coccia, "Performance assessment and validation of piezoelectric active-sensors in structural health monitoring," *Smart Materials and Structures*, vol. 15, no. 6, p. 1673, 2006.

[180] M. Golub, I. Buethe, A. Shpak, C. Fritzen, H. Jung, and J. Moll, "Analysis of lamb wave excitation by the partly debonded circular piezoelectric wafer active sensors," in *Proceedings of 11th European Conference on Non-Destructive Testing*, 2014.

[181] B. Poddar, C. R. Bijudas, M. Mitra, and P. M. Mujumdar, "Damage detection in a woven-fabric composite laminate using time-reversed lamb wave," *Structural Health Monitoring*, vol. 11, no. 5, pp. 602–612, 2012.

[182] H. Tinoco and A. Serpa, "Voltage relations for debonding detection of piezoelectric sensors with segmented electrode," *Mechanical Systems and Signal Processing*, vol. 31, pp. 258–267, 2012.

[183] G. Lanzara, Y. Yoon, Y. Kim, and F.-K. Chang, "Influence of interface degradation on the performance of piezoelectric actuators," *Journal of Intelligent Material Systems and Structures*, vol. 20, no. 14, pp. 1699–1710, 2009.

[184] J. Moll, M. Golub, E. Glushkov, N. Glushkova, and C.-P. Fritzen, "Non-axisymmetric lamb wave excitation by piezoelectric wafer active sensors," *Sensors and Actuators, A: Physical*, vol. 174, no. 1, pp. 173–180, 2012.

[185] I. Mueller and C.-P. Fritzen, "Inspection of piezoceramic transducers used for structural health monitoring," *Materials*, vol. 10, no. 1, 2017.

[186] C. Liang, F. Sun, and C. Rogers, "Coupled electro-mechanical analysis of adaptive material systems — determination of the actuator power consumption and system energy transfer," *Journal of Intelligent Material Systems and Structures*, vol. 5, no. 1, pp. 12–20, 1994.

[187] F. P. Sun, Z. Chaudhry, C. Liang, and C. A. Rogers, "Truss structure integrity identification using pzt sensor-actuator," *Journal of Intelligent Material Systems and Structures*, vol. 6, no. 1, pp. 134–139, 1995.

[188] G. Park, H. Sohn, C. Farrar, and D. Inman, "Overview of piezoelectric impedance-based health monitoring and path forward," *Shock and Vibration*, vol. 35, no. 6, pp. 451–463, 2003.